

School of Electrical Engineering, Computing and
Mathematical Sciences

**Atomistic Simulations of Diamond:
Implantation, Annealing, Deformation and Relaxation**

Alireza Aghajamali

(ORCID iD: 0000-0003-0932-0513)

This thesis is presented for the Degree of
Doctor of Philosophy
of
Curtin University

February 2020

Declaration

To the best of my knowledge and belief this thesis contains no material previously published by any other person except where due acknowledgement has been made. This thesis contains no material which has been accepted for the award of any other degree or diploma in any university.

Alireza Aghajamali

6th February 2020

Abstract

Carbon is one of the most fascinating elements in the periodic table due to its ability to form different hybridizations of electron orbitals: sp , sp^2 and sp^3 . A large variety of carbon allotropes with a wide array of properties result from controlling these hybridizations. In this thesis the focus is on diamond, where the hybridization is sp^3 . Using computer simulation, we employ a molecular dynamics (MD) methodology to study annealing, implantation, mechanical deformation and structural relaxation in various forms of diamond. The systems studied range from nanodiamonds (NDs) found in meteorites, diamond nanopillars bent in an electron microscope and epitaxial diamond interfaces in semiconductor heterostructures. Two chapters address the fundamentals of computer simulation of carbon, while the other four chapters are closely motivated by experimental results from collaborators and the literature.

In Chapter 2, we examine a common variant of the widely-used Tersoff potential in which the coefficient of the upper cutoff is increased to 2.45 Å to improve the properties of amorphous carbon. We demonstrate that this modification leads to nucleation of diamond nanocrystals during annealing of amorphous carbon. This behavior, which we show to be unphysical, occurs due to interactions between the cutoff function and the second neighbor shell. It does not, unfortunately, represent a new pathway for synthesizing diamond.

In Chapter 3, we study fourteen well-known and commonly used interatomic potentials for carbon and compare their capability to model carbon. Surprisingly, no two potentials are found to yield the same result. GAP, ReaxFF and

EDIP are the best transferable potentials for the disordered carbon structures, and from the computational cost perspective, EDIP is found to be the most efficient interatomic potential. In addition, we develop a web application tool, www.carbonpotentials.org, which collates all the data from our findings and enables users to perform a real-time comparison of any combination of data sets.

In Chapters 4 and 5, MD simulations are used to answer two important astrophysical questions: (i) how do noble gases become incorporated into meteorite NDs? and (ii) how are noble gases released from NDs upon thermal annealing? Chapter 4 is motivated by ion-implantation experiments at the University of Huddersfield, UK, where xenon is implanted into NDs. We provide atomistic simulations into the irradiation process to understand the experimental results and investigate the implantation of noble gas into NDs of different sizes and factor in different implantation energies. We show that the low energy of noble gas implantation into the meteoritic size of ND is a suitable mechanism for entrapment of noble gases into NDs. In Chapter 5, a large number of simulations are employed to provide detailed atomistic insight into the thermal release patterns of implanted noble gases from NDs. Intriguingly, these results predict a unimodal temperature release distribution for the light noble gases and a bimodal behavior for the heavy noble gases, which is precisely the observation from meteoritic and laboratory study of NDs.

In Chapter 6, we use MD simulations to study the origin of unexpected plastic deformation of diamond nanopillars. This work is motivated by collaboration with an experimental group at the University of Technology Sydney. In their experiment, they employ the electron beam of a scanning electron microscope to charge nanopillars and their surroundings, and the resulting electrostatic forces cause the nanopillars to bend. We show that this new form of plastic deformation is strongly dependent on the size of the nanopillar and crystallographic orientation of the diamond. With atomistic simulations, we find that this mechanical deformation of (001)-oriented nanopillars can be explained by the emergence of

a new phase of carbon, O8-carbon, which is localized to the deformed regions of the bent diamond nanopillars.

Finally, in Chapter 7, atomistic simulations are performed to understand the nature of the interface between diamond and silicon carbide. This work is motivated by collaboration with an experimental group at the University of Melbourne, where they studied heteroepitaxial growth of silicon carbide on diamond. Atomistic simulations show that the large lattice mismatch of 22% is resolved through bonding reconstructions at the interface, which alleviates the lattice strain via point dislocations in a plane without forming extended defects in three dimensions. The methodology developed in this chapter can potentially be applied to other heterostructures with large lattice mismatches such as silicon on silicon-carbide.

Acknowledgements

I would like to take this opportunity to express my immense gratitude to my supervisor, A/Prof. Nigel Marks, for his continuous guidance, support and advice, and for assisting me in each step towards completing this thesis. My deepest gratitude goes to him for his kindness, patience, availability, and constant encouragement.

I would also like to thank my co-supervisors, Dr. Irene Suarez-Martinez and Dr. Carla de Tomas for sharing their expertise and continuous encouragement. Thank you so much for always having your door open to me, and being willing to discuss anything and everything that needed discussing. Nigel, Irene and Carla, this work would not have been possible without your always helpful support.

I acknowledge the HDR Mobility Scholarship for supporting my expenses to visit Prof. Igor Aharonovich and Prof. Milos Toth's group at University of Technology Sydney (UTS), which gave me an opportunity to work closely with our collaborators. My appreciations extend to Dr. Brendan McGann and the academic and professional staff in the Department of Physics & Astronomy for providing a vibrant and supportive research environment.

Lastly, my deepest gratitude goes to my family and friends. Thanks to my parents, sister and brother for their tremendous support and encouragement from the very beginning. Finally, my love goes to my beautiful wife, Dr. Parisa Shams. I could not have done this without her infinite support. Parisa, you are my everything!

List of publications

During my Ph.D., I have co-authored 5 papers, which are listed below in the order in which they appear in the chapters. The papers marked with an asterisk (*) resulted from our collaboration with experimental groups. The experimental context of these studies have been presented in the Introduction (Chapter 1) and the corresponding chapters have been edited to focus on the computer simulations. The green numbers indicate the 2019 Impact Factors (IF).

- **Aghajamali, A.**, C. de Tomas, I. Suarez-Martinez and N. A. Marks (2018). Unphysical nucleation of diamond in the extended cutoff Tersoff potential. *Molecular Simulation* 44, 164–171. (IF: 1.72)
[doi: 10.1080/08927022.2017.1355555](https://doi.org/10.1080/08927022.2017.1355555)
(Chapter 2)
- de Tomas, C. †, **A. Aghajamali** †, J. L. Jones, D. L. Lim, M. L. Lopez, I. Suarez-Martinez and N. A. Marks (2019). Transferability of interatomic potentials for carbon. *Carbon* 155, 624–634. (IF: 8.82)
[doi: 10.1016/j.carbon.2019.07.074](https://doi.org/10.1016/j.carbon.2019.07.074)
(Chapter 3)
- Fogg, J. L., **A. Aghajamali**, J. A. Hinks, S. E., Donnelly, A. A. Shiryaev and N. A. Marks (2019). Modification of nanodiamonds by xenon implantation: A molecular dynamics study. *Nuclear Instruments and Methods in Physics Research Section B* 453, 32–40. (IF: 1.27)

† These authors contributed equally to this work.

[doi: 10.1016/j.nimb.2019.05.062](https://doi.org/10.1016/j.nimb.2019.05.062)

(Chapter 4)

- Regan. B., **A. Aghajamali**, J. Froech, T. Trong Tran, J. Scott, J. Bishop, I. Suarez-Martinez, Y. Liu, J. M. Cairney, N. A. Marks, M. Toth and I. Aharonovich (2020). Plastic deformation of single crystal diamond nanopillars. *Advanced Materials* 32, 1906458. (*) (IF: 27.39)

[doi: 10.1002/adma.201906458](https://doi.org/10.1002/adma.201906458)

(Chapter 6)

- A. Tsai, **A. Aghajamali**, N. Dontschuk, B. C. Johnson, M. Usman, A. K. Schenk, M. Sear, C. I. Pakes, L. C. L. Hollenberg, J. C. McCallum, S. Rubanov, A. Tadich, N. A. Marks, and A. Stacey. (2020). Epitaxial formation of SiC on (100) diamond. *ACS Applied Electronic Materials* 2, 2003–2009. (*)

[doi: 10.1021/acsaelm.0c00289](https://doi.org/10.1021/acsaelm.0c00289)

(Chapter 7)

The statements of contributions from co-authors of the publications are presented in Appendix A. Also, I warrant that I have obtained in Appendix B permission from the copyright owners to use any third party copyright material reproduced in the thesis (e.g., questionnaires, artwork, unpublished letters), or to use any of my own published work (e.g., journal articles) in which the copyright is held by another party (e.g., publisher, co-author).

Statement of candidate contributions

This thesis includes five original published papers (Chapters 2, 3, 4, 6 and 7) and one paper (Chapter 5) will be submitted for publication in peer-reviewed journal. Data collection and data analysis of all the simulation studies and also writing up of all the papers in the thesis were the principal responsibility of myself, Alireza Aghajamali, working under the supervision of A/Prof. Nigel Marks, Dr. Irene Suarez-Martinez and Dr. Carla de Tomas. The statement of candidate contribution to the papers are specified below.

- **Chapter 2:**

I was instrumental in data collection (100%), data analysis (100%) and production of figures and movie (100%). All the authors have contributed to the writing and editing the paper.

- **Chapter 3:**

It was primarily my responsibility to conceptualise, collect ($\sim 60\%$) and analyse data ($\sim 80\%$) and produce figures ($\sim 80\%$). All the authors have contributed to the writing and editing of the paper. Web application tool is created by Jake Jones, and I uploaded $\sim 60\%$ of data and also modified the text.

- **Chapter 4:**

Jason Fogg collected most of the data, and I analysed the data ($\sim 50\%$)

and produced figures ($\sim 50\%$) and movies (100%). All the authors have contributed to the writing and editing of the paper.

- **Chapter 5:**

It was primarily my responsibility to conceptualise, collect and analyse data, produce figures and movies, write and edit the paper, with editorial input from my principal supervisor.

- **Chapter 6:**

I was instrumental in designing the methodology (100%), data collection (100%), data analysis (100%) and the production of figures and movies (100%) for all phases of the MD simulation study. Irene Suarez-Martinez did the DFT calculation. Blake Regan, Ph.D. candidate at the University of Technology Sydney, did the experimental study of the work. All the authors have contributed towards editing the paper and participated in the final corrections.

- **Chapter 7:**

I was instrumental in designing the methodology (100%), data collection (100%), data analysis (100%) and the production of figures and movies (100%) for all phases of the simulation study. Alexander Tsai, Ph.D. candidate at the University of Melbourne, did the experimental phase of the study. All the authors have contributed to editing the paper.

We the undersigned agree with the above stated proportion of work undertaken for each of the above papers contributing to this thesis:

Alireza Aghajamali

(Candidate)

A/Prof. Nigel Marks

(Principal supervisor)

List of conference presentations during the Ph.D. program

Details of nine conference presentations during my Ph.D. are listed below.

1. **Aghajamali, A.**, C. de Tomas, I. Suarez-Martinez and N. A. Marks (December, 2016). Unphysical nucleation of diamond in the extended cutoff Tersoff potential. *Australian Symposium on Computational Chemistry*, The University of Western Australia, Perth, Australia.
2. **Aghajamali, A.**, C. de Tomas, I. Suarez-Martinez and N. A. Marks (July, 2016). Unphysical nucleation of diamond in the extended cutoff Tersoff potential. *Carbon*, Melbourne, Australia.
3. **Aghajamali, A.**, C. de Tomas, I. Suarez-Martinez and N. A. Marks (September, 2017). Unphysical nucleation of diamond in the extended cutoff Tersoff potential. *Molecular Modelling*, Margaret River, Australia.
4. **Aghajamali, A.**, C. de Tomas, I. Suarez-Martinez and N. A. Marks (November, 2017). Unphysical nucleation of diamond in the extended cutoff Tersoff potential. *Australian Institute of Physics Western Australian Postgraduate*, The University of Western Australia, Perth, Australia, 2017.
5. **Aghajamali, A.** and N. A. Marks (November, 2018). Noble gases release upon thermal annealing of nanodiamonds: A molecular dynamics study.

Australian Institute of Physics Western Australian Postgraduate, The University of Western Australia, Perth, Australia.

([Aghajamali and Marks, 2018](#))

6. **Aghajamali, A.** and N. A. Marks (December, 2018). Noble gases release upon thermal annealing of nanodiamonds: A molecular dynamics study. *Australian Carbon Society Student*, The University of Sydney, Sydney, Australia.
7. **Aghajamali, A.** and N. A. Marks (December, 2018). Xenon release upon thermal annealing of nanodiamonds: A molecular dynamics study. *23rd Australian Institute of Physics Congress*, The University of Western Australia, Perth, Australia.
8. **Aghajamali, A.** and N. A. Marks (June, 2019). Predicting noble gases release temperatures of pre-solar nanodiamonds. *Carbon Science & Technology Workshop*, Curtin University, Perth, Australia.
9. **Aghajamali, A.** and N. A. Marks (November, 2019). Predicting release temperatures of noble gases in pre-solar nanodiamonds. *2nd Western Australia Computational Chemistry Conference*, The University of Western Australia, Perth, Australia.

List of abbreviations

<i>a</i> -C	Amorphous Carbon
ABOP	Analytic Bond Order Potential
AIREBO	Adaptive Intermolecular REBO
COMB	Charge Optimized Many Body
CVD	Chemical Vapor Deposition
DNP	Diamond Nanopillar
DNW	Diamond Nanowire
EDIP	Environment Dependent Interaction Potential
FFT	Fast Fourier Transform
GAP	Gaussian Approximation Potential
HPHT	High Pressure High Temperature
HRTEM	High Resolution Transmission Electron Microscope
LAMMPS	Large-scale Atomic/Molecular Massively Parallel Simulator
LCBOP	Long-range Carbon Bond Order Potential
LJ	Lennard-Jones
MD	Molecular Dynamics
MEAM	Modified Embedded Atom Method
MIAMI	Microscope and Ion Accelerator for Materials Investigations

List of abbreviations

ML	Machine Learning
MSD	Mean Squared Displacement
ND	Nanodiamond
NEXAFS	Near Edge X-ray Absorption Fine Structure
NVE	MD ensemble (constant number of particles, volume and energy)
NVP	MD ensemble (constant number of particles, volume and pressure)
NVT	MD ensemble (constant number of particles, volume and temperature)
OVITO	Open Visualization Tool
RDF	Radial Distribution Function
ReaxFF	Reactive Force Field
REBO	Reactive Empirical Bond-Order
RIE	Reactive Ion Etching
RSS	Reaction State Summation
SED-AIREBO	Screened Environment Dependent AIREBO
SRIM	Stopping and Range of Ions in Matter
STM	Scanning Tunneling Microscopy
SWCNT	Single-Walled Carbon Nanotubes
TEM	Transmission Electron Microscope
UDD	Ultradispersed Detonation Diamond
ZBL	Ziegler-Biersack-Littmark

Contents

Declaration	i
Abstract	ii
Acknowledgements	v
List of publications	vi
Statement of candidate contributions	viii
List of conference presentations during the Ph.D. program	x
List of abbreviations	xii
List of movies	xviii
1 Introduction	1
1.1 Experimental context	18
1.1.1 Ion-implantation and thermal release mechanism	19
1.1.2 Deformation of diamond nanopillars	27
1.1.3 Epitaxial diamond interfaces	35
1.2 Computational method	40
1.2.1 Molecular dynamics simulations	41

1.2.2	Periodic boundary conditions	45
1.2.3	Interatomic potentials for carbon	46
1.2.4	ZBL potential	54
1.2.5	Thomson problem	56
1.2.6	Analysis methods	57
1.2.7	Overview of LAMMPS and OVITO	61
1.3	Thesis structure and overview of chapters	62
2	Unphysical nucleation of diamond in the extended cutoff Tersoff potential	64
2.1	Introduction	65
2.2	Methodology	68
2.3	Results and discussion	71
2.4	Conclusion	82
3	Transferability of interatomic potentials for carbon	83
3.1	Introduction	84
3.2	Methodology	86
3.3	Results	93
3.3.1	Amorphous carbons (<i>a</i> -C)	93
3.3.2	Graphitization of <i>a</i> -C under annealing	94
3.4	Discussion	109
3.5	Conclusion	112
4	Modification of nanodiamonds by xenon implantation	113
4.1	Introduction	114
4.2	Methodology	115

4.3	Results and discussion	120
4.4	Conclusion	137
5	Predicting release temperatures of noble gases in pre-solar nan-	
	odiamonds	139
5.1	Introduction	140
5.2	Methodology	141
5.2.1	Simulation methods	141
5.2.2	Mapping to experimental temperatures	144
5.3	Results and discussion	148
5.3.1	Individual implantation and thermal release events	148
5.3.2	Statistical analysis	151
5.3.3	Comparison with experiment	155
5.3.4	Isotopic effects	159
5.4	Conclusion	162
6	Plastic deformation of single crystal diamond nanopillars	163
6.1	Introduction	164
6.2	Methodology	165
6.3	Results and discussion	170
6.3.1	Stretching simulations	170
6.3.2	Crystal structure and properties of O8-carbon	175
6.3.3	Bending simulations	180
6.4	Conclusion	181
7	Epitaxial formation of silicon carbide on (100) diamond	183
7.1	Introduction	184

Contents

7.2	Methodology	186
7.3	Results and discussion	188
7.3.1	Number of unit cells	188
7.3.2	Interface reconstruction	190
7.3.3	Interfacial energy	194
7.4	Conclusion	196
8	Conclusion and future work	198
8.1	Conclusion	198
8.2	Future work	202
	Appendices	204
A	Co-author contribution on statements	205
B	Copyright information	212
C	<i>www.carbonpotentials.org</i>	218
D	Front cover image of journal	220
E	List of additional publications during the Ph.D. program	222
	Bibliography	226

List of movies [†]

Movie 1.1: This footage depicts a diamond nanopillar (100 orientation) in the elastic regime. Conditions which would subject the pillar to electrostatic force, yet not enough to undergo plastic deformation, were met to show a “wobble” effect which usually preceded the Plastic regime. 34
([Link](#)) or see Supporting Information in [Regan et al. \(2020\)](#).

Movie 1.2: This footage depicts a (111)-oriented diamond pillar undergoing deformation in identical conditions to its (100) plane counterpart. The video depicts a brief elastic regime, then structural failure. This result was a primary prediction of the Phase change model for plastic deformation in diamond structures. . . 35
([Link](#)) or see Supporting Information in [Regan et al. \(2020\)](#).

Movie 2.1: Time evolution of nucleation of diamond during the annealing process. The grey atoms represent amorphous carbon and cubic and hexagonal diamond are shown with blue and orange, respectively. 72
([Link](#))

Movie 4.1: Sequence of images showing the geometric relationship between a 4.0 nm diameter nanodiamond and the 25 initial xenon locations (shown in blue). These locations are solutions to the 25-point Thomson problem. 119
([Link](#)) or see Supplementary Data in [Fogg et al. \(2019\)](#).

[†] The movies can be accessed on my personal website via the provided links.

Movie 4.2: Time evolution of implantation into a 3.1 nm diameter nanodiamond for a xenon energy of 2 keV. This corresponds to the top panel of Figure 4.5 in the main text. Carbon atoms and the xenon are shown as red and blue circles, respectively. 120
([Link](#)) or see Supplementary Data in [Fogg et al. \(2019\)](#).

Movie 4.3: Time evolution of implantation into a 3.1 nm diameter nanodiamond for a xenon energy of 6 keV. This corresponds to the middle panel of Figure 4.5 in the main text. Carbon atoms and the xenon are shown as red and blue circles, respectively. 120
([Link](#)) or see Supplementary Data in [Fogg et al. \(2019\)](#).

Movie 4.4: Time evolution of implantation into a 3.1 nm diameter nanodiamond for a xenon energy of 40 keV. This corresponds to the bottom panel of Figure 4.5 in the main text. Carbon atoms and the xenon are shown as red and blue circles respectively. The gradual leftwards drift of the nanodiamond is a consequence of subtracting the net momentum of the system from all atoms. The same process occurs for the lower implantation energies, but is less visually apparent. ... 120
([Link](#)) or see Supplementary Data in [Fogg et al. \(2019\)](#).

Movie 5.1: Time evolution of helium release process from ~ 3.9 nm diameter nanodiamond during the high-temperature annealing (as discussed at the Figures 5.4(a) and (b)). The thickness of the slice is 1 nm. Helium is shown as a orange circle and the pink lines indicate the helium trajectory. Carbon atoms are shown as red, green and blue circles with sp , sp^2 and sp^3 hybridizations, respectively. 149
([Link](#))

Movie 5.2: Time evolution of xenon release process from ~ 3.9 nm diameter

nanodiamond during the high-temperature annealing (as discussed at the Figures 5.4(c) and (d)). Xenon is shown as a orange circle and the pink lines indicate the xenon trajectory. The other color coding and thickness of the slice are the same as in [Movie 5.1](#). 150
([Link](#))

Movie 6.1: Close-up view showing the development of O8-carbon during the stretching of the (001)-oriented diamond nanopillar. The thickness of the slice is 1 nm, and red, green and blue circles denote carbon atoms with sp , sp^2 and sp^3 hybridizations, respectively. 169
([Link](#)) or see Supporting Information in [Regan et al. \(2020\)](#).

Movie 6.2: Unit cell structure of O8-carbon. Green and blue circles denote carbon atoms with sp^2 and sp^3 hybridizations, respectively. 171
([Link](#)).

Movie 6.3: Bending process of the (001)-oriented diamond nanopillar from molecular dynamics simulations. O8-carbon appears when the nanopillar is bent to large angles. The thickness of the slice is 1 nm, and red, green and blue circles denote carbon atoms with sp , sp^2 and sp^3 hybridizations, respectively. The pink atoms corresponding to the fixed regions as discussed in the text (shown in blue in Figure 6.8). 178
([Link](#)) or see Supporting Information in [Regan et al. \(2020\)](#).

Movie 6.4: Bending process of the (111)-oriented diamond nanopillar from molecular dynamics simulations. The nanopillar undergoes brittle fracture when bent to large angles. The color coding and thickness of the slice are the same as in [Movie 6.2](#). 178
([Link](#)) or see Supporting Information in [Regan et al. \(2020\)](#).

Chapter 1

Introduction

Carbon is the fourth most abundant element in the universe after hydrogen, helium and oxygen, and is often found in the sun, stars, comets, and in the planets' atmosphere. It is also the fifteenth most widely distributed element in the Earth's crust and the second most detected element in the human body (Haggerty, 1999). Hence, carbon makes an interesting topic in nanoscience and nanotechnology across all scientific disciplines such as physics, chemistry, materials science and engineering. Carbon is the sixth element in the periodic table and has two tightly bound ($1s$) and four valence electrons (two in the $2s$ and two in the $2p$). The ground electronic configuration of carbon is $1s^2 2s^2 2p^2$, which allows it to form three different bonds; single, double and triple bonds. Figure 1.1 illustrates the

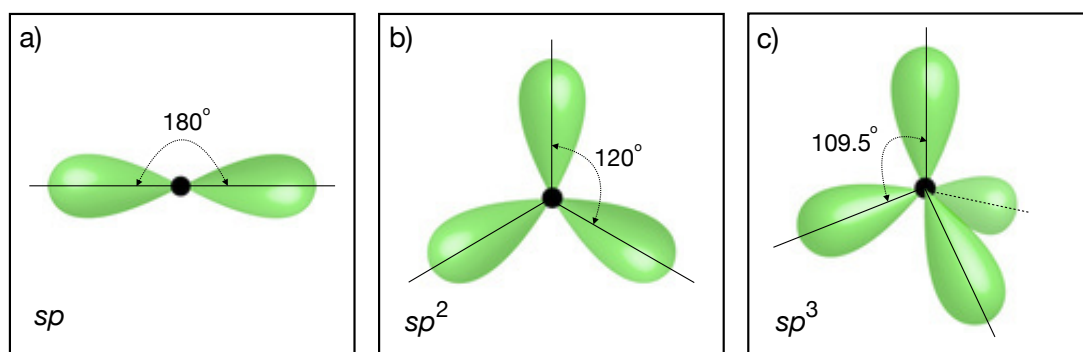


Figure 1.1: Three different hybrid orbitals of carbon. (a) linear sp hybrid orbitals, (b) trigonal planar sp^2 hybrid orbitals and (c) tetrahedral sp^3 hybrid orbitals.

three different spatial hybrid orbitals of carbon. A carbon atom forms bonds with one to four neighbouring atoms. Depending on the degree of hybridization, the compounds show different structural features:

- sp hybridization: one s -orbital hybridizes with one of the p -orbitals to make two sp -hybridized orbitals with linear symmetry. It has a linear geometry with the angle 180° between orbitals. (Figure 1.1(a))
- sp^2 hybridization: one s -orbital is mixed with two of the p -orbitals to make three hybridized orbitals with trigonal symmetry. It has a trigonal planar geometry and the angle between orbitals is 120° . (Figure 1.1(b))
- sp^3 hybridization: one s -orbital is mixed with all three p -orbitals to make four hybridized orbitals. It has a tetrahedral geometry with an angle of 109.5° between orbitals. (Figure 1.1(c))

The two well-known bulk allotropes of carbon are graphite and diamond. Graphite has sp^2 bonds, each atom being bound to three nearest neighbors, while the bonds in diamond are sp^3 , each carbon being bound to four nearest neighbors (Pierson, 1993a,b). Graphite and diamond are the most important form of carbon due to their unique variety of physical properties and application. For example, graphite is soft, opaque and black, and it has very high conductivity. Diamond is the hardest material known and highly transparent, with a very low electrical conductivity. Graphite is the most thermodynamically stable form of carbon at ambient conditions. Diamond is thermodynamically unstable under normal pressures and at sufficiently high temperatures diamond transforms into graphite. However, due to a high activation energy barrier, the transition of diamond into graphite is extremely slow at room temperature as to be unnoticeable. A brief description of the structure and properties of graphite and diamond are presented below.

Graphite - The atoms are arranged in a hexagonal unit cell containing four carbon atoms. The unit cell has dimensions of $2.456 \text{ \AA} \times 2.456 \text{ \AA} \times 6.708 \text{ \AA}$ (see

Figure 1.2) and a density of 2.27 g/cm^3 (Wyckoff, 1963). Graphite consists of distinct graphene layers – which is a two-dimensional sheet of carbon atoms arranged in six-membered hexagonal rings – and, as shown in Figure 1.2, these layers are arranged on a xy -plane and stacked in a z -direction. Within one graphene sheet, carbon atoms are connected to each other via three σ -bonds which correspond to sp^2 hybridization. Note that only three out of four valence electrons participate in hybridization and the remaining electrons form π -bonds are delocalized over the entire graphitic planes. The in-plane distance between adjacent atoms is 1.415 \AA and the distance between adjoining graphene sheets is 3.354 \AA . The weak van der Waals interactions between stacked layers allow graphite to be easily exfoliated, and layers can easily shift in parallel against each other (Krüger, 2010).

Generally, graphite has two known stacking sequences: hexagonal (AB) and rhombohedral (ABC). Both structures have very similar physical properties, except that their stacked layers are positioned slightly different. The graphene layers in the hexagonal structure have an ABAB stacking sequence, when the atoms of layer B are located above the centers of the hexagons in layer A. A ball-and-stick schematic of this structure is shown in Figure 1.2(a). In rhombohedral graphite, the layers are stacked according to the sequence ABCABC (Figure 1.2(b)). In a hexagonal cell, the rhombohedral one has six carbon atoms in its unit cell and

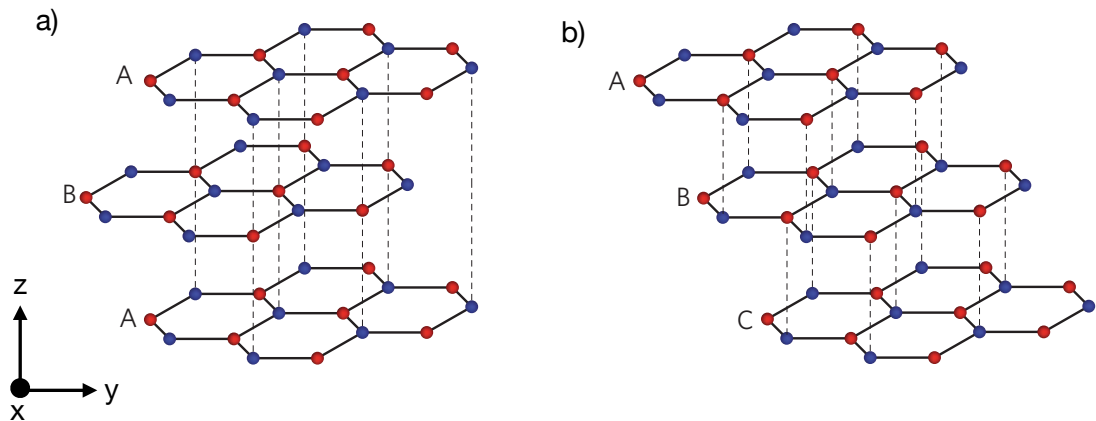


Figure 1.2: A ball-and-stick schematic of both (a) hexagonal and (b) rhombohedral graphite. Dashed lines indicates atoms above and below same position. The lattice structures adapted from Yacoby (2011).

the dimensions are $2.456 \text{ \AA} \times 2.456 \text{ \AA} \times 10.062 \text{ \AA}$. Note that as the hexagonal form is more thermodynamically stable, the rhombohedral form would transform into the hexagonal form when it is heated above 1300°C (Fitzer et al., 1995). A thorough description of some of the physical properties of graphite has been given by Pierson (1993b). As the topic of applications and properties of graphite is out of the scope of this thesis, we will not get into further details.

Diamond - Diamond is another well-known allotrope of carbon. Each carbon atom in diamond has its nearest neighbors located at the corners of a tetrahedron. All carbon atoms are sp^3 -hybridized and connected to four equidistant carbon atoms with four σ -bonds, where the bond length is 1.545 \AA . Generally, there are two types of diamond: cubic and hexagonal. The unit cell of cubic diamond – the most abundant type – contains eight carbon atoms, which is associated with the $Fd\bar{3}m$ space group with a lattice parameter of 3.567 \AA and a density of 3.514 g/cm^3 (Krüger, 2010). The cubic diamond structure is stacked according to a ABCABC sequence (Figure 1.3(a)). Hexagonal diamond, however, is rare in nature and was first discovered in meteorites (Lewis et al., 1987). The hexagonal lattice is built from tetrahedrons of carbon, similar to the cubic type, but the carbon atoms are arranged in a different way. As shown in Figure 1.3(b), the

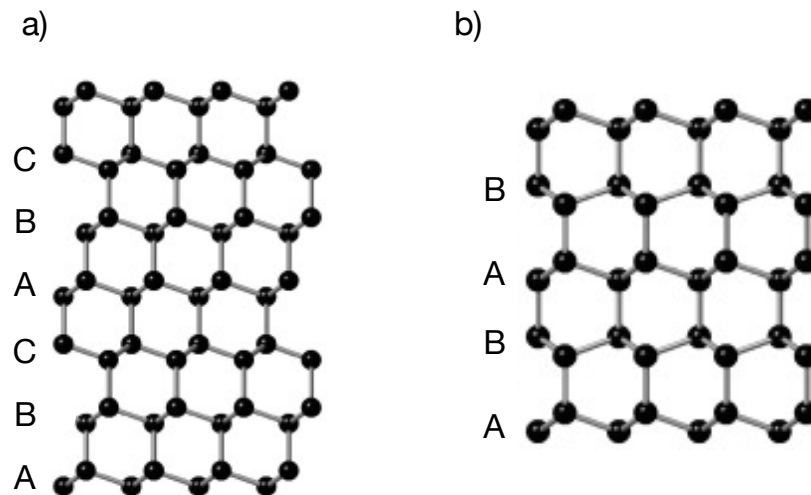


Figure 1.3: The lattice structure of (a) cubic and (b) hexagonal diamond. Figures adapted from Salzmann et al. (2015).

hexagonal diamond structure has an ABAB stacking sequence and its unit cell contains four carbon atoms.

There are two categories of diamond: natural and synthetic. Natural diamonds can be found in and around meteorite impact sites and also they can grow under high pressure high temperature (HPHT) conditions within the Earth. They differ considerably in size and quality. These diamonds are formed in the Asthenosphere part of the mantle of Earth at a depth of about 150 kms. They are formed at a pressure of more than 4.5 GPa and at temperatures between 900 and 1500°C ([Haggerty, 1986](#); [Krüger, 2010](#); [Fedorov et al., 2002](#)). Diamonds are spread out over the Earth's surface in Kimberlite deposits that volcanic eruptions bring to the surface ([Richardson et al., 1984](#); [Nowicki et al., 2004](#); [Sobolev et al., 2004](#)). Meteoric impacts on the Earth's surface can be another source of natural diamond. Natural meteoric diamonds might have formed terrestrially ([Lewis et al., 1987](#)) or else from carbonaceous material under the high pressure high temperature conditions of impact ([Hanneman et al., 1967](#); [Koeberl et al., 1997](#)).

Manufacturing of synthetic diamonds has been an interesting topic during the past few decades and has seen several advances in techniques. The HPHT method that imitates natural diamond formation is the most commonly used technique to produce large volumes of diamonds, mainly suitable for industrial purposes such as grinding and cutting tools. Another method to produce synthetic diamond is chemical vapor deposition (CVD). In the CVD growth method, diamond grows through a chemical reaction from carbonaceous gases deposits onto seed substrates at moderate pressure (below one atmosphere) and temperatures (200 – 1200°C). [Figure 1.4](#) shows the schematic of the HPHT and CVD methods. We will not get into further details on the applications, properties and formation of bulk diamond since this topic would be beyond the scope of this thesis.

In the past two decades, the availability of high-resolution microscopy techniques such as Transmission Electron Microscopy (TEM) and Scanning Tunneling Microscopy (STM) has advanced research in the area of carbon nanomaterials.

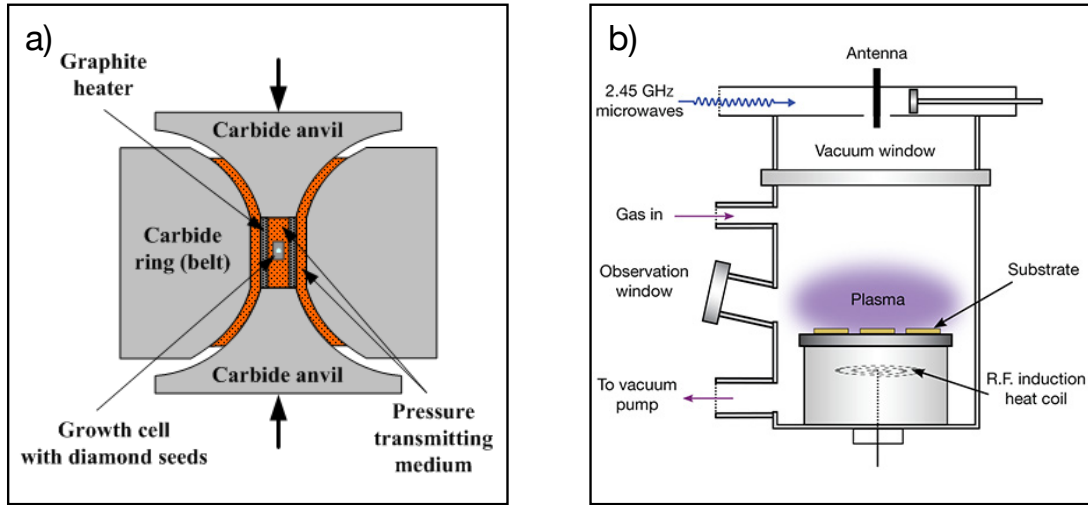


Figure 1.4: A schematic of the producing synthesis diamond with (a) HPHT and (b) CVD methods. Panel (a) adapted from www.gemrockauctions.com and panel (b) adapted from [Eaton-Magana and Shigley \(2016\)](#).

In what follows, we briefly explore the structure and properties of the five most famous nano-allotropes of carbon: graphene, fullerenes, carbon onions, nanodiamonds and diamond nanopillars (Figure 1.5).

Graphene - Graphene is a one atom-thick layer of sp^2 -hybridized carbon atoms arranged in a honeycomb structure (Figure 1.5(a)). Each carbon atom has one π -bond which is oriented out-of-plane as well as three σ -bonds to its three neighbors, with the bond length being about 1.415 Å. It is the basic structure of some carbon allotropes such as graphite, fullerenes and carbon nanotubes. The theory of graphene was first investigated by [Wallace \(1947\)](#) when he studied the electronic properties of graphite, and for the first time TEM image of graphene was observed ([Evans and Phaal, 1962](#)). In a pioneering study [Novoselov et al. \(2004\)](#) extracted graphene from bulk graphite. Several synthesis methods have been employed to generate graphene, such as exfoliation, hydrothermal self-assembly, epitaxy, nanotube slicing and ion-implantation.

Graphene has some unique physical, thermal and electrical properties compared to other allotropes of carbon. Graphene has the highest electrical conductivity among the carbon materials. It also shows high transparency; a single

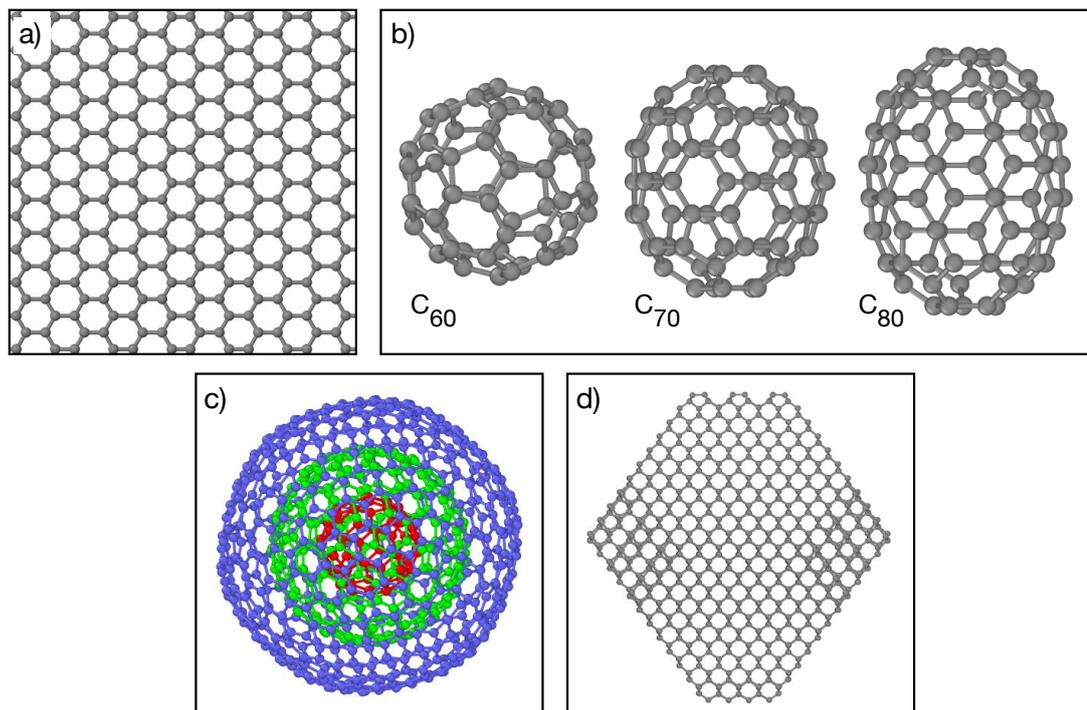


Figure 1.5: (a) Graphene; (b) Three different fullerene isomers; C_{60} , C_{70} and C_{80} . The geometry of C_{60} is the same as that of a soccer ball; (c) Carbon onion; (d) Nanodiamond (ND) particle (truncated octahedral geometry). XYZ-coordinates of panels (b) and (c) are taken from www.nanotube.msu.edu.

layer of graphene absorbs about 2.3% of white light with potential as a transparent conducting coating (Nair et al., 2008). As graphene has an ultimate tensile strength of 130 GPa and a Young's modulus of 1000 GPa, it is the strongest monolayer material (Lee et al., 2008). It is capable of carrying very high currents and demonstrating a high thermal conductivity. Balandin et al. (2008) reported an extraordinarily large thermal conductivity of approximately 5300 W/m/K for suspended graphene. Note that this value strongly depends on the sample history and temperature.

Graphene is expected to be a potential material for future optoelectronic devices, including solar cells and liquid crystal displays to substitute indium tin oxide, which has downsides relating to high cost, limited supply and brittle nature of indium (Guo et al., 2010). Considering its extraordinary thermal, chemical and mechanical stability, high transparency and atomic layer thickness, graphene can

be an ideal material to use in transparent electrodes. Graphene has also been used as a transistor for its unique 2D structure and high mobility (Chen et al., 2007) and is employed as an electron acceptor in such photovoltaic devices as the layered graphene-quantum dot hybrid (Yin et al., 2012). Graphene's tunable bandgap and its large optical absorptivity make it a prospect for efficient light absorbers. Graphene field-effect transistors can be used in chemical and biological sensors for providing low noise, high sensitivity and chemical stability as well as their biocompatible nature (Schedin et al., 2007; Fowler et al., 2009).

Fullerenes - Fullerenes or buckyballs are molecular allotropes of carbon with geodesic graphene-like structures that contain pentagons (i.e., five-membered rings) and hexagons of carbon atoms, which bend the graphene sheet into spheres, ellipses or cylinders (Figure 1.5(b)). Fullerenes were discovered by Kroto et al. (1985) and were named after Richard Buckminster Fuller for their resemblance to his geodesic domes. The discovery of fullerenes sparked a research interest in finding new forms of carbon, which had previously been limited to graphite, diamond, and amorphous carbon. Interestingly, in addition to being discovered in the laboratory by experimental observation, fullerene also exists in nature and space. Buseck et al. (1992) found fullerene in a family of minerals known as "shungites". Cami et al. (2010) observed fullerene in a cloud of cosmic dust surrounding a star and, recently, by using the Hubble Space Telescope, interstellar fullerenes were detected in the space between two stars (Cordiner et al., 2019).

Fullerenes must consist of at least twelve pentagons due to their closed cage structure (Dresselhaus and Dresselhaus, 1995). All carbon atoms have a sp^2 hybridization and are bonded to three other carbon atoms. The molecular structure of a fullerene is edgeless, without any dangling bonds. These characteristics make the fullerene structure unique and different from such crystalline structures as graphite and diamond with edges and dangling bonds at the surface. C_{60} is composed of 60 carbon atoms and comprises of 12 pentagons and 20 hexagons, with each pentagon being surrounded by hexagon once alone. Another common

fullerene structure is C₇₀, but fullerenes with different numbers of carbon atoms are also commonly obtained (Krüger, 2010).

Fullerenes have many interesting physical properties (such as solubility, spectroscopic, thermodynamic, X-Ray diffraction, electronic, electrical, optical properties) and a number of notable potential applications (such as solar cells, chemical sensors, gas storage and gas separation, fuel cells and hydrogen storage, storage for radioactive isotopes, superconductor, lubricants, and direct bandgap semiconductor) (Krüger, 2010). An extended discussion of the applications and properties of fullerene is beyond the scope of this thesis and we refer the reader to Krüger (2010) for a thorough description of the physical and chemical properties of fullerenes and their manufacturing methods.

Carbon Onions - Another nano form of carbon are carbon onions which were first synthesized by Iijima (1980) in arc discharge experiments. Carbon onions, also known as onion-like carbon or carbon nano-onions, are a member of fullerene family, with quasi-spherical concentric fullerene-like shells that range from double to multilayered structures (Figure 1.5(c)). The intershell distance in carbon onions is about 3.4 Å which is close to the distance between graphene layers in graphite. Their properties include thermodynamic, electronic, electrical and optical properties as well as the possibility of conversion into other forms of carbon (Krüger, 2010; Butenko et al., 2010). For example, they have high electrical conductivities and relatively easy dispersibility compared to graphene, making them promising materials for electrochemical applications. They are ideal additives to battery and supercapacitor electrode for high power applications due to their excellent capacitance retention at high current densities. Carbon onions also have potential applications in tribological, catalysis, composite materials, and electromagnetic devices (Krüger, 2010; Zeiger et al., 2016).

During nearly the past four decades, in addition to arc discharge, which is the most common approach to generating carbon onions, other synthesis methods have been employed. These methods include electron beam irradiation (Ugarte,

1992; Xu and Tanaka, 1995; Troiani et al., 2003), laser irradiation (Gorelik et al., 2003), high-temperature nanometer-sized diamond annealing (Kuznetsov et al., 1994; Qiao et al., 2006; Xiao et al., 2014), implantation of carbon ions onto metal particles (Cabioch et al., 1997; Thune et al., 2003) and CVD. It should be noted that with the exclusion of the CVD method, all the above-mentioned methods are costly due to their high-temperature processes, and they produce only a limited number of carbon onions in highly condensed forms. On the contrary, the CVD method is a better synthesis method for generating pure carbon onions in large amounts (He and Zhao, 2010).

Nanodiamonds - Nanodiamonds (NDs) are small diamond particles of 100 nm (Krüger, 2010) and Kharisov et al. (2010, 2012). There are several methods to produce NDs such as hydrothermal synthesis (Nickel et al., 2008), gas-phase nucleation at ambient pressure (Frenklach et al., 1991), chlorination of carbide material at moderate temperatures (Gogotsi et al., 2001), ion and laser bombardment, microwave plasma CVD techniques (Lewis III et al., 2007) and detonation methods. Based on the production process, NDs can be divided into two different categories. The first one is nano-crystalline diamond which refers to materials with particles less than 100 nm in size, and the second one is ultra-nano-crystalline diamond whose particles are smaller than 10 nm. It is important to note that ultra-nano diamond (ultra-ND) particles have been found in meteorites, proto-planetary nebulae, and interstellar dusts (Xiao et al., 2014). The fact that the mechanisms of their origin and formation are still ambiguous has made them an interesting topic in astrophysics. It is generally thought that NDs can be formed during the CVD-like method in stellar atmospheres in the evolutionary sequence of becoming type-I and type-II supernova (Haggerty, 1999). Another possibility is that the NDs may originate from a kind of shock wave synthesis inside a supernova (Krüger, 2010). Figure 1.6 illustrates the comparison mechanism of formation of NDs in both types of supernova.

Isolated ND particles (see Figure 1.5(d)) with sizes of tens of nanometers

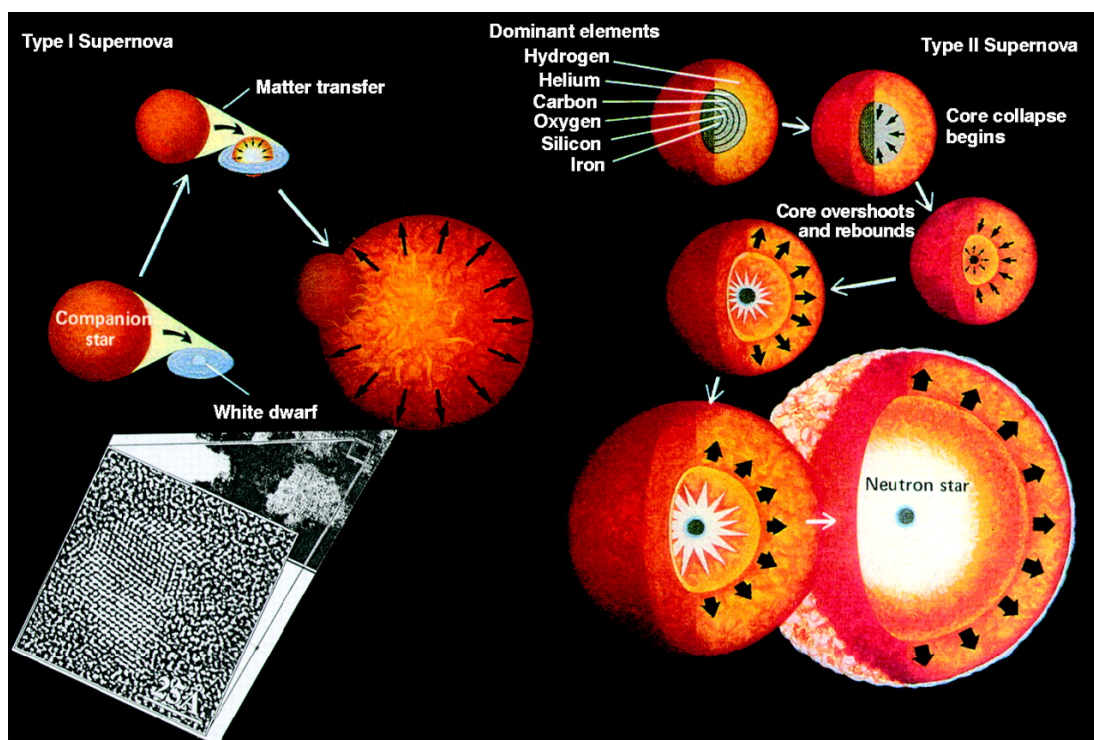


Figure 1.6: Schematic mechanism of formation of diamonds in type-I and type-II supernovae. Left panel shows the evolutionary sequence of becoming type-I supernova by explosion of dense white dwarf. In a type-II supernova, right panel, a single star undergoes a gradual and then a catastrophic collapse as core fuels in sequential layers are expended. On final implosion and rebounding, the outermost envelopes are blasted into the interstellar media. Inset is an electron image of a diamond from the Murchison meteorite. Figure taken from [Haggerty \(1999\)](#).

are one type of ND structures ([Shenderova and McGuire, 2006](#)). This type of NDs can be produced with HPHT diamond synthesis, CVD technique, and as shown in Figure 1.6, with CVD-like method in stellar atmospheres. For example, [Regueiro et al. \(1992\)](#) reported that at room temperature and at high static pressure buckyballs (C_{60} buckminsterfullerene) can be transferred to diamond. Also, transformation of fullerenes and nanotubes to diamond under high pressure and high temperature are discussed by [Ma et al. \(1994\)](#) and [Cao et al. \(2001\)](#), respectively. Stability of ND particles have been investigated by many groups. For example, for the first time, [Badziag et al. \(1990\)](#) showed, using a simple atomistic model, that NDs with a size below ~ 3 nm in diameter are energetically favoured over polycyclic precursors to graphite, without requiring the high pres-

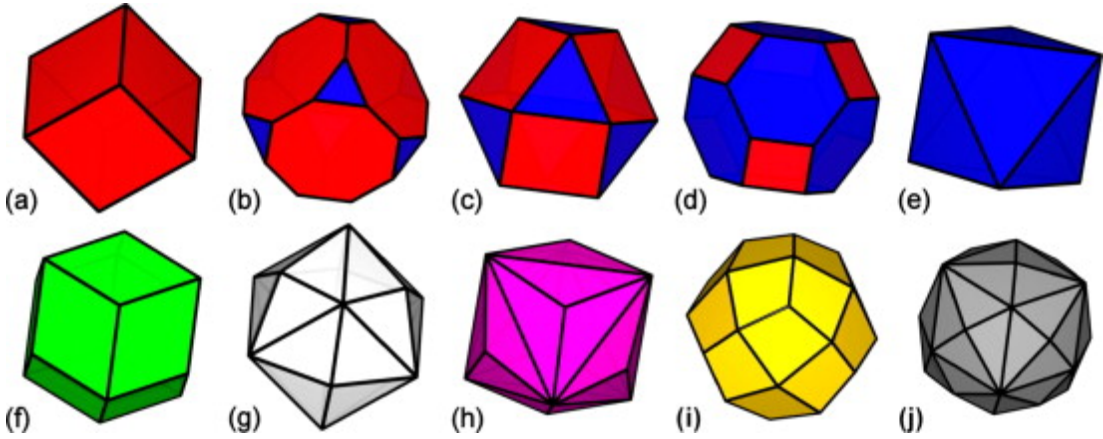


Figure 1.7: Common geometry morphologies of ND particles. (a) Hexahedron, (b) Truncated hexahedron, (c) Cuboctahedron, (d) Truncated octahedron, (e) Octahedron, (f) Rhombic dodecahedron, (g) Tetrakis hexahedron, (h) Triakis octahedron, (i) Deltoidal icositetrahedron and (j) Hexakis octahedron. Figure taken from [Barnard \(2011\)](#).

tures or extreme kinetic conditions usually associated with diamonds. Moreover, in a series of studies Barnard carried out simulations on the phase stability of ND particles ([Barnard and Zapol, 2004](#); [Barnard et al., 2003b](#); [Barnard, 2011, 2014a](#)). These modeling studies predict that the truncated octahedron geometry is the stable morphology for dehydrogenated NDs. Figure 1.7 shows common geometry morphologies of ND particles. Note that as the topic of ND particles is the main focus of studies in Chapters 4 and 5, further details can be found in Section 1.1.1.

Diamond Nanopillars - Diamond nanopillars (DNPs), also known as diamond nanowires, are one form of ND structures that have been of particular interest for a long time due to their interesting applications on nanomechanical and optoelectronic nanodevices ([Appell, 2002](#)). DNPs were discovered by [Shiomi \(1997\)](#) and have been synthesized by various techniques, which are summarized in a review by [Yu et al. \(2014\)](#). [Baik et al. \(2000\)](#) used a method involving air plasma etching of polycrystalline diamond films to produce aligned diamond whiskers (see Figure 1.8(a)). The CVD method is used to fabricate polycrystalline diamond nanocylinders ([Masuda et al., 2001](#)). [Ando et al. \(2004\)](#) combined microwave plasma treatment with reactive ion etching to form single crystalline DNPs (see

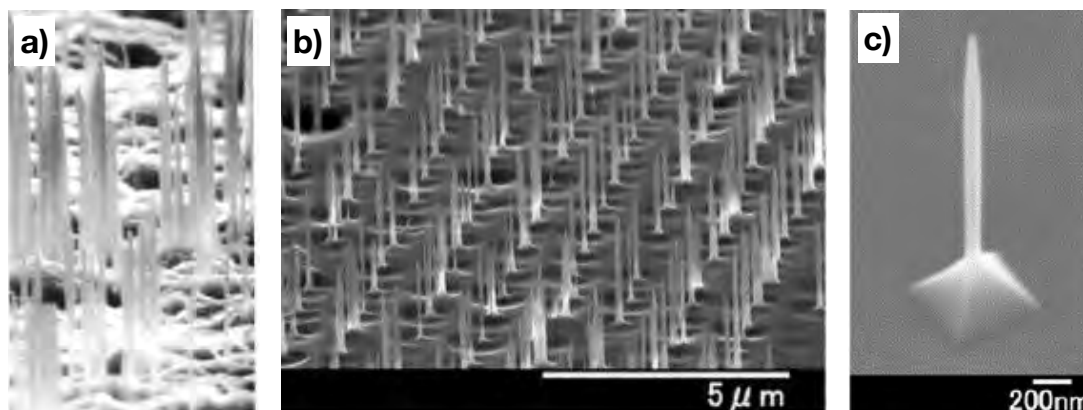


Figure 1.8: Scanning electron microscope micrograph of (a) diamond nano-whiskers, (b) array of diamond rods and (c) single nanorod. Panel (a) is from Baik et al. (2000) and panels (b) and (c) are from Ando et al. (2004).

Figure 1.8(b) and (c)). In addition to these experimental studies, some researchers have used computer modeling to study the thermodynamic and geometry stability of DNPs (Barnard et al., 2003a; Shenderova et al., 2003; Barnard, 2004; Okada, 2009). In addition to the stability of the DNPs, Barnard (2005) predicts that the thin DNPs (diameter less than about 1.8 nm) have a considerably small band gap compared to the bulk diamond. This theoretical study also suggests that based on the diameter of the DNP, the morphology of the surface and degree of surface hydrogenation, DNPs can be semiconductor or semimetal structures. Note that as the topic of DNPs is the main focus of Chapter 6, the mechanical properties of DNPs will be reviewed in more details in this chapter under Section 1.1.2.

New allotropes of carbon

Many new allotropes have been theoretically predicted or experimentally synthesized. These new allotropes have either two- or three-dimensional configurations and possess some interesting properties. In what follows, we briefly explore the structure and properties of a variety of new carbon allotropes. In order to easily compare these allotropes, they are divided into two groups based on their parent structures, graphene (sp^2 bonded) and diamond (sp^3 bonded). Note that full details and properties of all new allotropes would be beyond the scope and purpose

of this thesis; hence, only a brief overview of these allotropes is provided in what follows to help contextualize our findings in Chapter 6.

The new two-dimensional allotropes with graphene root have semiconductor and metallic behaviours. Figure 1.9 represents seven of these new allotropes. Graphenylene, which is also known as biphenylene carbon (panel (a)), has been predicted in modeling studies (Balaban et al., 1968) and observed in experiment

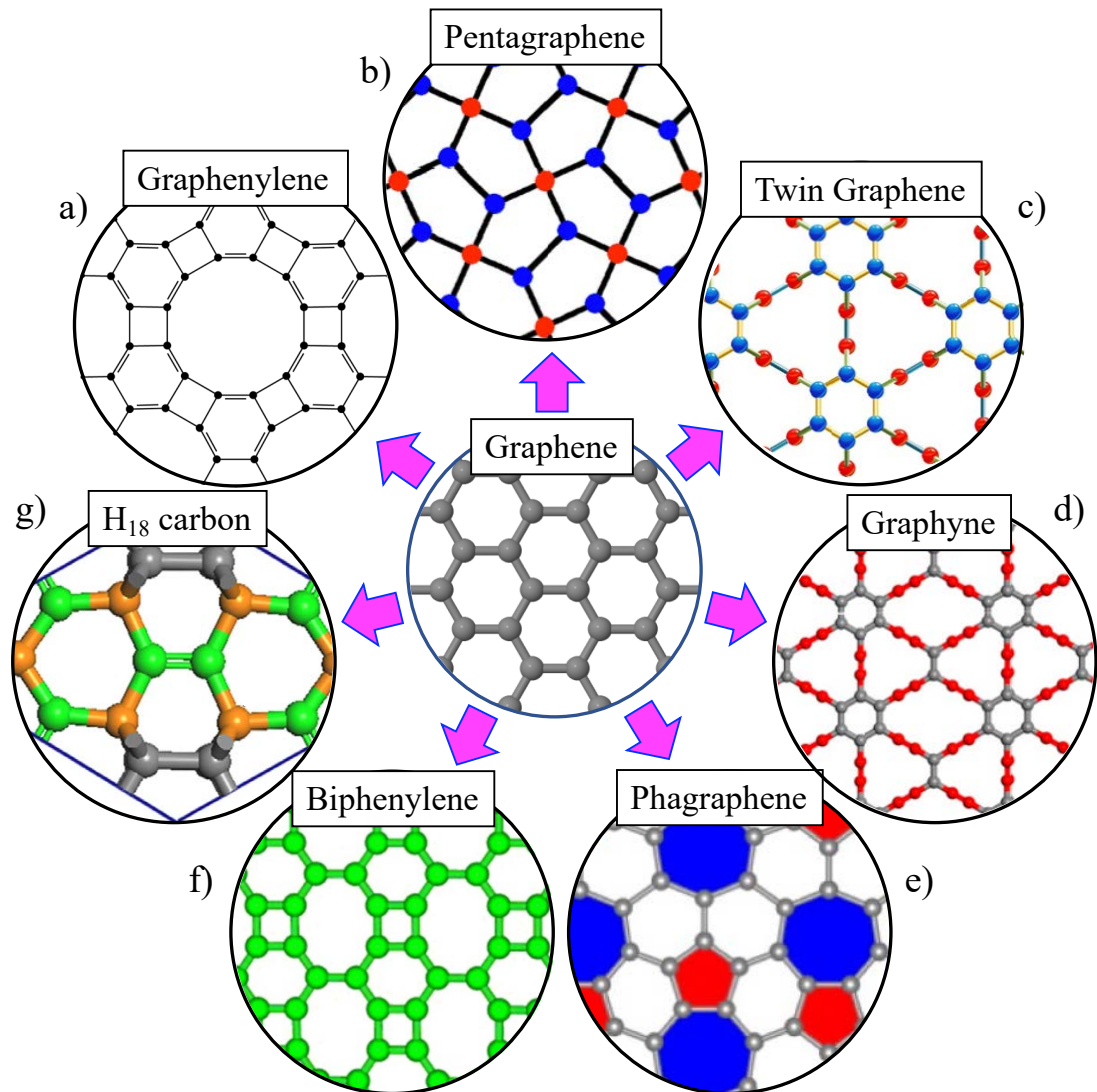


Figure 1.9: New carbon allotropes based on graphene. (a) graphenylene; (b) pentagraphene; (c) twin graphene; (d) graphyne; (e) phagraphene; (f) biphenylene; (g) H_{18} carbon. As described in the text, the colour coding in panels (b)–(d) showing the hybridizations, i.e., sp^2 and sp^3 , and in panel (g) showing Wyckoff positions of atoms.

(Du et al., 2017; Totani et al., 2017). All the 12 carbon atoms in graphenylene's unit cell are sp^2 -hybridized, and in terms of energy it is less stable than graphene. Graphenylene is also a semiconductor due to its small electronic bandgap. Pentagraphene is another semiconductor metastable allotrope of carbon which has only been proposed theoretically (Zhang et al., 2015). Panel (b) shows the lattice structure of pentagraphene, which consists of 6 atoms with sp^2 (blue) and sp^3 (red) hybrids. Twin graphene (panel (c)) is a semiconductor allotrope of carbon which was theoretically predicted by Jiang et al. (2017). Its unit cell has 18 atoms and contains two types of inequivalent carbon atoms, (i) on the surface planes and (ii) on the mid-plane, which are depicted by blue and red spheres, respectively. Graphyne (Balaban et al., 1968) and its family (i.e., graphdiyne, graphyne-3 and graphyne-4) are other semiconductor allotropes of carbon, and so far only graphdiyne has been experimentally synthesized (Haley et al., 1997). The crystal structure of graphyne is illustrated in panel (d), with the colour coding showing the atoms on the surface (grey) and mid-plane (red).

Phagraphene and biphenylene are two metallic allotropes of carbon which have been shown in Figure 1.9(e) and (f). Phagraphene is a theoretically stable allotrope and all sp^2 -hybridized carbon atoms construct pentagonal, hexagonal and heptagonal rings (Wang et al., 2015). Another new metallic allotrope is biphenylene, which was synthesized by Lothrop (1994). As seen from panel (f) in Figure 1.9, by rotating two C–C bonds in the hexagonal ring in the graphene, biphenylene with square and octagonal rings is generated. Also, biphenylene is energetically less stable than graphene and phagraphene. H_{18} carbon is another theoretically energetically stable metallic allotrope of carbon that has not yet been found in the experiments. It was predicted by Zhao et al. (2016) and has a three-dimensional sp^2 - and sp^3 -hybridized carbon bonding structure. The structure of the H_{18} carbon is illustrated in panel (g), with the colour coding showing Wyckoff positions of atoms.

Three-dimensional diamond-based new allotropes of carbon, similar to the

graphene-based ones, have some novel mechanical or physical properties such as metallic and superhard behaviours. Figure 1.10 illustrates the seven three-dimensional new allotropes of carbon. Hex-C₁₈ is a metallic allotrope of carbon that has been theoretically predicted (Liu et al., 2017). So far, it has not been experimentally observed but XRD calculations suggest that hex-C₁₈ might exist in detonation soot (Chen et al., 2003; Pantea et al., 2006). Hex-C₁₈ can be gen-

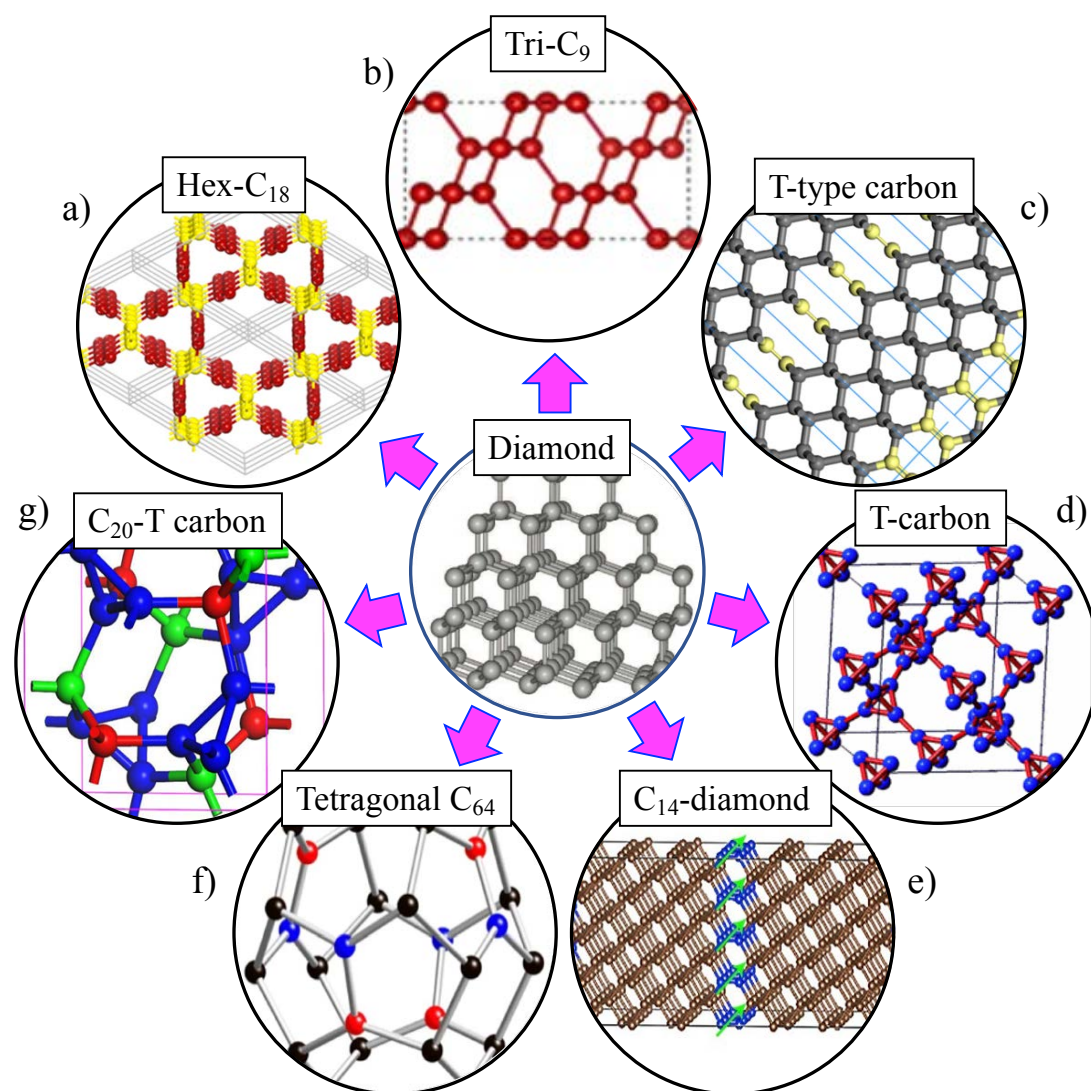


Figure 1.10: New carbon allotropes based on diamond. (a) Hex-C₁₈; (b) Tri-C₉; (c) O-type and T-type carbon; (d) T-carbon; (e) C₁₄-diamond; (f) tetragonal C₆₄; (g) C₂₀-T carbon. Colour coding showing the hybridizations, i.e., sp^2 and sp^3 , as described in the text.

erated by rotating some bonds in graphene and its unit cell consists of 18 carbon atoms with sp^2 and sp^3 hybrids. The lattice structure of this allotrope is shown in panel (a), with the colour coding showing the hybridization (yellow = sp^3 and red = sp^2). Panel (b) illustrates another metallic structure that has been theoretically predicted is called tri-C₉ (Cheng et al., 2016). Although it has not been synthesized in experiment, modeling studies predict that it can be generated by compressing graphite. Also, simulations suggest that it is a thermodynamically and mechanically stable allotrope. O-type and T-type carbon are two other metallic carbon allotropes which have been proposed theoretically (Liu et al., 2018). These allotropes can be generated by using self-assembling diamond nanostripes and C=C bond as linkers. Panel (c) illustrates the T-type carbon using colour coding to indicate the hybridization (sp^2 and sp^3 atoms are shown as grey and yellow, respectively). O-type, with orthorhombic symmetry, corresponds to an odd number of diamond nanostripes, while tetragonal symmetry allotrope (T-type) corresponds to an even number. So far, only one of the T-type family which is named T10 carbon has been experimentally observed (Xu et al., 2015). In addition, from a theoretical point of view, both types of allotropes are mechanically and thermodynamically stable.

T-carbon is one of the well-known new allotropes of carbon that was theoretically predicted by Sheng et al. (2011) and has recently been synthesized in experiment (Zhang et al., 2017; Xu et al., 2019). Figure 1.10(d) illustrates the unit cell of T-carbon which contains two tetrahedrons with eight carbon atoms. Theoretical studies proposed that due to narrow direct electronic band gap, this allotrope is a semiconductor, and from a thermodynamical point of view, it is metastable compared to diamond and graphite. Panel (e) shows a C₁₄-diamond allotrope, with the colour coding showing the hybridization (brown = sp^3 and blue = sp^2). As its structure is nearly similar to diamond, this allotrope is thermodynamically stable (Wu et al., 2017). Tetragonal C₆₄ is another semiconductor allotrope of carbon with tetragonal symmetry (Wei et al., 2017). The crystal

structure of this allotrope is illustrated in panel (f), with sp^2 denoted by blue and red spheres, while the black spheres depict sp^3 hybridization. Theoretical study predicts that this allotrope is dynamically and mechanically stable. Wang et al. (2016) theoretically proposed another stable allotrope of carbon which is called C_{20} T-carbon (panel (g)) and contains 20 carbon atoms in its unit cell with sp^3 hybrid.

During the past decade, in addition to the above mentioned 14 new allotropes of carbon, many other allotropes have been proposed such as P-carbon (Pan et al., 2017), D-carbon (Fan et al., 2018), bcc-carbon (Liu et al., 2008), M-carbon (Kiyohara et al., 2006; Li et al., 2009), Novamene (Burchfield et al., 2017), Protomene (Delodovici et al., 2018), Zayedene (Delodovici et al., 2019), K_4 crystal (Itoh et al., 2009), W-carbon (Wang et al., 2011), O-carbon (Wang et al., 2012), tricyclobutabenzene carbon (TBBC) (Zhang et al., 2018), porous CY carbon (Zhu and Wang, 2016), K_6 carbon (Niu et al., 2014), m - C_8 (Sung et al., 2017), three-dimensional pentagon carbon (3D- C_5) (Zhong et al., 2017), cyclo[18]carbon (C_{18}) (Kaiser et al., 2019), and Pentadiamond (Fujii et al., 2020). Note that due to the industrial and academic significance of new allotropes of carbon, there has been increasing interest in recent years in discovering more carbon allotropes. As a result, new forms keep being proposed every now and then but it is more a theoretical exercise than an experimental synthesis. I have thus provided an overview of the 14 most famous allotropes together with a list of other recently found forms to help contextualize our findings in Chapter 6 (i.e., a new O8-carbon allotrope).

1.1 Experimental context

In this thesis, the focus is on diamond, and we apply atomistic simulations techniques to study implantation, annealing, mechanical deformation, and structural relaxation in various forms of diamond. In the following section we will provide a brief overview of experimental studies from the literature and our collaborators. This section is divided into four main parts: (i) ion-implantation into nano-

sized diamond at the University of Huddersfield, UK, (ii) meteoritic literature of stepped pyrolysis of meteoritic and synthetic nanodiamond, (iii) mechanical deformation of diamond nanopillars in an electron microscope at the University of Technology Sydney, and (iv) epitaxial diamond interfaces in semiconductor heterostructures at the University of Melbourne.

1.1.1 Ion-implantation and thermal release mechanism

Nanodiamonds are one of the most abundant grains found in primitive meteorites (Ott, 1993), yet their origin is poorly understood. It has long been debated whether or not NDs originated at a time prior to the formation of the Solar System. In this regard, NDs provide a record of nuclear and chemical processes in stars and in the interstellar medium as well as sensitive astrophysical information on galactic mixing (Ott, 1993; Koscheev et al., 2001; Nittler, 2003; Huss, 2005). In addition, NDs contain isotopically anomalous noble gases and preserve them for billions of years (Koscheev et al., 2001; Huss, 2005). The fact that these trapped noble gases are isotopically anomalous has been taken as evidence that the meteoritic NDs came from outside the Solar System and are presolar grains; that is, they formed before the Sun’s formation. For this reason, they can provide us with information on the history of nucleosynthesis in the galaxy. Their characteristics also provide clues to the conditions encountered in interstellar space, in the solar nebula, and in the host meteorites. Meteoritic NDs are the least well understood presolar grains due to their small size ranging between 0.2 and 10 nm in diameter, with an average diameter of $\sim 2.7\text{--}3.0$ nm (Lewis et al., 1987; Daulton et al., 1996; Dai et al., 2002; Huss, 2005; Daulton, 2006).

The discovery of nanodiamonds was made possible through the isotopically anomalous xenon which is trapped in the diamonds. This isotopically strange xenon is different from the “normal” Solar System xenon in that it is enriched in *Heavy* and *Light* isotopes simultaneously. The trapped gas component, which is called HL, also contains P3 which is another isotopically different component of

Xe. The P3 gas component has isotopic ratios close to Solar System xenon, but its isotopic composition is distinct (Huss, 2005). Figure 1.11 shows the isotopic pattern of anomalous HL component for xenon (Xe-HL), where it shows pronounced excesses in the *Light* isotopes ^{124}Xe and ^{126}Xe , and in the *Heavy* isotopes ^{134}Xe and ^{136}Xe . The light and heavy nuclides are produced from nucleosynthesis in supernovae (Clayton, 1989; Howard et al., 1992; Ott, 1996; Daulton, 2006). The nuclear origin of the ^{124}Xe and ^{126}Xe is the *p*-process and the so-called proton capture, while ^{134}Xe and ^{136}Xe are formed through the *r*-process, also known as neutron capture process. Neither of these processes occur within the Solar System, which indicates that NDs contained within the meteorites come from a pre-solar source in which heavy and light isotopes are preferentially produced.

The mechanism through which these noble gases became incorporated into the NDs is not well understood, and there are doubts over whether meteoritic NDs are solar or pre-solar. To date, many different theories have been proposed to identify the cosmic origin of the ND, but none is without problems. Some of these theories include CVD, hydrothermal, ion and laser irradiation, microscale plasma (microplasma), and microwave plasma CVD (Angus and Hayman, 1988; Bach-

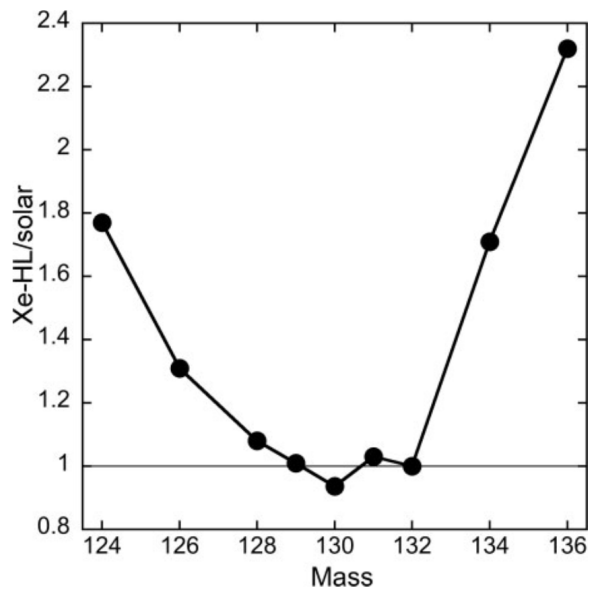


Figure 1.11: Isotopic composition for the pure Xe-HL component which are normalized by the solar ratios (^{132}Xe). Figure is taken from Amari (2009).

mann et al., 1991; Kharisov et al., 2010; Schwander and Partes, 2011; Kharisov et al., 2012; Kumar et al., 2013; Xiao et al., 2014). In addition to experimental studies on the generation of NDs, some computational modeling for synthesizing nanodiamond have been reported (Barnard et al., 2005; Adler and Pine, 2009; Adler et al., 2009; Marks et al., 2012). Note that the topic of formation of ND is out of the scope of this thesis, and thus we will not get into further details.

Ion-implantation mechanism

So far, two theories have been seriously considered as mechanisms for incorporation of noble gases into NDs. It has been hypothesised that gasses could be captured during the diamond growth process (Matsuda et al., 1991, 1995), and secondly, through an ion implantation method (Lewis and Anders, 1981; Lewis et al., 1987; Anders and Zinner, 1993; Daulton et al., 1996; Verchovsky et al., 1998; Koscheev et al., 2001; Gilmour et al., 2005). Ion implantation is the most popular and plausible mechanism through which noble gases are incorporated into the NDs. A strong evidence for an ion implantation hypothesis was explored in the laboratory by Verchovsky et al. (2000) and Koscheev et al. (2001). For context, Verchovsky et al. (2000) implanted about 1000 eV (argon, krypton and neon) and Koscheev et al. (2001) used an implantation energy of about 700 eV (helium, argon, krypton and xenon) into ultradispersed detonation diamonds (UDD) of very similar size to meteoritic NDs (Huss and Lewis, 1994a,b). They showed that low energy ion implantation is a suitable mechanism for trapping noble gases in NDs.

In addition to experimental studies, some computational modeling for ion implantation has been reported (Biersack and Haggmark, 1980; Ziegler et al., 1985; Verchovsky et al., 2001, 2003, 2004). For example, Biersack and Haggmark (1980) used Stopping and Range of Ions in Matter (SRIM) simulation to calculate the interaction of ions with the matter. SRIM is popular computer program in the ion implantation research and technology community and also used widely in other

branches of radiation material science. Verchovsky et al. (2003) used Monte-Carlo Transport of Ions in Matter (TRIM) simulation, which is developed by Ziegler (2004), to model noble gas ions implantation into spherical grains in free space. Note that they considered the natural abundance isotope of noble gases, i.e., ^4He , ^{22}Ne , ^{36}Ar , ^{84}Kr and ^{132}Xe . They observed that for implantation energies of a few hundred keV or less, the projected and lateral scattering, and also backscattering are important factors. In addition, they determined the dependence of ion implantation on the grain size and ion angle of incidence. Figure 1.12 illustrates the ion scattering as a function of implantation depth of neon and xenon, while it is obvious that the scattering process of neon is substantially different from that of xenon which is the heaviest noble gas.

Based on the above-mentioned arguments, the mechanism of noble gases implantation into NDs and also the impact of the size of the NDs and implantation energy remain to be studied in detail. Recently, Shiryaev et al. (2018) reported a combined experimental and computational study of xenon implantation into NDs of widely different sizes. They used the Microscope and Ion Accelerator for Materials Investigations (MIAMI) facility at the University of Huddersfield in the United Kingdom to irradiate ND clusters with xenon ions. They considered three different kind of NDs clusters: (i) natural NDs extracted from meteoritic ND with

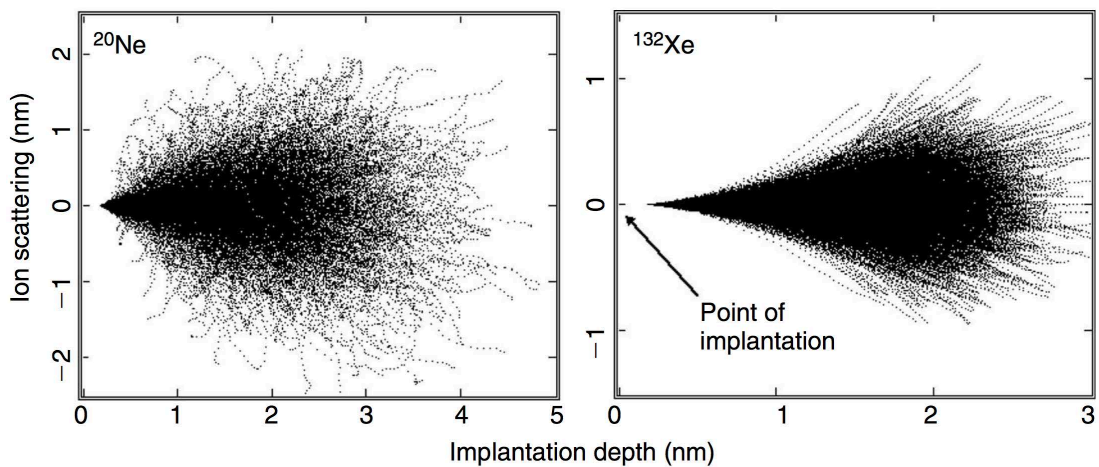


Figure 1.12: Monte-Carlo TRIM simulation of 1.2 keV of neon and xenon implantation into spherical diamond. Figure is taken from Verchovsky et al. (2003).

a long-normal size distribution and a mean size of 2.7–3 nm (Lewis et al., 1987; Daulton et al., 1996; Dai et al., 2002; Huss, 2005; Daulton, 2006), (ii) synthetic NDs created by detonation NDs with mean size of 4–5 nm (Vlasov et al., 2010) and (iii) synthetic NDs with grain sizes of 30–40 nm which are produced from explosives (Shenderova et al., 2011). Shiryaev et al. (2018) used *in situ* transmission electron microscopy (TEM) imaging to monitor real-time evolution of an implantation experiment. While 6 keV ions quickly destroyed the small NDs (2–3 nm diameter), the larger grains (5 nm and above) were highly resistant to irradiation.

Figures 1.13 and 1.14 show TEM images displaying a cluster of NDs before (top panels) and after (bottom panels) irradiation by 6 keV xenon ions at room temperature. Figure 1.13(a) and (c) illustrate the TEM images of detonation ND, while panels (b) and (d) represent the meteoritic NDs. Figure 1.14 shows analysis of the evolution of detonation NDs. To identify the size of NDs of the clusters some of the NDs are highlighted based on the initial diameters (before

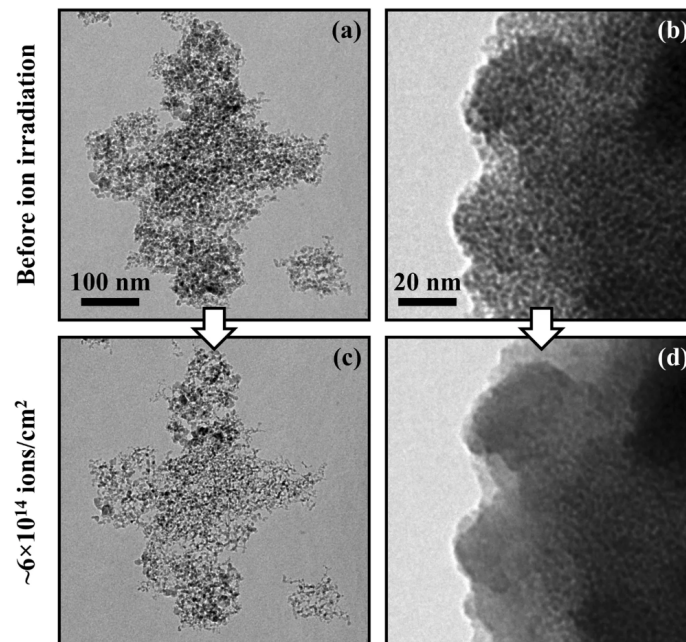


Figure 1.13: Transmission electron microscopy (TEM) images of (a) and (c) detonation NDs, and (b) and (d) meteoritic NDs before and after xenon irradiation. Figure is taken from Shiryaev et al. (2018).

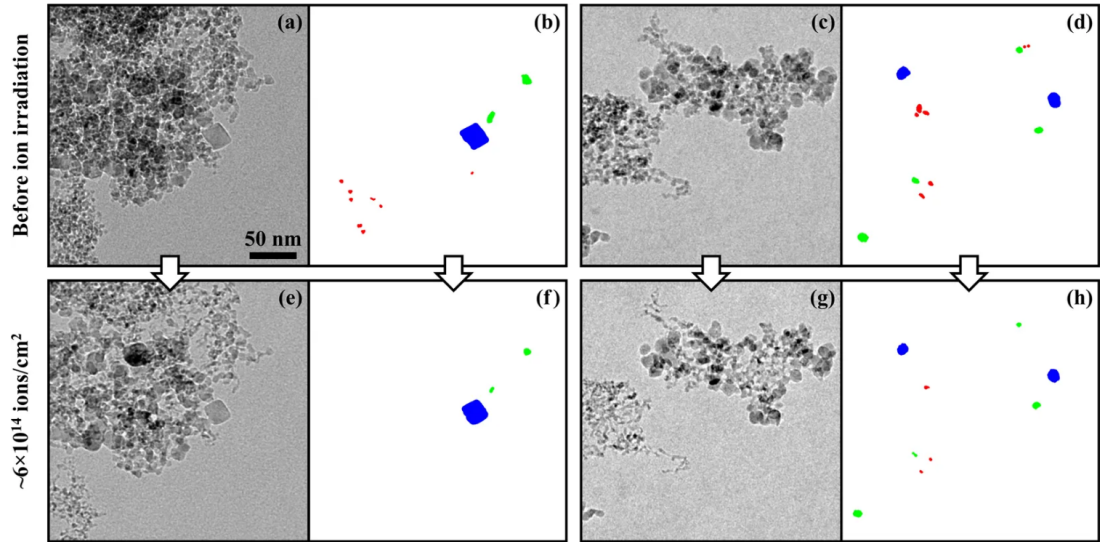


Figure 1.14: TEM images and analysis of detonation NDs, (a)–(d) before and (e)–(h) after irradiation with 6 keV Xe. Individually-identifiable NDs on the peripheries of the clusters are highlighted according to their initial diameters in red (<5 nm), green (~ 10 nm) and blue (>15 nm). All the panels have the same scale marker. Figure is taken from [Shiryaev et al. \(2018\)](#).

irradiation). As can be seen, after the irradiation, the smaller NDs are completely destroyed while the larger ones remain nearly unchanged. In the same study, MD simulations of the implantation process explained this result by showing that small NDs are heated to very high temperatures (over 3000 K) for several picoseconds. Larger NDs, however, have sufficient thermal mass to absorb the deposited energy and retain their diamond character.

Following on the above-mentioned ion-implantation experiments from [Shiryaev et al. \(2018\)](#), Chapter 4 of this thesis provides full details of the atomistic simulation of xenon implantation into NDs. The NDs range in size from 2 to 10 nm and the implantation energy of up to 40 keV are considered. In addition, in the first part of Chapter 5, low implantation energies (up to 700 eV) are considered to simulate and study the hypothesis explored by [Verchovsky et al. \(2000\)](#) and [Koscheev et al. \(2001\)](#). Chapter 5 also includes a mechanism for incorporation of noble gases into the meteoritic and synthetic NDs based on our atomistic simulations.

Thermal release mechanism

Thermal release behaviors of noble gases during the stepped pyrolysis of meteoritic NDs is still very much an open issue. As mentioned before, meteoritic NDs contain at least two different isotopic noble gas components, called P3 (with a nearly “normal” isotopic composition) and HL (with an “anomalous” isotopic composition). Laboratory stepped pyrolysis studies showed that different isotopic components of entrapped noble gases into the meteoritic NDs are released at different temperatures, which means that these components have different origins (Huss and Lewis, 1994a,b; Koscheev et al., 2001; Huss, 2005). Stepped pyrolysis experiments reveal that light noble gases (helium and neon) have a single broad peak temperature-release distribution, while for heavy ones (argon, krypton and xenon) the thermal-release distribution is bimodal (Huss and Lewis, 1994a,b). It is generally accepted that the P3 component is released from the NDs at low temperatures (up to 800°C), while the HL component is released at high temperatures (more than 1000°C) (Huss and Lewis, 1994a,b).

The origin of the uni- and bi-modal thermal release behaviors of noble gases, in particular helium and xenon, from meteoritic NDs is still very much an open issue. To date, many different hypotheses have been proposed to understanding the origin of the P3 and HL components to identify the incorporation of the noble gas, and gas release during pyrolysis. One of them suggests that the P3 gases are sited near the surface of ND grains (Huss, 2005; Nuth and Allen, 1992), and also probably because of some thermal event, these P3 gases are trapped between the surface graphitic-like structure of diamond grains and the bulk of ND grains (Fisenko and Semjonova, 2010). This hypothesis also suggests that the HL anomalous components are implanted into the NDs which is consistent with the *r*- and *p*-processes in supernova nucleosynthesis (Clayton, 1989; Howard et al., 1992; Ott, 1996). Another theory suggests that both P3 and HL components are implanted into separate ND grains and the concentration of both gases is strongly dependent on the size of ND grains (Verchovsky et al., 1998; Fisenko et al., 2004;

Gilmour et al., 2005; Fisenko et al., 2014). These studies suggested that the bi-modal release temperature could explain that both P3 and HL components are located in different ND grains with similar sizes.

Another laboratory explanation of thermal release behaviors of noble gases was proposed by Koscheev et al. (2001), where they implanted noble gas ions into synthetic ND. As discussed before, they showed that ion implantation is a suitable mechanism for trapping noble gases in diamond. Another remarkable experimental result suggests that implantation of a single isotopic composition can produce bi-modal temperature release from the same grains. This suggests that the isotopically anomalous (HL) and normal (P3) gases found in the NDs were probably implanted into them through events separated in time and space. That is, the HL component must have been implanted into the diamonds in a first stage, and the P3 component must have been incorporated at a different stage. In contrast with the previous hypothesis by Verchovsky et al. (2000), a series of experiments by Koscheev et al. (1998, 2001, 2004, 2005) suggest that both the P3 and HL gases can be located in the same or different populations. This suggests that the P3 component is released simultaneously at low and high temperatures, which means that P3 component is released along with the anomalous pure HL component at the high temperature peak. It is to be noted that, as shown in Figure 1.15, their pyrolysis measurements observed a single broad temperature distribution for He and Ne, and a bimodal distribution for Ar, Kr and Xe, corresponding almost exactly with those found for meteoritic NDs (Huss and Lewis, 1994a,b). Even though the implantations involved only a single component for each noble gas, a bimodal temperature-release distribution was found.

In summary, it is generally accepted that the anomalous HL gases are implanted into the meteorite NDs; and by graphitization of NDs at high temperature, HL component is released from NDs. In contrast, the incorporation and releasing process of P3 gases have remained ambiguous. In Chapter 5 of this thesis, a molecular dynamics approach is employed to detailed atomistic insight

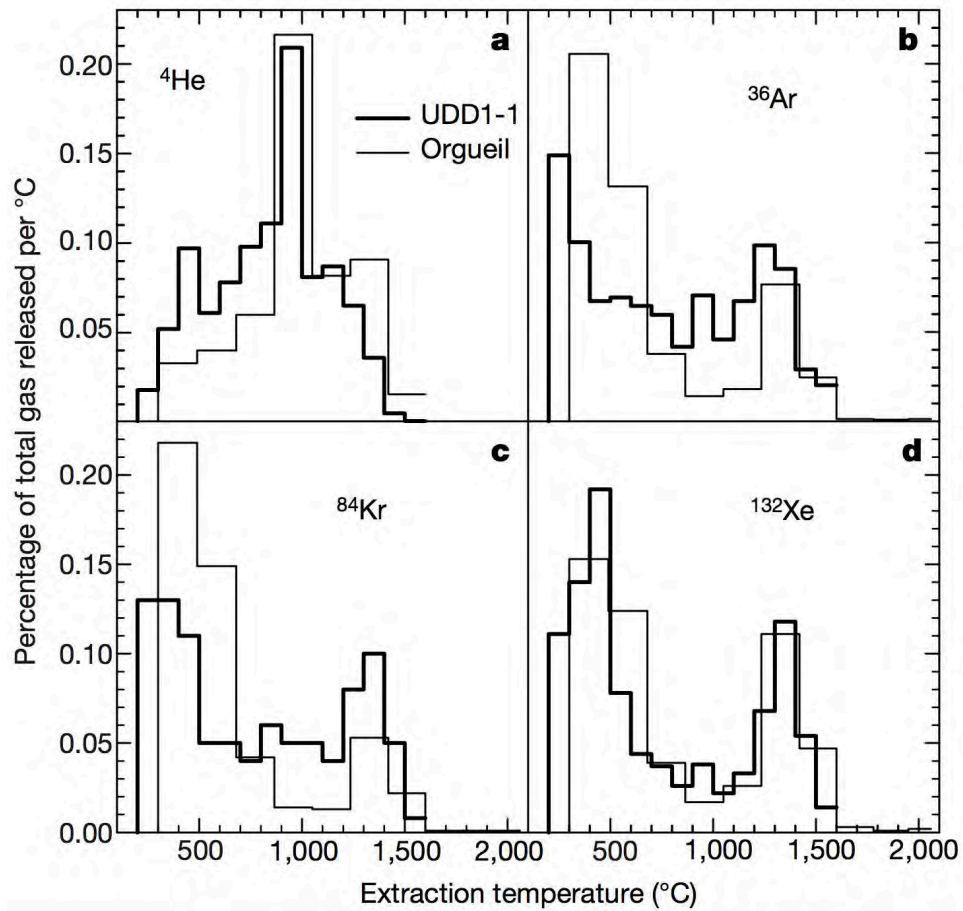


Figure 1.15: Thermal release patterns of noble gases during stepped pyrolysis of meteoritic (Orgueil) NDs (Huss and Lewis, 1994a,b) and terrestrial (UDD) NDs implanted with noble gas mixture (700 eV). Figure taken from Koscheev et al. (2001).

into the process of implantation and incorporation of noble gases into NDs and also presents a clear atomistic explanation for the release process of entrapped gases from NDs during the annealing.

1.1.2 Deformation of diamond nanopillars

Understanding of mechanical deformation and failure mechanisms, as well as ultimate damage tolerances of nanostructured materials, is crucially important for applications of nanomaterials into future generation nanodevices in sensing, defense and energy storage (Brinckmann et al., 2008; Jang and Greer, 2010; Taloni et al., 2018). Intriguingly, mechanical properties of bulk materials can be altered

dramatically when the material dimensions are reduced to the micro- and the nano-scale (Zepeda-Ruiz et al., 2007; Gu et al., 2012; Huang et al., 2014) as was demonstrated with metals (Gu et al., 2012) or silica glasses (Luo et al., 2015). Of a particular scientific and technological interest are the different carbon allotropes (Si et al., 2016; Bauer et al., 2016; Shiell et al., 2018).

Diamond, the hardest bulk material known so far, is remarkably stiff and durable (Banerjee et al., 2018). It has significant applications in a variety of research topics such as biomedicine, electronics, and photonics (Robinson, 1986; Zhu et al., 1998; Aharonovich et al., 2011; Mochalin et al., 2012; Wang et al., 2014; Zhu et al., 2016; Chen and Zhang, 2017). The mechanical properties of diamond have been of particular interest for a long time. To date, many theoretical studies and experimental investigations (Uemura, 1994, 1995; Telling et al., 2000; Roundy and Cohen, 2001; Xiong et al., 2007; Jiang et al., 2011; Guo et al., 2011; Jensen et al., 2015) have been performed to study its strength and elastic modulus under various loading conditions (Xiong, 2011). Elastic and plastic deformation of diamond have also been studied intensively and form the basis of many devices and technologies developed in the field of integrated electronics, catalysis and nanophotonics.

Recently, Banerjee et al. (2018) experimentally reported the ultralarge and reversible elastic deformation of $\langle 111 \rangle$ -oriented diamond nanoneedles. They observed this deformation in nanoneedles of both single-crystalline and polycrystalline diamond. Figure 1.16(a) shows the elastic deformation and full recovery to original shape. They also demonstrated catastrophic fracture along the $\{111\}$ planes after the critical displacement of the needle (see Figure 1.16(b)). Very recently, our experimental collaborators at the University of Technology Sydney used the electron beam of a scanning electron microscope (SEM) to induce an electrostatic-deformation of nanoscale diamond pillars (Regan et al., 2020). They showed that DNP bent through large angles and can undergo reversible plastic deformation in (100)-oriented nanopillars, while (111)-oriented nanopillars un-

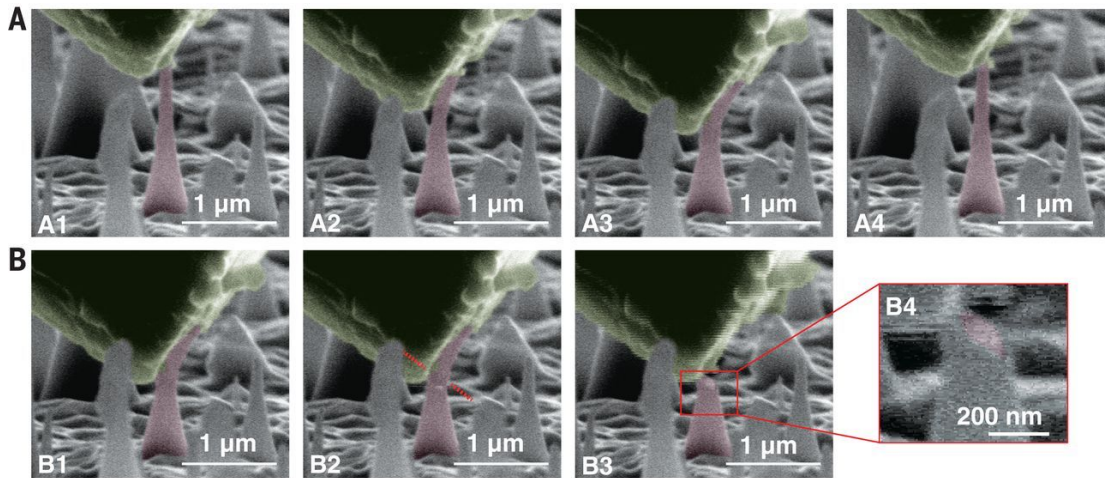


Figure 1.16: (a) Scanning electron microscope (SEM) micrographs of ultralarge elastic deformation in a single-crystalline nanoneedle during loading and subsequent full recovery after unloading. (b) Larger deformation of the same nanoneedle in panel (a) to the point of catastrophic fracture. Figure adapted from [Banerjee et al. \(2018\)](#).

dergo elastic deformation and brittle fracture. As our findings in Chapter 6 are motivated by their remarkable results, the full details of their experimental results are provided in what follows.

In their deformation experiments, the beam was used to locally charge diamond nanopillars and their surroundings, generating Coulomb forces that are sufficiently strong to deflect the nanopillars. This technique is unique and attractive because physical contact is not needed to induce bending. It is also, rapid and reversible and enables real-time imaging of deformation dynamics with high spatial resolution. Employing this technique, they were able to characterize the deformation dynamics of a large number of nanopillars, and to delineate dependencies on the size and crystallographic orientation of nanopillars.

Tapered diamond nanopillars were fabricated from single crystal diamond with (001) and (111) orientations using a reactive ion etching (RIE) process. The fabrication process is shown in Figure 1.17. A colloidal solution of SiO_2 microbeads was dispersed on the bulk diamond surface, followed by an RIE step in an oxygen plasma. They utilized conditions that favored resputtering, resulting in local micromasking of the SiO_2 microbeads to obtain diamond nanopillars

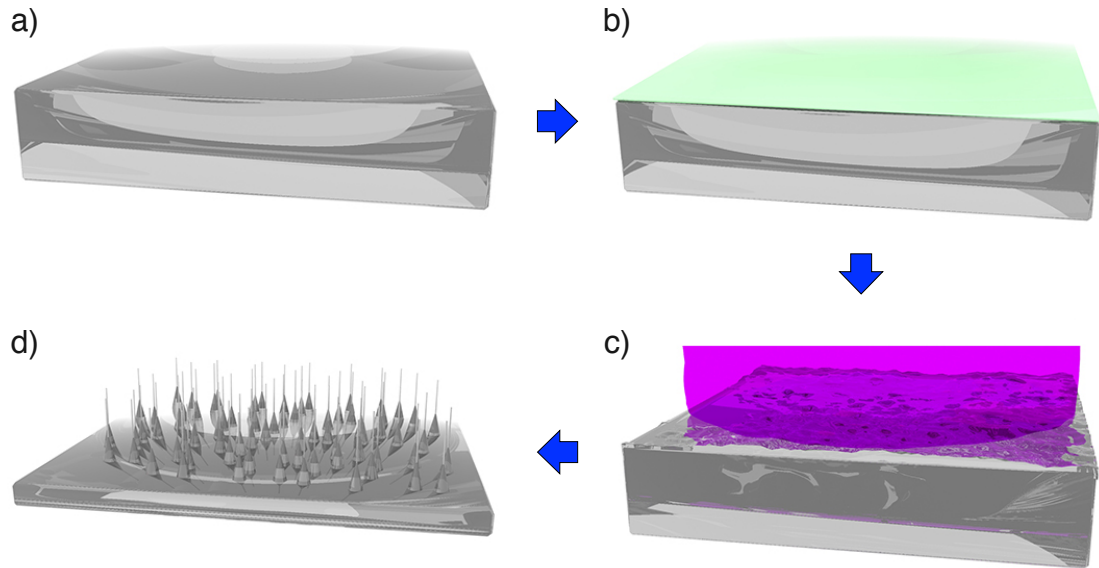


Figure 1.17: Schematic diagram of fabrication procedure, taking a bulk CVD-overgrown diamond and undergoing a dry etch procedure to fabricate diamond nanopillars. (a) A bulk diamond is (b) coated with a Silica (SiO₂) bead solution. (c) Inductively coupled plasma-reactive ion etching (ICP-RIE) of the bulk diamond is being done into the described conditions. (d) The fabricated diamond nanoneedles undergo a cleaning process and are complete. Figure adapted with permission from the Supplementary Materials of [Regan et al. \(2020\)](#).

with diameters ranging from ~ 200 nm to ~ 20 nm. Further details have been provided in [Regan et al. \(2020\)](#). The density of diamond nanopillars ranges from closely packed to isolated, as shown in Figure 1.18(a) and (b). This is useful for controlling charging of the nanopillars in an SEM, as is discussed below. The shape of the diamond nanopillars, shown in Figure 1.18(b), is typically tapered with a minimum diameter of ~ 15 nm, situated on a conical base that is ~ 200 nm wide.

To study the deformation dynamics of diamond, the fabricated nanostructures were pre-irradiated and imaged using the focused electron beam of a SEM, as shown schematically in Figure 1.18(c). Under the conditions used here, electron irradiation does not generate defects in diamond ([Martin et al., 2015](#)). It does, however, give rise to localized charge accumulation ([Cazaux and Lehuede, 1992](#)) due to electron injection/emission into/from the nanopillars and surrounding diamond, generating electrostatic forces that are sufficiently strong to bend

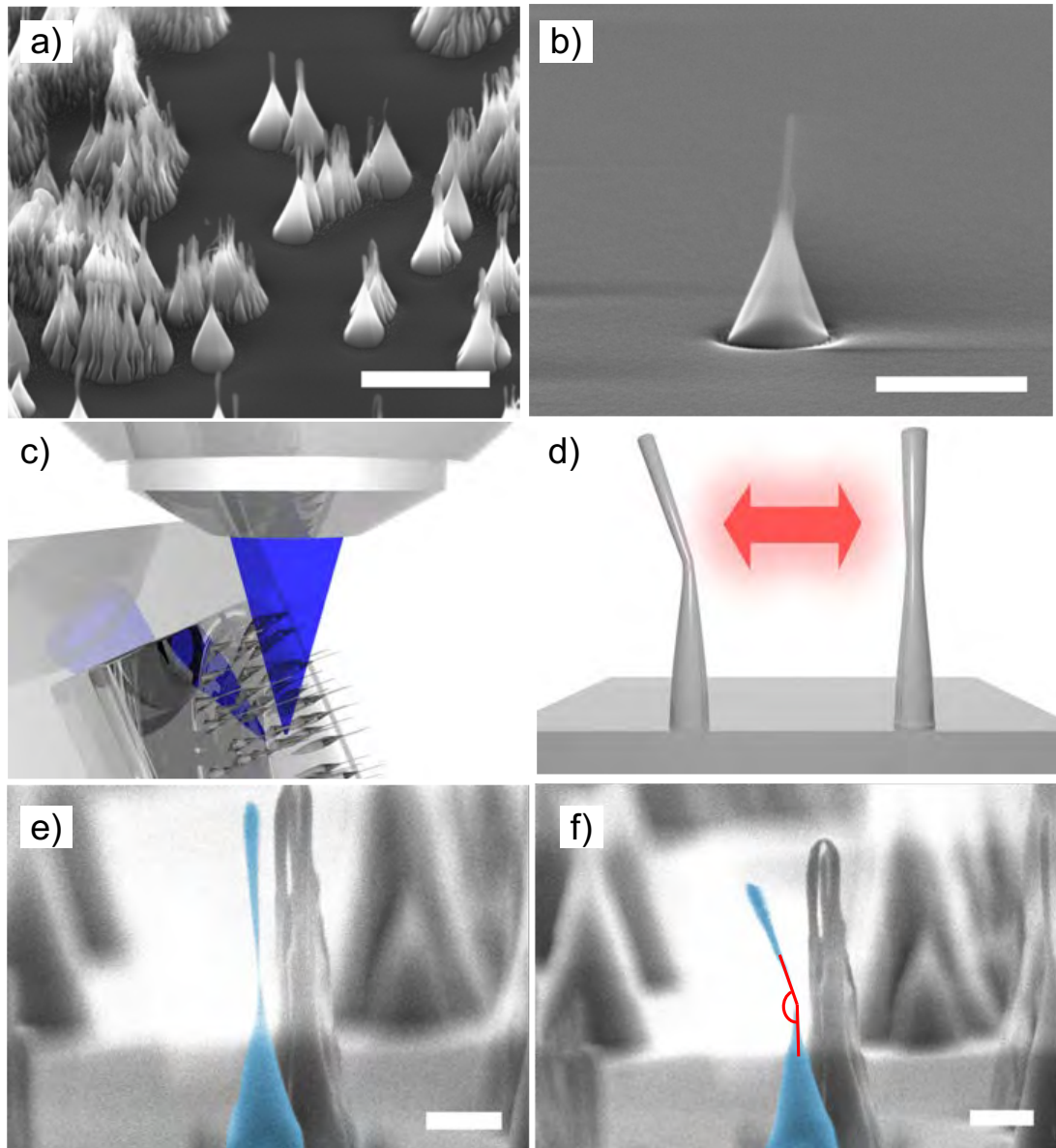


Figure 1.18: Deformation of (001)-oriented single crystal diamond nanopillars. (a) Distribution of diamond nanopillars after fabrication. The scale bar corresponds to $2\ \mu\text{m}$. (b) Isolated tapered nanopillar showing the typical shape. The scale bar corresponds to $500\ \text{nm}$. (c) Schematic of the experimental setup used to deform and image nanopillars. The blue colour indicates a focused electron beam. (d) Schematic of the underlying charging mechanism that was utilized to bend diamond nanopillars. (e) False-color SEM image of a diamond nanopillar before deformation. (f) The same nanopillar after bending induced by an electrostatic force with deflection of ~ 25 degrees. Scale bars correspond to $100\ \text{nm}$. Figure adapted with permission from [Regan et al. \(2020\)](#).

the nanopillars (Figure 1.18(d)). A free standing nano structure charges positively when the material volume is small relative to the interaction volume of the

electron beam. In contrast, large volumes (in relation to the electron interaction volume) such as the bulk will charge negatively. The charging effect is amplified by the strongly insulating nature of diamond, which prohibits charge neutralization through the bulk. As the electron beam was focused on a larger diamond structure next to a nano pillar with a narrow neck, positive charges accumulated, resulting in a Coulomb force. A typical example is shown in Figure 1.18(e) and (f), by an SEM image pair of a nanopillar before and after localized electron beam irradiation was used to deform it. The deformation of the diamond nanopillar was limited to the narrow, tapered section of the diamond, where the nanopillar diameter has a minimum. Note that localized scanning of the diamond by the electron beam, as well as spot-irradiations can be used to redistribute the charges, alter the electric field distribution and therefore reversibly bend the nanopillars in arbitrary directions.

Previous reports ([Humble and Hannink, 1978](#); [Huang et al., 2014](#); [Banerjee et al., 2018](#)) on mechanical indentation of diamond nanopillars show elastic deformation, followed by brittle fracture or restoration of the nanopillars to their original positions upon stress relief. In contrast, deformation of our (001)-oriented nanopillars is permanent, indicating a deformation beyond the elastic response, into the plastic regime. The plastic nature of the deformation was confirmed by imaging of nanopillars after exposure to atmosphere, and confirmed by the conventional elastic behaviour (and brittle fracture) of (111)-oriented nanopillars that is demonstrated below.

The act of plastic deformation requires the formation and propagation of defects (e.g. dislocations) within the lattice that does not result in brittle fracture. Previous works by [Huang et al. \(2014\)](#) and [Humble and Hannink \(1978\)](#) have shown that in diamond, the (111) plane exhibits such dislocations under specific conditions, due to a lower binding energy along this direction. On the molecular scale, plastic deformation requires breaking and re-formation of interatomic bonds. Yet, in diamond, the covalent bonds are highly directional and thus

strongly resist deformation, leading typically to brittle fracture along a crystallographic plane. However, the plastic deformation observed here suggests that the nanopillars are sufficiently small for the Gibbs Free energy to be lower, to induce ductile rather than a brittle deformation. The nanometre scale of the pillars is required for plastic behaviour to occur, which was indeed observed in experiments that we used to identify the ultimate diameter below which deformation was observed. Figure 1.19(a) shows the results from a statistical study of over 50 nanopillars, with an approximate threshold of ~ 40 nm, above which no bending was observed. Figure 1.19(b) and (c) show typical examples of the deformation of nanopillars with minimum diameters of 18 nm and 21 nm, respectively. An example of a nanopillar that is sufficiently thick in order not to exhibit any bending is shown in Figure 1.19(d). The video of the deformation process is

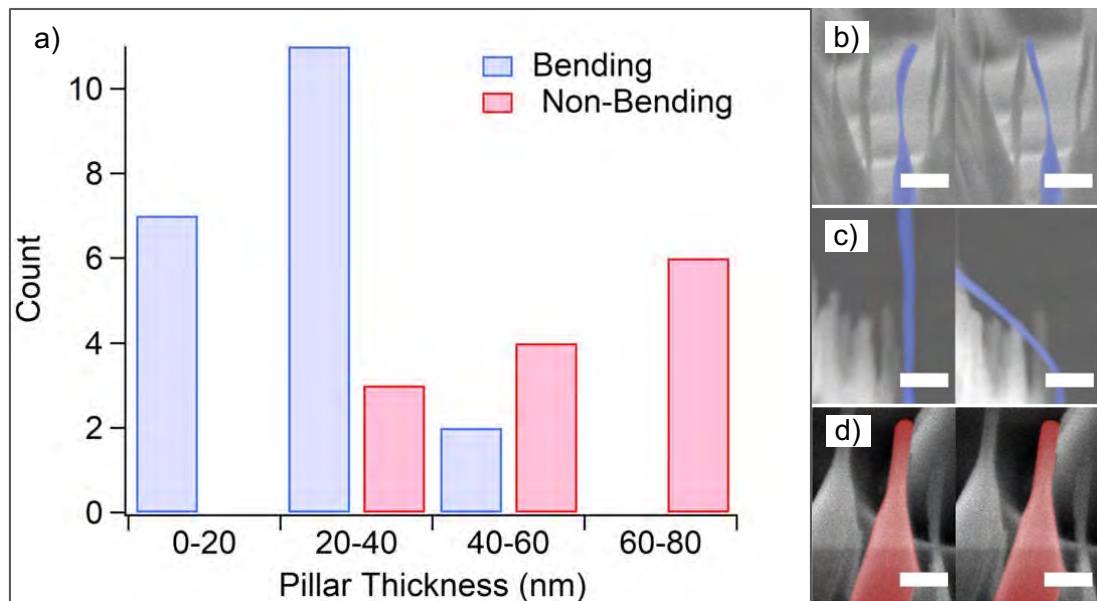


Figure 1.19: Size-dependence of the deformation behaviour of (001)-oriented nanopillars. (a) Histogram of nanopillars that were observed to bend/deform as a function of size. Blue and red bars designate nanopillars that did and did not bend, respectively. (b) SEM image pair showing a typical example of a “thin” nanopillar with a minimum diameter of 18 nm bending from its initial position (left) to the plastically-deformed position (right). (c) Analogous example of plastic deformation of a nanopillar with a minimum diameter of 21 nm. (d) Typical example of a “thick” nanopillar with a minimum diameter of 70 nm that did not undergo deformation. Scale bars in (b)–(d) are 200 nm. Figure adapted with permission from [Regan et al. \(2020\)](#).

provided in [Movie 1.1](#). We note that, in some cases, the nanopillars undergo a noticeable vibration prior to plastic deformation, which indicates that the electrostatic force was initially too weak to exceed the elastic regime. The vibrations increase during electron imaging/irradiation, and deformation would occur when the electron beam was localized to the thinnest region of the nanopillar.

The plastic behaviour seen in [Figures 1.18](#) and [1.19](#) was not observed in (111)-oriented nanopillars subjected to the same deformation conditions. In contrast, these nanopillars exhibit elastic deformation and brittle fracture, which is typical deformation behaviour of bulk diamond. The effect is illustrated in [Figure 1.20](#), where the thin diamond nanopillar was irradiated with the electron beam but was fractured (rather than bent). Video of the fracture is shown in [Movie 1.2](#). The dramatic difference between the deformation dynamics of (001) and (111)-oriented nanopillars serves as direct evidence for the underlying mechanisms revealed by the simulation results presented in [Chapter 6](#), and for the fact that the plastic behaviour exhibited by (001)-oriented nanopillars is not an artifact of hysteresis of the electron-beam-induced charging process that we used to deform the nanopillars. Note that we exclude damage caused by the electron beam, amorphisation or surface termination as plausible causes for the plastic deformation, since those would have been identical for both (001) and (111) oriented pillars. Intuitively, the elastic behaviour of (111)-oriented diamond seen in [Figure 1.20](#) is consistent with the fact that the (111) plane of face-centered cubic structures has the lowest bonding energy. It is therefore a natural shear direction, suggesting that (111)-oriented diamond pillars will be most susceptible to brittle failure.

In [Chapter 6](#), we complement these experimental results with molecular dynamics simulations of the deformation process that reveal the underlying mechanism. Our simulations provide atomistic details of the plastic, elastic and brittle failure of diamond nanopillars. Our results reveal that strain induces the emergence of a new ordered allotrope of carbon – which we term O8-carbon – that mediates the plastic deformation process.

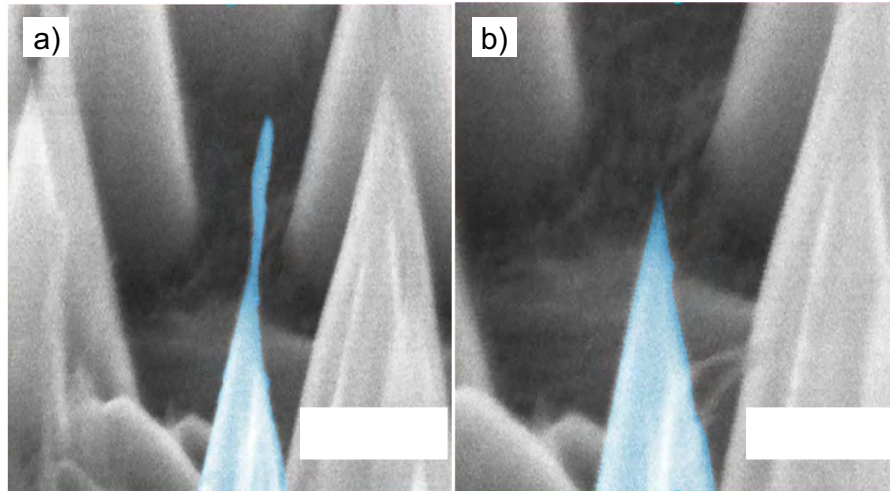


Figure 1.20: Brittle fracture of (111)-oriented diamond nanopillars. (a) False-color SEM image of a nanopillar before deformation. (b) The same nanopillar after brittle fracture. Scale bars correspond to 100 nm. Figure adapted with permission from [Regan et al. \(2020\)](#).

1.1.3 Epitaxial diamond interfaces

Semiconductor heterojunctions are routinely formed to exploit the superior properties of two different materials. However, to attain good quality material properties and optimized device performance, control over the interface crystallinity and defect formation is required. In the case of a pair of materials with a high degree of lattice mismatch, such a coherent interface is typically prohibited, limiting the available options for heterojunction engineering. The emergence of advanced epitaxial or so-called textured growth techniques has developed new interesting research topics on materials and heterostructures, surprisingly for materials with huge lattice mismatch. In recent years, studies have reported the epitaxial growth of diamond on different materials with a close lattice structure, such as silicon (Si) and silicon-carbide (SiC). Due to its scalability and thermal expansion, Si is a promising substrate material for the epitaxial growth of diamond, and this mechanism has been previously reported ([Narayan et al., 1988](#); [Williams and Glass, 1989](#); [Jeng et al., 1990](#); [Jiang et al., 1993](#); [Robertson, 1995](#); [Schreck and Stritzker, 1996](#)). On the contrary, due to the huge lattice mismatch ($\sim 32\%$) and significant surface energy differences (1.51 and 5.60 J/m² for Si and diamond, respectively

(Hong and Chou, 1998)), diamond nuclei on Si did not coalesce with neighboring nuclei (Yaita et al., 2018).

Lee et al. (2000) reported that by using a cubic polytype silicon carbide (3C-SiC) intermediate layer, diamond can make nuclei on the Si substrate. Based on this experimental result and due to the smaller lattice mismatch between diamond and SiC ($\sim 18\%$) compared to diamond and Si ($\sim 32\%$), epitaxial 3C-SiC buffer layers on Si substrates are useful for diamond epitaxy (see Figure 1.21). Also, by using the high-resolution transmission electron microscope (HRTEM), Wen et al. (2009) studied the interface structure of 3C-SiC and Si, and investigated the interfacial misfit defects. Based on their analysis, four different types of misfit dislocations at 3C-SiC/Si interface were determined. In addition to experimental studies on SiC/Si heterostructure, few computational studies of the SiC/Si interface have been reported. A series of works from Cicero et al. (2002a,b) and Pizzagalli et al. (2003) studied the misfit dislocations at the SiC/Si interface using classical and first-principles calculations. They showed that according to the computed configuration energy, it is favorable to have carbon atoms at the reconstructed interface. Also the edge dislocations at the interface were the most efficient mechanism for the strain relaxation. Their results were in agreement with laboratory observations by Long et al. (1999).

In the case of epitaxial growth of diamond on SiC, which has exactly the same crystal structure, a few experimental studies have been reported (Walmsley

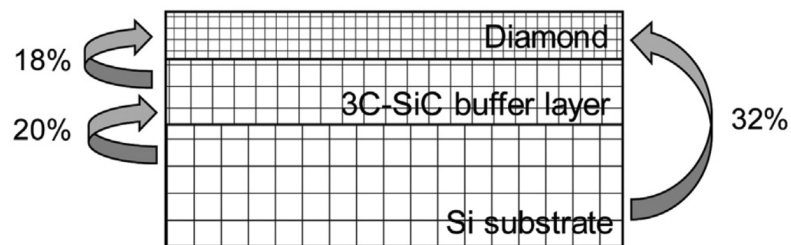


Figure 1.21: A schematic demonstration of diamond thin film on Si substrate with 3C-SiC buffer layers. Percentage of the lattice mismatch of layers are shown. Figure is taken from Yaita et al. (2018).

and Lang, 1983; Chang et al., 2000; Voronin et al., 2001; Park et al., 2006, 2007). These studies used TEM to investigate the microstructural behaviour of the interface of diamond and cubic SiC (β -SiC). The main outcome of these experiments is that an orientation relationship exists between diamond and SiC composites (Matthey et al., 2017). Similarly, Stoner and Glass (1992) reported the heteroepitaxial growth of diamond on (001)- β -SiC substrates. They employed an *in situ* bias pretreatment by standard microwave plasma chemical vapor deposition. Based on their scanning electron microscopy results, $\sim 50\%$ of the initial diamond nuclei are textured with the (001) planes parallel to the (001)-SiC substrate and [110] directions are aligned within 3° . Park et al. (2007) experimentally pointed out the relationship between {111}-diamond and {111}-3C-SiC and also $\langle 011 \rangle$ -diamond and $\langle 112 \rangle$ -3C-SiC, and they observed about 5% lattice mismatch in the diamond/3C-SiC interface. In a recent experiment, Yaita et al. (2017) reported epitaxial nucleation of diamond on the (001)-3C-SiC/(001)-Si substrates with a small tilt of the planes and small misfit dislocations. In addition, Suto et al. (2017) successfully fabricated a highly oriented (111)-diamond film on (111)-3C-SiC/(111)-Si substrates.

Recently, our experimental collaborators at the University of Melbourne went one step further than the studies mentioned above, and for the first time, they demonstrated local coherent heteroepitaxial growth of (100)-SiC on (100)-diamond with minimal strain (Tsai et al., 2020). They performed high-resolution transmission electron microscopy (HRTEM) to confirm the quality and atomic structure near the interface. Note that as these experimental results are a point of focus in this thesis, in what follows we will provide detailed descriptions of the performed experiments to help contextualize our findings in Chapter 7.

A HRTEM image of the fabricated SiC-on-diamond interface is shown in Figure 1.22 with accompanying Fast Fourier Transforms (FFTs) and a Near Edge X-ray Absorption Fine Structure (NEXAFS) spectrum. Figure 1.22(a) shows three distinct layers: a protective layer of graphite used for TEM handling, the grown

SiC film with a cubic lattice structure, and the diamond substrate. The 3C-SiC layer is confirmed with NEXAFS in Figure 1.22(b) (Chang et al., 1999; Prado et al., 2003; Liu et al., 2017). The grown 3C-SiC layer, seen in Figure 1.22(a), is approximately 10 nm thick and not atomically smooth nor perfectly homogeneous with noticeable shadow contrasting around the interface. This is due to changes in material density that occur through the sample lamella (~ 100 nm thick) and strain from localized and extended defects. Despite this, the crystallinity in both the grown layer and substrate is evident, as seen in the inset which is the calculated FFT of the TEM image Figure 1.22(a). Importantly, no major strain-relieving threading dislocations are observed to propagate into the bulk on either side of the interface. Figure 1.22(c) is the enlarged area highlighted in Figure 1.22(a) with a dashed box where high coherence between 3C-SiC and diamond is seen to be over 8 nm wide. Despite the coherence, the two materials are very slightly misoriented by approximately 1° , as shown in orange, compa-

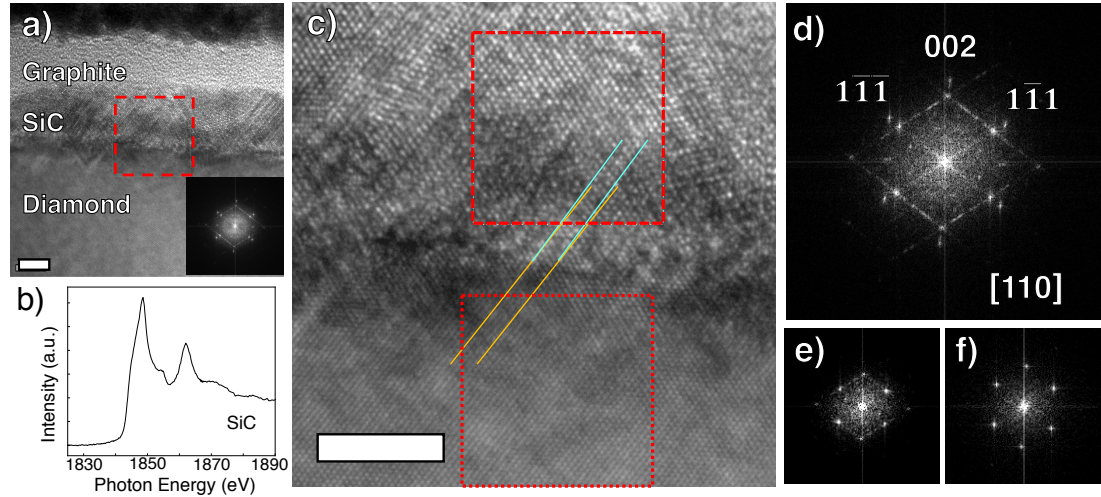


Figure 1.22: (a) Cross-sectional HRTEM (5 nm scale bar) of the prepared sample, showing graphite, SiC and diamond layers. The image is taken in the $[110]$ direction, and the inset shows the FFT of the entire image. (b) SiC NEXAFS of the surface after 1350°C anneal. (c) Magnification of the selected area in (a) demonstrating a coherent interface between SiC and diamond; slight misorientation is shown via the orange and light blue lines. (d) is the FFT of (c) with clear and largely oriented SiC and diamond signals. (e) and (f) are FFTs of the dashed and dotted regions, respectively, highlighted in (c) that verify the crystal quality of SiC and diamond. Figure adapted with permission from Tsai et al. (2020).

rable to the literature values of 0.52° when diamond was seeded on a 3C-SiC substrate (Yaita et al., 2017). Coherence over 5–10 nanometres without extended defects in the grown layer indicates that a periodic bonding structure exists at the interface.

The quality of the interface is further demonstrated by the FFT shown in Figure 1.22(d), which is calculated from Figure 1.22(c). Here, the bright diffraction signals are arranged into inner and outer hexagons which are calculated from the delineated areas in Figure 1.22(c); these are caused by 3C-SiC and diamond, respectively. From these FFTs it is clear that the misalignment between the two materials, if any, is very slight with $[1\bar{1}\bar{1}]$, $[002]$ and $[1\bar{1}1]$ signals showing a strong linear dependency, thus providing strong evidence that the grown 3C-SiC used the diamond as a template for crystallization. From these diffraction points, the lattice constants for 3C-SiC and diamond are derived to be 4.42 \AA and 3.61 \AA , respectively. The signal peaks were located by fitting Gaussians to intensity line cuts that went through opposing $[002]$ diffraction points to achieve sub-pixel accuracy. The calculated values are within 2% accuracy of the literature lattice constant values of $a_{\text{SiC}} = 4.360 \text{ \AA}$ (Taylor and Jones, 1960; Järrendahl and Davis, 1998) and $a_{\text{diamond}} = 3.567 \text{ \AA}$ (Krüger, 2010) and are well within instrumental error margins. This, in conjunction with the FFT plots, indicate that there is minimal strain between the materials despite a lattice mismatch of 22%. Outside the area of high quality crystallinity; however, stacking faults and defects begin to appear in the grown 3C-SiC layer as shown by fault lines in Figure 1.22(d) which are barely evident in Figure 1.22(e). The formation of low-strain SiC locally on single-crystal diamond provides strong evidence that this fabrication procedure has promise in bypassing the polycrystalline limitations of diamond growth seen in other diamond heterostructures (Koizumi et al., 2018).

A microscopic understanding of the atomic structure and the chemical environment at the interface, which plays a significant role in the physical properties of semiconductor heterojunctions, still remains hardly accessible to any above-

mentioned experimental technique. Atomistic simulations are a powerful tool for complementing the experiments. To understand the formation of SiC/diamond heterostructure and provide atomistic details of the SiC/diamond interface, classical molecular dynamics simulations are used in Chapter 7. In that chapter, we provide an atomic-level discussion of dislocations and reconstructions on the SiC/diamond heterojunctions interface.

1.2 Computational method

Computer simulations, also known as virtual experiments, are principal methods in all different disciplines of scientific research. They are playing a significant role in enhancing the understanding of laboratory (real) experiments. Computer simulations can accompany experimental as a way to model what happens in real-world experiments. Atomistic simulation methods calculate the interaction energies between atoms/molecules in a system (or atomic nuclei and electrons), and also determine the evolution of such systems with time. In the scope of atomistic simulations are various methods, from the most accurate quantum mechanical methods to more approximate empirical pair potential methods. Basically, the accuracy of the methods has an inverse relation with the computational cost of calculations. The quantum mechanic methods can be applied to small systems (e.g., less than 100 atoms) for picosecond timescale, while the empirical methods can handle large systems with millions of atoms over nanosecond periods of time.

Calculating the energy of a system of atoms is the substantial requirement to carry out atomistic simulations. Time and space derivatives of this energy give rise to all calculable properties of the systems such as electronic properties, optimized atomic configuration, and thermodynamic and elastic properties. In this section, we briefly introduce the computational method that has been used in this thesis.

1.2.1 Molecular dynamics simulations

Molecular Dynamics (MD) simulation is a well-established computational method used to provide understanding of the equilibrium and transport properties of nano-structure materials by using classical mechanics. Nowadays, MD method is broadly used in different scientific research areas such as physics, chemistry, astrophysics and biology.

MD technique solves Newton's equations of motion of a system of N particles (called N -body system). The general protocol of MD simulation has three steps: (i) set up initial systems and conditions such as position and initial velocity of each atom, (ii) by applying classical potential method, atomic and molecular forces are calculated, and (iii) the new configuration of the system for each time step is identified by using Newton's equations of motion. These steps are then repeated until the required time for the simulation is achieved. Note that the physical properties of the system are usually ensemble or time averages. In other words, as MD simulations propagate the equations of motion of the system, to compute the properties of the system relies on post-processing of trajectory information.

Equations of motion

Classical Newton's equation of motion of N -body system is used to calculate the force between the particles. The force is equal to the negative derivative of the potential energy as

$$\mathbf{F}_i = -\frac{\partial U(\mathbf{r}_1, \mathbf{r}_2, \dots, \mathbf{r}_N)}{\partial \mathbf{r}_i}, \quad (1.1)$$

where \mathbf{F}_i is the force acting on the i th particle, U is the potential energy and \mathbf{r} is the position of the particles. To calculate the force between the particles the above equation is integrated over the time. Various algorithms exist to integrate the equation of motion. These algorithms are derived from a third-order Taylor expansion of the position (coordinate of the particle) forward and backward in

time t :

$$\mathbf{r}(t + \Delta t) = \mathbf{r}(t) + \mathbf{v}(t)\Delta t + \frac{\mathbf{F}(t)}{2m}\Delta t^2 + \frac{\Delta t^3}{3!}\mathbf{F}'(t) + \mathcal{O}(\Delta t^4), \quad (1.2)$$

and

$$\mathbf{r}(t - \Delta t) = \mathbf{r}(t) - \mathbf{v}(t)\Delta t + \frac{\mathbf{F}(t)}{2m}\Delta t^2 - \frac{\Delta t^3}{3!}\mathbf{F}'(t) + \mathcal{O}(\Delta t^4). \quad (1.3)$$

For the MD simulations in this thesis the velocity-Verlet algorithm is used. Based on the Verlet algorithm ([Verlet, 1967](#)) the position of the particles can be defined by summing Equations (1.2) and (1.3),

$$\mathbf{r}(t + \Delta t) + \mathbf{r}(t - \Delta t) = 2\mathbf{r}(t) + \frac{\mathbf{F}(t)}{m}\Delta t^2 + \mathcal{O}(\Delta t^4) \quad (1.4)$$

or

$$\mathbf{r}(t + \Delta t) \approx 2\mathbf{r}(t) - \mathbf{r}(t - \Delta t) + \frac{\mathbf{F}(t)}{m}\Delta t^2. \quad (1.5)$$

The estimate of the new position contains an error that is of order Δt^4 , where Δt is the time step in MD scheme and m is the mass. This equation suggest that we can generate the next position of the particle ($\mathbf{r}(t + \Delta t)$) by using the current position ($\mathbf{r}(t)$) and the previous position ($\mathbf{r}(t - \Delta t)$) along with the current force ($\mathbf{F}(t)$). Note that the Verlet algorithm does not use the velocity to compute the new position, whereas the velocity at time t can be calculated from previous positions using

$$\mathbf{r}(t + \Delta t) - \mathbf{r}(t - \Delta t) = 2\mathbf{v}(t)\Delta t + \mathcal{O}(\Delta t^3) \quad (1.6)$$

or

$$\mathbf{v}(t) = \frac{\mathbf{r}(t + \Delta t) - \mathbf{r}(t - \Delta t)}{2\Delta t} + \mathcal{O}(\Delta t^2). \quad (1.7)$$

This expression for the velocity is only accurate to order Δt^2 ([Frenkel and Smit, 2001](#)). For more accurate the velocity a Verlet-like algorithm must be used, like the velocity-Verlet algorithm. The velocity form of the Verlet algorithm is

given by the following equations,

$$\mathbf{r}(t + \Delta t) = \mathbf{r}(t) + \mathbf{v}(t)\Delta t + \frac{\mathbf{F}(t)}{2m}\Delta t^2 \quad (1.8)$$

$$\mathbf{v}(t + \Delta t) = \mathbf{v}(t) + \frac{\mathbf{F}(t + \Delta t) + \mathbf{F}(t)}{2m}\Delta t. \quad (1.9)$$

In this method, we can calculate the new velocities only after we have calculated the new positions.

Physical quantities

MD simulations computes quantities such as position of the particles and their velocities. In order to convert those quantities into macroscopic observables such as pressure, energy and temperature we need statistical measurement. For example, the temperature is calculated by taking the average of velocity over all particles in system by the following expression,

$$\langle T \rangle = \frac{1}{3(N-1)k_B} \left\langle \sum_n m_n \mathbf{v}_n \cdot \mathbf{v}_n \right\rangle, \quad (1.10)$$

where \mathbf{v}_n is the velocity of n th particle, k_B is Boltzmann's constant and N is the total number of particles in the system. Pressure is calculated by

$$\langle P \rangle = \frac{Nk_B \langle T \rangle}{V} + \frac{1}{3V} \left\langle \sum_{n_1} \sum_{n_2} \mathbf{F}_{n_1 n_2} \cdot \mathbf{r}_{n_1 n_2} \right\rangle, \quad (1.11)$$

where V is the volume of the system and $\mathbf{F}_{n_1 n_2}$ is the force acting between n_1 and n_2 particles and $\mathbf{r}_{n_1 n_2}$ is the distance between two particles.

MD simulations can be performed in a number of ensembles which are defined by three different physical variables such as the number of particles (N), volume (V), temperature (T), total energy (E) chemical potential (μ) and pressure (P). Different ensembles can be generated depending on which three variables are constant or constrained. The simplest ensemble is the NVE ensemble that

is called microcanonical ensemble and stands for a constant number of particles, constant volume and constant total energy. Other well-known ensembles are the NVT (also named canonical) and NPT (also called isothermal-isobaric) ensembles. There are different methods to control temperature, such as Andersen (Andersen, 1980), Nosé-Hoover (Hoover, 1985) and Bussi (Bussi et al., 2007) thermostats. The most popular methods for controlling the pressure in the NPT ensemble are Andersen (Andersen, 1980), Nosé-Hoover (Hoover, 1985) and ParrinelloRahman (Parrinello and Rahman, 1981) barostats. All the simulations in Chapters 2, 3 and 7 are performed in an NVT ensemble using the Bussi thermostat to control the temperature, while in Chapters 4 and 5 we use an NVE ensemble. Also, most of the simulations in Chapter 6 are performed in an NVT ensemble using the Bussi thermostat and some of them are performed in an NPT ensemble using the Nosé-Hoover thermostat.

Potential energy and force (see Equation 1.1) of the system can be calculated in several ways, such as force fields, pair potentials, many-body potentials, tight-binding and *ab initio* methods. Force fields usually use harmonic expressions to describe the bond breaking and stretching. They are composed of atomic interaction parameters and formula with two different terms. The nonbonded or so-called noncovalent term contains pairwise energy components such as electrostatic and Lennard-Jones (LJ), whereas the bonded/covalent part includes covalent energy terms, such as angle bending, bond stretching, torsion angle and dihedral energies. Pair potentials include the LJ potential and calculate the total energy by summing over all pairs of atoms. Tight-binding is the simplest quantum mechanical calculation method that includes electrons in the simulations. *Ab initio* methods, such as density functional method, approximate the energy from first principles based on the laws of quantum mechanics. Many-body potentials are another way to calculate the force and energy of the system, which are higher-order terms of analytical potentials. We will discuss these potentials later in Section 1.2.3.

1.2.2 Periodic boundary conditions

Molecular dynamics simulations are usually implemented systems of thousands of particles. In order to generate bulk material and eliminate edge effects, we use periodic boundary conditions. A schematic of periodic boundary conditions in two-dimensions is shown in Figure 1.23. In a simulation with periodic boundary conditions, as a particle moves in the original simulation box (primitive cell), its periodic images of the particle in neighboring simulation boxes move in exactly the same way. Note that the particles in the primitive cell interact not only with the other particles in the cell but with their periodic image in each adjacent box as well. Hence, particles can pass through the box boundary and enter the neighboring box. When this happens, the image of the same particle will enter the main simulation box from the opposite side, keeping the mass in the box constant and eliminating edge effects (Allen and Tildesley, 1989).

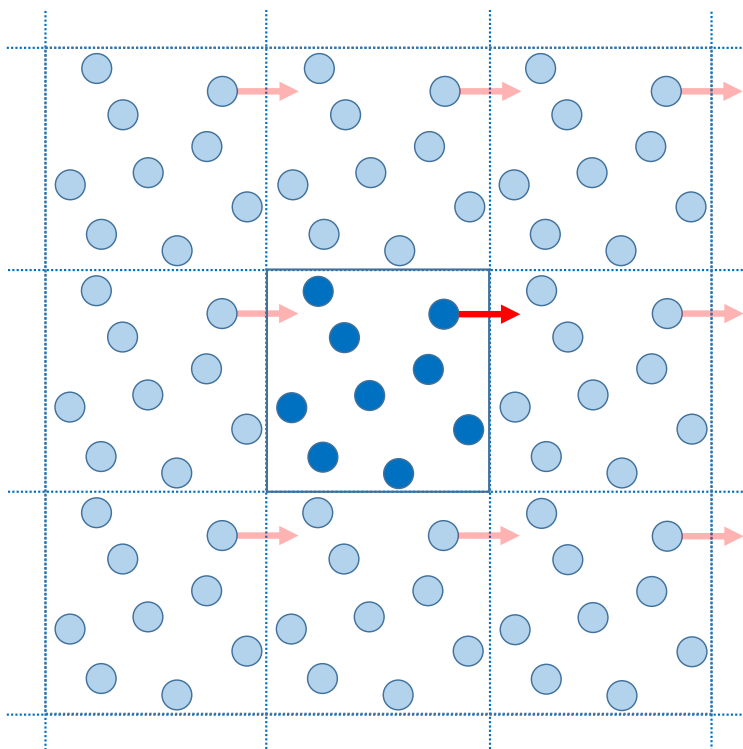


Figure 1.23: A two-dimensional schematic of periodic boundary conditions. The central simulation box is repeated to generate a bulk material.

1.2.3 Interatomic potentials for carbon

The interatomic potential, which is used to describe the interaction between atoms, is a crucial part of the MD simulations. Generally, a proper potential function is required to have a realistic MD outcome. Hence, when generating the potential, in the first step, a suitable functional form should be determined. In the second step, parameters of the function are matched to a database of values that explain physical properties such as lattice parameters and bulk elastic constants. Modern potentials are usually matched to a wide comprehensive set of values, resulting in very accurate predictions under conditions for which the potentials are fitted. However, a broad fitting procedure does not commit the performance of the potential in all various kinds of simulations. This leads to choosing the functional form and the parameters' value in the fitting procedure and plays an essential role in the transferability of the potential, i.e., how well it performs in situations to which it was not fitted (Sand, 2015).

Carbon has always been a challenge for interatomic potential and computational study, which is due to having various hybridizations and forms, as discussed earlier in this chapter. The first useful interatomic potential for carbon was developed by Tersoff (1988). This potential, which describes the different hybridizations of carbon, opened a new field in the study of different carbon materials such as fullerenes, nanotubes, diamond and amorphous carbon. Despite its utility, the Tersoff potential has some shortcomings: there is no long-range attraction between graphitic planes, nor is there a dihedral term to penalize the rotation of π -bonds. Historically, one of the most significant improvements was the Reactive Empirical Bond-Order (REBO) potential developed by Brenner (1990), and since then many other credible carbon potentials have been proposed, most of which can trace their lineage to the original Tersoff potential model. These newer potentials improve on the Tersoff and REBO potentials in various ways, adding medium-range/long-range terms (e.g., LCBOP (Los and Fasolino, 2003; Los et al., 2005a), AIREBO (Stuart et al., 2000), EDIP (Marks, 2001, 2002b),

ReaxFF (van Duin et al., 2001)), or incorporating screening (e.g., SED-REBO (Perriot et al., 2013), REBO-S (Pastewka et al., 2008), Tersoff-S (Pastewka et al., 2013)).

So far, at least 46 carbon potentials have been developed (de Tomas et al., 2019). Some of these potentials are only suitable for carbon, and some are suited to other chemical species such as hydrogen, oxygen and silicon (de Tomas et al., 2016). In Tables 1.1, 1.2 and 1.3, we summarize the main details of all carbon potentials developed to date. Potentials are catalogued by families according to the nature of their functional form. The tables collect the main characteristic of each potential formalism and capacity to describe other chemical species. Key acronyms in both tables are as follows: REBO, Reactive Empirical Bond Order; AIREBO, Adaptive Intermolecular REBO; SED-AIREBO, Screened Environment Dependent AIREBO; ABOP, Analytic bond-order potential; EDIP, Environment-dependent interaction potential; ReaxFF, Reactive Force Field; LCBOP, Long-range Carbon Bond Order Potential; MEAM, Modified Embedded Atom Method; RSS, Reaction State Summation; COMB, Charge Optimized Many Body; ML, Machine Learning; GAP, Gaussian Approximation Potential. As a side note, many of these carbon potentials are not coded into the free MD packages such as LAMMPS (we will describe this package later in Section 1.2.7); full details of the Tables 1.1, 1.2 and 1.3 including their availability in LAMMPS are provided in www.carbonpotentials.org and also in the Supplementary Materials of de Tomas et al. (2019).

A detailed discussion of the history of carbon potentials and a comparison of the merits of dominant models have been provided by Marks (2010) and de Tomas et al. (2016). In what follows, we summarize the four potentials that will be used in this thesis: Tersoff, REBO, EDIP and ReaxFF. As providing full details of these potentials and other listed potentials would be beyond the scope and purpose of this thesis, a brief overview of these potential is presented below.

Tersoff potential (Tersoff, 1988) - This is the first potential for carbon

Table 1.1: Summary of carbon potentials detailing their main characteristics and capacity to describe other chemical species. The potentials are grouped by families and arranged in chronological order. Where relevant the historical basis of the potential is specified.

Family	Name of potential	Year	Main characteristic	Builds on	Other species	Reference
 Tersoff	Tersoff	1988	Reparametrization for carbon	Si Tersoff		(Tersoff, 1988)
	Tersoff	1989	Generalization to multicomponent systems	Si Tersoff	Si	(Tersoff, 1989)
	Tersoff	1990	Reparametrization to treat C defects in Si	Tersoff 1989	Si	(Tersoff, 1990)
	Tersoff	1994	Minor change in parameters	Tersoff 1990	Si	(Tersoff, 1994)
	Tersoff	1995	Variable cutoff rescaled with system volume	Tersoff 1989	Si	(Tang and Yip, 1995)
	Nordlund	1996	Adds van der Waals and uses larger cutoff	Tersoff 1988		(Nordlund et al., 1996)
	Tersoff	1998	Adds nitrogen and boron	Tersoff 1989	Si/B/N	(de Brito Mota et al., 1998) & (Matsunaga et al., 2000)
	Ext. Tersoff	2005	Extended cutoff	Tersoff 1988		(Titantah and Lamoen, 2005)
	Tersoff-S	2013	Environment-dependent screening function	Tersoff 1988		(Pastewka et al., 2013)
	mTersoff/Nordlund	2011	Fermi-type cutoff. Adds van der Waals	Tersoff/Nordlund		(López et al., 2011)
 REBO	REBO	1990	Adds hydrogen. Treats carbon radicals.	Tersoff	H	(Brenner, 1990)
	REBO-II	2002	Adds dihedral. New short-range treatment.	REBO	H	(Brenner et al., 2002)
	AIREBO	2000	Adds van der Waals (Lennard-Jones)	REBO-II	H	(Stuart et al., 2000)
	AIREBO-II	2002	Minor change in two parameters	AIREBO	H	(Kum et al., 2003)
	REBO-CHO	2004	Adds oxygen	REBO-II	H/O	(Ni et al., 2004)
	AIREBO	2008	Environment-dependent van der Waals	AIREBO	H	(Liu and Stuart, 2008)
	REBO2-S	2008	Environment-dependent screening function	REBO-II	H	(Pastewka et al., 2008)

Table 1.2: Continue of Table 1.1

Family	Name of potential	Year	Main characteristic	Builds on	Other species	Reference
REBO	qAIREBO	2012	Adds oxygen and charge equilibration	AIREBO	H/O	(Knippenberg et al., 2012)
	SED-REBO	2013	Environment-dependent screening function	REBO-II		(Perriot et al., 2013)
	AIREBO-M	2015	Replaces Lennard-Jones with Morse	AIREBO	H	(O'Connor et al., 2015)
	Heggie	1991	Wigner-Seitz treatment of local bonding	Tersoff 1988		(Heggie, 1991)
	Andriobet	1996	Simpler functional form. More efficient.	Heggie		(Andriobet et al., 1996)
	Broughton	1999	Valence bond treatment. No angular terms.	Tersoff 1988		(Broughton and Mehl, 1999)
ABOP	Pettifor	1999	Analytic approximation of tight-binding		H	(Pettifor and Oleinik, 1999) & (Oleinik and Pettifor, 1999)
	Mrovec	2007	Improved σ bond term	Pettifor	H	(Mrovec et al., 2007)
	Zhou	2015	Reparametrization for pure carbon	Pettifor		(Zhou et al., 2015)
EDIP	EDIP	2000	Long-range π -repulsion. Dihedral terms.	Si EDIP		(Marks, 2000)
ReaxFF	ReaxFF	2001	Flexible and general functional form		H	(van Duin et al., 2001)
	ReaxFF _{CHO}	2008	Adds oxygen	ReaxFF	H/O	(Chenoweth et al., 2008)
	ReaxFF- <i>lg</i>	2011	Adds low gradient London dispersion	ReaxFF	H/O/N	(Liu et al., 2011)
	ReaxFF _{C2013}	2015	Reparametrization for solid carbon	ReaxFF _{CHO}	H/O	(Srinivasan et al., 2015)
	ReaxFF _{C2013-II}	2017	Reparametrization for defect in graphite	ReaxFF _{C2013}	H/O	(Smith et al., 2017)
	ReaxFF _{CHO-2016}	2017	Improve chemistry of combustion kinetics	ReaxFF _{CHO}	H/O	Ashraf and van Duin (2017)

Table 1.3: Continue of Table 1.2

Family	Name of potential	Year	Main characteristic	Builds on	Other species	Reference
LCBOP	LCBOP-I	2003	Simultaneous bond-order & long-range fit	REBO		(Los et al., 2005a)
	LCBOP-I+	2004	Adds torsional term	LCBOP-I		(Ghiringhelli et al., 2004)
	LCBOP-II	2005	Improved bond dissociation energetics	LCBOP-I+		(Los et al., 2005b) & (Ghiringhelli et al., 2005)
	Erhart/Albe	2005	Hybrid Tersoff/REBO. Reparametrization.	Tersoff/REBO	Si	(Erhart and Albe, 2005)
MEAM	Lee/Lee	2005	Reparametrized for C. Long-range term.	MEAM		(Lee and Lee, 2005)
	Uddin	2010	Developed for Ni catalysis of nanotubes.	MEAM	Ni	(Uddin et al., 2010)
	Nouranian	2014	Saturated bonds only (i.e., no π -bonds).	MEAM	H	(Nouranian et al., 2014)
	MEAM-BO	2017	Extended to unsaturated hydrocarbons.	MEAM	H	(Mun et al., 2017)
	RSS	2008	Short-range interactions. No sp^3 bonds.	RSS		(Shi, 2008)
	Kumagai	2009	Screening function and dihedral term.	REBO		(Kumagai et al., 2009)
ML	ANN	2010	Employs neural network algorithms			(Khaliullin et al., 2010)
	GAP	2017	Employs machine learning			(Deringer and Csányi, 2017)
COMB	COMB3	2013	Charge dependent short-range interactions	REBO-II	H/O/N	(Liang et al., 2013)
	ChIMES	2017	Force-matching against liquid DFT data	REBO-II		(Lindsey et al., 2017)

that was developed based on an earlier potential for silicon. Tersoff is a widely used potential since it is fast and straightforward compared to other potentials (computational cost for different carbon interatomic potentials are provided in Chapter 3). The strengths of bonds, according to the number of neighbors, are modified by the treatment of multiple hybridization states and bond-order. Note that bond-order is the number of chemical bonds between a pair of atoms and indicates the stability of a bond. The Tersoff potential is a short-range potential and applies a switch cutoff function to recognize the nearest neighbors. The short cutoff is 2.1 Å that is intermediate between the first and second neighbors and has a cosine shape cutoff function between 1.8 and 2.1 Å. By choosing the short cutoff, we can calculate that the potential energy involves relatively few atoms; however, the lack of any interaction more than 2.1 Å means there is no attraction/repulsion between graphene layers. This results in the Tersoff potential predicting nearly the same density for graphite and diamond (3.5 g/cc), whereas from an experimental point of view, graphite is much less dense than diamond. So far, a variety of modifications have been employed to the Tersoff's cutoff function. For example, Nordlund et al. (1996) extended the Tersoff potential to include van der Waals attraction by adding an attractive long-range term and increasing the cutoff to 2.46 Å. Further, in order to improve the properties of amorphous carbon, some studies modified the coefficient of the upper cutoff. An example of an aspect of the modification is presented in Chapter 2, where we modify the Tersoff potential by increasing the upper cutoff to 2.45 Å. We also show that although this modification leads to an improvement in the amorphous carbon at high densities, it is owing to unphysical nucleation of nanocrystal diamond during the annealing of amorphous carbon. As a side note, Table 1.1 provides a number of modified Tersoff potentials. This includes the adding of nitrogen and boron (de Brito Mota et al., 1998) as well as using an environment-dependent screening function (Pastewka et al., 2013) and a Fermi-type cutoff function (López et al., 2011) to improve the description of bond making and breaking.

REBO potential (Brenner, 1990) - The first modifications of the Tersoff potential is REBO potential, which added hydrogen interaction and improved the description of the radicals. In the beginning, REBO potential was developed for simulating the chemical vapor deposition of diamond. Since then, it has been applied to a wide range of problems involving carbon and hydrocarbon systems. One disadvantage of the REBO potential is that it cannot simulate the pathway for breaking and making of bonds. To improve the short-range bonding, a modified version of the potential called REBO-II was released. When Brenner et al. (2002) changed the functional form, an improved database was used for the fitting of parameters and a dihedral term was added to discipline rotation of π -bonds. Similar to the Tersoff potential, REBO and REBO-II potentials have cosine shape cutoff functions, but range is between 1.7 and 2.0 Å. Hence, they cannot accurately predict the density of graphite and diamond as REBO-II potential predicts that graphite is 3% denser than diamond. The adaptive intermolecular REBO (AIREBO) potential (Stuart et al., 2000) is another generation, where the Lennard-Jones interaction is employed to extend the long-range interaction between the sp^2 sheets, and a switching function is used to deactivate the long-range term at short distances. Similar to the Tersoff potential, a considerable number of REBO potential versions have been developed so far (see Tables 1.1 and 1.2). For example, Ni et al. (2004) added oxygen and Pastewka et al. (2008) and Perriot et al. (2013) used an environment-dependent screening function to improve the description of bond making and breaking. Also, O'Connor et al. (2015) replaced the Lennard-Jones form with a Morse expression.

EDIP potential (Marks, 2000) - This potential is not related to the Tersoff and REBO potentials and involves an entirely different functional form. It is based on the earlier EDIP potential for silicon, where an atom-centered bond-order is employed. As a side note, EDIP for silicon is one of the most commonly used potentials for MD simulation of silicon-based structures, including amorphous silicon (Voyles et al., 2001), silicon defective structures (Justo et al., 2000;

Nord et al., 2002) and epitaxial growth of silicon (Bernstein et al., 2000). The EDIP potential for carbon was originally developed for simulating the growth of amorphous carbon thin films and liquid quenched carbon systems. The cutoff functional form of EDIP potential differs from Tersoff- and REBO-like potentials and uses a generalized coordination term to capture long-range π -repulsion and dihedral rotation penalties. EDIP potential predicts the energetics of bond making and breaking by robust numerical fitting to density-functional-theory data for the transformation between diamond and rhombohedral graphite as this reaction changes the hybridization from sp^3 to sp^2 . Owing to this cutoff treatment, the EDIP potential is relatively long-ranged, extending to 3.2 Å. Beyond this point, there is no interaction beyond this cutoff, which means EDIP cannot describe the van der Waals attraction between graphitic layers. Besides this, as EDIP potential uses an atom-centered bond-order, it does not penalize isolated sp^2 atoms, which should have raised energy by being π radicals. Despite these shortcomings of EDIP potential, it is capable of simulating layered structures (Lau et al., 2007; Suarez-Martinez et al., 2010; Powles et al., 2009), as in many situations the driving force for layering is the long-ranged π -repulsion between sp^2 -bonded layers (de Tomas et al., 2016). It is useful to point out that, on the positive side, EDIP potential is a fast and robust potential and has previously been successful in simulations of many different forms of carbon such as diamond (Marks et al., 2012; Fairchild et al., 2012; Buchan et al., 2015), carbon onions (Lau et al., 2007), amorphous carbon (Marks, 2002a; Best et al., 2020), glassy carbon (Shiell et al., 2018, 2019; Huang et al., 2020), nanotubes (Suarez-Martinez and Marks, 2012) and carbide-derived carbons (de Tomas et al., 2017, 2018).

ReaxFF potential (van Duin et al., 2001) - This potential proposes a completely different procedure for modeling carbon. Although chemical intuition is used to design most of carbon potentials, the framework of ReaxFF is as general as possible and is parametrized against a large data set. Components of this potential include many different chemical possibilities, including bond order, charge

transfer, van der Waals, under/over-coordination and torsion (de Tomas et al., 2016). The ReaxFF potential developed for simulating the hydrocarbons and has since been expanded to describe many other chemical species, including oxygen, nitrogen, sulfur and many metals. The ReaxFF potential has made a significant contribution to understanding a wide variety of research topics such as proteins, fuel cells and catalysis. However, it has two main shortcomings. The first one is the liquid state, which it cannot describe with the same accuracy as EDIP potential. The second shortcoming is poor performance for solid carbon phases. So far, a few versions have been developed to improve the ReaxFF potential (see Table 1.2), such as reparametrization to improve the solid carbon phase (Srinivasan et al., 2015), an improved parameter for defects in graphite (Smith et al., 2017) and improving the chemistry of combustion kinetics Ashraf and van Duin (2017).

Finally, a comprehensive comparative study by de Tomas et al. (2016) compared the performance of six well-known carbon potentials (Tersoff, REBO-II, EDIP, ReaxFF_{C2013}, LCBOP-I and COMB3) and analyzed their ability to explain amorphous carbon and the graphitization process. As the study found that no two potentials yield the same results and none of the possibilities is perfect, further study on the performance of interatomic potentials for carbon is required. In this regard, in Chapter 3, we expand this comparative study with eight additional commonly used potentials (AIREBO, REBO2-S, Erhart/Albe, ABOP, GAP, Tersoff-S, Tersoff/Nordlund and Tersoff with modified cutoff) and study their capability to model carbon.

1.2.4 ZBL potential

In MD simulations, all interatomic potentials that were mentioned in Section 1.2.3 are equilibrium potentials, which do not work well when two atoms are very close to each other. In order to describe the close-range interaction, these potentials can be splined with a suitable potential. One well-known potential to describe short-

range interaction is the standard Ziegler-Biersack-Littmark (ZBL) pair potential (Ziegler et al., 1985). The ZBL potential is a Coulomb potential with a screening function (Φ) which is described as

$$U_{\text{ZBL}}(r_{ij}) = \frac{1}{4\pi\epsilon_0} \frac{Z_i Z_j e^2}{r_{ij}} \Phi(r_{ij}), \quad (1.12)$$

where ϵ_0 is the vacuum permittivity, Z_i is the atomic number of atom i , r_{ij} is the interatomic separation and $\Phi(r_{ij})$ is the screening function, is given by

$$\Phi(r_{ij}) = \sum_{i=1}^4 c_i \exp\left(\frac{-d_i r_{ij}}{a}\right) \quad (1.13)$$

where the c_i and d_i are constants, and a is the screening length and is given by

$$a = \frac{0.46850}{Z_i^{0.23} + Z_j^{0.23}}. \quad (1.14)$$

The ZBL potential can join with equilibrium potentials and applies to interatomic distance less than ~ 1 Å. This combination is commonly used in ion-implantation simulations where equilibrium potential describes the chemical bonding regime, while ZBL potential describes the nuclei regime. For example, EDIP potential is successfully coupled with the ZBL potential for simulation of radiation damage cascades in graphite (Christie et al., 2015; Vuković et al., 2018) and diamond (Buchan et al., 2015). Interpolation process used to switch between EDIP and ZBL potentials is described by using two Fermi-type scaling functions (F_{EDIP} and F_{ZBL}). These functions are defined by the position of the midpoint of each function (r_{EDIP} and r_{ZBL}) and the width (w) of the switching region. Details of switching between EDIP and ZBL potentials is provided by Christie et al. (2015) where they choose the values as $r_{\text{EDIP}} = 1.05$ Å, and $r_{\text{ZBL}} = 0.45$ Å and $w = 0.07$ Å. These values are selected to ensure a smooth transition between the two regimes. The same approach has been used in the ion-implantation simulations presented in Chapters 4 and 5, and also in the simulations by Marks

et al. (2003), Pearce et al. (2005), Christie et al. (2015), Buchan et al. (2015) and Vuković et al. (2018).

1.2.5 Thomson problem

In MD simulations of ion-implantation, the initial position of the implanted species should be systematically varied in order to collect robust statistics across various crystallographic orientations as well as generating a wide variety of implantation conditions. The most intuitive way of accomplishing this is to uniformly sample across the surface of a sphere. However, uniformly distributing a large number of points on the surface of the sphere is a non-trivial task with no analytical solution. This is a mathematical problem outlined by Thomson (1904) whilst attempting to determine the arrangement of point charges in the atom. The so-called Thomson problem has been generalised to finding the minimum energy for N point charges on a sphere and has formed a significant area of research applicable to a multitude of real-world problems. A notable study of solving the Thomson problem was carried out by Wales and Ulker (2006). They used a global minimum search algorithm to systematically classify the minimum energy solution for $N < 400$. However, for large N , the number of local minima increases exponentially and finding the global minimum using simple numerical algorithms becomes a time-consuming task. Their data are available on the Cambridge Cluster Database website (Wales et al., 2006). As another pioneering work, Robinson and Marks (2014) have provided a general application software, called *NanoCap*, where numerical optimization algorithms are applied to solving the Thomson problem (Robinson et al., 2013).

In Chapters 4 and 5, to simulate the experimental studies of ion-implantation into the nano-sized diamond particles, as discussed in Section 1.1, the initial position of the implanted species is taken from the solution to the Thomson problem for 25 charge points as generated by the *NanoCap* software (Robinson and Marks, 2014). Those points are illustrated in Figure 1.24 and the Cartesian coordinates

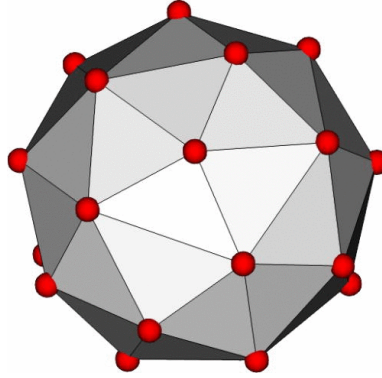


Figure 1.24: Solution to the Thomson problem for $N = 25$ in which point charges (shown in red) are uniformly distributed over the surface of a sphere. Figure taken from [Buchan et al. \(2015\)](#).

are listed in Table 1.4. This useful method has been previously used in ion-implantation simulation studies by [Robinson et al. \(2012, 2014\)](#), [Robinson et al. \(2012\)](#), [Buchan et al. \(2015\)](#), [Christie et al. \(2015\)](#) and [Shiryaev et al. \(2018\)](#).

1.2.6 Analysis methods

In this section, we briefly describe three common micro-properties that we typically use to analyze the data in this thesis.

Radial distribution function (RDF)

The pair distribution function or pair correlation function in a system of particles, which is also called the radial distribution function (RDF) or $g(r)$, is an important structural characteristic. It gives consideration to the local environment around any given atom in a short distance and describes how density varies as a function of distance ([Ding, 2014](#)). We consider a homogeneous atomic system as shown in Figure 1.25 where the blue particle is as the reference particle to be at the origin O and green particles are those whose centers are within the pink circular shell. If N and V are, respectively, the total number of particles and the volume of the system, then $\rho = N/V$ is the average number density of particles; hence, the local

Table 1.4: Cartesian coordinates of the 25 initial position of the implanted species as shown in Figure 1.24.

Point Number	Cartesian coordinate (Å)		
	x	y	z
1	-0.9143482794	-0.4046281859	0.0155966333
2	-0.4462573799	-0.8944780327	0.0276296905
3	0.0746127557	-0.8753324908	0.4777300148
4	0.2772515579	-0.9205606381	-0.2751357576
5	-0.4652896722	-0.5055030020	0.7266169801
6	0.1441925433	0.9031588475	0.4043669206
7	0.7426358958	0.6570505272	0.1295242481
8	-0.2078223871	0.1502121179	0.9665641080
9	-0.8049328937	-0.0847035038	-0.5872889858
10	0.3378908664	0.3456088997	-0.8754337500
11	0.9265616574	0.0185767307	0.3756839097
12	-0.4901596387	0.6643035144	0.5643087534
13	0.3420189067	-0.3156641019	0.8850871381
14	0.4475328912	0.3969758313	0.8013267127
15	-0.3961370122	0.5700861474	-0.7197758346
16	-0.3419401154	-0.6974554982	-0.6297878891
17	-0.8459163602	0.0589062130	0.5300524215
18	0.3977043253	-0.4189540221	-0.8162774019
19	0.2851312370	0.8712593786	-0.3995087893
20	-0.3749527143	0.9201308752	-0.1130028073
21	0.6975555148	-0.6407731763	0.3206649968
22	0.8646077760	-0.4008923973	-0.3028839371
23	0.8621272936	0.2642757087	-0.4323134039
24	-0.8994545745	0.4252221756	-0.1008343673
25	-0.2130261777	-0.0859557607	-0.9732581645

time-averaged density at a distance r from O is $\rho \times g(r)$. Another point to consider is that RDF involves determining how many particles are within a distance of r and $r + dr$ away from the origin (blue particle). The RDF is usually normalized as the ratio between the number of local particles and the average number density of particles in the system. The normalized RDF can be calculated as

$$g(r) = \frac{dn(r)}{\rho 4\pi r^2 dr}, \quad (1.15)$$

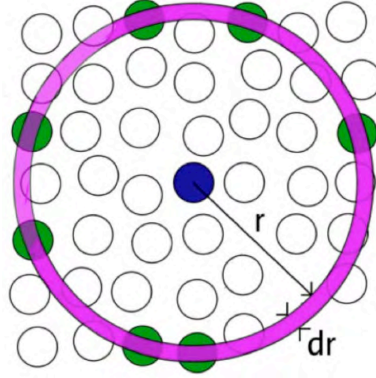


Figure 1.25: A homogeneous atomic system for calculation of the RDF. Figure taken from [Ding \(2014\)](#).

where $dn(r)$ is the number of atoms in the shell of thickness dr (see [Figure 1.25](#)).

Coordination number

The coordination number is the total number of neighbors of each atom within a certain distance that bonded to it. As noticed earlier the coordination number of each carbon atom in the diamond structure is four, while the coordination number in graphite is three. The coordination number of disordered system is calculated through the pair distribution function ([Waseda, 1980](#); [Vahvaselka and Mangs, 1988](#)). The first coordination number can be determined by taking the average number of neighbors in the first spherical shell with a radius between r_0 and r_1 , i.e., from the starting point to the position of the first minimum of $g(r)$,

$$n_1 = 4\pi \int_{r_0}^{r_1} r^2 g(r) \rho dr. \quad (1.16)$$

Note that at the starting point ($r_0 = 0$), $g(r)$ is zero and r_1 is the position of the first minimum of $g(r)$. Therefore, n_1 is the area under the first peak of $g(r)$ (see [Figure 1.26](#)). The second (n_2) and the third (n_3) coordination numbers can be defined by following a similar expression for the second and third shells. It is useful to point out that in this thesis the coordination numbers of carbon-based

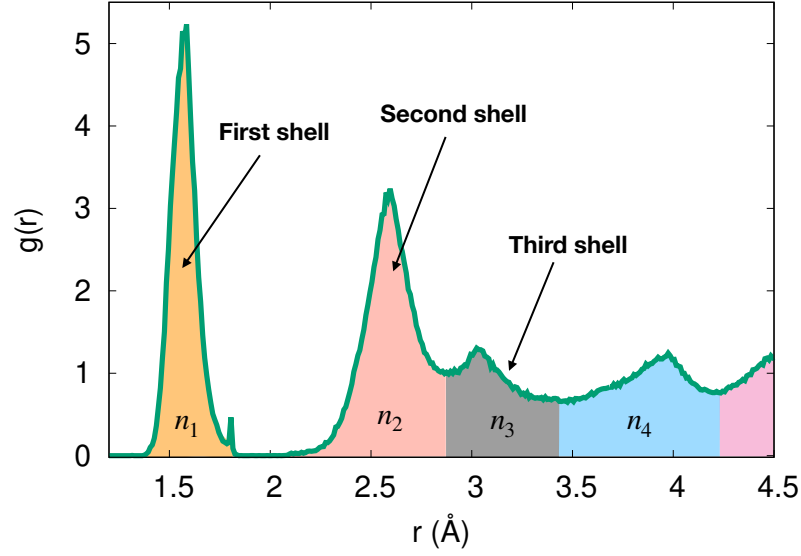


Figure 1.26: Representation of coordination numbers in pair distribution function of simulated graphitised amorphous carbon. Data is taken from a web application tool, www.carbonpotentials.org.

systems are determined by counting the number of nearest neighbors within a radius of 1.85 Å where the pair distribution function has dropped to zero (see Figure 1.26).

Mean squared displacement (MSD)

One of the main purposes of mean squared displacement (MSD) analysis is calculating the deviation of the position of a particle with respect to a reference position over time and another purpose is measuring the diffusion coefficient value. The MSD is calculated as:

$$\text{MSD}(t) \equiv \langle \Delta r^2(t) \rangle = \frac{1}{N} \sum_{n=1}^N |\mathbf{r}_n(t) - \mathbf{r}_n(0)|^2 = \langle |\mathbf{r}_n(t) - \mathbf{r}_n(0)|^2 \rangle \quad (1.17)$$

where N is the number of particles in the systems, $\mathbf{r}_n(0)$ is the initial position of the particle and the position of each particle at time t is denoted by $\mathbf{r}_n(t)$. The MSD also contains information on the diffusion of atoms. For solids the MSD goes towards a constant value as t increases due to atoms not moving freely in the system but fluctuating around their lattice position. However, for gases and

liquids the MSD will increase linearly as a function of time and it is possible to investigate the behaviour of a system looking at the slope of the MSD. The slope of the MSD or the so-called diffusion constant D is defined by:

$$D = \lim_{t \rightarrow \infty} \frac{1}{6t} \text{MSD}(t). \quad (1.18)$$

The same approach has been used to study the diffusion of the liquid carbon in Chapters 2 and 3. Note that in our simulations, the MSD is calculated by in-house or open-source classical MD code, which is discussed in the following section.

1.2.7 Overview of LAMMPS and OVITO

A popular open-source classical molecular dynamics code is LAMMPS (Large-scale Atomic/Molecular Massively Parallel Simulator), which was developed by Sandia National Labs (USA) and Temple University (Plimpton, 1995). Due to its large library of force field potentials, LAMMPS can model different systems such as atomic, polymeric, metallic and biological systems ranging from several atoms to millions. As LAMMPS can be run on a laptop and any multi-core computer cluster, it is widely used in a variety of research studies. One of the advantages of LAMMPS is that researchers can easily improve and modify codes and also add a new force field into its large potential library. All the molecular dynamic simulations in Chapters 2, 3, 6 and 7 are performed by using LAMMPS.

To display, animate and analyze the MD simulation data and also assess how the structure is changing during the simulation, we use OVITO (Stukowski, 2010), which is an open-source software available to all main operating systems. We have particularly used OVITO for rendering images and movies as well as analyzing some parts of our simulation data. One advantage of using OVITO is that it has a comprehensive variety of data analysis functions such as coordination number and radial distribution function calculation. It also contains different

data manipulation and visualization tools such as slicing, interactive selection of particles and bonds, diamond structure identification, colour coding functions and display of periodic images and wrapping/unwrapping of particle trajectories. Some of the above-mentioned analysis functions and tools are used in Chapters 2, 3, 4, 5, 6 and 7. Another advantage of using OVITO is being well-suited to import and export LAMMPS data.

1.3 Thesis structure and overview of chapters

This thesis is comprised of eight chapters. Chapters 2 and 3 deal with the fundamentals of computer simulation of carbon, while Chapters 4, 5, 6 and 7 are directly motivated by experimental results from collaborators and the literature discussed in Section 1.1. The materials in Chapters 2, 3, 4, 6 and 7 have already been published, and the materials in Chapter 5 are to be submitted for publication. Each chapter outlines its own objectives and has abstract, methods, results, discussion and conclusion sections. This format makes it easier to read any chapter with minimal referral to previous chapters. Although every effort has been made to provide a comprehensive yet nonrepetitive literature review, some limited overlap inevitably occurs given the preparation of chapters as “papers”.

Chapters 2 and 3 are organized in accordance with fundamentals of the simulation of carbon and benchmark some of the most commonly used interatomic potentials for carbon. In Chapter 2, we examine Tersoff potential, a widely used potential in which the coefficient of the upper cutoff is increased to improve the properties of amorphous carbon. In Chapter 3, we perform a comparative study of fourteen well-known and commonly used carbon interatomic potentials: Tersoff, Tersoff-S, Tersoff/Nordlund, Extended-cutoff Tersoff, REBO-II, AIREBO, REBO2-S, ReaxFF, EDIP, LCBOP-I, COMB3, Erhart/Albe, ABOP and GAP.

Once a reasonable interatomic potential is chosen, we study the implantation of xenon into nanodiamonds while comparing it with ion-implantation experiments (Chapter 4). Chapter 5 outlines the thermal release patterns of implanted

noble gases from nanodiamonds during the annealing process through comparison with experimental studies of synthetic and meteoritic nanodiamond. In Chapter 6, we study the origin of novel macroscopic and unexpected plastic deformation of diamond nanopillars. Lastly, in Chapter 7, atomistic simulations are performed to understand the nature of the interface between diamond and silicon carbide. The atomistic results in Chapters 6 and 7 are compared with experimental observations performed by our collaborators. General conclusion and future research directions are discussed in Chapter 8. Details of author contribution and copyright information are provided in Appendixes A and B, respectively. Appendix C provides some screenshots of an online application tool “www.carbonpotentials.org” which is developed in Chapter 3. Finally, front cover of the *ACS Applied Electronic Materials* journal which is highlighted our results in Chapter 7 is provided in Appendix D.

Chapter 2

Unphysical nucleation of diamond in the extended cutoff Tersoff potential

The main text and most of the figures comprising this chapter have been published in *Molecular Simulation* 44, (2018) 164–171. In this chapter, we examine a common modification to the widely-used Tersoff potential in which the coefficient of the upper cutoff is increased to improve the properties of amorphous carbon. Using molecular dynamics simulations, we show that this so-called extended cutoff Tersoff model leads to nucleation of diamond nanocrystals during annealing of amorphous carbon. By varying the density of the system, and examining the radial distribution function in conjunction with the modified cutoff function, we demonstrate that this behaviour is unphysical, and does not represent a new pathway for synthesizing diamond.

2.1 Introduction

When Tersoff developed the first useful interatomic potential for carbon in 1988 (Tersoff, 1988), a new era in computational carbon science commenced. Based on a bond-order formalism proposed several years earlier by Abell (1985), the Tersoff potential was the first empirical potential capable of describing the multiple hybridization states of carbon. With a straightforward functional form and low computational cost, the Tersoff potential found widespread use across the entire spectrum of carbon materials, including graphite, diamond, fullerenes, nanotubes and amorphous carbon. Presently around 1200 articles cite the original work.

The computational efficiency of the Tersoff potential arises from the short-range nature of the potential, in which nearest-neighbor contributions dominate. The general functional form of the Tersoff potential is given by

$$U = \frac{1}{2} \sum_i^N \sum_{j \neq i}^N f_C(r_{ij}) \left[f_R(r_{ij}) + b_{ij} f_A(r_{ij}) \right], \quad (2.1)$$

where U is the total energy of the system, N is the number of atoms and r_{ij} is the interatomic distance, i.e., the distance between the atoms i and j . The functions f_R and f_A are the repulsive and attractive pair potentials, respectively. The function f_C is a smooth cutoff function, which limits the range of the potential. The function b_{ij} is the essential part of the potential and represents a measure of the bond order. It is a monotonically decreasing function of the coordination numbers of atoms i and j , and is given by

$$b_{ij} = \left(1 + \beta^n \zeta_{ij}^n \right)^{-1/2n} \quad (2.2)$$

where

$$\zeta_{ij} = \sum_{k \neq i, j} f_C(r_{ik}) g(\theta_{ijk}) e^{\lambda^3 (r_{ij} - r_{ik})^3} \quad (2.3)$$

Here, β , n and λ are adjustable parameters and the function $g(\theta)$ describes the

angular dependence. All the parameters can be found in (Tersoff, 1988). Finally, the cutoff function, f_C , which varies smoothly from unity to zero according to the functional form is given by

$$f_C(r) = \begin{cases} 1 & r \leq R \\ \frac{1}{2} + \frac{1}{2} \cos \left[\pi(r - R)/(S - R) \right] & R < r < S \\ 0 & r \geq S \end{cases} \quad (2.4)$$

where $R = 1.8 \text{ \AA}$ and $S = 2.1 \text{ \AA}$. The corresponding cutoff function is shown by the blue curve in Figure 2.1. Exactly the same cutoff function is used in the REBO potential, except with slightly different parameters ($R = 1.7 \text{ \AA}$ and $S = 2.0 \text{ \AA}$).

For the main crystalline forms of carbon, i.e., graphite and diamond, the precise values of R and S do not affect bond-lengths, elastic constants and cohesive energies. As long as R exceeds the nearest neighbor bond-length, and S is below the second neighbor bond-length, varying R and S does not alter these properties of these bulk phases. As a result, the cutoff parameters are often considered as

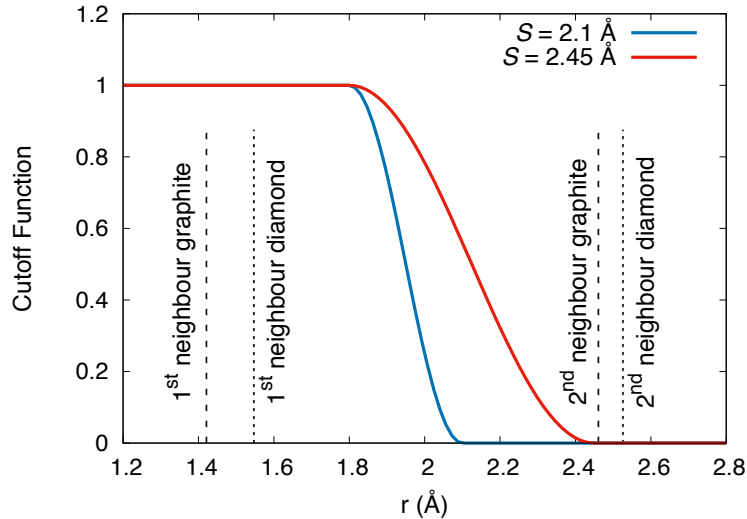


Figure 2.1: Cutoff function for the Tersoff potential (see Equation 2.4) using the original parameters (blue curve, $S = 2.1 \text{ \AA}$), and the extended cutoff Tersoff potential (red curve, $S = 2.45 \text{ \AA}$). Dotted lines indicate the determined experimentally interatomic distances for the first and second coordination shells in graphite and diamond.

free parameters which can be tuned according to the task at hand. There are numerous examples of this philosophy with both the Tersoff and REBO family of potentials, particularly for studies of fracture and amorphous carbon. In the case of fracture simulations, the majority of which involve defects and grain boundaries in graphene, it is common to use a step-function cutoff (i.e., set $R = S$) to avoid non-physical strain hardening in stress-strain curves (Shenderova et al., 2000; Belytschko et al., 2002). As an aside, this practice should be strongly discouraged, as it results in discontinuous energies and forces, and alters the dynamics of bond rupture as detailed in the study by Gamboa et al. (2015). Fracture simulations typically use only a single value of the cutoff; values employed in the literature include: 1.92 Å (Grantab et al., 2010; Wei et al., 2012; Zhang et al., 2012; Wu and Wei, 2013), 1.95 Å (He et al., 2014), 2.0 Å (Zhao and Aluru, 2010; Cao and Qu, 2013; Jhon et al., 2014; Dewapriya et al., 2004) and 2.1 Å (Rajasekaran et al., 2016). In studies of amorphous carbon, a variety of modifications have been employed, mostly motivated by the desire to increase the sp^3 fraction at high densities. In simulations using the REBO potential, Jäger and Albe (2000) chose values of $R = 1.95$ Å and $S = 2.25$ Å, while Titantah and Lamoen (2005) and Sha et al. (2013) each performed Tersoff potential simulations leaving the original value of R unchanged, but with S increased to 2.45 Å. The cutoff function for this case is shown by the red line in Figure 2.1. A very similar value of $S = 2.46$ Å was also proposed by Nordlund et al. (1996) in an extension of the Tersoff potential to include van der Waals attraction.

In this chapter, we use molecular dynamics (MD) simulations to explore the ramifications of increasing the cutoff of the Tersoff potential. We focus on the modification suggested in Titantah and Lamoen (2005) and Sha et al. (2013) for amorphous carbon, in which R is unchanged and $S = 2.45$ Å. Using a variety of values of S spanning the range 2.1 to 2.45 Å we construct amorphous carbon structures using the liquid quenching method (Marks, 1997) and subsequently anneal at high temperature. For the largest cutoff we observe unphysical nu-

creation of diamond at certain densities. Using the radial distribution function, we correlate this effect to interactions between the second neighbor coordination shell and the cutoff itself. This observation demonstrates that Tersoff potential with an extended cutoff is not as robust as has been assumed.

2.2 Methodology

Our MD simulations are performed using LAMMPS software (Plimpton, 1995), and are broadly similar to the comparative study of six common interatomic carbon potential by de Tomas et al. (2016). The MD workflow is illustrated schematically in Figure 2.2. The first step involves choosing a value of S , and making the appropriate change in the parameter file for the Tersoff potential. Four values of S are considered: 2.1, 2.2, 2.3 and 2.45 Å. The original value of $R = 1.8$ Å is left unchanged.

For each value of the cutoff S , amorphous carbon networks are created for ten different densities from 1.5 to 3.2 g/cc to cover the experimental density range observed experimentally. For each density, the same initial configuration was used for the different cutoff values. To create the amorphous structure, a liquid is first created at the desired density, and then quenched to 300 K in 1 ps to form the amorphous solid (Marks, 1997). The liquid is generated via the spontaneous melting of a randomized simple cubic lattice, and is equilibrated at 9000 K for 5 ps. In the study of the unmodified Tersoff potential by de Tomas et al. (2016) a temperature of 8000 K was used to equilibrate the liquid; this rather high value is necessary as the melting point of carbon with the original Tersoff potential is around 6000 K, an overestimate of roughly 2000 K (Tersoff, 1988). For the values of S used in this chapter we find that an even higher value of 9000 K is required to ensure a highly diffusive liquid as measured by the mean-squared-displacement (MSD). An example plot of the MSD for $S = 2.45$ Å at a density of 3.0 g/cc is shown in Figure 2.3(a); the MSD increases linearly with time and has a significant slope, indicative of a fully equilibrated liquid.

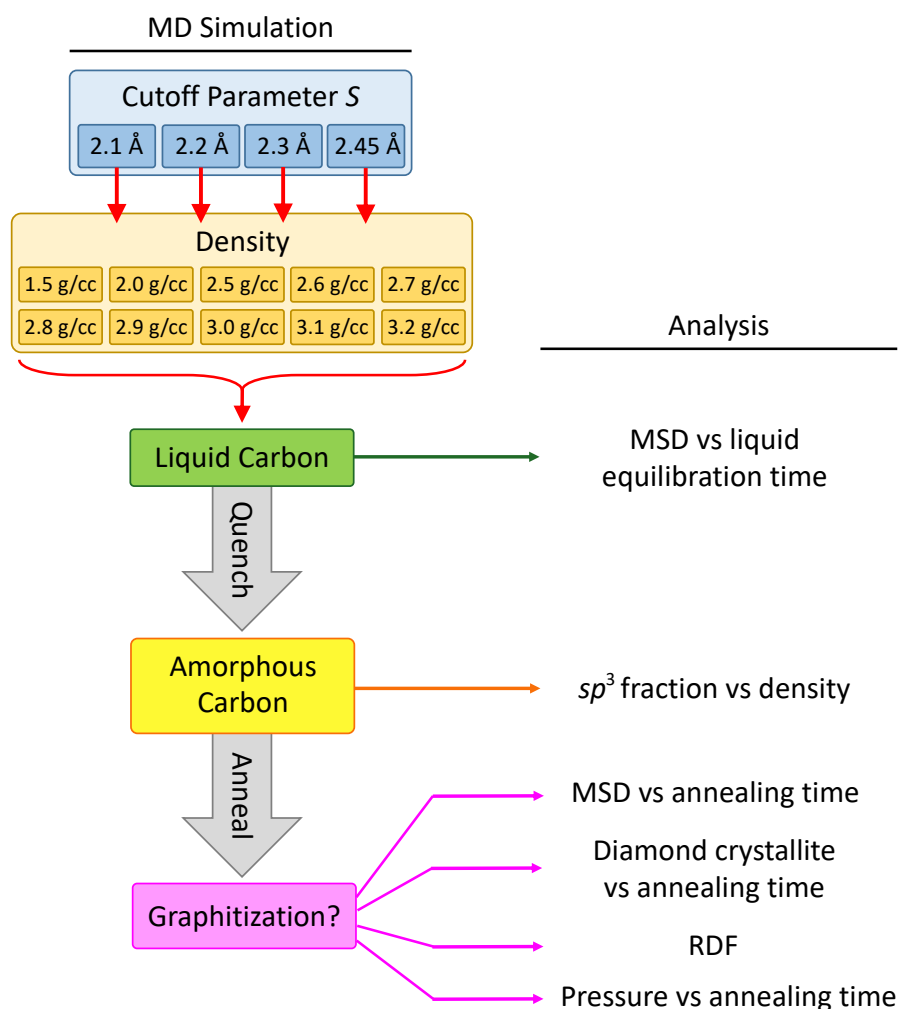


Figure 2.2: Schematic of the workflow used to study the performance of the extended-cutoff Tersoff potential.

Once the amorphous structure is created, it is annealed for 400 ps at a temperature of 6000 K. This approach is identical in spirit to the work by [de Tomas et al. \(2016\)](#) in which high-temperature annealing was used to study structural evolution and transformation. As with the liquid, the MSD is used to select the annealing temperature, but in this case the goal is to have some atomic rearrangement without melting the structure, allowing atomic displacements up to 5 Å (\sim twice the lattice parameter in graphite). Panel (b) of Figure 2.3 shows representative data of the MSD for annealing of the same 3 g/cc system shown in panel (a). In this case the MSD increases with time in a sub-linear manner, and the

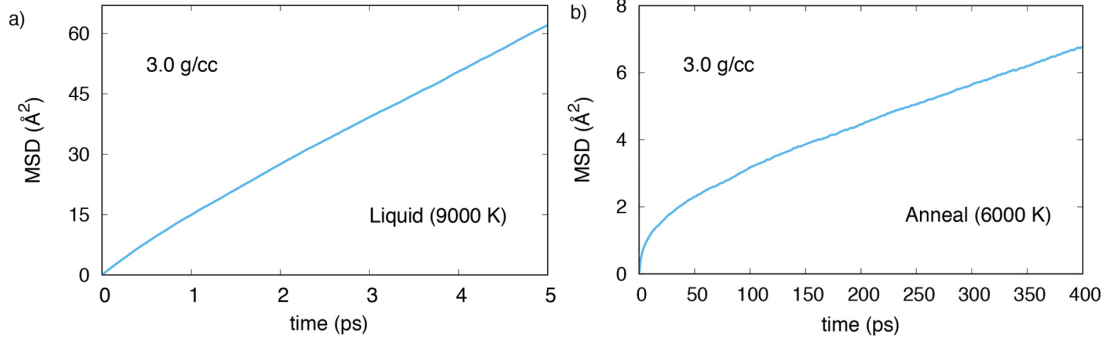


Figure 2.3: Representative data showing the mean-squared-displacement (MSD) as a function of time for $S = 2.45 \text{ \AA}$ and a density of 3 g/cc. (a) MSD at 9000 K showing significant diffusion demonstrating the structure is in the liquid phase, and (b) MSD at 6000 K showing very little diffusion, less than 3.0 \AA after 400 ps, associated with structural evolution during annealing.

average absolute displacement (computed by taking the square-root of the MSD) is less than 3.0 \AA after 400 ps. This demonstrates that there is rearrangement without the structure becoming a liquid.

After annealing, the structures are minimized to zero Kelvin and structural analysis is performed. This energy minimization removes kinetic energy and thermal vibration allowing accurate structure analysis. Coordination analysis was performed by counting the number of nearest neighbours using a cutoff of 1.85 \AA . For the purposes of analysis and visualization, atoms are considered to be sp , sp^2 and sp^3 hybridized if they have two, three and four neighbours, respectively. Diamond crystallites are identified using the diamond structure identification tool (Maras et al., 2016) in the OVITO visualization package (Stukowski, 2010). Atoms are classified as diamond if all of their first and second neighbours are positioned on diamond lattice sites (either cubic or hexagonal). If some of the second neighbours are absent, atoms are still counted as diamond if all four neighbours are positioned on a lattice site.

All simulations (creation of amorphous and annealing) are performed in the NVT ensemble using the Bussi thermostat (Bussi et al., 2007) to control the temperature (see Section 1.2.1). The equations of motion are integrated using the velocity Verlet algorithm and a time step of 0.1 fs is used. All simulations contain

32,768 atoms in a cubic simulation box (originally from an initial $32 \times 32 \times 32$ simple cubic lattice of carbon atoms) with periodic boundary conditions in all three dimension (see Section 1.2.2). The magnitude of the randomization used to destabilize the simple cubic lattice is 0.2 \AA . Note that our original aim in performing these simulations was simply an exercise in benchmarking the performance of the modified Tersoff potential.

2.3 Results and discussion

Using the technique outlined in the Methodology in Section 2.2, amorphous carbon structures are created for a range of densities from 1.5 to 3.2 g/cc. The accuracy of the results is compared to experimental data, for which it is well-known that the sp^3 fraction of amorphous carbon varies linearly with the density (Schwan et al., 1996). Figure 2.4 presents the sp^3 fraction of these amorphous carbons and for a range of densities and values of the cutoff S . For the original value of S , namely 2.1 \AA , the sp^3 fraction differs substantially from experimental values shown as black circles. The discrepancy is particularly large at high densities,

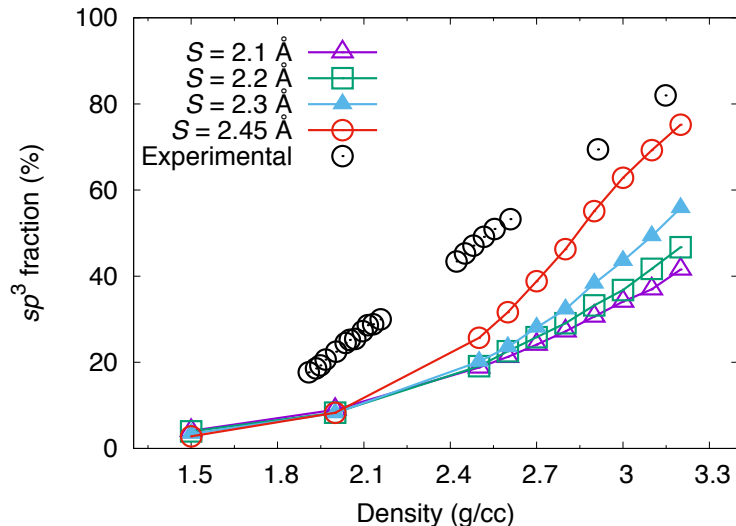


Figure 2.4: Amorphous carbon sp^3 fraction as a function of density for different values of the cutoff parameter S . Experimental data is from Schwan et al. (1996).

where the sp^3 fraction is underestimated by around a factor of two. Increasing the value of S doesn't change the sp^3 fraction at the lowest two densities, but for all other densities an effect is seen, particularly at the highest density of 3.2 g/cc and largest value of S . In this case the sp^3 fraction rises to $\sim 75\%$, very close to the experimental value. This improvement in the sp^3 fraction of high density amorphous carbon is the reason that larger values of S have been proposed by [Titantah and Lamoen \(2005\)](#) and [Sha et al. \(2013\)](#).

The next step in the simulations is the annealing of the amorphous carbon structures for 400 ps to study structural evolution. Based on the study of the original Tersoff potential and five other carbon potentials ([de Tomas et al., 2016](#)), we expected that the higher density annealed carbons would resemble the annealed structure by the original Tersoff potential, remaining amorphous and retaining similar coordination fractions (see [Figure 2.5](#) which is extracted from [de Tomas et al. \(2016\)](#)). However, to our surprise, we find that in some cases diamond crystals gradually appear within the amorphous matrix. An example of one such simulation is shown in [Figure 2.6](#) where $S = 2.45 \text{ \AA}$ and the density is 2.8 g/cc.

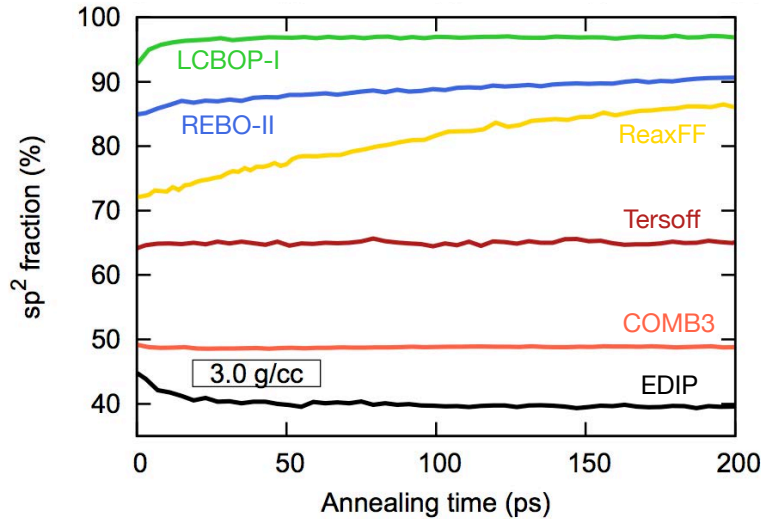


Figure 2.5: Evolution of the sp^2 fraction for the first 200 ps of annealing of 3.0 g/cc amorphous carbon for six different carbon potentials (Tersoff, REBO-II, EDIP, LCBOP-I, ReaxFF and COMB3). Note that the calculations (except ReaxFF) have reached equilibrium by this time. Figure taken from [de Tomas et al. \(2016\)](#).

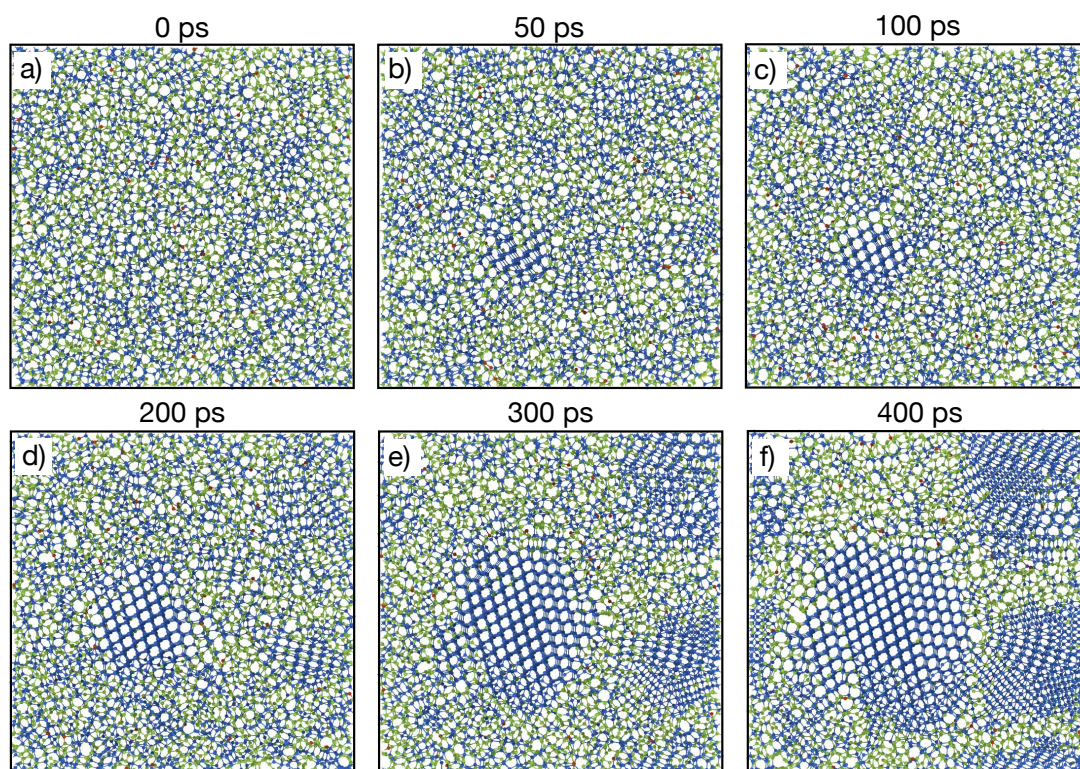


Figure 2.6: Time evolution during annealing of a 2.8 g/cc amorphous carbon system using $S = 2.45 \text{ \AA}$. Annealing is performed at 6000 K, and the cross-sectional slices are 1 nm in thickness. Red, green, and blue circles depict sp , sp^2 , and sp^3 bonding, respectively.

The initial structure seen in panel (a) is the amorphous carbon structure, and the network is seen to be fully disordered, as shown by the colouring which depicts the hybridization state (red is sp , green is sp^2 and blue is sp^3). The remaining panels depict varying stages in the annealing, which is performed at 6000 K. At first very little change is discernible, but after 50 ps a small region of blue can be seen near the centre of the slice. These atoms are all sp^3 hybridized, and furthermore, the angle of the cross-sectional slice reveals the characteristic hexagonal channels of diamond. As the annealing continues, this crystallite continues to grow, and additional crystallites appear in the simulation cell, though not always with the axis aligned along the viewing direction. After 400 ps has elapsed, more than half of the atoms in the viewing plane are blue, and one of the crystallites is nearly half the width of the simulation cell. A video animation of time evolution

of diamond nucleation during the annealing process is provided in [Movie 2.1](#).

To highlight the diamond crystals in a more quantitative manner, we used a coordination-number-based topology tool within OVITO as discussed in the [Section 2.2](#). The results of this analysis are shown graphically in [Figure 2.7](#), with atoms in a diamond topology shown in orange and all others in black. The figure shows the final structure after 400 ps of annealing for six different densities; all of the data shown used $S = 2.45 \text{ \AA}$. Note that [Figure 2.7\(b\)](#) can be directly compared to the final panel in [Figure 2.6](#), with a clear one-to-one correspondence between concentrations of orange in the former and blue atoms in crystallites in the latter. While no distinction is made in the figure between cubic and hexagonal diamond, the cubic phase dominates, typically amounting for around 60% of the diamond atoms. Considering the six densities in [Figure 2.7](#), it is

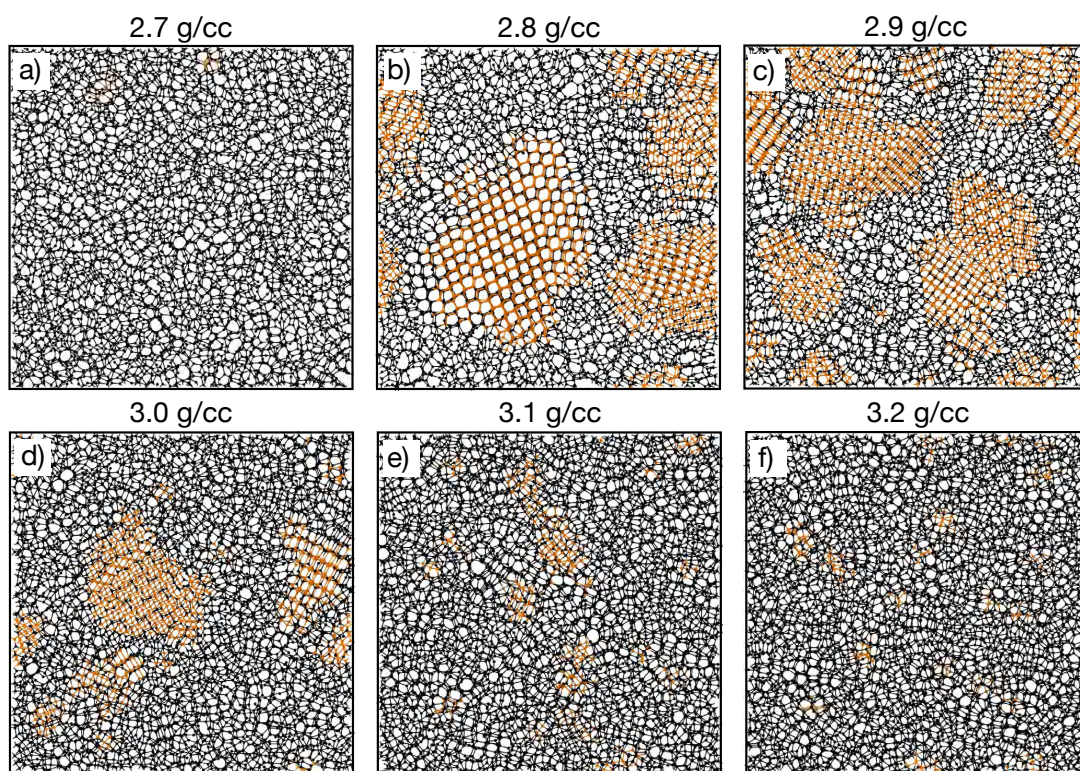


Figure 2.7: Effect of density on diamond formation in annealing simulations using $S = 2.45 \text{ \AA}$. Atoms with a local diamond topology are shown in orange. All other atoms are shown in black. Annealing is performed at 6000 K and the cross-sectional slices are 1 nm in thickness and show the final structure after 400 ps of annealing.

evident that 2.8 g/cc is some type of threshold, above which diamond crystals can nucleate out of the amorphous structure during annealing. At 2.8 and 2.9 g/cc, the crystallites grow to dominate the simulation cell, while at 3.0 g/cc there is a reduced amount of diamond, diminishing to quite small relative diamond fraction at 3.1 and 3.2 g/cc. We note that, as discuss later in this section, the pressure at the densities associated with nucleation process is extremely high. In addition, it should be noted that the density range at which the diamond nucleates is far below the experimental diamond density of 3.52 g/cc. This large difference and very high pressure are suggestive that the diamond nucleation is unphysical.

The time evolution of the in-growth of the diamond is quantified in Figure 2.8. At the densities of 2.6 and 2.7 g/cc, which is below the critical threshold, no diamond appears anywhere in the structure. For the 2.8 and 2.9 g/cc densities the fraction of atoms which are diamond increases to around 45% after 400 ps, at these densities equilibrium has yet to be reached, and the diamond fraction would continue to increase if the simulation are run longer. For example, at densities of 2.8, 2.9 and 3.0 g/cc after 600 ps of annealing, the diamond fraction increases to around 76%, 68% and 23%, respectively. At the higher densities

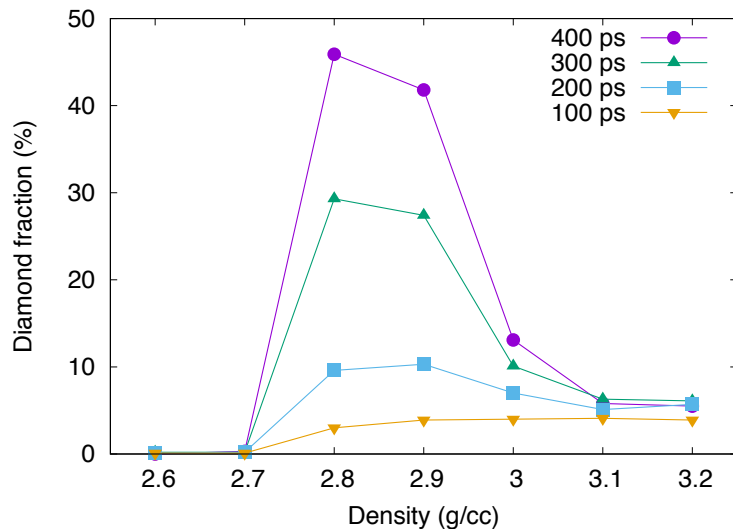


Figure 2.8: Percentage fraction of atoms in a diamond environment as a function of density at four different times during the annealing. Calculations performed using $S = 2.45 \text{ \AA}$.

of 3.1 and 3.2 g/cc, little change occurs after a couple of hundred picoseconds. Visual inspection of the atomistic structure reveals that, at these densities, small nanocrystals of diamond nucleate, amounting to around 6% of the total system, but these do not grow in size as occurs at the lower densities.

During the crystallization of the nanocrystals the atoms do not move far from their original positions in the amorphous carbon. Taking the square-root of the MSD of the all atoms in a simulation box for the entire annealing process yields an average displacement of 6.5 Å at 2.8 g/cc, reducing to just 1.6 Å at 3.2 g/cc. This observation that the atoms don't migrate far during the annealing emphasizes how the diamond nucleation occurs locally as the atoms rearrange themselves and change their hybridization in order to access a more stable configuration.

Insight into the nature of the diamond crystallites is gained by computing the radial distribution function (RDF), also known as $g(r)$. This information is plotted in Figure 2.9 for seven densities. At the lower densities the RDF has the characteristic broad peaks of an amorphous material, but at 2.8 and 2.9 g/cc sharp peaks appear superimposed on the broad background, indicative of the diamond phase. Even though diamond crystals can be seen at 3.0 g/cc in Figure 2.7, these do not produce a clear peak in the RDF, while at the highest densities the RDF resembles that of an amorphous structure.

In addition to highlighting the diamond structure, the RDF also serves to indicate the nature of the diamond itself. The dashed vertical lines in the figure indicate the expected locations of the first three neighbours assuming the experimental diamond nearest neighbour distance of 1.545 Å (note that the Tersoff potential predicts almost exactly the same value: 1.544 Å). However, it is apparent that these lines do not coincide with the peaks for the 2.8 or 2.9 g/cc structures. Rather, the peaks at these two densities are instead shifted to larger distances by a fixed multiplicative factor, indicating that the diamond is stretched in both cases. The stretching factors are slightly different for each case, being 1.039 for 2.8 g/cc and 1.031 for 2.9 g/cc. The peaks corresponding to these stretched di-

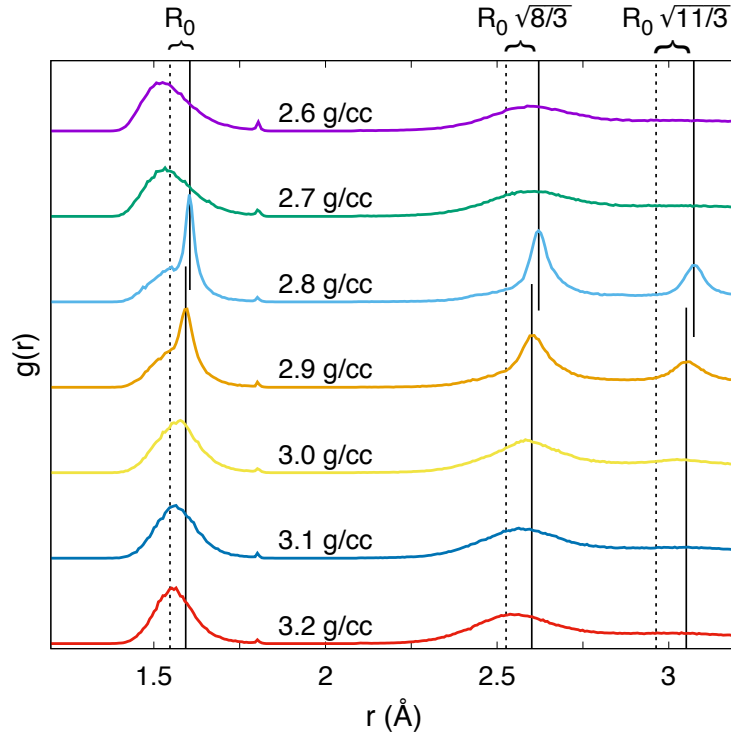


Figure 2.9: Radial distribution function after annealing for seven different densities using $S = 2.45 \text{ \AA}$. The dashed vertical lines indicate the position of the first three neighbours in ideal diamond, while the solid lines indicate the corresponding positions of stretched diamond as described in the text. The geometric factors at the top of the figure relate higher-order neighbours to the nearest neighbour distance R_0 .

amongst distances are shown as solid vertical lines. Note that only the first peak position is fitted to the data, while the position of the second and third peaks is computed using the geometric factors for the distances in diamond. As expected, the computed position of the second and third peaks corresponds exactly with the peaks in the RDF. This stretching of the diamond reduces the density of the nanocrystals to 3.15 and 3.22 g/cc for the systems with overall density of 2.8 and 2.9 g/cc, respectively. By comparison, the density of ideal diamond is 3.52 g/cc. This stretching in part reflects the tension that the crystals experience due to being embedded in a matrix with a density much lower than diamond itself.

To understand how the appearance of stretched diamond relates to the cutoff itself, quenching and annealing simulations at 2.8 g/cc are performed with four different cutoffs. The RDFs for both the amorphous and annealed samples are

presented in Figure 2.10, along with the associated cutoff function which is plotted in red using the right-hand axis. For the lowest three values of S the RDF of the amorphous and annealed structures are virtually identical, consistent with the behaviour of the unmodified potential in which the annealed structures remain amorphous. Only for the highest value of $S = 2.45 \text{ \AA}$ does the RDF develop the sharp peaks indicative of the appearance of the diamond crystallites. This demonstrates conclusively that the appearance of the diamond upon annealing is not a physical effect, but instead is an artifact of the modified potential itself.

The origin of the problem can be understood intuitively via the inset shown in Figure 2.10(e) which plots both of the RDFs and the cutoff function for the small region indicated in panel (d). This distance range corresponds to the onset of the second neighbour peak as well as the distance at which the cutoff function is decaying away to zero. The inset shows how there is considerable overlap between the tail of the cutoff function and the leading edge of the second RDF peak of the amorphous structure. However, after annealing the RDF has shifted significantly and there is much less overlap with the cutoff function. Inspection of the other three cases shows that this effect is unique to the case $S = 2.45 \text{ \AA}$. For small values of S the cutoff function either terminates completely prior to the onset of second neighbour distances, or has minimal overlap.

The changes seen in the inset in Figure 2.10 lie at the heart of the unphysical diamond at large values of S and provide a rationalization for the behaviour. In the Tersoff potential the cutoff function has two roles; (i) it limits the range of the potential to first neighbours only, and (ii) it controls which distances contribute to the bond-order itself. The problems with extending the cutoff arise when there is significantly overlap between the cutoff function and the second neighbour of the RDF. When this happens additional repulsion between second neighbours occurs, and the bond order changes such that the effective coordination number increases. Both of these effects combine to stabilise higher coordinated structures, which explains why the amorphous structure, which contains a mixture of sp^2 and

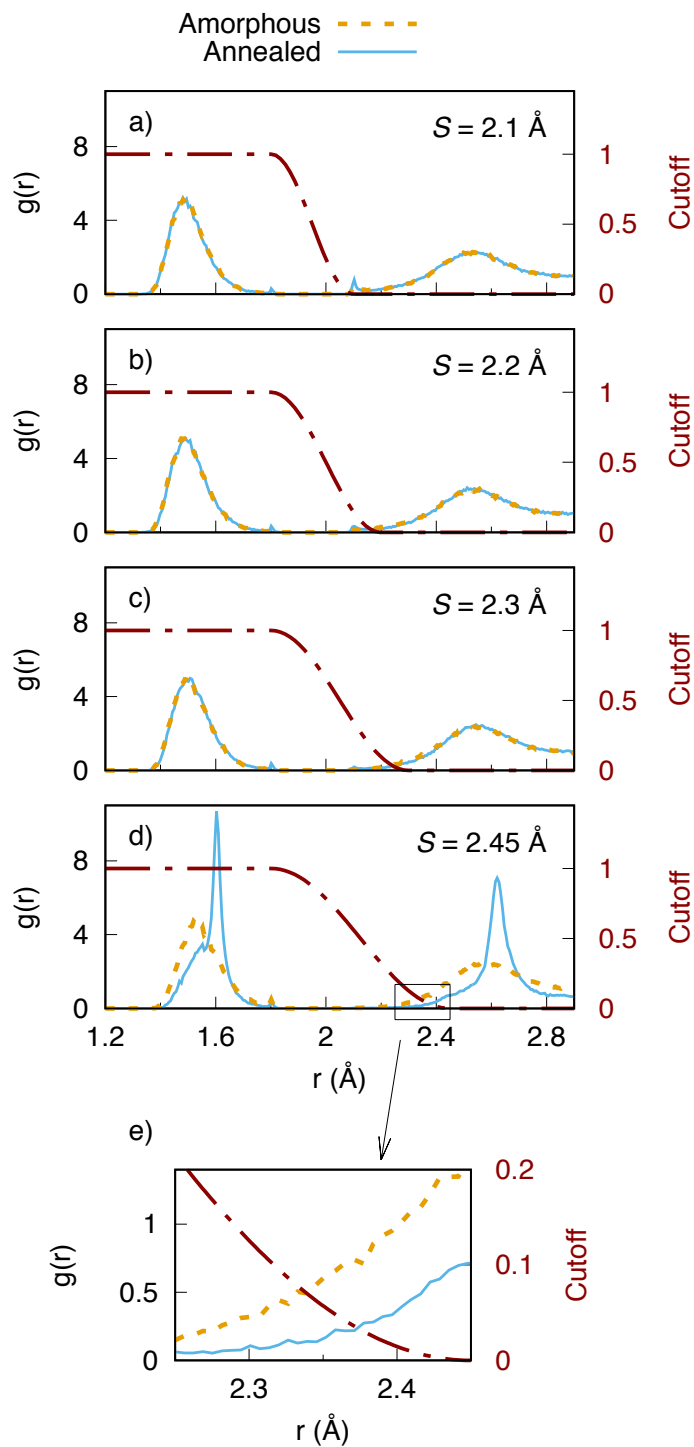


Figure 2.10: (a)–(d) Effect of the cutoff parameter S on the radial distribution function of amorphous carbon (gold dotted line) and annealed carbon (solid blue line). The corresponding cutoff function is shown in red using a dash-dot line. Panel (e) shows an inset as indicated for the case $S = 2.45 \text{ \AA}$.

sp^3 bonding, gradually transforms into a structure with a much higher fraction of sp^3 bonds.

Since the behaviour is unphysical, we have not explored the reasons why large diamond crystals are not favoured at 3.1 and 3.2 g/cc with $S = 2.45 \text{ \AA}$, but two possible explanations present themselves. One is that the dynamics is simply too slow at 6000 K and higher temperatures are required, but an alternative rationale is that the stretching of the diamond is an important requirement to avoid interactions between second neighbours, and hence higher densities make the formation of diamond disfavoured as the distances between atoms would be too close to those of ideal diamond itself.

Further insight into the effect of increasing the cutoff comes from the time evolution of the hydrostatic pressure shown in Figure 2.11. The upper panel shows that for $S = 2.45 \text{ \AA}$ the pressure is extremely high, initially greater than 100 GPa for 3.0 and 3.1 g/cc. For comparison, the Berman-Simon phase-boundary line separating graphite and diamond sits at around 12 GPa at high temperature (Bundy et al., 1996). Despite such high values, the pressure only drops by $\sim 20\%$ during the simulation. In contrast, at the densities associated with diamond nucleation (i.e., 2.8 and 2.9 g/cc), the fall in pressure is substantial, and is still falling at the conclusion of the simulation. This reduction is understandable, since the diamond nanocrystals (even in stretched form), pack more efficiently, giving rise to reduced pressure in the system overall. At the lowest density shown, 2.7 g/cc, the pressure is still substantial but no reduction occurs, consistent with the lack of structural evolution during annealing. Figure 2.11(b) emphasizes the earlier observations that qualitatively different behaviour occurs when the value of S encroaches upon the second neighbour distances. As the value of S increases, the pressure in the system increases monotonically; clearly it is wrong that the pressure should depend on the value of the cutoff. The highest cutoff value of $S = 2.45 \text{ \AA}$ corresponds to the same data shown in panel (a); here the pressure reduces substantially due to the appearance of the nanocrystals,

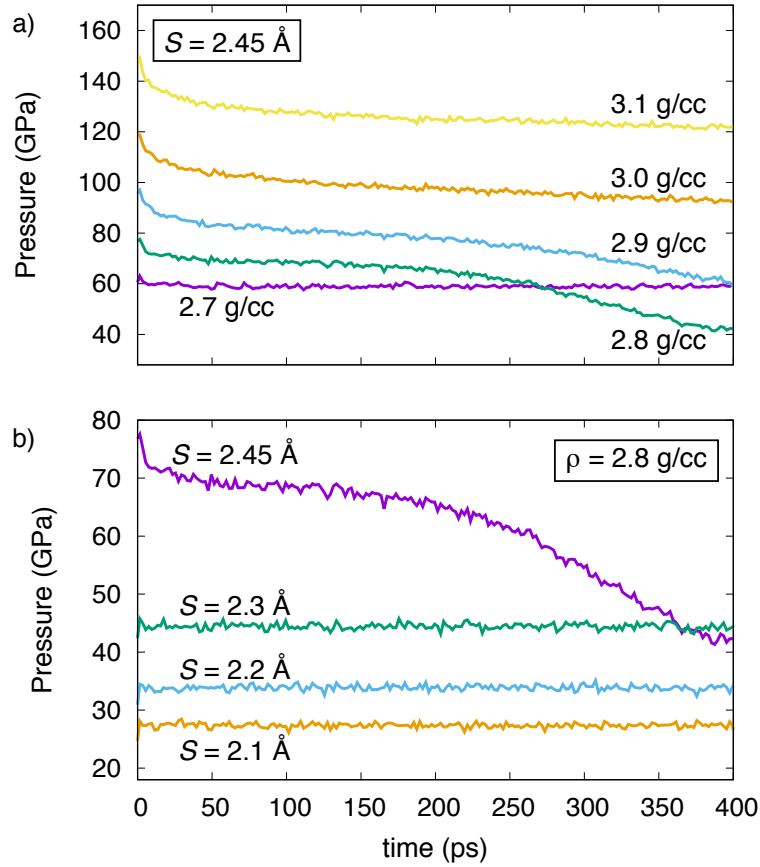


Figure 2.11: Time evolution of pressure during annealing of amorphous carbons. (a) Effect of varying the density for a fixed cutoff of $S = 2.45 \text{ \AA}$. (b) Effect of varying the cutoff S for a fixed density of 2.8 g/cc .

eventually dropping below the value for $S = 2.3 \text{ \AA}$.

As a final comment, we note that reducing the value of S to avoid the unphysical stabilization of diamond is not a useful option, since reducing S rapidly decreases the sp^3 fraction of the high density amorphous carbon as seen in Figure 2.4. Since a high sp^3 fraction is the original reason for increasing S , it would appear that this strategy does not have an optimal operational region in which to operate. As an aside, it is interesting to note that in the simulations of Jäger and Albe (2000) which used the REBO potential and increased cutoffs ($R = 1.95 \text{ \AA}$ and $S = 2.25 \text{ \AA}$), they too observed an increase in the sp^3 fraction, but at the expense of five-fold coordinated atoms and a large delta-function spike in the RDF. Both of these properties are unphysical, and reinforce the message of this work

that the cutoff function of the potential cannot be used as an arbitrary tuning parameter, particular for the amorphous carbons where a range of bondlengths are present.

2.4 Conclusion

In this chapter we consider the practice of increasing the cutoff of the Tersoff potential to 2.45 Å and show how this modification leads to unexpected behaviour during our annealing process of amorphous carbon. We demonstrate that diamond nanocrystals nucleate out of the amorphous phase, eventually converting a large portion of the structure. By systematically varying the value of the cutoff and the density, we show that this behaviour is unphysical and arises for numerical reasons associated with interactions between the cutoff function and the second neighbour peak as measured by the radial distribution function. These observations provide an important lesson not only for carbon simulations but for other material systems where there is temptation to tweak parameters to improve a particular property of the potential. The experience of this study is that this practice, while appealing, should be performed with a high degree of caution, and extremely thorough testing should be performed to ensure that the improvement in one property is not offset by a huge reduction elsewhere.

Chapter 3

Transferability of interatomic potentials for carbon

The main text and most of the figures comprising this chapter have been published in *Carbon* 155, (2019) 624–634. In this chapter, we test eight common carbon potentials, i.e., AIREBO, REBO2-S, Erhart/Albe, ABOP, GAP, Tersoff-S, Tersoff/Nordlund and Tersoff with modified cutoff, and compare their ability to describe disordered carbon structures. Using molecular dynamics simulations we produce and anneal amorphous carbon structures of different densities. Characterization using coordination analysis, ring statistics, radial distribution functions and diffraction intensity show that no two potentials give the same result for each property. To address this lack of transferability, we have developed a web application tool, www.carbonpotentials.org which collates all carbon potentials and enables real-time and equivalent comparison. Unlike a traditional publication that is frozen in time, the tool is expandable and can accommodate new potentials and data.

3.1 Introduction

In recent years there have been two large community efforts to collate the parameters of interatomic potentials and benchmark their performance. The most complete resource is the Knowledgebase of Interatomic Models, or OpenKIM ([Tadmor et al., 2011, 2013](#)), which archives interatomic potentials for the entire periodic table. OpenKIM provides standardized tests to evaluate performance and also includes an Application Programming Interface (API) integrated with common simulation packages such as LAMMPS ([Plimpton, 1995](#)) and GULP ([Gale, 1997](#)). Though not as complete as OpenKIM, the Interatomic Potentials Repository ([Becker et al., 2013](#)) hosted by the National Institute for Standards and Technology (NIST) is also an excellent resource for many elements, including multi-component alloys. These two websites reflect both a maturation of the field as well as an increasing complexity which can create difficulties for new entrants. For a summary of the rich variety of methods available for interatomic potentials, see recent reviews by [Akimov and Prezhdo \(2015\)](#) and [Harrison et al. \(2018\)](#).

For the specific case of carbon these efforts towards standardization and collation have been less effective due to the lack of an universal functional form. Unlike the Lennard-Jones or Embedded Atom Method potentials, for example, where parameters exist for many systems and the functional form is fixed, new carbon potentials continue to be developed that require their own unique code-base and/or library. Consequently, many popular carbon potentials are not available in the OpenKIM or NIST databases, and often considerable user effort is required to use new potentials, even for the relatively standard LAMMPS package.

In an interesting study, [de Tomas et al. \(2016\)](#) summarized the situation for carbon potentials by collating all potentials known to us and performing standardized tests involving liquid quenching and annealing on six common methods: Tersoff, REBO-II, EDIP, LCBOP-I, ReaxFF_{C2013} and COMB3. The simulations were made as similar as possible and all calculations were performed with

LAMMPS. Surprisingly they observed substantial differences between the potentials, with the sp^3 fraction, radial distribution function, topology and layering varying dramatically. Since this article was published there have been a number of developments which motivate further study. Firstly, at least five new potentials have appeared, including the Gaussian Approximation Potential (GAP) machine learning approach (Deringer and Csányi, 2017) which is perhaps the most accurate (and computationally costly) potential for carbon presently available. We have also become aware of three potentials that escaped in de Tomas et al. (2016). Further progress was an additional study by Aghajamali et al. (2018) as discussed in Chapter 2, where we analyzed a common variant of the Tersoff potential and showed that unphysical nucleation of diamond occurs from an excessively large cutoff parameter. Finally, the AIREBO potential implementation in LAMMPS was updated, removing a bug that had previously prevented equilibration of a liquid.

In this chapter we extend upon de Tomas et al. (2016) study by performing simulations of liquid quenching and amorphous carbon annealing at four different densities using the GAP, AIREBO, REBO2-S, Tersoff-S, Erhart/Albe, extended Cutoff Tersoff, ABOP and Tersoff/Nordlund potentials. Combined with the six potentials examined in de Tomas et al. (2016) study, this brings the total number of potentials studied up to 14. Such a large set of data creates problems for comparison and evaluation, and so we have also created a website, www.carbonpotentials.org, which collates all the data from our studies and enables the user to perform real-time comparison of any combination of data sets. The website contains a 3D visualisation tool to inspect the structures and also includes a list of all carbon potentials in the literature that are known to us. Our intention is that this resource be expanded over time, both by ourselves and also in collaboration with the carbon science community.

This chapter is structured as follows. In Section 3.2, we summarize our Methodology, paying particular attention to the rationale used to choose tempera-

tures for the liquid quenching and annealing phases. In Section 3.3 we present our results for (i) amorphous carbon generated by liquid quenching, and (ii) graphitization of amorphous carbon due to high-temperature annealing. The focus is on the annealing phase as this reveals the greatest variations between potentials. We also include a selection of results from our earlier study to provide context. In Section 3.4 we present a discussion of the results and provide details on the functionality of the website.

3.2 Methodology

In this chapter, we test the performance and evaluate the transferability of the following eight carbon potentials:

- the extended-cutoff Tersoff potential (Ext. Tersoff) first suggested by [Tiantah and Lamoen \(2005\)](#) where the only modification from the original Tersoff potential ([Tersoff, 1988](#)) is increasing the cutoff parameter from 2.1 to 2.45 Å
- the Erhart-Albe potential (Ehart/Albe) developed by [Ehart and Albe \(2005\)](#) which targets SiC and whose functional form incorporates terms from the original Tersoff ([Tersoff, 1988](#)) and REBO potentials ([Brenner, 1990](#))
- the screened Tersoff potential (Tersoff-S) by [Pastewka et al. \(2013\)](#) where an environment-dependent function is added to the original Tersoff potential ([Tersoff, 1988](#)) to improve the description of making and breaking bonds
- the modified Tersoff-Nordlund potential (mTersoff/Nordlund) by [López et al. \(2011\)](#) where a smooth Fermi-type cutoff is implemented in the original Tersoff potential and van der Waals interactions are added following Nordlund’s formalism ([Nordlund et al., 1996](#))

- the screened version of the second generation REBO potential (REBO2-S) by [Pastewka et al. \(2008\)](#) which implements an environment-dependent function on REBO-II potential ([Brenner et al., 2002](#)) to improve the description of making and breaking bonds
- the Adaptive Intermolecular REBO potential (AIREBO) by [Stuart et al. \(2000\)](#) based on the second generation REBO potential ([Brenner et al., 2002](#)) where long-range interactions are described by a Lennard-Jones term with a switching function to restrict their effect at short distances
- the Analytical Bond Order Potential (ABOP) by [Zhou et al. \(2015\)](#) which uses the latest reparametrization of the original ABOP potential ([Pettifor and Oleinik, 1999](#)) developed from tight-binding theory
- the Gaussian Approximation Potential (GAP) recently developed by [De-ringer and Csányi \(2017\)](#) where kernel-based machine learning is employed instead of a classic empirical functional form

Most simulations are performed in a highly parallelized manner using LAMMPS on a Cray XC40 supercomputer. The only exception was the mTersoff/Nordlund simulations which are performed on a Dell workstation using a serial in-house code. The computational cost of the LAMMPS simulations is shown in Figure 3.1, with the GAP simulations over three-orders of magnitude more expensive than the Tersoff variants. Due to this extreme computational cost, the GAP simulations are more modest than the other potentials, involving substantially fewer atoms, shorter annealing times, and half the number of densities.

The structures for the extended-cutoff Tersoff system are taken from [Aghajamali et al. \(2018\)](#) which is discussed with more details before in Chapter 2 and reanalyzed. In the case of the ABOP potential ([Zhou et al., 2015](#)), we obtained the parameters directly from the authors and performed tests to confirm that the published results were reproduced. The Tersoff-S and REBO2-S simulations used

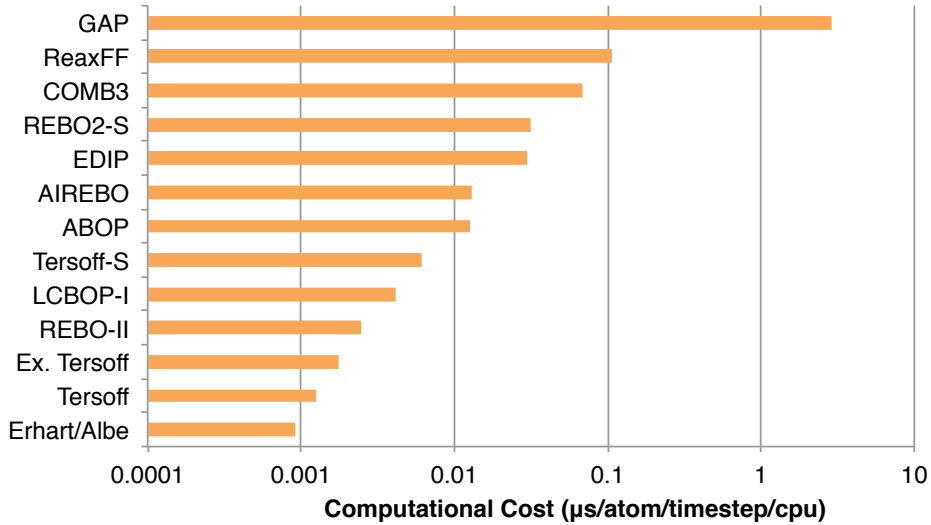


Figure 3.1: Computational cost for different carbon potentials in LAMMPS simulations on a Cray XC40. Values are calculated from a 10,000-step annealing simulation of a 1.5 g/cc amorphous structure using 48 processors.

routines from the *Atomistica* package (www.atomistica.org) which is compiled separately and linked into LAMMPS. For the GAP simulations, LAMMPS was built with the QUIP module including GAP routines from www.libatoms.org (Bartók et al., 2010, 2013). The AIREBO and Erhart/Albe simulations are straightforward to implement, using routines and parameters built into LAMMPS.

The molecular dynamics (MD) workflow follows the same approach as used by de Tomas et al. (2016) and broadly similar to our previous Chapter 2 (see Figure 2.2). For each potential, we generate four amorphous carbon structures via liquid quenching with densities of 1.5, 2.0, 2.5 and 3.0 g/cc (only 1.5 and 3.0 g/cc for GAP simulation) to cover the experimental density range observed experimentally. The starting configuration is a slightly randomized simple cubic lattice of $32 \times 32 \times 32$ unit cells containing 32,768 carbon atoms ($16 \times 16 \times 16$ with 4,096 atoms for GAP simulation) which is large enough to accommodate statistical variation. Box lengths vary from 7.58 nm for the 1.5 g/cc structures to 6.02 nm for 3.0 g/cc (from 3.79 nm to 3.01 nm correspondingly in the case of GAP simulation). Velocities are initialized at 100 K. This unstable configuration quickly melts, after which the liquid is equilibrated for 5 ps at a temperature T_{liquid}

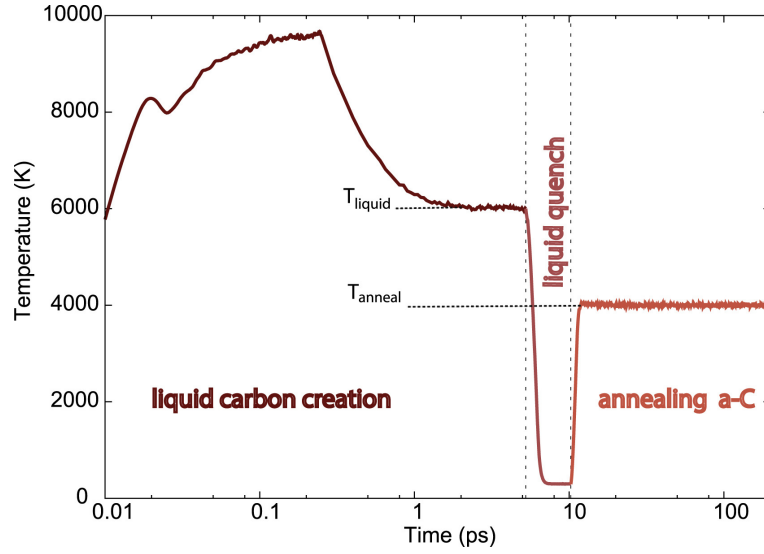


Figure 3.2: Example of the temperature profile during the creation of the amorphous structure and annealing. Figure is taken from [de Tomas et al. \(2016\)](#).

which depends on the potential. The amorphous carbon structure is obtained via rapid (1 ps) quenching of the liquid followed by equilibration at room temperature for 5 ps. The amorphous structure is then annealed for 400 ps (200 ps for GAP simulation) at a temperature T_{anneal} to induce graphitization. An example of the temperature profile through this protocol is illustrated in Figure 3.2.

The final structure is minimized using a conjugate gradient scheme and then characterized to determine all structural analysis. This includes snapshots, time evolution of the coordination fractions, ring statistics, radial distribution functions and the Debye diffraction intensity. Coordination fractions are calculated by counting neighbours within a cutoff distance of 1.85 Å. Shortest-path ring statistics are calculated using the algorithm of [Franzblau \(1991\)](#), using an in-house code developed by Nigel Marks (my principal supervisor) and previously used to study amorphous carbon ([Marks et al., 2002](#)). Due to the large system size, a single frame is sufficient for the radial distribution function analysis. The diffraction scattering intensity computed using the Debye scattering equation ([Warren, 1990](#)), which was code in fortran by Nigel Marks with a scattering factor of a single carbon atom.

To select T_{liquid} we vary the temperature in coarse steps of 1000 K and compute the mean-square displacement (MSD) to ensure that self-diffusion is broadly similar between all of them. A comparison of the MSD behavior for 3.0 g/cc liquid carbon is shown in Figure 3.3, with the corresponding temperatures listed in Table 3.1. Although the diffusion constant reduces with increasing density, for simplicity we choose just a single value of T_{liquid} for each potential. For most of the potentials a temperature of 8000-10000 K yields comparable diffusion coefficients at a given density. The only exception is REBO2-S potential for which a value of 16000 K is required at the highest density of 3.0 g/cc. This extremely high temperature indicates that self-diffusion is inhibited under these conditions, perhaps due to the action of the screening term. Notably different is the GAP potential for which a significantly lower temperature of 6000 K gives equivalent diffusion behavior. For comparison, the EDIP potential from [de Tomas et al. \(2016\)](#) work is also shown in Figure 3.3, and like GAP potential, it uses a T_{liquid} value of 6000 K. Since GAP and EDIP potentials are both fitted to density-functional-theory data on liquid carbon, this suggests that most of the other potentials overestimate the temperatures required to reproduce liquid state behavior.

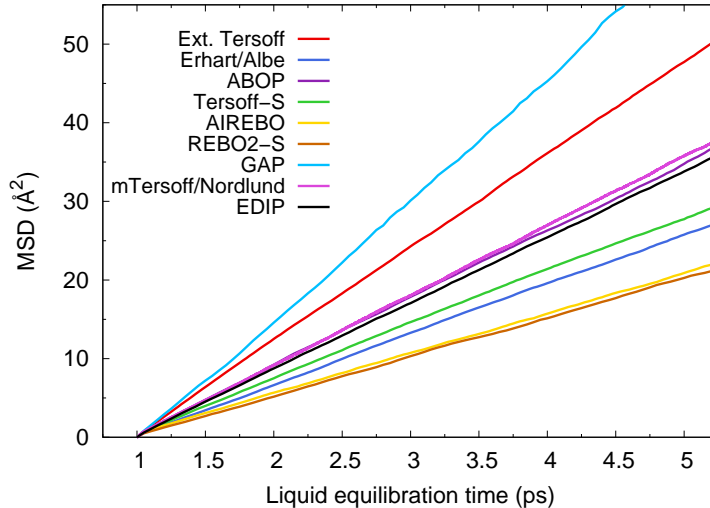


Figure 3.3: Time evolution of the mean-square displacement (MSD) of 3 g/cc liquid carbon for various potentials. Data collection starts at $t = 1$ ps to allow time for the liquid to equilibrate. The temperature used for each potential is listed in Table 3.1.

Table 3.1: Temperatures used for equilibration of the liquid and annealing of the amorphous carbons. Data for the Tersoff, REBO-II, EDIP, LCBOP-I, ReaxFF_{C2013} and COMB3 potentials is from [de Tomas et al. \(2016\)](#)

Name of potential	T_{liquid} (K)	T_{anneal} (K)			
		density (g/cc)			
		1.5	2.0	2.5	3.0
Ext. Tersoff	9000	5000	5000	5000	6000
Erhart/Albe	9000	4000	4000	4000	4000
ABOP	8000	2500	3000	4000	4000
Tersoff-S	9000	4500	4000	4000	5000
AIREBO	10000	4000	4000	4000	4500
REBO2-S	*10000	3500	3500	4000	4500
GAP	6000	3500	-	-	3000
mTersoff/Nordlund	8000	3500	3500	3500	4000
Tersoff	8000	5000	5000	4500	4500
REBO-II	6000	4500	4500	4000	4000
EDIP	6000	4000	4000	3000	3000
LCBOP-I	8000	5500	5500	5000	5000
ReaxFF _{C2013}	6000	3500	3500	3000	3000
COMB3	6000	4000	4000	4000	4000

* T_{liquid} for 3.0 g/cc is 16000 K.

The second stage involves annealing the amorphous carbons at a temperature high enough to allow atomic rearrangement, but not so great that it melts the structure. To find this temperature, which depends on both the potential and the density, it is helpful to examine the MSD in conjunction with the sp^2 fraction. As an example, Figure 3.4 shows data used to determine T_{anneal} for the Erhart/Albe potential at a density of 1.5 g/cc. The data in panel (a) shows that at 5000 K the MSD is varying linearly; this is indicative of melting and hence this temperature is too high. At 4000 and 4500 K the MSD is varying in a manner more akin to the square root of time, see inset in panel (a), which is much more reasonable for an

annealing process. After 100 ps the MSD corresponds to average movement of 3.3 and 5.5 Å, respectively; again, both values are reasonable for diffusion within a solid. However, consideration of the sp^2 fraction as shown in panel (b) shows that more graphitization has occurred at the lower temperature, and hence 4000 K was selected. This process of examining the MSD and sp^2 fraction was performed for all potentials and all densities in steps of 500 K; the chosen values of T_{anneal} are listed in Table 3.1. Generally speaking, the higher densities required a slightly higher annealing temperature, with the only exceptions being GAP potential,

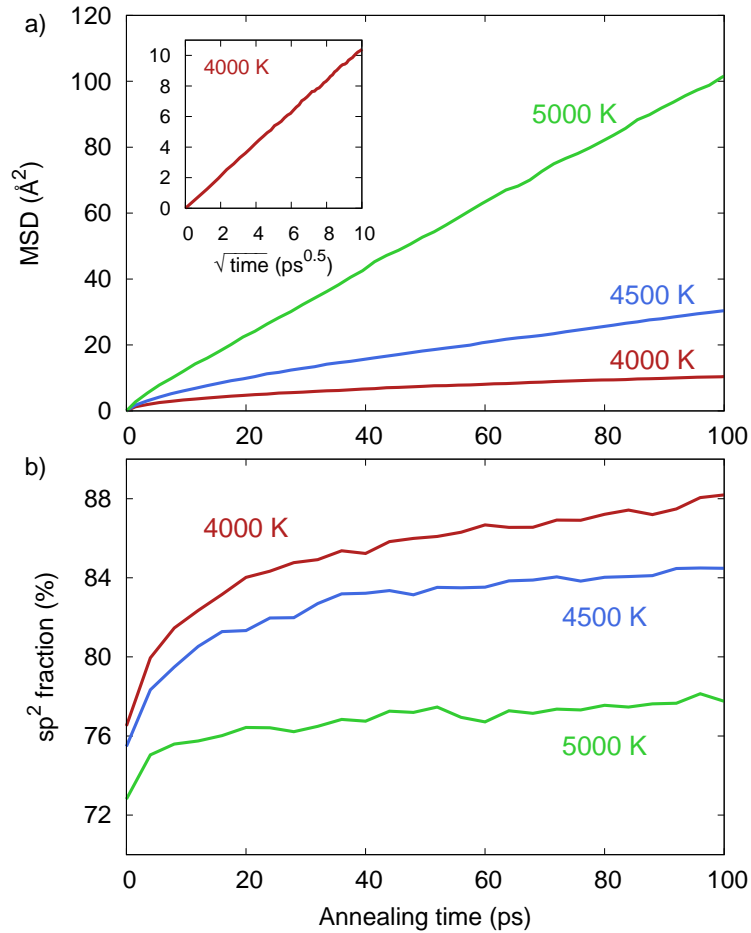


Figure 3.4: Data used to select the annealing temperature for the Erhart/Albe potential simulation at 1.5 g/cc. (a) Time evolution of the mean-square displacement (MSD) for three temperatures. (b) Time evolution of the sp^2 fraction for the same three temperatures. The inset in panel (a) shows that for a suitable annealing temperature the MSD varies as the square-root of time.

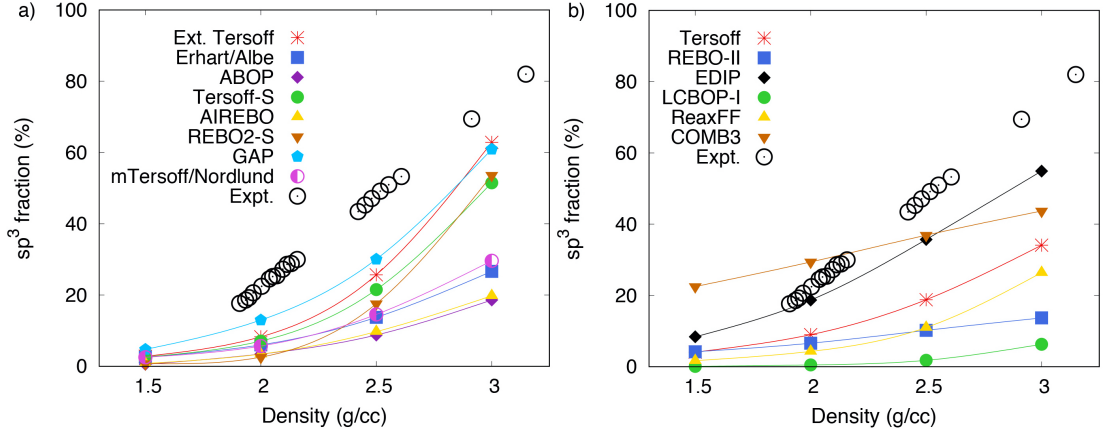


Figure 3.5: Fraction of sp^3 bonding as a function of density in amorphous carbons created by liquid quenching. Open circles show experimental data from Schwan et al. (1996). Panel (a) is from this work and panel (b) is from de Tomas et al. (2016).

where the reverse behavior is seen, and Erhart/Albe potential, where the same temperature was selected for all densities.

3.3 Results

3.3.1 Amorphous carbons (*a-C*)

It is well known from experimental and density-functional-theory (DFT) studies that the sp^3 fraction of amorphous carbons increases linearly with density, and hence this relationship represents one of the simplest tests of the transferability of a carbon potential. Figure 3.5(a) shows the sp^3 fraction versus density for the eight potentials studied in this work, while panel (b) shows the same data from de Tomas et al. (2016). Experimental data from Schwan et al. (1996) is shown as empty circles; note that DFT studies (Marks et al., 2002) almost exactly reproduce the experimental trend.

At low densities all eight potentials in panel (a) have sp^3 fractions consistent with experiment and DFT, but as the density increases significant deviations occur. Broadly speaking, the eight potentials can be split into two groups. The first group, containing ABOP, Erhart/Albe, AIREBO and mTersoff/Nordlund poten-

tials, have sp^3 fractions of 20–30% at 3.0 g/cc, underestimating the experimental value by approximately a factor of three. The second group, containing GAP, extended Tersoff, Tersoff-S and REBO2-S potentials, have values clustered around 60%, considerably closer to experiment. This observation of a wide spread of sp^3 fractions at high density mirrors the results from our findings from [de Tomas et al. \(2016\)](#) as seen in Figure 3.5(b).

While the relation between sp^3 fraction and density of amorphous carbon is an excellent first step in assessing a potential, it does not provide a guarantee of transferability. For example, as investigated in Chapter 2, on the extended Tersoff potential we observed that the high sp^3 fraction at high densities is associated with overlap of the cutoff function into the second neighbor shell. This leads to unphysical nucleation of diamond during annealing of the amorphous structures. In the next section, we will see a similar effect for the Tersoff-S potential.

3.3.2 Graphitization of a -C under annealing

To assess the ability of the potentials to describe the making and breaking of bonds, the amorphous structures were annealed at high temperatures until equilibrium was reached. With the exception of GAP potential, the annealing time was 400 ps for all potentials. The high temperature enables a substantial rearrangement of the structure, leading to significant time evolution of the coordination fractions as shown in Figure 3.6. At the lowest density of 1.5 g/cc all eight potentials exhibit broadly similar behaviour, showing an increase in the fraction of sp^2 bonds. This development of graphitic bonding during annealing is the expected behaviour for a carbon system heated to high temperatures. Despite the similarities, the sp^2 fraction at 200 ps still varies somewhat, from as little as 82% for REBO2-S potential, to a high of 97% for GAP potential. Note that as can be seen from the Figure 3.6 and Table 3.2, most of the coordination fractions (sp , sp^2 and sp^3) have already reached equilibrium by this time. Full details of the coordination fractions after 200 and 400 ps of annealing are provided in Table 3.2.

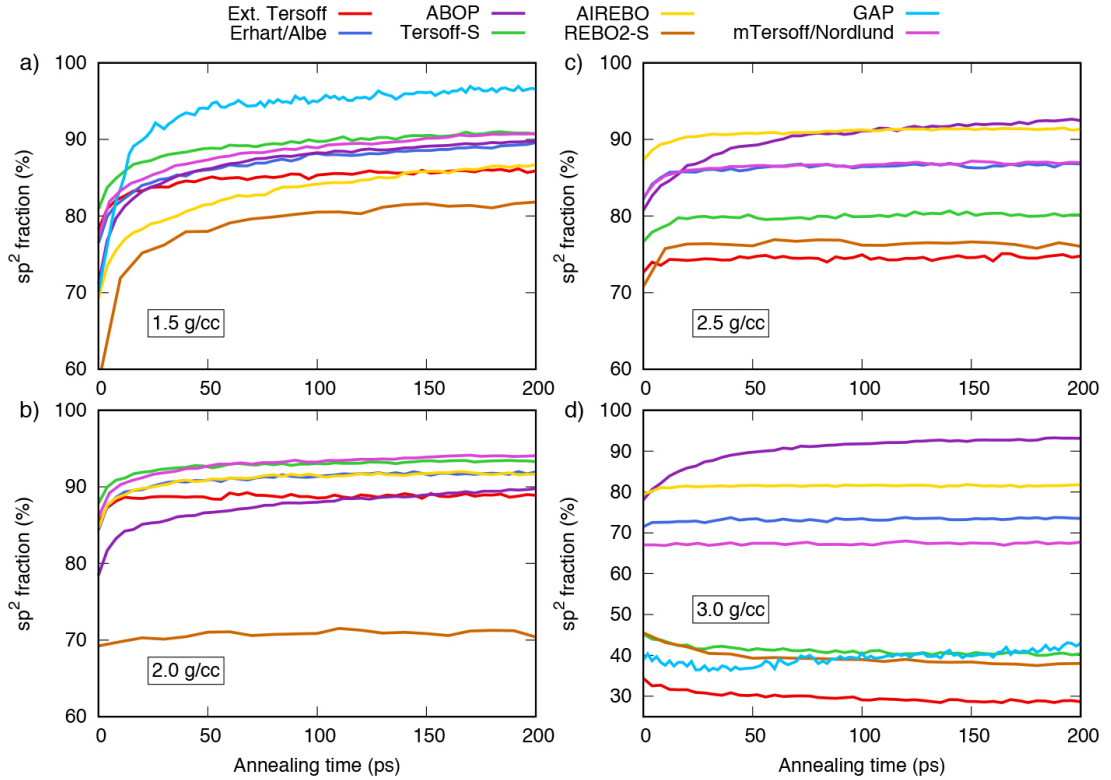


Figure 3.6: Evolution of sp^2 bonding for the first 200 ps of annealing of amorphous carbon. Data is shown for each potential at densities of (a) 1.5 g/cc, (b) 2.0 g/cc, (c) 2.5 g/cc and (d) 3.0 g/cc.

The time-evolution of pressure during the annealing simulations for the 1.5 g/cc and 3.0 g/cc structures is shown in Figure 3.7. For comparison, data for EDIP potential is also included. After a few tens of picoseconds the pressure fluctuates around a constant value.

As the density increases, large differences appear between the potentials. Even at 2.0 g/cc (Figure 3.6(b)), the REBO2-S structure has substantially fewer sp^2 atoms than the other potentials, and a high sp fraction approaching 30%. At 2.5 g/cc (Figure 3.6(c)) the sp^2 fractions are spread out, with no particular value more common than other. At the highest density (Figure 3.6(d)) the sp^2 fraction varies from less than 30% for extended Tersoff potential to 94% for ABOP potential. Similar to what was observed for amorphous carbon in Figure 3.5(a), the potentials can be divided into the same two groups, indicating that highly sp^3 amorphous carbon transforms into annealed structure with a high sp^3 fraction,

Table 3.2: Percentage coordination fractions for carbon structures generated using all fourteen potentials and four densities. Data is shown for amorphous carbon (a -C) prepared by liquid quenching and subsequently annealed carbons at two stages (200 and 400 ps). Data for the Tersoff, REBO-II, EDIP, LCBOP-I, ReaxFF_{C2013} and COMB3 potentials is from [de Tomas et al. \(2016\)](#). The melting and annealing temperatures used are given in Table 3.1.

Name of potential		1.5 g/cc			2.0 g/cc			2.5 g/cc			3.0 g/cc		
		sp	sp^2	sp^3									
Tersoff	a -C	23.9	71.6	4.1	12.1	78.9	9.0	4.4	76.8	18.8	1.6	64.1	34.1
	200 ps	11.0	84.8	4.2	8.2	85.7	6.1	2.4	81.5	16.1	0.9	65.0	34.1
	400 ps	9.9	85.4	4.7	8.3	85.9	5.8	2.6	81.4	16.0	1.0	65.3	33.7
REBO-II	a -C	18.4	77.1	4.2	9.4	84.0	6.6	3.3	86.5	10.2	1.3	85.0	13.7
	200 ps	2.9	92.6	4.5	4.1	89.3	6.6	1.7	89.3	9.0	0.7	90.7	8.6
	400 ps	2.1	93.8	4.1	3.6	89.6	6.7	1.4	90.0	8.6	0.5	93.3	6.2
EDIP	a -C	29.6	62.0	8.4	15.0	66.3	18.7	4.0	60.3	35.7	0.3	44.8	54.9
	200 ps	3.7	93.9	2.4	2.5	93.9	3.6	0.9	62.8	36.3	0.2	39.6	60.2
	400 ps	2.8	95.5	1.7	2.3	95.0	2.7	0.7	65.0	34.3	0.2	39.3	60.6
LCBOP-I	a -C	36.6	62.7	0.1	13.0	86.5	0.5	4.2	94.0	1.8	1.0	92.7	6.3
	200 ps	24.5	74.9	0.2	8.8	90.8	0.4	1.4	97.9	0.7	0.6	96.9	2.5
	400 ps	23.2	76.2	0.2	9.0	90.6	0.4	1.4	97.9	0.7	0.6	97.0	2.4
ReaxFF _{C2013}	a -C	37.7	60.5	1.7	20.3	75.1	4.3	7.8	81.2	11.0	1.5	72.1	26.4
	200 ps	3.6	95.2	1.2	3.5	94.5	2.0	1.1	94.4	4.5	0.2	86.0	13.8
	400 ps	1.9	97.1	1.0	1.8	97.1	1.1	0.7	96.0	3.3	0.1	90.2	9.7
COMB3	a -C	18.0	58.4	22.5	14.3	55.4	29.4	9.8	52.3	36.9	6.0	49.2	43.7
	200 ps	14.3	51.0	33.2	10.6	49.4	39.5	6.6	49.8	43.2	3.6	48.8	47.6
Extended Tersoff	a -C	22.7	74.2	2.8	9.4	82.3	8.3	2.4	71.9	25.7	0.2	36.8	62.8
	200 ps	12.1	85.7	2.1	5.7	89.0	5.2	1.6	74.6	23.8	0.3	28.9	70.7
	400 ps	10.9	86.9	1.9	5.9	88.8	5.2	1.6	75.0	23.4	0.3	27.7	72.0
Erhart/Albe	a -C	28.1	69.0	2.6	14.9	78.9	6.0	7.3	78.9	13.7	3.4	70.0	26.6
	200 ps	8.6	89.6	1.7	5.3	91.9	2.8	2.6	86.8	10.5	1.0	73.5	25.4
	400 ps	7.8	90.4	1.8	5.8	91.3	2.8	2.7	86.5	10.8	0.9	74.3	24.8
ABOP	a -C	38.9	53.9	0.5	24.9	68.0	3.4	12.1	77.6	8.8	5.1	76.1	18.6
	200 ps	6.9	89.8	1.7	5.7	89.8	1.9	4.9	92.5	1.1	3.7	93.1	3.1
	400 ps	5.9	90.1	1.9	5.1	91.2	1.4	4.2	93.6	0.9	3.3	94.2	2.5
Tersoff-S	a -C	18.4	78.9	2.6	7.7	85.2	7.1	1.9	76.8	21.5	0.4	48.1	51.5
	200 ps	6.7	90.7	2.5	3.1	93.2	3.6	1.0	80.2	18.8	0.6	40.3	59.1
	400 ps	5.9	91.5	2.5	2.8	93.9	3.3	1.0	80.5	18.5	0.5	39.5	60.0
AIREBO	a -C	38.7	60.0	0.8	18.1	78.3	3.4	5.4	84.9	9.7	1.5	78.4	19.8
	200 ps	11.5	86.7	1.7	5.9	91.7	2.5	0.8	91.3	7.8	0.3	81.7	18.0
	400 ps	8.5	89.2	2.2	5.7	92.0	2.3	0.8	91.3	7.9	0.3	81.8	17.9
REBO2-S	a -C	41.0	58.2	0.8	28.2	69.2	2.6	11.6	70.8	17.6	0.9	45.5	53.6
	200 ps	16.6	81.8	1.5	27.9	70.4	1.7	17.8	76.1	6.1	0.6	38.0	61.3
	400 ps	16.1	82.3	1.6	27.2	71.0	1.8	17.5	76.6	5.9	0.6	37.6	61.7
GAP	a -C	25.1	70.1	4.7	9.0	78.0	13.0	2.0	67.9	30.1	0.1	38.9	60.9
	200 ps	2.3	96.6	1.1	–	–	–	–	–	–	0.03	43.0	56.4
mTersoff/Nordlund	a -C	22.1	75.3	2.4	9.2	85.1	5.7	3.4	82.1	14.5	0.9	69.4	29.6
	200 ps	7.8	90.8	1.4	3.2	94.1	2.7	1.2	87.1	11.7	0.7	68.1	31.1
	400 ps	6.2	92.1	1.6	3.0	94.5	2.5	1.2	87.3	11.5	0.8	68.1	31.3

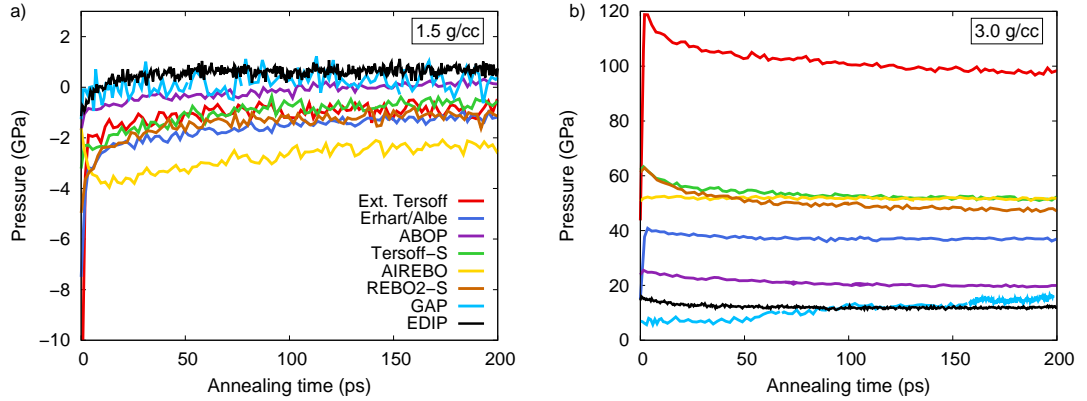


Figure 3.7: Evolution of pressure during the annealing of the 1.5 g/cc (panel (a)) and 3.0 g/cc structures (panel (b)).

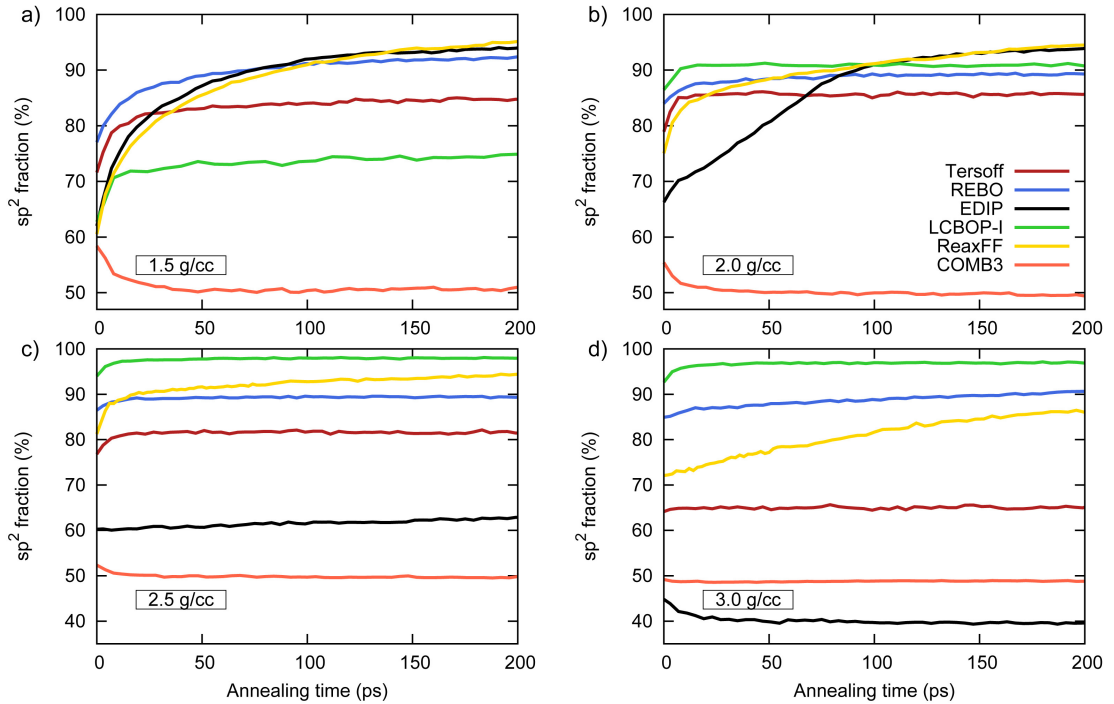


Figure 3.8: Evolution of sp^2 bonding for the first 200 ps of annealing of amorphous carbon for the Tersoff, REBO-II, EDIP, LCBOP-I, ReaxFF_{C2013} and COMB3 potentials. Figure is taken from [de Tomas et al. \(2016\)](#).

and vice-versa. The significant variability between the different potentials mirrors our previous study where large variations also emerged during the annealing process (for the analogous plot see Figure 3.8 which extracted from [de Tomas et al. \(2016\)](#)). This demonstrates that based on our methodology, carbon in-

teratomic potentials do not produce equivalent structures, but rather generate a broad spectrum of possibilities.

Figures 3.9 and 3.10 show cross-sectional slices of the 1.5 and 3.0 g/cc annealed structures. These are all slices from the center of the simulation cell; however, due to the periodic boundary conditions this is an arbitrary choice. Atoms are coloured by bonding type, with red, green and blue denoting sp , sp^2 and sp^3 hybridization, respectively. For comparison, also shown in the figures are the most important structures from de Tomas et al. (2016). The GAP structures have half the box-length of the other structures and hence a 2×2 tiling (panel (g) of both figures) provides a convenient means to display the structure on the same scale.

Looking first at the 1.5 g/cc structures in Figure 3.9, an enormous range of variability is evident, even though all the structures are highly sp^2 bonded. Grouping the potentials by microstructure, three broad categories can be identified. In the first category, containing extended Tersoff, Erhart/Albe, Tersoff-S, AIREBO, mTersoff/Nordlund and Tersoff, the structures are highly disordered, with small graphene fragments and a few pores. In the second category, containing ABOP, REBO-II, REBO2-S and ReaxFF, there is an increase in short-range order and larger graphene fragments are present. These graphene fragments are curved/entangled, but are not stacked. In the third category, containing EDIP and GAP, the structures show the highest degree of order, with stacking of layers present in EDIP structure and the onset of this behavior in GAP structure. Due to the small system size with GAP structure it is not possible to observe a large number of stacked layers.

The 3.0 g/cc structures in Figure 3.10 exhibit an even wider range of variability, spanning a combination of different bonding types and microstructures. In this case, five categories can be identified. In the first category, containing Erhart/Albe, AIREBO, mTersoff/Nordlund and Tersoff, the structures are fully disordered/amorphous with majority sp^2 bonding (seen by the excess of green

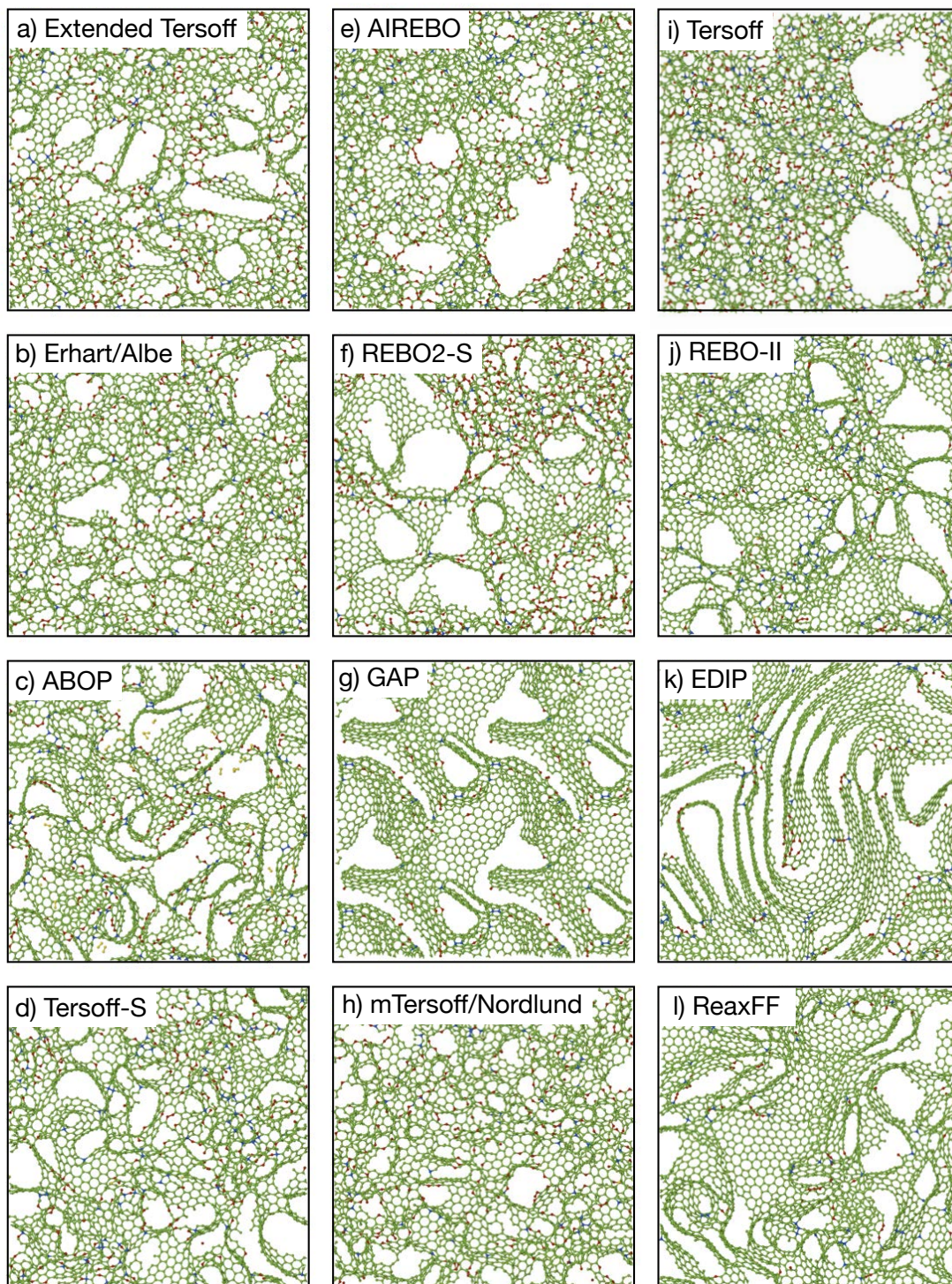


Figure 3.9: Cross-sectional slice of 1 nm thickness for 1.5 g/cc annealed carbons generated using twelve different potentials. Panels (a)–(h) are from this work and panels (i)–(l) are from [de Tomas et al. \(2016\)](#). The GAP structure in panel (g) is a 2×2 tiling. Red, green and blue atoms denote sp , sp^2 and sp^3 bonding, respectively.

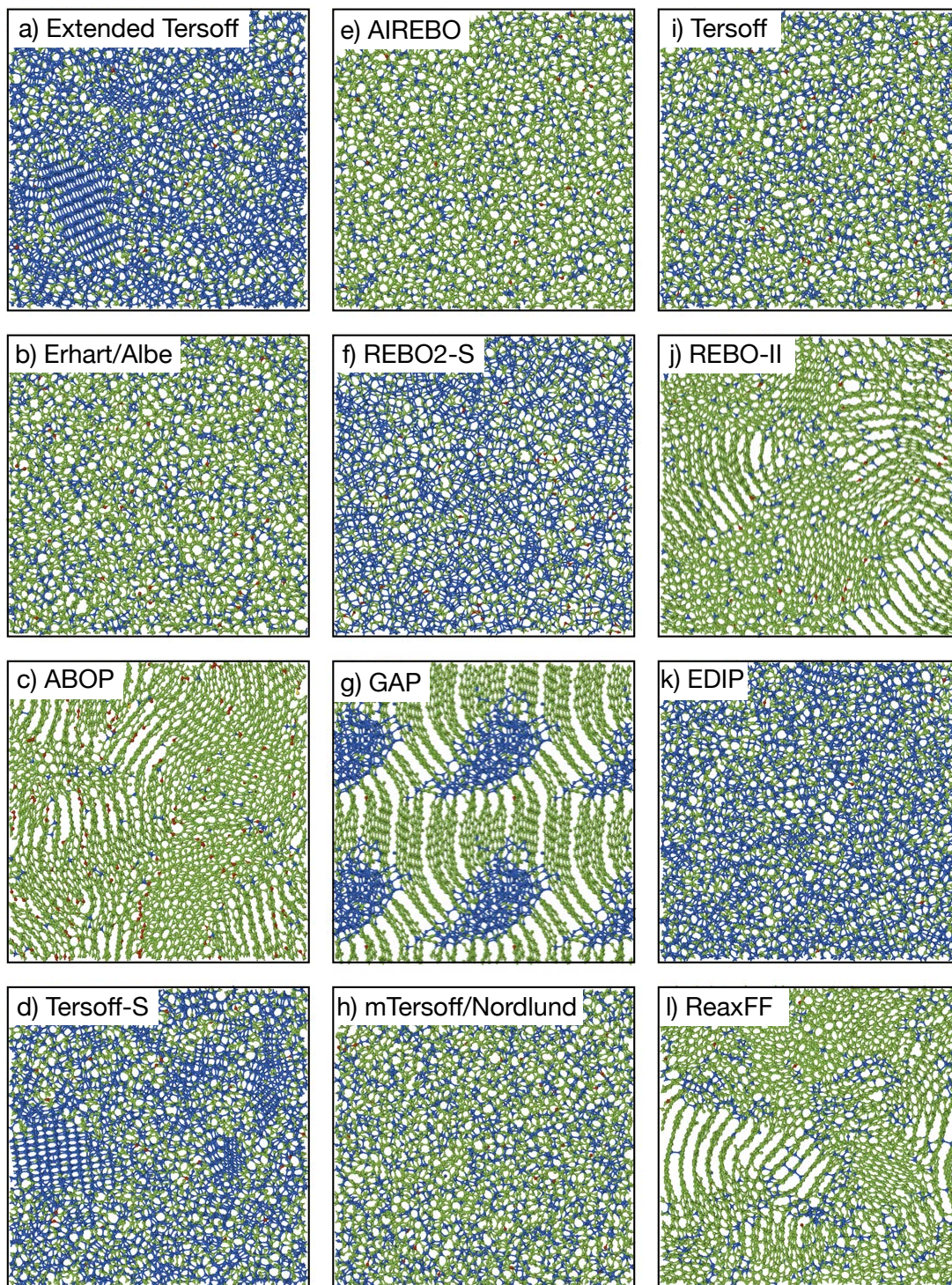


Figure 3.10: Cross-sectional slice of 1 nm thickness for 3.0 g/cc annealed carbons generated using twelve different potentials. Panels (a)–(h) are from this work and panels (i)–(l) are from [de Tomas et al. \(2016\)](#). The GAP structure in panel (g) is a 2×2 tiling. The colour codings details are the same as Figure 3.9.

in the snapshots). In the second category, containing REBO2-S and EDIP, the structures are also amorphous but predominantly sp^3 bonded, as seen by the abundance of blue-coloured atoms. In the third category, containing extended Tersoff and Tersoff-S, the structure is predominantly sp^3 bonded but contains a mixture of amorphous and diamond crystallites. In the fourth category, containing ABOP, REBO-II and ReaxFF, the structures are highly sp^2 bonded and contain randomly oriented stacked layers. The GAP structure exists in a category all of its own, being the only potential to produce phase separation into stacked layers and a dense disordered phase. Inspection of the structure showed that the disordered phase is tetrahedral amorphous carbon (*ta-C*), with around 80% sp^3 bonding and an absence of crystallites.

We have shown in Chapter 2 that the diamond crystallites seen for the extended Tersoff potential are an artifact arising from overlap of the cutoff function with the second neighbour shell. The observation of crystallites with Tersoff-S suggests this behavior is also an artifact. To analyze this behavior, we follow the same approach in Chapter 2 and performed additional simulations and employed the diamond structure identification tool (Maras et al., 2016) in the OVITO visualization package. Amorphous carbon and annealed structures were generated for densities between 2.7 and 3.2 g/cc, in intervals of 0.1 g/cc. Figure 3.11 shows the time evolution of diamond nucleation for Tersoff-S and extended Tersoff structures, revealing that the process occurs in a narrow density window. The original Tersoff potential and other modifications (Erhart/Albe and mTersoff/Nordlund potentials) do not produce diamond crystallites. Further analysis showed that the 3.0 g/cc REBO2-S structure, which uses the same screening approach as Tersoff-S structure, also contained a small amount (2.1%) of diamond crystallites. This suggests the crystallite nucleation is an anomaly due to the screening function.

Another anomaly is the observation of five-fold coordinated atoms in the 3.0 g/cc GAP structure. The developers of GAP potential also observed some five-fold atoms in simulations of thin-film deposition (Caro et al., 2018) and these

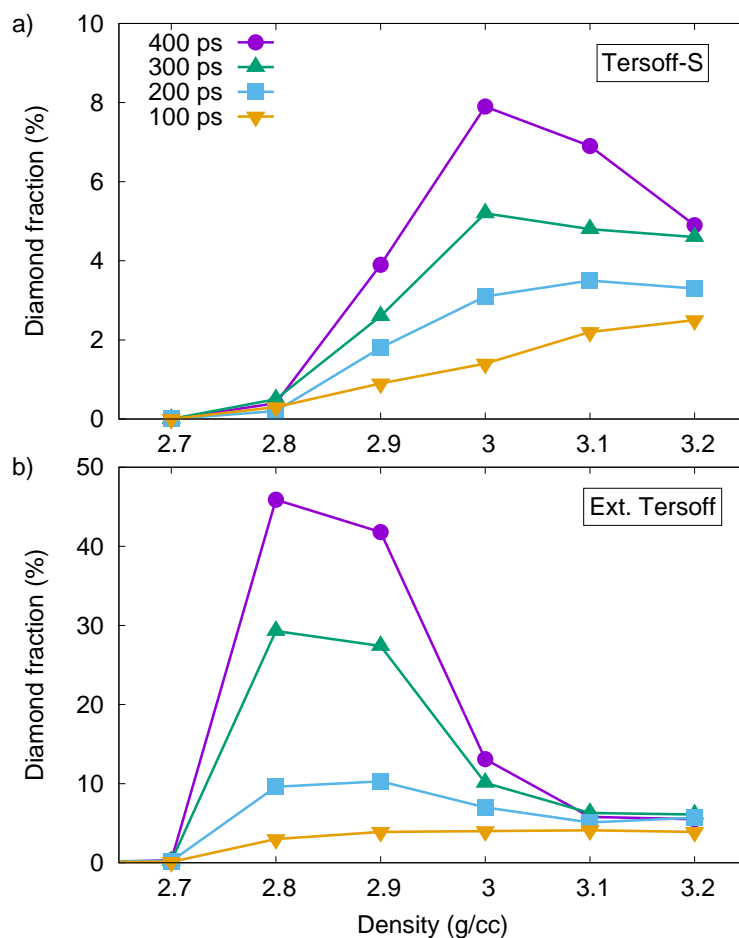


Figure 3.11: Time evolution of the fraction of atoms in a crystalline diamond environment as a function of density. Panels (a) and (b) correspond to Tersoff-S and extended Tersoff structures, respectively; data in panel (b) is from Chapter 2 and replotted.

are presumably an artifact of the machine learning approach. In our simulations, around 0.5% of the atoms are five-fold coordinated, forming four families of motifs

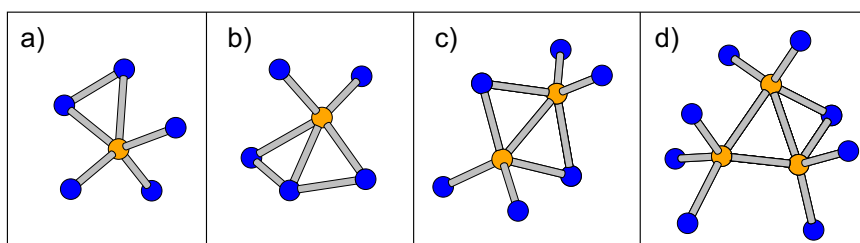


Figure 3.12: Four types of unphysical bonding motifs involving five-fold coordinated atoms (yellow circles) in the GAP structure at 3.0 g/cc. Panel (a) shows the most common motif, while the others are less frequent. Blue circles denote sp^3 atoms.

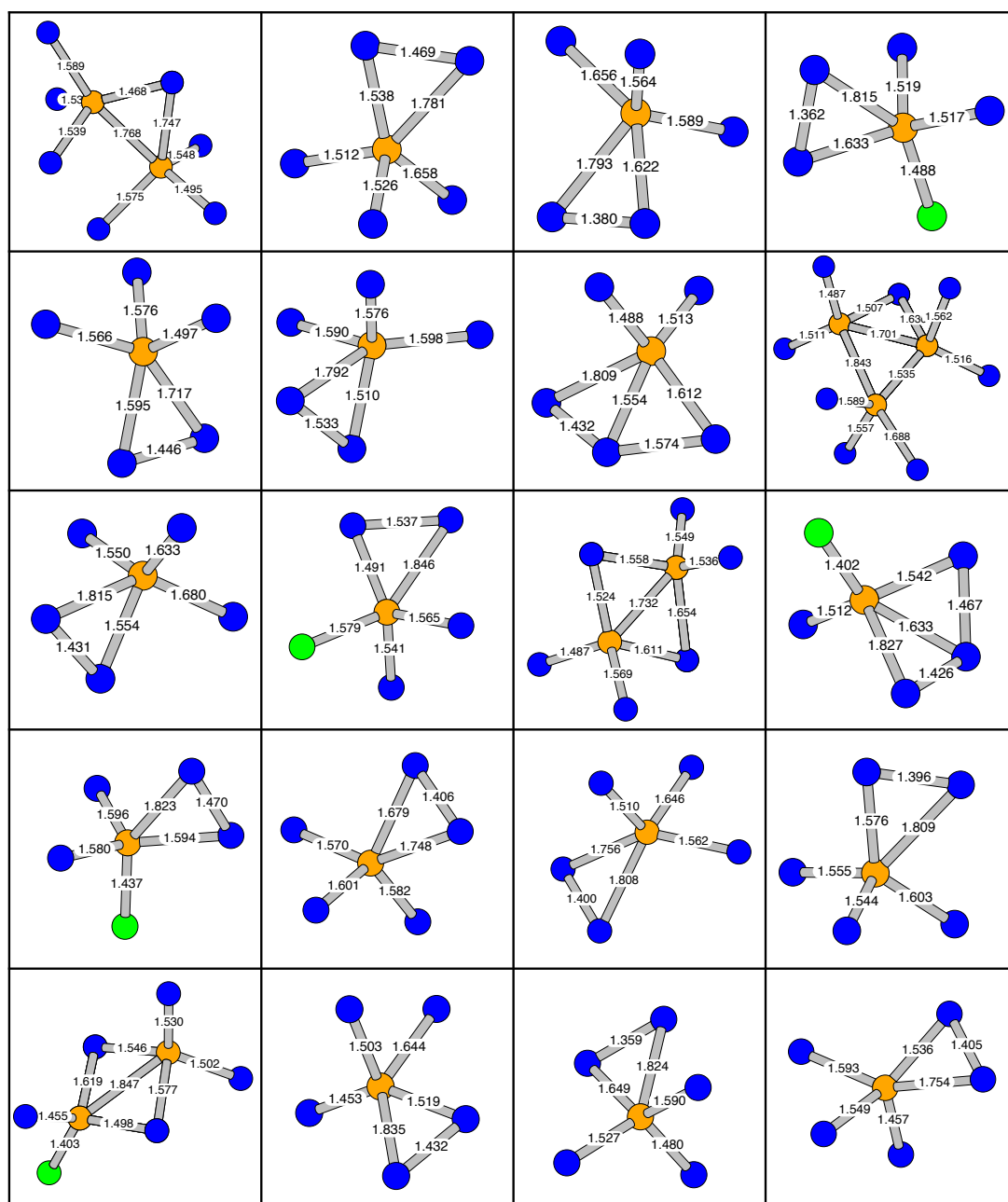


Figure 3.13: Local environment and bondlengths of all atoms with five-fold coordination in the 3.0 g/cc GAP structure. Green, blue and yellow circles indicate atoms with 3, 4 and 5 neighbors respectively. Number of neighbors determined using a 1.85 Å cutoff.

as shown in Figure 3.12; the structure in panel (a) is by far the most common. All of these motifs are chemically unlikely; for full details showing all configurations and bond lengths, see Figure 3.13. Several other potentials (Tersoff, REBO-II, extended Tersoff, Tersoff-S and AIREBO) had the occasional five-fold atom, but

the fraction was at least a factor of ten lower than those in the 3.0 g/cc GAP structure and typically far smaller.

The radial distribution functions (RDFs) for the eight potentials studied in this work are shown in Figure 3.14(a), with the vertical dotted lines indicating the bond length of graphite and diamond. Based on the cross-sectional slices and high sp^2 fractions, one might expect that the RDFs would all have their first peak close to the ideal graphite value of 1.42 Å. Surprisingly, most of the first neighbor peaks are intermediate between graphite and diamond, with the Tersoff family of potentials often closer to diamond. Only GAP potential (and possibly ABOP potential) predicts an RDF centred around the ideal graphite value. Large variations between the potentials can also be seen in the position and shape of the second and third neighbor peaks of Figure 3.14(a). Only ABOP potential has a pronounced third peak at a distance of 2.84 Å as expected for graphene. As shown in panel (d), EDIP potential also exhibited a clear third peak, while for REBO-II and ReaxFF potentials it is less pronounced.

At higher densities, the RDF of GAP potential is clearly distinct from the other potentials, as seen by the bimodal first neighbor peak in Figure 3.14(b). The two peak positions align with graphite and diamond, as expected based on visual examination of the cross-section in Figure 3.10(g). The extended Tersoff, Tersoff-S and REBO2-S potentials all have their first peaks aligned with the diamond bond length, consistent with the observation of diamond crystallites. The Erhart/Albe and mTersoff/Nordlund potentials, both of which are closely related to the original Tersoff potentials, have their first peak intermediate between graphite and diamond. In fact, for these three potentials the first peak position does not change with density. Of the eight potentials, only ABOP and AIREBO potentials have the first peak centered on graphite. However, while AIREBO structure is amorphous (Figure 3.10(e)), the ABOP structure shows stacked layers (Figure 3.10(c)) with sufficient order to produce a third peak in the RDF (Figure 3.14(b)). Layering and a third peak in the RDF was similarly

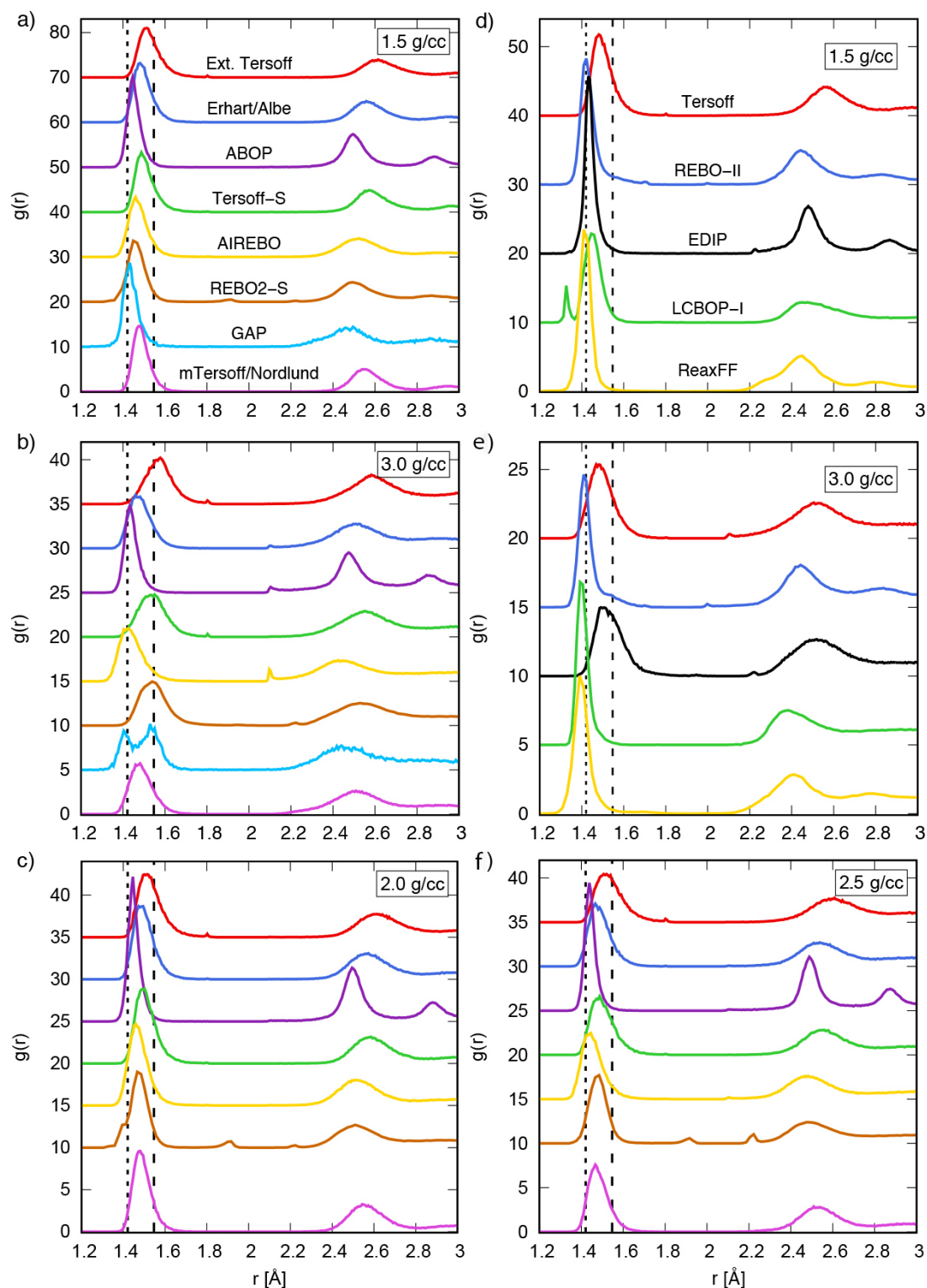


Figure 3.14: Radial distribution function of the annealed structures. Panels (a), (b), (c) and (f) are from this work, while panels (d) and (e) are from [de Tomas et al. \(2016\)](#). The vertical dotted lines indicate the bond length for graphite and diamond.

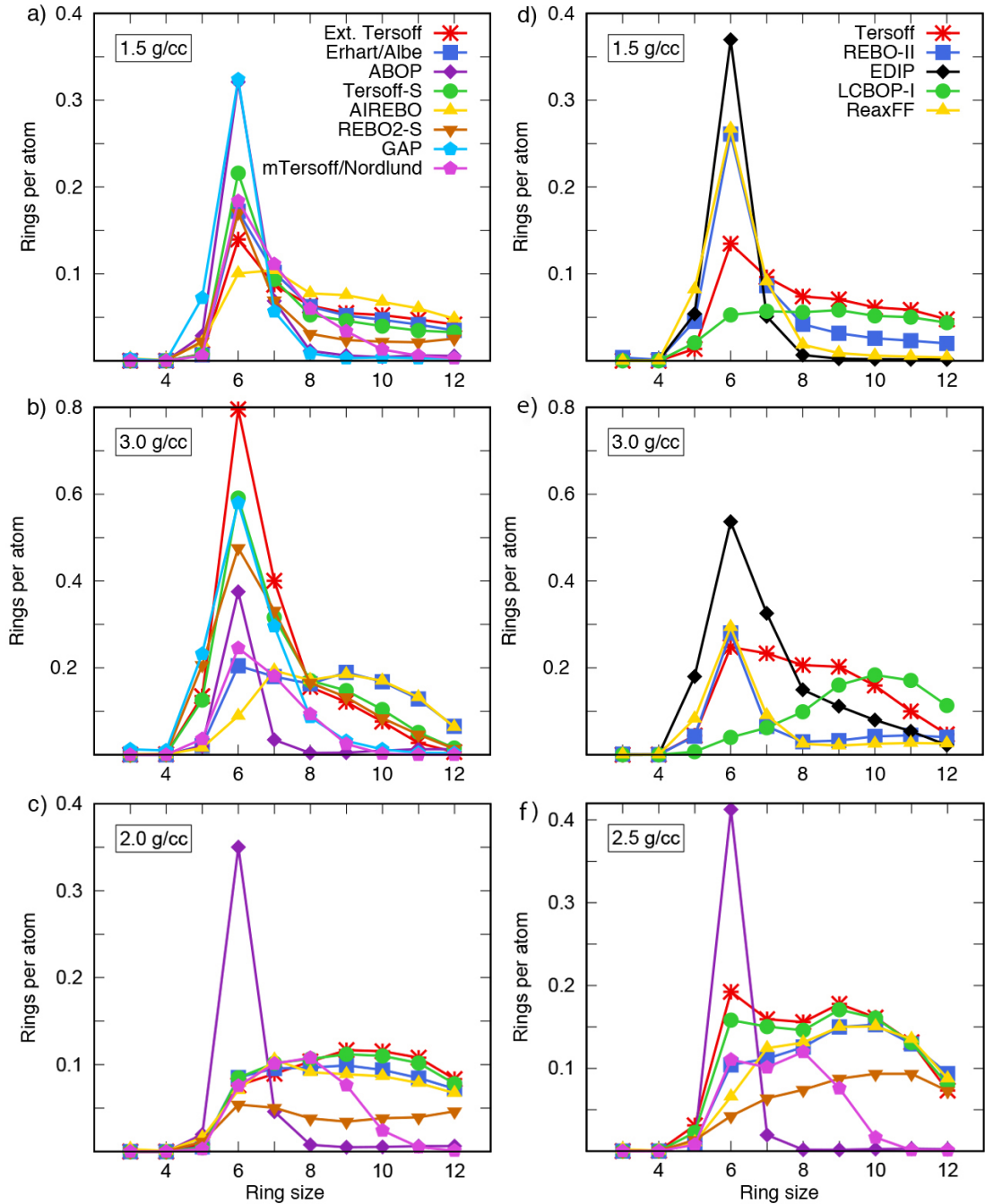


Figure 3.15: Ring statistics of the annealed structures. Panels (a), (b), (c) and (f) are from this work, while panels (d) and (e) are from [de Tomas et al. \(2016\)](#).

observed in [de Tomas et al. \(2016\)](#) for ReaxFF and REBO-II potentials (see Figure 3.14(e)). For comparison, data for the 2.0 and 2.5 g/cc structures from this study are also shown in panels (c) and (f), respectively.

To characterize the topology of the structures we compute ring statistics from triangles to dodecagons. Figure 3.15(a) shows data for the eight potentials at low density, with the number of rings normalized per atom. Consistent with the high sp^2 fraction, most of the potentials show a predominance of hexagons over other rings, with AIREBO structure being a notable exception, favouring heptagons over hexagons. While this result may look surprising, a preference for heptagons was also found by the AIREBO potential developers themselves in a study of amorphous carbon (Stuart et al., 2006). Their study also found the same relationship between sp^3 fraction and density as reported here. The greatest number of hexagons occur for GAP and ABOP structures, which overlap each other for much of the ring distribution; only the EDIP structure (Figure 3.15(d)) has more hexagons. For reference, note that a pure graphite structure contains 0.5 hexagons per atom, while a pure diamond structure contains 2 hexagons per atom.

It is instructive to consider a subset of structures in Figures 3.15(a) and (d) for which octagons and above are negligible. All of these structures, which include ABOP, GAP, ReaxFF and EDIP, contain a large fraction of hexagons and a smaller fraction of pentagons and heptagons. The pentagon/heptagon ratio confers local curvature to the structure, and can be correlated with the graphene fragments seen in Figure 3.9. The large graphene layers seen with GAP and EDIP structures are consistent with similar amounts of pentagons and heptagons, implying flat curvature, while the smaller fragments seen for ABOP and ReaxFF structures are consistent with negative curvature implied by an excess of heptagons over pentagons. The remaining structures show poor crystallinity reflected in a significant amount of larger polygons. The most extreme case is AIREBO structure with a comparatively flat ring distribution, resulting in an amorphous structure as seen in Figure 3.9(e). Similar behavior was observed in LCBOP-I structure, and to a lesser extent for Tersoff structure (see Figure 3.9(d)).

In the case of the high density structures in Figure 3.15(b), each of the eight

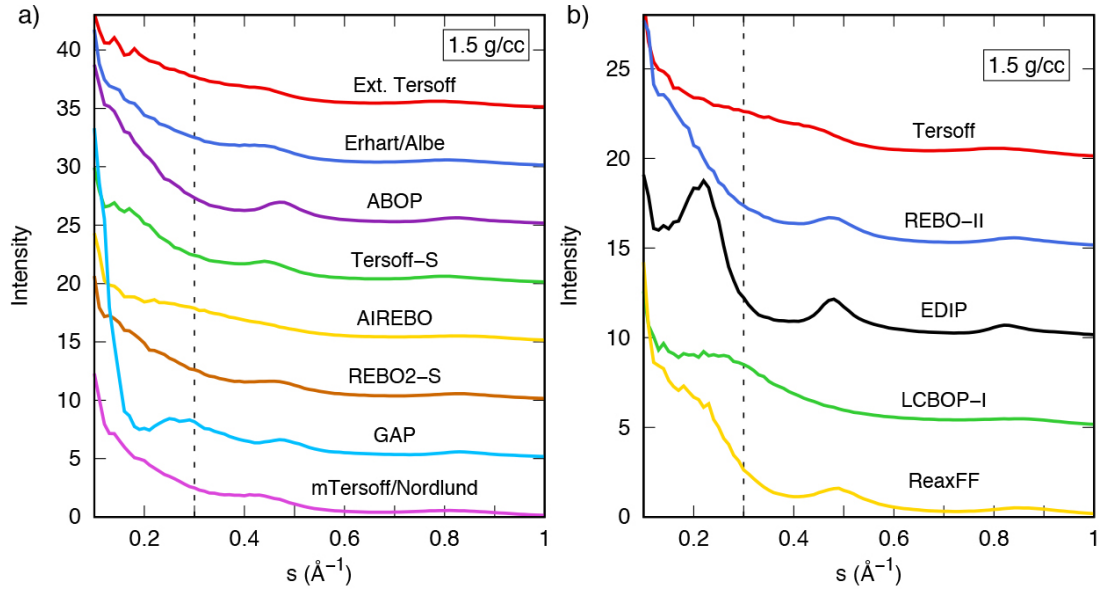


Figure 3.16: Diffraction intensity computed using the Debye scattering equation for the 1.5 g/cc annealed structures. Panel (a) is from this work and panel (b) is from [de Tomas et al. \(2016\)](#). The dashed line indicates the position of the 002 scattering peak corresponding to the graphite interlayer spacing of 3.35 Å.

potentials shows a different trend, with no two structures possessing the same ring distribution. Whereas earlier it was possible to group the potentials according to their microstructure or RDF, here each distribution is unique, emphasizing that the potentials do not generate equivalent structures. The greatest number of hexagons occurs for extended Tersoff due to the nucleation of the large diamond crystallites. The other two structures with diamond crystallites (Tersoff-S and REBO2-S) also have large number of hexagons, as does the GAP structure due to the presence of the *ta*-C phase. At the other extreme, the AIREBO structure contains only a small number of hexagons and the peak is shifted towards large rings, not dissimilar to LCBOP-I structure (Figure 3.15(e)). For comparison, data for the 2.0 and 2.5 g/cc structures from this study are also shown in panels (c) and (f), respectively. The story of complexity and variability between potentials extends to these intermediate densities, and is nicely summarized by panels (c) and (f) which shows that the topology of the annealed structures are strikingly different to the low and high densities discussed in the main text.

Figure 3.16 presents diffraction intensities for the 1.5 g/cc structures, with the vertical dotted line showing the position of the 002 peak indicative of graphitic ordering. None of the eight structures in panel (a) exhibit an 002 peak, with the exception of GAP potential which has a small shoulder at the expected position. A similar situation occurred in [de Tomas et al. \(2016\)](#) (see Figure 3.16(b)), with only EDIP potential producing a sharp 002 peak. Even then, the EDIP 002 peak is in the wrong location as the absence of van der Waals interactions means the spacing is too large, and hence the corresponding value of s is too small. At the slightly higher density of 2.0 g/cc, EDIP, ABOP and ReaxFF structures all exhibit layering, in agreement with recent ReaxFF simulations by [Li et al. \(2018\)](#) who used a similar methodology to ourselves to study graphitization. Generally speaking, the data in Figure 3.16 are in conflict with a well-known result for glassy carbon, namely that high-temperature annealing of a precursor at this density should produce stacked graphitic layers ([Harris, 2004](#)). The absence of this feature in most of the potentials is a clear demonstration that further development of carbon potentials is required.

3.4 Discussion

In this chapter we systematically analyze the performance of eight carbon potentials, extending upon [de Tomas et al. \(2016\)](#) study of six other potentials. Having reached a total of 14 potentials, most at four different densities, we have a substantial data set with which to evaluate transferability via amorphous carbon and annealing. Disturbingly, there are large differences between the various potentials, covering all aspects of the microstructure, topology and hybridization. Even though the potentials produce very similar results for graphite and diamond, the study of disordered phases reveals that each potential deals with the complexity of non-crystalline bonding in very different ways. This provides clear evidence that the challenge of developing an efficient and accurate carbon potential is yet to be solved.

A significant number of potentials (ABOP, REBO-II, ReaxFF, AIREBO, Tersoff, Erhart/Albe, mTersoff/Nordlund and LCBOP-I) favour sp^2 dominant structures, regardless of the density, a result which is almost certainly incorrect. At high density, the extended Tersoff, Tersoff-S and REBO2-S potentials predict high sp^3 fractions for both the amorphous and annealed structures, but the annealed carbons exhibit diamond crystallites which are unphysical. For the extended Tersoff potential, as discussed in Chapter 2, this behaviour can be directly linked to overlap of the cutoff function with the second neighbour coordination shell, while for the screened potentials (Tersoff-S and REBO2-S) the behaviour is likely connected to the screening function. The screening function is also presumably the reason for the extraordinarily high temperature of 16000 K required for the liquid equilibration in the REBO2-S 3.0 g/cc structure. As our previous work shows, the COMB3 potential is currently unsuitable for modelling disordered carbons due to a bias for triangles. EDIP potential provides good all-round performance at all densities, while ReaxFF potential also behaves well at densities below that of graphite. In principle, the machine learning approach of GAP potential offers the best way forward, but presently this potential is limited by the enormous computational cost, which is two to three orders of magnitude greater than the alternatives. The observation of five-fold coordination in the high-density GAP structures is also a cause for concern that requires further investigation.

To facilitate interactive analysis of the data set we have constructed an online tool, www.carbonpotentials.org,* which collates all of the data from our study. Even for the present work it is not possible to satisfactorily compare all data in a single plot, and this problem will only become worse as more potentials are developed. On the website the user can select one or more potentials to examine, and has access to all characterization data, plus 3D interactive visualization. Atomic coordinates are available for download, and tabs provide quick navigation between data sets at different densities. Our tool is live, and can be expanded

* Screenshots of the online application tool are provided in Appendix C.

over time, providing a modern approach in which all information related to carbon potentials is gathered into a single hub. We invite researchers developing future potentials to contribute data using the same computational methodology.

A secondary role of the website is to provide a point of collation for all carbon potentials known to us. [de Tomas et al. \(2016\)](#) identified 39 carbon potentials which they categorized into families according to their developmental lineage. The information was presented in a table which summarized the main characteristics of each potential, the ability to describe elements other than carbon and whether or not the potential was available in LAMMPS. An updated version of this table with 46 potentials is available on the website (see [Figure C.3](#)) and is also shown before in [Chapter 1](#) (see [Tables 1.1](#), [1.2](#) and [1.3](#)). We have intentionally excluded from this table potentials that are specific to graphene and its layered derivatives (bilayer graphene, graphite, etc). While this class of potentials (examples include ([Kolmogorov and Crespi, 2005](#); [Tewary and Yang, 2009](#); [Zalizniak and Zolotov, 2017](#); [Rowe et al., 2018](#); [Wen et al., 2018](#))) can provide excellent performance for graphene-type systems, they are not transferable to a general system of carbon atoms. These graphene-oriented potentials assume a fixed hybridization, planar geometry and typically use a pre-assigned atomic index to distinguish between inter-layer and intra-layer interactions.

The merits of performing systematic comparison of carbon potentials have also been demonstrated by a number of recent studies by other authors, all of which have used LAMMPS. These works have considered elastic constants of graphene, diamond and nanotubes ([Gayk et al., 2018](#); [Lebedeva et al., 2019](#)), liquid carbon ([Dozhnikov et al., 2017](#)), fracture mechanics ([Tangarife et al., 2019](#)) and amorphous carbon thin-film deposition ([Li et al., 2018](#)). Broadly speaking, these five studies observe similar trends to those seen in this work, reporting large variations between potentials and in the case of the fracture study, unphysical behavior related to the switching function.

3.5 Conclusion

To summarize, we have demonstrated a lack of transferability in carbon potentials and the need for thorough testing before selecting a potential to describe a particular carbon system. This is an important message not only for modellers, but for the whole carbon community, as awareness of the limitations of a potential is crucial for the proper interpretation of simulations. Our results also provide impetus for developing better and more efficient potentials that can accurately describe carbon in a wide variety of situations. While machine learning frameworks such as GAP potential offer a promising way forward, these potentials are presently extremely costly. For large systems and long simulation times, EDIP and ReaxFF remain the best potentials, with ReaxFF potential having the advantage that the parameters are available for hydrogen and oxygen. However, to use a colloquial expression, the devil is in the details, and it remains the responsibility of each researcher to ensure that their use of a potential is consistent with its design. To this end, we anticipate that our www.carbonpotentials.org tool will aid in this task and provide a forum for further development of potentials.

Chapter 4

Modification of nanodiamonds by xenon implantation

The main text and figures comprising this chapter have been published in *Nuclear Instruments and Methods in Physics Research Section B 453*, (2019) 32–40. This chapter is motivated by experiments of ion-implantation into nanodiamonds (NDs) at the University of Huddersfield, UK, as discussed in Section 1.1.1. Here, we provide molecular dynamics simulations for the irradiation process to understand experimental results. The NDs vary in size from 2 to 10 nm, and xenon energies of 50 eV up to 40 keV are considered. For small NDs an energy-window effect occurs in which xenon energies of around 6 keV destroy the ND, while in larger NDs the radiation cascade is increasingly similar to those in bulk material. Destruction of the small NDs occurs due to thermal annealing associated with the small size of the particles and the absence of a heat-loss path. Simulations are also performed for a range of impact parameters, and for a series of double-nanodiamond systems in which a heat-loss path is present. The latter shows that the thermal shock caused by the impact occurs on the timescale of a few picoseconds. These findings are relevant to ion-beam modification of nanoparticles by noble gases as well as the meteoritic studies discussed in Chapter 5.

4.1 Introduction

Nanodiamonds (NDs) are found in primitive chondritic meteorites at concentrations as high as 1500 ppm (Ott, 1993; Huss, 2005). Within these NDs are trace amounts of xenon and other noble gases whose unusual isotopic abundances indicate a pre-solar origin and provide information on nucleosynthesis processes in supernovae. Ion-implantation is the most popular explanation for the presence of the noble gases in NDs (Lewis et al., 1987; Anders and Zinner, 1993; Daulton et al., 1996; Verchovsky et al., 1998), although another possibility is that the noble gases were incorporated during growth of the ND. The implantation hypothesis was studied experimentally by Verchovsky et al. (2000) and Koscheev et al. (2001) using low-energy implantation into detonation nanodiamonds, which are similar in size to meteoritic NDs. Even though their studies employed only a single implantation energy and used isotopes of natural abundance, many of the characteristics observed in the meteoritic data were observed.

Recently, Shiryaev et al. (2018) performed a combined experimental and computational study of xenon implantation into NDs of varying size. Implantation experiments were performed *in situ* in a transmission electron microscope (TEM), enabling real-time monitoring of irradiation effects. While large NDs (40 nm diameter) were resistant to the ion beam, the small NDs (2–3 nm) were gradually destroyed under 6 keV irradiation. Stopping and Range of Ions in Matter (SRIM) calculations do not predict this effect, while molecular dynamics (MD) simulations explained these observations via a temperature effect, which anneals the smaller-sized NDs. The success of the MD approach is that it goes beyond the binary-collision approximation used by SRIM, and captures all the thermal motion associated with the collision cascade.

In this chapter our MD studies of xenon implantation into ND are performed in two main ways: (i) low implantation energies are considered to study the hypothesis explored by Verchovsky et al. (2000) and Koscheev et al. (2001), and (ii) a second ND particle is introduced to capture thermal conduction effects

relevant to the *in situ* experiments by [Shiryaev et al. \(2018\)](#) at the University of Huddersfield, UK (see Section 1.1.1). We also examine the effect of varying the impact parameter and include a comprehensive description of the simulation approach, including the description of the xenon–carbon interactions and the methodology for generating the ND coordinates. The latter is a useful starting point for further investigations of noble gases within NDs as studied in Chapter 5.

4.2 Methodology

Atomic interactions between carbon atoms were described using the environment dependent interaction potential (EDIP) for carbon, coupled with the Ziegler-Biersack-Littmark (ZBL) potential ([Ziegler et al., 1985](#)) to describe close-range pair interactions between carbon atoms. Further details of the interpolation process used to switch between the EDIP and ZBL forms are provided earlier in Section 1.2.4. In the comparison study of carbon interatomic potential in Chapter 3, we found that EDIP potential has excellent transferability across a wide range of conditions, and is superior to many common carbon potentials. One aspect of EDIP potential which is still being developed is the ability to describe hydrogen, and hence all NDs in the simulations are dehydrogenated.

For the xenon–carbon (Xe–C) interactions, we used the standard ZBL potential coupled with a Lennard-Jones (LJ) potential of the form

$$U_{\text{LJ}}(r) = 4\varepsilon \left\{ \left(\frac{\sigma}{r} \right)^{12} - \left(\frac{\sigma}{r} \right)^6 \right\}, \quad (4.1)$$

with parameters $\varepsilon_{\text{Xe-C}} = 0.0114$ eV and $\sigma_{\text{Xe-C}} = 3.332$ Å as given in [Simonyan et al. \(2001\)](#). For simplicity, we did not employ the anisotropic terms as implemented in [Simonyan et al. \(2001\)](#). Interpolation between the LJ form and the ZBL interaction was described in the same manner as [Christie et al. \(2015\)](#) and [Buchan et al. \(2015\)](#), using Fermi-type switching functions. The parameters were empirically determined to provide a smooth transition from the strong re-

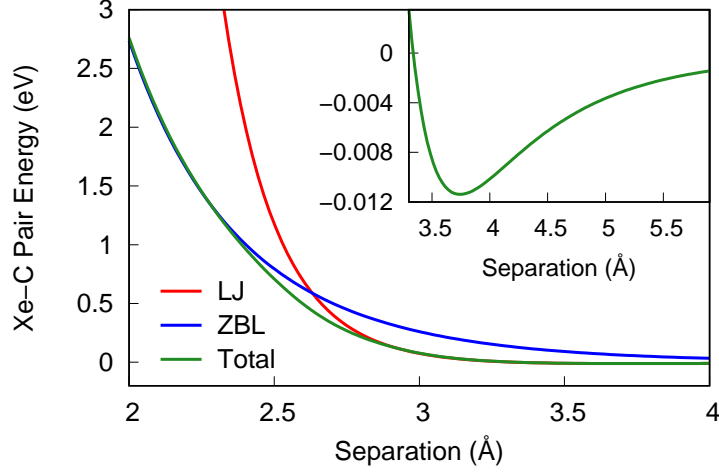


Figure 4.1: Interaction energy between the xenon and carbon atoms (green line). At close approach the interaction is pure ZBL (blue line), while at distances around equilibrium and greater a Lennard-Jones (LJ) expression is used (red line). Interpolation at intermediate distances is performed using a Fermi-like switching function as described in the text.

pulsive region of the ZBL to the weakly attractive region of the LJ potential. The resulting functional form of the energy for xenon–carbon interactions is

$$U_{\text{Total}}(r) = \left[U_{\text{ZBL}}(r) \times f(r + \delta) \right] + \left[U_{\text{LJ}}(r) \times (1 - f(r - \delta)) \right], \quad (4.2)$$

where $f(r)$ is a Fermi-type switching function, $\delta_{\text{Xe-C}} = 0.07 \text{ \AA}$. The Fermi function is given by

$$f(r) = \left[1 + \exp(b_F(r - r_F)) \right]^{-1} \quad (4.3)$$

where b_F controls the sharpness of the transition and r_F is the cutoff distance; these parameters are chosen manually to ensure smoothness. For xenon–carbon we use $b_F = 8 \text{ \AA}$ and $r_F = 2.7 \text{ \AA}$, the same as the recent implantation study by [Shiryaev et al. \(2018\)](#). A plot of the xenon–carbon interaction energy covering the ZBL and LJ regimes is shown in Figure 4.1, with the attractive region shown in the inset.

The simulations are performed using an in-house MD package developed by Nigel Marks (my principal supervisor). All calculations are performed in an NVE

ensemble (constant number of particles, volume and energy), using Verlet integration and a variable timestep. The algorithm for the timestep automatically adjusts the timestep using the metric $\|\mathbf{F}_{\max}\|\Delta t$ as described in [Marks and Robinson \(2015\)](#). During close approaches the timestep was reduced to values as small as 10^{-5} fs, and was subsequently increased as kinetic energy was dispersed and the system equilibrated. Periodic boundary conditions are not employed. Prior to ballistic implantation, all ND coordinates are relaxed by steepest descent and equilibrated at 300 K. The majority of the simulations are 1 ps in length, which is sufficient to model the ballistic phase of the Xe implantation onto the ND ([Shiryayev et al., 2018](#)), which involves the transferring of kinetic energy from the xenon to the carbons. A smaller number of longer simulations extending up to 85 ps are performed to study annealing effects and thermal transport. Temperatures are determined using the kinetic energy of the main carbon cluster; the xenon atom and any ejected carbon atoms are excluded from the calculation and the net momentum of the cluster is subtracted prior to computing the temperature.

Construction of the nanodiamond coordinates is a non-trivial problem. The question of stable nanodiamond morphologies has been extensively studied by [Barnard and Zapol \(2004\)](#) and some sets of Cartesian coordinates are available online ([Barnard, 2014b](#)). For dehydrogenated NDs, as discussed earlier in [Chapter 1](#), they showed that the relevant stable geometry is the truncated octahedron, formed by cleaving a carbon nanoparticle out of diamond such that it has only $\{100\}$ and $\{111\}$ faces (see [Figure 1.7](#)). One important detail of dehydrogenated NDs is that the $\{100\}$ surfaces need to be reconstructed in a 2×1 arrangement to eliminate dangling bonds (two-fold coordinated atoms) on the $\{100\}$ surface. The key idea is to cut the ND out of an infinite crystal using clipping planes in the $\langle 100 \rangle$ and $\langle 111 \rangle$ directions to obtain the truncated octahedron structure. All of these aspects are implemented in a Fortran program written by Nigel Marks (my principal supervisor). The program generates a ND of arbitrary size, with all

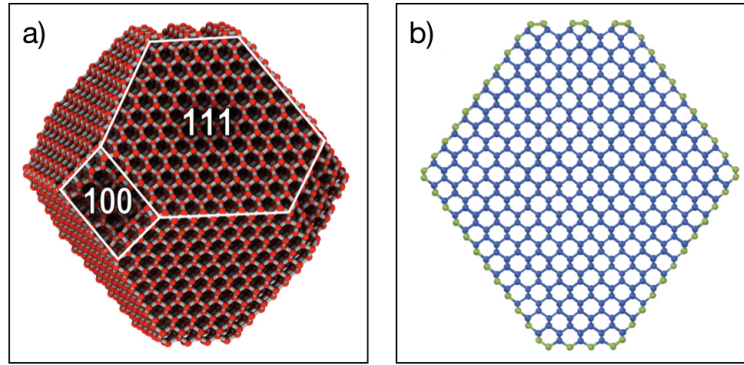


Figure 4.2: Two views of the 3.9 nm diameter ND. (a) Perspective view showing the truncated octahedral geometry. Carbon atoms are shown in red and the white lines highlight the $\{100\}$ and $\{111\}$ faces. (b) Cross-sectional view (1 nm slice) using colour coding to indicate the hybridization: sp^2 and sp^3 atoms are shown as green and blue circles, respectively.

atoms at the surface being sp^2 bonded (the $\{100\}$ surface due to the reconstruction, and the $\{111\}$ surface by design). Figure 4.2 represents the perspective and cross-sectional views of an example of ND. Table 4.1 lists all of the NDs studied in this chapter; the parameters $d_{\{100\}}$ and $d_{\{111\}}$ are the distances from the origin to the $\{100\}$ and $\{111\}$ planes, respectively. The radius was measured by com-

Table 4.1: Parameters (number of atoms and distances), diameter and sp^3 fraction for the twelve NDs studied in this chapter.

Diameter (nm)	N_{atoms}	$d_{\{111\}}$ (Å)	$d_{\{100\}}$ (Å)	sp^3 (%)
2.1	837	9	10	69.9
2.6	1639	12	14	74.9
3.1	2793	14	17	78.4
3.6	4363	15	21	81.0
4.0	5975	18	21	83.7
4.6	8389	20	24	85.4
5.1	11591	22	27	86.6
6.0	18977	26	31	88.8
7.1	29359	30.5	35.5	90.4
8.0	46393	35	46	91.3
9.0	61849	39	46	92.4
10.2	90395	44	49	93.5

puting the average distance between sp^2 bonded atoms and the centre-of-mass of the ND. The NDs studied in this chapter span the typical range observed for meteoritic ND (range of 1–10 nm, with average diameter of around 3 nm; (Dai et al., 2002; Huss, 2005)) and detonation ND (average of 4–5 nm). Our largest ND of 10 nm is of sufficient size to exhibit bulk-like behavior, and hence we did not simulate the 40 nm diamonds studied in Shiryaev et al. (2018).

The energy of the implanting xenon is varied between 2 and 40 keV, with most simulations perform using 6 keV to provide a comparison to Shiryaev et al. (2018) experimental results. The initial position is always a few ångströms (e.g., 5 Å) beyond the edge of the ND and for most simulations the initial velocity vector was towards the centre of the ND. In a small number of simulations the initial position of xenon is displaced perpendicular to the initial velocity vector to study the effect of varying the impact parameter (see Figure 4.3(a)). To collect robust statistics across the various crystallographic orientations, the xenon atom is introduced at 25 different locations distributed uniformly (Thomson points) around the ND. Further details are discussed earlier in Section 1.2.5. A schematic

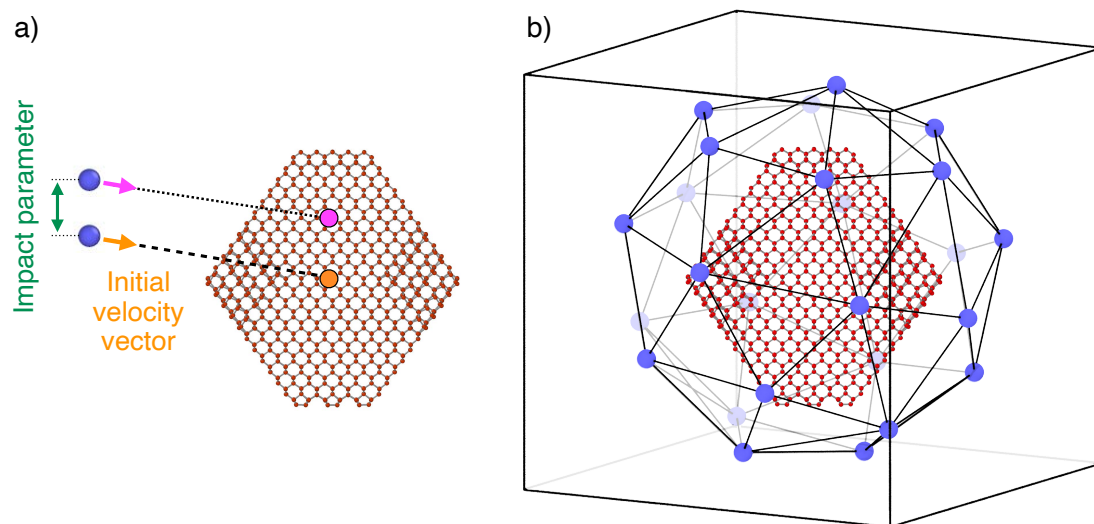


Figure 4.3: (a) Schematic showing the initial velocity vector of the xenon towards the centre of the ND and the impact parameter. The ND atoms are shown in red, and in this example a 4.0 nm diameter ND is shown. (b) The typical geometric relationship between a ND and the initial xenon locations. The initial xenon locations (shown in blue) are solutions to the 25-point Thomson problem (see Section 1.2.5).

indicating a ND and the various xenon positions is shown in Figure 4.3(b) and [Movie 4.1](#); note that the location of the xenon atoms has been expanded outwards for clarity. Also, the Cartesian coordinates of the xenon atoms are listed in Table 1.4. Note that during simulations statistical data is recorded, in particular the sp^3 and sp^2 fractions taken as a percentage of the unit sphere. This leads to the ability to track ND deformation during implantation simulations which is represented graphically. Throughout implantation simulations other statistical data is tracked such as temperature, atoms ejected and energy ejected as to gain information about the damage caused during ND irradiation by xenon.

4.3 Results and discussion

The implantation of a xenon atom into the ND is a highly energetic event, leading to substantial disruption in certain cases. Figures 4.4 and 4.5 show representative implantations for varying impact energies incident onto a 3.1 nm diameter ND. In each case the initial position and velocity vector is the same; Figure 4.4 plots the time-variation of the cluster temperature and sp^3 fraction, while Figure 4.5 shows a series of snapshots. Note that the cluster temperature refers only to carbon atoms retained within the cluster, with the xenon and any ejected carbon atoms excluded from the calculation. Video animation sequences of all three impacts are shown in [Movie 4.2](#), [Movie 4.3](#) and [Movie 4.4](#).

At 2 keV the xenon atom deposits almost all of its kinetic energy into the ND. As shown in the top panel of Figure 4.5, the xenon takes 0.2 ps to travel through the ND, ejecting a small number of carbon atoms (six) in the process. For the case shown, the xenon exits the ND with just 24 eV of energy, while for other impact directions the xenon end-of-range sometimes falls within the ND. The transfer of kinetic energy into the ND rapidly increases the temperature of the ND, as shown in Figure 4.4(a); after a very short period (less than 0.1 ps) the temperature reaches equilibrium at a value slightly above 2000 K. This temperature is sufficient to slightly reduce the number of sp^3 bonds (see

Figure 4.4(b)) in the ND, principally at the $\{111\}$ edges on the right-hand side of the ND where a small amount of graphitization occurs. Figure 4.4(b) also shows that for the 2 keV impact the sp^3 fraction undergoes oscillations which gradually die away; these reflect a “ringing” of the structure in which sound waves reflect back-and-forth across the ND.

The bottom panel of Figure 4.5 shows that implantation of a 40 keV xenon has a similar effect on the ND as seen at 2 keV. The chief difference is that the xenon passes through the ND extremely quickly, taking around 0.02 ps as seen in the figure. The xenon exits the ND with a very high kinetic energy (23.2 keV), and also ejects a significant number of carbons (23 atoms). The

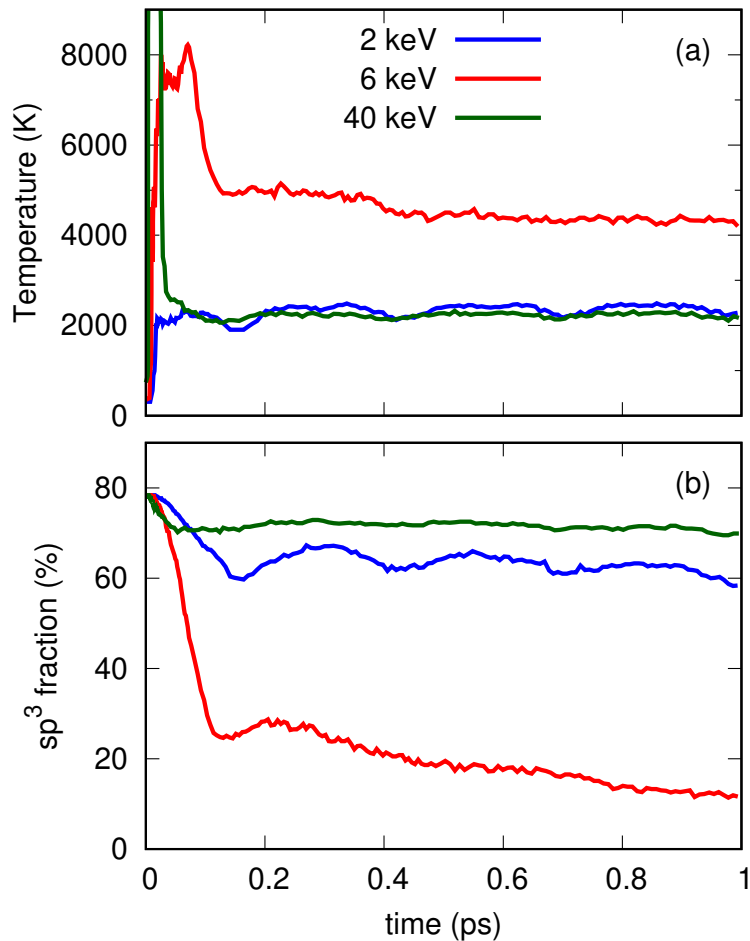


Figure 4.4: Time evolution of (a) the cluster temperature and (b) sp^3 fraction for the three xenon implantation events shown in Figure 4.5.

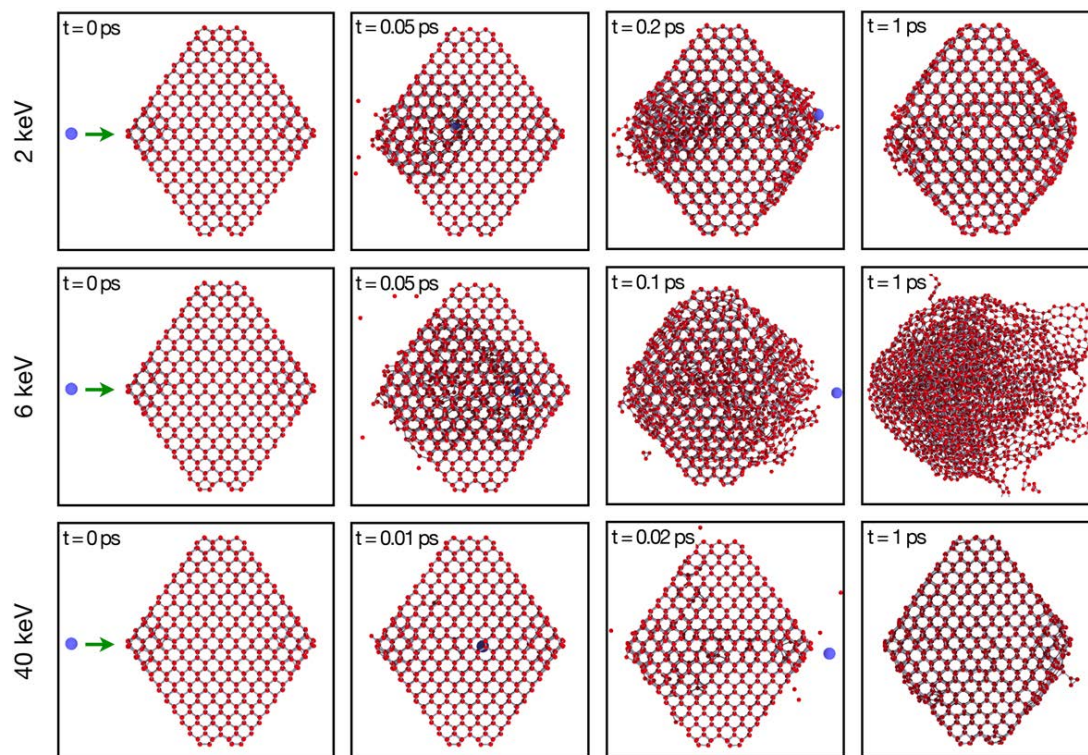


Figure 4.5: Time evolution of three typical implantation events into a 3.1 nm diameter ND for impact energies of 2, 6 and 40 keV. In each case the xenon exits the ND. Only at 6 keV is there any significant destruction of the ND. Carbon atoms and the xenon are shown as red and blue circles, respectively.

combined kinetic energy of the ejected carbons is 15.0 keV, meaning that only 1.8 keV of the original impact energy is deposited into the ND. This results in an equilibrium ND temperature of around 2000 K as shown in Figure 4.4(a). Since the temperature is slightly less than for the 2 keV case, the annealing effect which reduces the sp^3 fraction is also less significant, as can be seen in Figure 4.4(b).

The behaviour at 6 keV is completely different to the higher and lower energy cases. Here, a much larger amount of kinetic energy is transferred to the ND. As shown in the sequence in the middle row of Figure 4.5, the xenon exits the ND after 0.1 ps, but even at this stage there is already a significant amount of structural damage to the ND. The final kinetic energy of the xenon is 0.4 keV, while a total of 67 carbon atoms are ejected, with a combined kinetic energy of nearly 1 keV. In total, around 4.7 keV of kinetic energy is transferred to the

ND, increasing the instantaneous temperature to well above the melting point as shown in Figure 4.4(a). Note that the melting point of the bulk diamond is circa 4300–4500 K for EDIP, similar to experimental studies which find a value around 4500–5000 K with higher values more likely; see [Savvatimskiy \(2015\)](#) for a rigorous discussion of the complexities of molten carbon. Even once the system has equilibrated, the temperature is extremely high, at just over 4000 K. At such a high temperature there is substantial conversion of sp^3 into sp^2 bonding in combination with some evaporation of atoms. As seen in Figure 4.4(b), the sp^3 fraction is greatly reduced, and after 1 ps the majority of the tetrahedral bonding is lost. Due to the high temperature, running the 6 keV simulation beyond the 1 ps point drives further structural rearrangement. Figure 4.6 shows

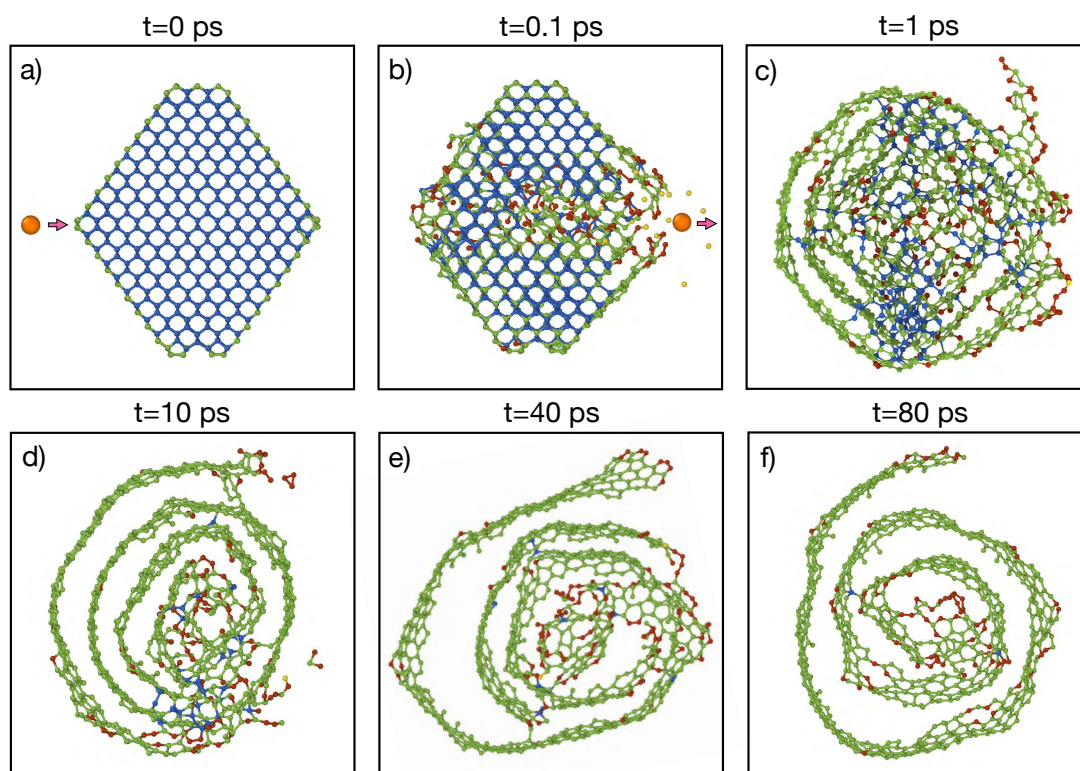


Figure 4.6: Cross-sectional snapshots (1 nm slices) for the time evolution of a 3.1 nm ND impacted by a 6 keV xenon ion. Note that this is the same impact as shown in Figure 4.5, the difference being that the simulation continues up to 80 ps to show the effect of long-time annealing. Red, green and blue circles denote sp , sp^2 and sp^3 hybridization, respectively. Yellow atoms have just one neighbor and xenon is presented as a large orange circle.

snapshots of the system up to a time of 80 ps, using colour coding to indicate the hybridization. Note that the images in Figure 4.6 are cross-sectional slices, whereas those in Figure 4.5 show all atoms. After some tens of picoseconds, the ND has graphitized into a carbon onion structure, with spirals evident in cross-section. In the context of the implantation experiments, however, it is by no means apparent that such long annealing of an isolated ND is appropriate. We will return to this point later on by considering heat-loss paths which limit the amount of time the system spends at high temperature.

Ion implantation processes are sensitive to the impact parameter of the primary collision and crystallographic orientation, and hence it is necessary to average over many different directions to collect accurate statistics. In the case of the 6 keV impact, for example, we found that for our 25 initial directions the final temperature of the ND varied from a low of 2520 K to a high of 4160 K. Similar variability was observed in other quantities we extracted from the data. The merits of averaging are seen in Figure 4.7 which shows the variation in the temperature, sp^3 fraction and number of carbon atoms ejected as a function of xenon energy. The error bars indicate the standard deviation, and even though the spread is substantial, the lines linking the mean values themselves are quite smooth, particularly for the temperature and sp^3 fraction. When the xenon energy is around 6 keV damage to the ND is maximal, with the sp^3 fraction (see Figure 4.7(b)) reduced to well under half its initial value and around 50 carbon atoms being ejected (see Figure 4.7(c)). For higher xenon energies the nuclear stopping efficiency decreases significantly, leading to a lower residual temperature and much less damage (as measured by the sp^3 fraction and number of atoms ejected). At the highest energy considered, 40 keV, the effect of the xenon is very similar to that at 2 keV, consistent with the single impact sequences shown in Figure 4.5.

The energy dependence of all three quantities in Figure 4.7 are closely correlated, highlighting that the heating of the ND is the critical quantity that drives

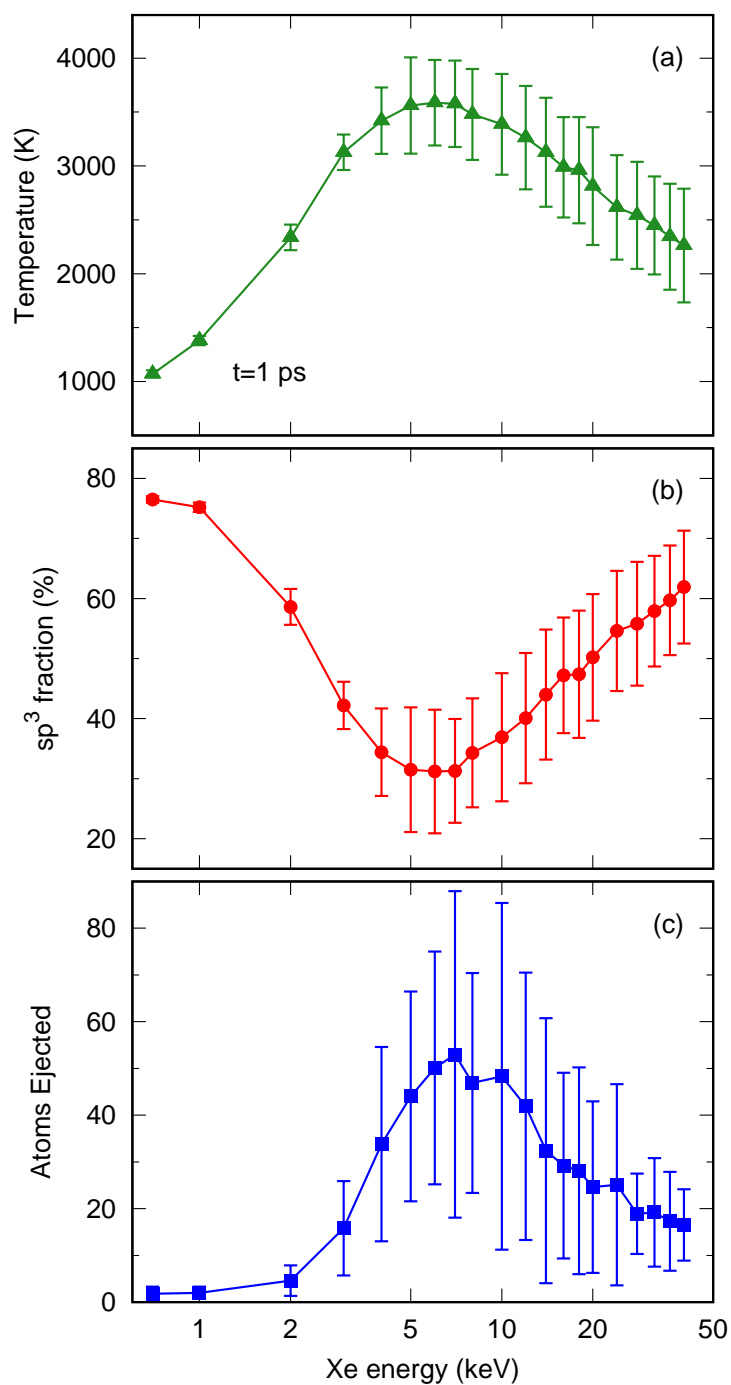


Figure 4.7: Effect of impact energy for xenon implantation into a 3.1 nm diameter ND. All properties computed 1 ps after initiation of the event. (a) Cluster temperature, (b) sp^3 fraction and (c) number of carbon atoms ejected.

the damage process. When the ND temperature is 1000 K or so the sp^3 bonds are able to withstand the implantation due to the high melting point of diamond.

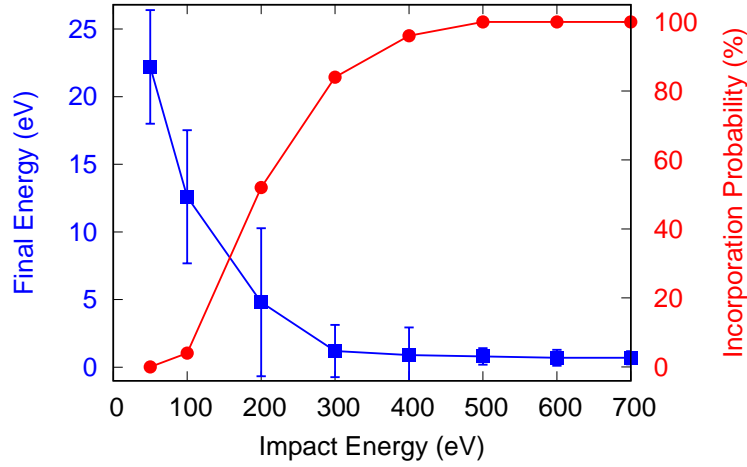


Figure 4.8: Final kinetic energy of the xenon atom (left-axis, blue squares), and implantation probability (right-axis, red circles) for 25 low-energy implantations onto a 3.1 nm ND. Error bars indicate one standard deviation.

However, when the temperature approaches several thousand degrees, sp^3 bonded atoms change to sp^2 and the ND begins to convert to a nested fullerene structure, or carbon onion, as shown in Figure 4.10(a). The large number of sp^2 bonded atoms is seen in the large number of green atoms, consistent with the sp^3 fraction of $\sim 30\%$ at 6 keV as seen in Figure 4.7.

It is instructive to examine more closely the low-energy regime in Figure 4.7, since this is relevant to the ion-implantation experiments (Verchovsky et al., 2000; Koscheev et al., 2001) performed to interpret xenon release from meteoritic NDs. Figure 4.8 shows that for very low xenon energies (i.e., 50 eV) the xenon does not incorporate into the ND, and is reflected with around half its initial kinetic energy. For an incident energy of 200 eV there is a $\sim 50\%$ probability that the xenon will be incorporated, increasing to 100% at around 500 eV. For context, as discussed in Section 1.1.1, the experiments by Koscheev et al. (2001) used an implantation energy of ~ 700 eV while those of Verchovsky et al. (2000) used ~ 1000 eV and hence their experiments fall in a regime where the xenon is always implanted at least several atomic layers into the ND, but not with sufficient energy to pass through the ND. As a secondary observation, the modest energies used in their experiments implies only a small amount of heating as seen in Figure 4.7; as a

result there will be no annealing effect such as occurs for implantations in the vicinity of 6 keV. To clarify, these comments on the experimental implantation studies apply only to a single impact, while the experiments used doses of order 10^{15} ions/cm², corresponding to tens of ions per square-nanometre. At these doses, individual NDs may be struck multiple times, leading to accumulated damage beyond that considered in the present simulations.

As described in the Methodology, for a 6 keV impact energy the effect of the impact parameter was determined by displacing the ND perpendicular to the direction of the initial velocity vector. The displacement was varied from 1 to 13 Å, and for each displacement 25 different initial directions were considered. Figure 4.9 shows the effect of the impact parameter on the cluster temperature and sp^3 fraction after 1 ps has elapsed. The number of carbon atoms ejected is shown in panel (c). The result was as intuitively expected; namely that the greatest damage to the ND occurs for the direct collision and a higher impact parameters progressively transfers less energy to the ND and fewer sp^3 -bonded atoms are lost, tending to zero effect when the xenon grazes the edge of the ND. Interestingly, the number of ejected atoms is quite insensitive to the impact parameter, showing an approximately constant value between 0 and 10 Å.

All of the data discussed to this point has been for a 3.1 nm diameter ND. To study the effect of varying the ND size, a series of calculations were performed using a 6 keV xenon and NDs ranging from 2.1 to 10.2 nm. Cross-sectional snapshots in Figure 4.10 demonstrate that the size of the ND strongly influences the nature of the damage created by the xenon impact. For larger diameters, such as the 5 and 6 nm NDs seen in panels (c) and (d), there is minimal disruption to the ND itself, and damage is concentrated along the trajectory of the Xe. In the case of the 6 nm ND, the residual damage consists of isolated point defects, much the same as for cascades in bulk diamond; see simulations by [Buchan et al. \(2015\)](#). For the 4 nm ND the damage caused by the xenon is much more substantial, with a wide damage track and graphitization on several {111} faces, while at 3 nm the

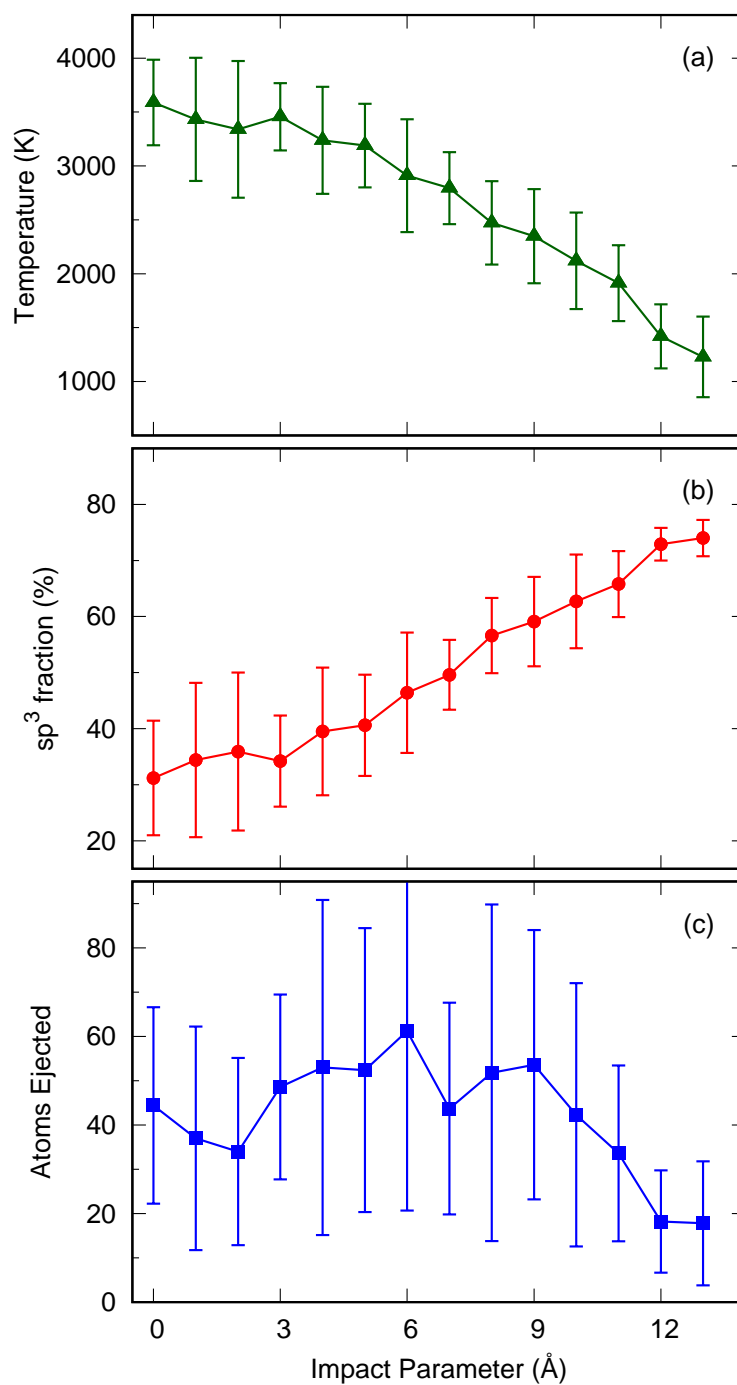


Figure 4.9: Effect of impact parameter on (a) temperature, (b) sp^3 fraction and (c) number of atoms ejected for 6 keV xenon impacts onto a 3.1 nm ND. Error bars indicate one standard deviation.

ND is largely transformed into a carbon onion.

The size-dependence effect seen in Figure 4.10 is explained by Figure 4.11

which quantifies the temperature, sp^3 fraction and kinetic energy absorbed by the ND. Panel (a) shows that the cluster temperature falls off rapidly as the size of the ND increases; at 3 nm the average temperature after 1 ps is above 3500 K, drawing near to the melting point of diamond. This high temperature explains the spherical graphitization behavior seen in Figure 4.10(a). For a 4 nm ND, the temperature is around 700 K lower, reducing the extent of spherical graphitization but still sufficient to cause some structural rearrangement as seen in Figure 4.10(b). For the 5 and 6 nm NDs the average temperature at 1 ps is circa 1900 and 1300 K, respectively, far below the diamond melting point, explaining why the damage tracks resemble those of bulk diamond.

Figure 4.11(b) quantifies the amount of kinetic energy which the xenon deposits into the ND. This quantity is determined by summing the kinetic energy

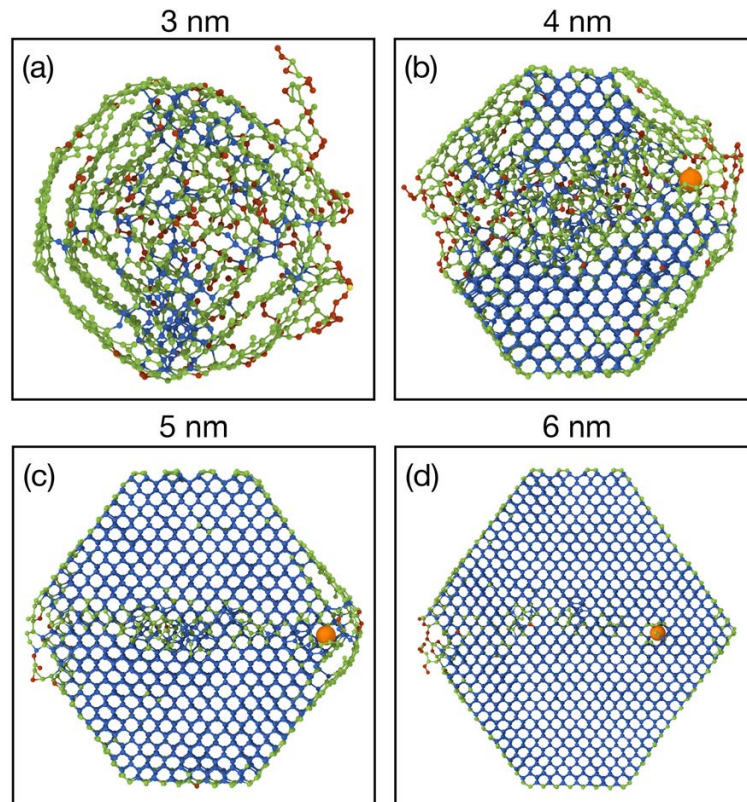


Figure 4.10: Cross-sectional snapshots (1 nm slices) showing how the size of the ND influences damage following implantation of a 6 keV xenon from the left of frame. All snapshots are 1 ps after impact. Colour codings are the same as Figure 4.6.

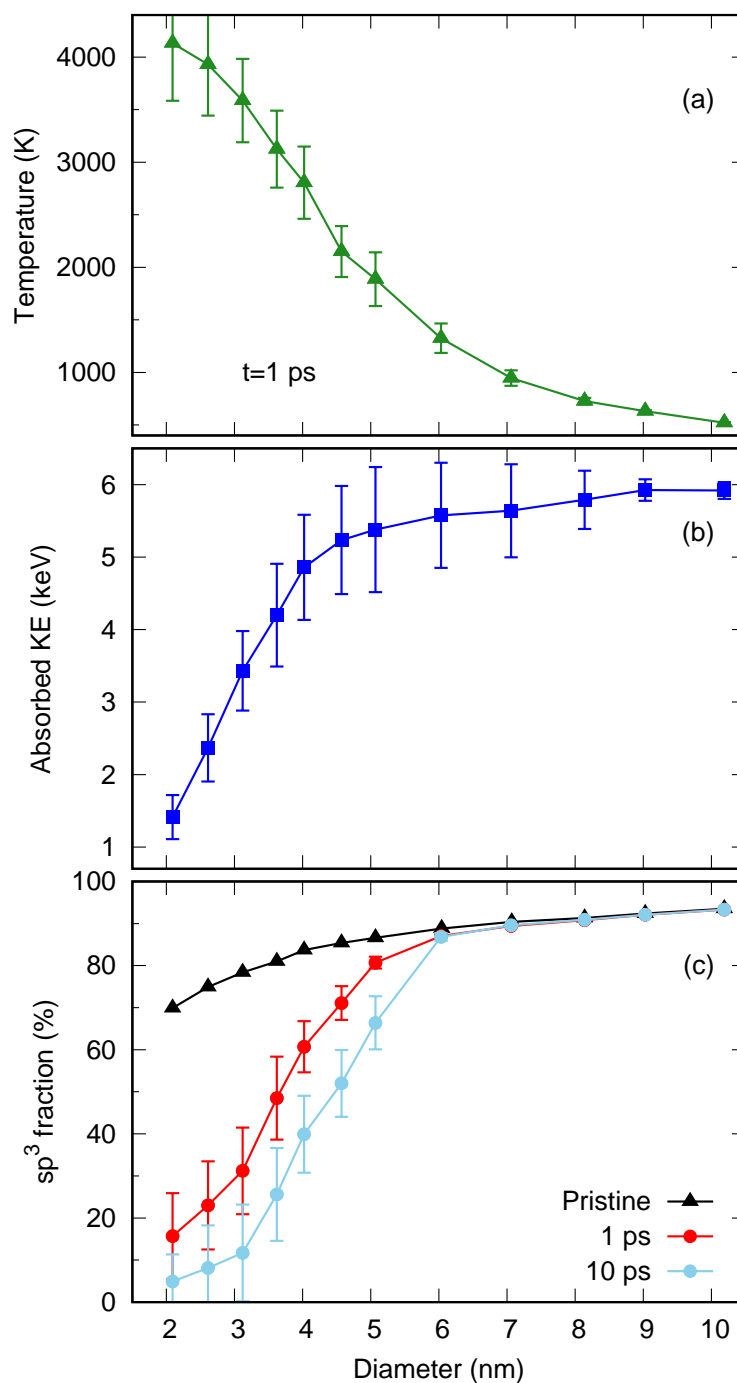


Figure 4.11: Effect of ND diameter for xenon implantation at a fixed impact energy of 6 keV. All properties computed 1 ps after initiation of the event. (a) Cluster temperature, (b) sp^3 fraction and (c) kinetic energy absorbed by the ND.

of all ejected particles (xenon plus carbons) and calculating the difference from the original value of 6 keV. The graph shows that the small NDs absorb only

a small fraction of the total implantation energy, while for the large NDs the entire energy of the xenon is deposited into the ND. Even though more kinetic energy is absorbed by the large NDs, the final cluster temperature as shown in Figure 4.11(a) monotonically decreases with increasing diameter due to the rapid increase in number of atoms with diameter. This demonstrates an important aspect of ion implantation into nanoparticles, namely that a small particle will only absorb a modest fraction of the impact energy, but since a small particle contains few atoms, the resultant temperature increase is substantial.

Figure 4.11(c) quantifies the fraction of sp^3 bonds as a function of ND diameter; note that the maximum value (solid triangles) varies with diameter due to the changing surface-to-volume ratio. The loss of sp^3 bonding is particularly strong for the small NDs. After 1 ps, around 16% of the atoms in the 2 nm ND are sp^3 bonded, as compared to 70% sp^3 bonding in the original ND. As the diameter increases, the loss of sp^3 bonding gradually reduces, but remains significant in the 3–4 nm range. For NDs around 6 nm and above the sp^3 fraction is virtually unchanged due to the passage of the Xe.

The light-blue circles in Figure 4.11(c) show the sp^3 fraction after 10 ps has elapsed. Since the NDs in these simulations are isolated, the residual thermal energy drives an annealing process which gradually graphitizes the smaller NDs. In the experimental situation however, thermal conduction with surrounding NDs will provide a heat-loss path, and hence the annealing process will not continue indefinitely. This raises the question as to what simulation time should be used; thus far we have used 1 ps, but if thermal conduction is very rapid then a shorter simulation time should be used, and likewise, if thermal conduction is poor, then the NDs should be allowed to self-anneal for longer.

To address the question of thermal conduction between NDs, a second suite of calculations were performed in a system containing two identical NDs in varying degrees of thermal contact. The starting structure was the 3.1 nm ND, which was replicated and displaced along a vector correspond to one of the 25 Thomson

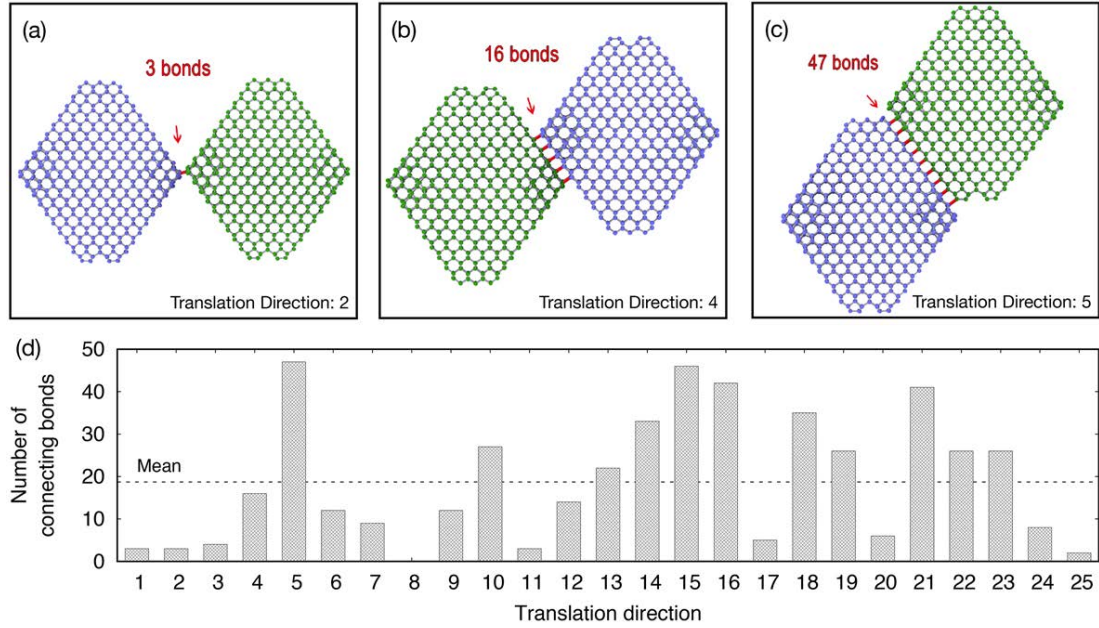


Figure 4.12: (a)–(c) Cross-sectional snapshots of three of the double-ND systems used to study the effect of thermal conduction. (d) Bar plot of the 25 different translation directions showing the number of bonds connecting the two NDs. Panel (a) shows the weakest thermal contact, comprising just 3 bonds. Panel (b) shows typical (average) thermal contact, with 16 bonds. Panel (c) shows the highest thermal contact, with 47 bonds. Connecting bonds are shown in red. Blue and green circles denote atoms and data for the primary and secondary ND, respectively.

points. The displacement was increased in small increments of 0.1 \AA until the smallest bondlength in the entire double-ND system exceeded a threshold of 1.3 \AA . The structure was then relaxed using steepest descent minimization. This process was repeated for the other 24 Thomson points, yielding a set of 25 double-ND systems exhibiting a wide range of thermal contact. The system with the weakest thermal contact is shown in Figure 4.12(a), containing just 3 connecting bonds (red lines) connecting the two NDs. In contrast, the best thermal contact involved 47 connecting bonds as shown in Figure 4.12(c). To determine a typical value of connections, we computed the number of connections for all 25 systems, as shown in the bar plot of Figure 4.12. This shows that the average number of connections is around 18, for which the structure in Figure 4.12(b) is a representative example.

For all 25 double-ND systems, two 6 keV simulations were performed. These ballistic simulations, which we refer to as either transverse or parallel, are shown

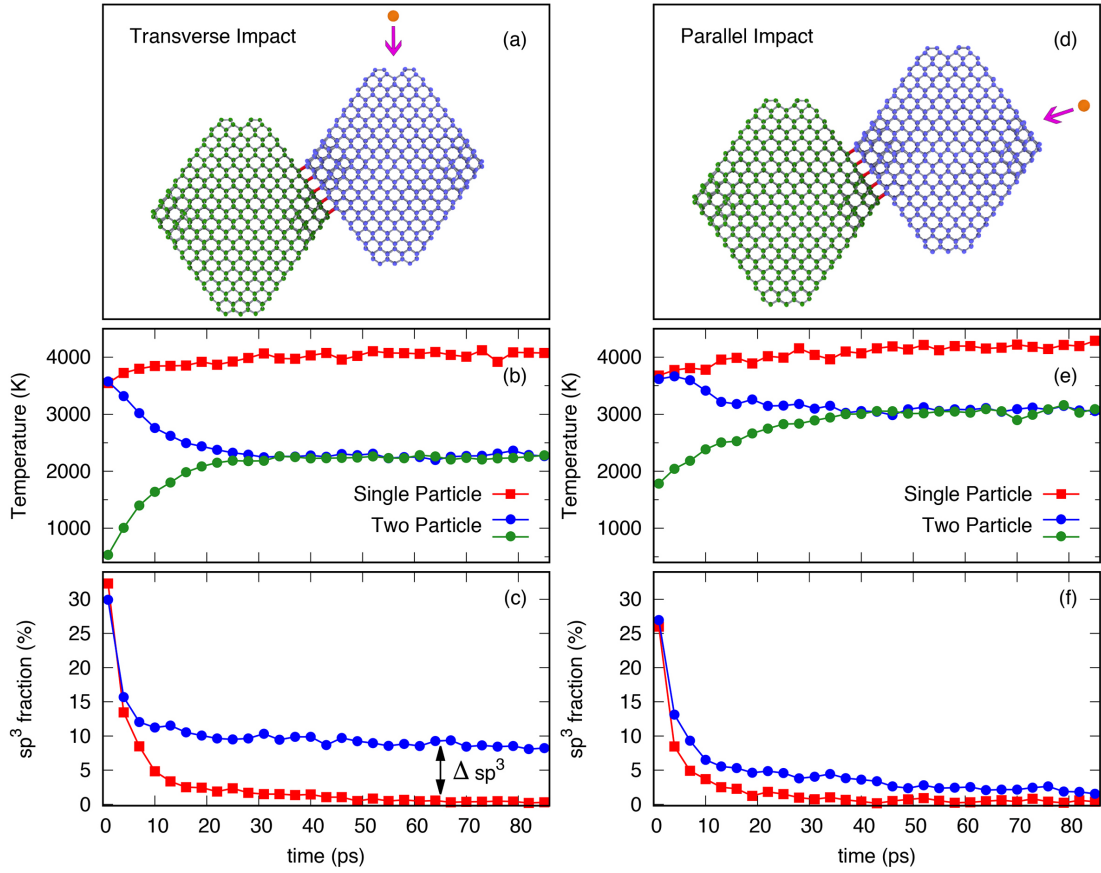


Figure 4.13: Time-evolution of temperature and sp^3 fraction for a 6 keV xenon impact into a double-ND system with average thermal contact (see Figure 4.12(b)). The first data point is 1 ps after initiation of the event, followed by data in 3 ps intervals. Panels (a)–(c) show the initial conditions and data for a transverse impact, in which the impact direction is maximally orthogonal to the translation vector. Panels (d)–(f) show the same quantities for a parallel impact, in which the impact direction is the same as the translation vector. Blue and green circles denote atoms and data for the primary and secondary ND, respectively. Red squares denote data for a single ND. The orange circle and pink arrow indicate the xenon atom and its initial direction, respectively.

in detail for the case of average thermal contact in Figure 4.13. Snapshots of the two systems after 85 ps has elapsed are shown in Figure 4.14. In the transverse impact case, the initial direction is the Thomson point vector which is maximally orthogonal to the translation vector, while for the parallel impact case the initial direction is the same as the translation vector. Note that the ND centred at the origin is considered as the primary-ND as in all simulations it is the ND to be first impacted by xenon hence the ND which has undergone a transition is

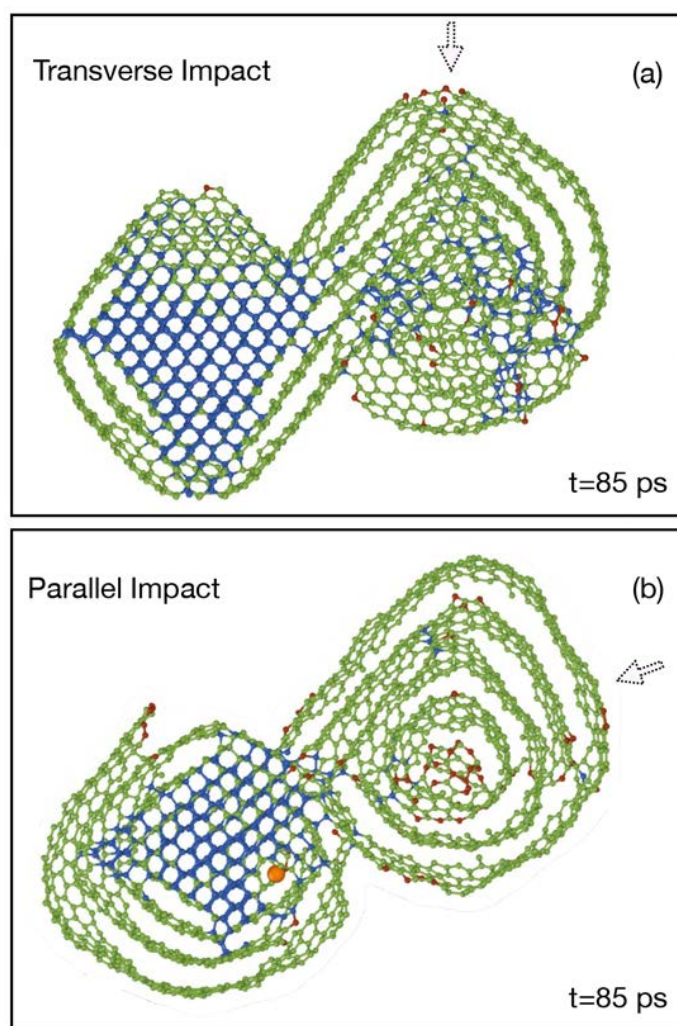


Figure 4.14: Cross-sectional snapshots (1 nm slices) showing the two double-ND systems seen in Figure 4.13 after 85 ps of annealing. Colour codings are the same as in Figure 4.6. The orange circle and dotted arrow indicate the xenon atom and its initial direction, respectively.

considered as the secondary-ND. The blue and green circles in Figure 4.13(b) show the temperature of the individual NDs as a function of time, using the same colour scheme employed in panel (a) for the atoms. The heat-loss path provided by the secondary ND (green circles) has an obvious effect on the temperature of the primary-ND, shown in blue. After approximately 30 ps the two NDs attain thermal equilibrium with each other, reaching a temperature of ~ 2250 K. The red squares in Figure 4.13(b) show the exact same impact for a single-ND system in which there is no heat-loss path. In this case, the temperature of the ND is

substantially higher, equilibrating at around 4000 K. The effect of this higher temperature on the sp^3 fraction of the primary-ND is shown in Figure 4.13(c), with red and blue circles corresponding to the single- and double-ND systems, respectively. For the single-ND case, all sp^3 bonding is lost and the ND transforms into a carbon onion, while for the double-ND around 8% of the sp^3 bonds persist (see primary ND in Figure 4.14(a)). While the effect of the heat-loss path is clearly apparent, it is important to recall that the original sp^3 fraction is 78%, and hence in both cases substantial modification of the ND occurs.

The parallel impact case shown in Figure 4.13(d)–(f) demonstrates that the effect of thermal contact is influenced by the initial direction. In this instance, the xenon atom is directed towards the centre of mass of both NDs, and this alignment means ballistic transfer of energy occurs between the primary and secondary NDs. As a result, the secondary ND is no longer just a heatsink as it was in the transverse impact case. Panel (e) shows that the equilibrium temperature is 3000 K, substantially higher than seen for the transverse impact, and much closer to the single impact data (red squares). As would be expected, the similarity in temperatures between the single- and double-ND systems means that the difference Δsp^3 in panel (f) is minimal. Due to the higher equilibrium temperature, the primary ND graphitizes completely into a carbon onion as seen in Figure 4.14(b).

The equilibration between the primary and secondary ND seen in the non-ballistic, transverse impact data of Figure 4.13(b) can be intuitively understood from a macroscopic perspective using Newton’s law of heating/cooling. Both temperature profiles are well-fitted by decaying exponentials, with exponents of 9.0 and 8.4 ps^{-1} for the primary and secondary ND, respectively. The solid lines in Figure 4.15 show the corresponding fitted exponential curves, along with data for the cases of strongest and weakest thermal contact. The average decay constant for the strongest contact is 4.2 ps^{-1} , while for the weakest contact case it is 20 ps^{-1} . These data provide a timescale for the heat-loss path when NDs

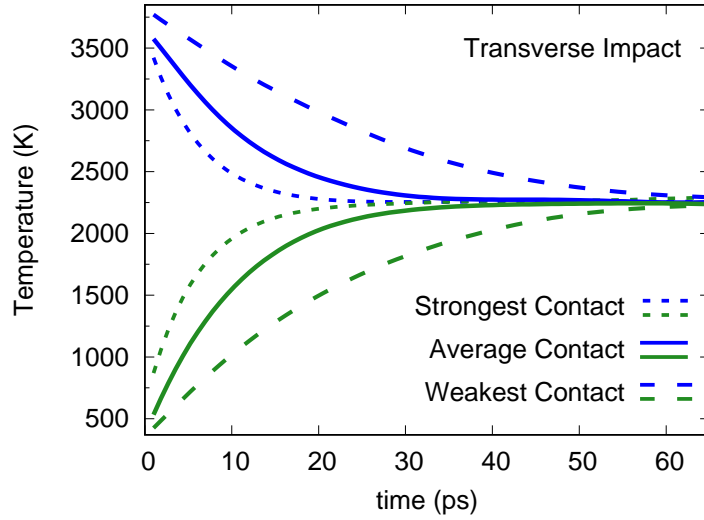


Figure 4.15: Time-evolution of temperature for a 6 keV transverse impact onto the double-ND systems corresponding to weakest thermal contact (Figure 4.12(a)), average thermal contact (Figure 4.12(b)) and strongest thermal contact (Figure 4.12(c)). The blue and green traces are decaying exponential fits to the raw data, and correspond to the primary and secondary ND, respectively.

are in contact with one another. This situation is directly relevant to the *in situ* implantation/TEM experiments by Shiryaev et al. (2018) which motivated the present simulations. In the experiments, NDs were suspended in ethanol and deposited onto a holey carbon grid, producing an aggregate of NDs that provide a heat-loss path. Based on the simulation results, it is reasonable to propose that 1 ps of annealing is about right, while 10 ps is certainly too much, particularly since each ND will have some degree of thermal contact with several other NDs.

The effect of having too much annealing is illustrated in Figure 4.16 which plots the quantity Δsp^3 (as defined in Figure 4.13) as function of annealing time for transverse and parallel impacts. These two situations can be considered as the extrema, with a typical impact falling somewhere in-between. All data points are averages across 25 different translation directions and the errors denote one standard deviation. This sample is of sufficient size to display a clear trend in which overly long annealing times lead to significantly different sp^3 fractions for transverse impacts. In contrast, there is little effect for parallel impacts as the kinetic energy of the atoms ejected from the primary-ND is deposited into

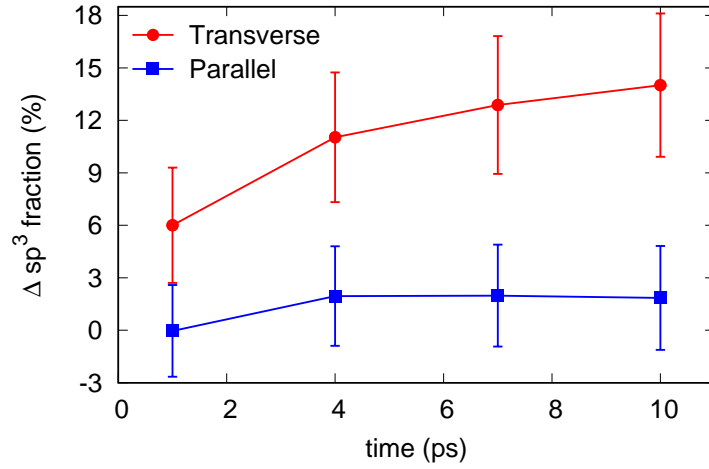


Figure 4.16: Effect of annealing time on the difference in sp^3 fraction between single- and double-ND systems for transverse (red circles) and parallel (blue squares) impacts. The sign convention is defined so that a positive difference means the double-ND value is higher. Data collected for all 25 of the translation directions (see Figure 4.12) and the error bars indicate one standard deviation.

the secondary-ND; this increases the temperature of the secondary-ND, thereby reducing the temperature gradient along the heat-loss path.

4.4 Conclusion

In this chapter, we showed how MD simulation can be quantitatively used to study implantation of xenon into NDs. Following on experimental study by [Shiryaev et al. \(2018\)](#), we provided detail on the key experimental/simulation result, namely, that an implantation energy around 6 keV provides maximal damage. We also detailed a pronounced size effect, showing that small NDs (below 3–4 nm diameter) are easily destroyed, losing many atoms and graphitizing those which remain. An important aspect of the damage process is the interplay between the amount of kinetic energy deposited in the ND, and the number of atoms in the ND itself. This energy transfer leads to thermal heating of the ND, with an effect seen only when the temperature approaches the rather high melting point of diamond. To assess the length of annealing that should be used in the simulations, we also studied a double-ND system in which two particles

are touching with varying degrees of thermal contact. This mimics the heat bath that occurs in the experiment, and suggests an annealing time of one picosecond is reasonable.

The methodology developed here can be easily extended to describe a variety of similar topics. The most obvious is the implantation of noble gases into NDs, which is relevant to presolar studies where all of the noble gases are important. To extend the present work to elements other than xenon one simply needs to take LJ parameters for noble gas interactions with carbon and bridge to the short-range ZBL expression. These parameters are easily obtainable due to the many studies of gas-adsorption onto carbon networks, and are conceptually straightforward due to the weak interactions between carbon and a noble gas atoms. Implantation involving other chemical species is also possible, but the interactions are less trivial due to the formation of formal chemical bonds. Beyond NDs, the noble gas implantation methodology can also be usefully applied to study ion-irradiation effects in a wide variety of different carbon nanoforms, such as graphene, graphene bilayers, fullerenes and nanotubes, as well as bulk materials.

Chapter 5

Predicting release temperatures of noble gases in pre-solar nanodiamonds

The main text and the figures comprising this chapter have been used in a paper which is to be submitted (preprint is available on [arXiv](#)). This chapter is motivated by experiments of stepped pyrolysis of meteorite and synthesis nanodiamonds, as discussed in Section 1.1.1. Here, by using molecular dynamics simulation, we show that low-energy ion-implantation is a viable way for the incorporation of noble gases into nanodiamonds. Our model also provides atomistic details of the thermal release patterns of implanted noble gases. The results reproduce all experimental results and show that with the implantation of only a single isotope noble gas atom, light noble gases are released in a single broad peak while the heavy elements are released in two distinct peaks. Accordingly, our model shows that the thermal release process of noble gases is highly sensitive to the impact and annealing parameters as well as to crystallographic orientation and types of defect.

5.1 Introduction

Trace quantities of xenon and other noble gases found within the primitive chondritic meteorites nanodiamonds (NDs) have isotopic distributions significantly different to terrestrial abundances, providing strong evidence that the NDs, and hence the meteorites, are pre-solar. To quantify the noble gas composition, the NDs are chemically separated from the host meteorite, pyrolyzed to release the gases and then analyzed with a mass spectrometer. Typically, one in every million NDs will contain a xenon atom, and one in ten will contain a helium (Huss, 2005). Stepped pyrolysis reveals that light elements (helium and neon) have a temperature-release distribution comprising a single broad peak, while for heavy elements (argon, krypton and xenon) the thermal-release distribution is bimodal (Huss and Lewis, 1994a,b).

As discussed earlier in Section 1.1.1, the bimodal character of the thermal-release during stepped pyrolysis has commonly been attributed to the presence of different components of xenon. The low-temperature peak around 500°C has an isotopic distribution close to terrestrial abundances and is referred to as P3, while the high-temperature peak around 1420°C is isotopically anomalous (Huss and Lewis, 1994a,b) and known as HL due to an excess of Heavy and Light isotopes. The other heavy noble gases (i.e., argon and krypton) also exhibit bimodal behavior, with the same release temperatures and isotopic anomalies. These isotopic anomalies have been extensively studied, since pre-solar material provides information on the history of nucleosynthesis and galactic mixing. For xenon, an excess of heavy and light isotopes is consistent with *r*- and *p*-processes in supernova nucleosynthesis (Clayton, 1989; Howard et al., 1992; Ott, 1996).

Understanding the origin and meaning of the P3 and HL components has proved challenging due to difficulties in identifying the specific processes responsible for (a) incorporation of the noble gas, and (b) gas release during pyrolysis. While one possibility is that the noble gases were trapped during growth of the NDs, the most popular explanation for incorporation is an implantation-type

process where noble gases are driven into pre-existing NDs (Lewis and Anders, 1981; Lewis et al., 1987; Verchovsky et al., 1998; Gilmour et al., 2005). The strongest support for the latter hypothesis comes from Koscheev et al. (2001) who implanted low energy (~ 700 eV) noble gas ions into synthetic NDs. Pyrolysis measurements observed a single broad temperature distribution for helium and neon, and a bimodal distribution for argon, krypton and xenon, corresponding closely to those found for meteoritic NDs (Huss and Lewis, 1994a,b). Even though the implantations involved gases with terrestrial abundances, a bimodal temperature-release distribution was found. Similar studies by Verchovsky et al. (2000) also found a bimodal distribution. This suggests that the P3 and HL components were probably implanted via different events at different stages in the history of the ND grains.

In this chapter, we use the molecular dynamics (MD) approach and apply it to the question of the single and bimodal temperature-release of noble gases. To the best of our knowledge, atomistic simulation methods have not previously been applied to this problem. We simulate the implantation and pyrolysis processes for helium and xenon, and find excellent agreement with experimental data collected from meteorites. We reproduce the single release peak for helium and bimodal release for xenon. The simulations explain how the mass, implantation depth and crystallographic location of the noble gases gives rise to the experimental observations, and for the first time provide an atomistic explanation of the release mechanism.

5.2 Methodology

5.2.1 Simulation methods

Our simulation methods are broadly similar to the previous chapter where we studied the modification of NDs by xenon implantation. The MD simulations are performed using the Environment Dependent Interaction Potential (EDIP)

(Marks, 2000) for carbon–carbon interactions in combination with the standard Ziegler-Biersack-Littmark (ZBL) potential (Ziegler et al., 1985). Further details are provided in Section 1.2.4. As explained before in Chapter 3, EDIP potential has proved itself to be highly transferable. To describe helium–carbon and xenon–carbon interactions, we use a Lennard-Jones (LJ) potential coupled with the ZBL potential, with interpolation between the two interactions controlled using Fermi-type switching functions as described earlier in Chapter 4. All parameters of the LJ potential (Equation 4.1), the total interaction energy (Equation 4.2) and the Fermi functions (Equation 4.3) for both helium–carbon and xenon–carbon interactions are provided in Table 5.1. Figure 5.1 illustrates the helium–carbon and xenon–carbon interaction energy covering the ZBL and LJ regimes.

We perform our simulations using an in-house MD package. Similar to the previous chapter, implantation simulations are carried out in an NVE ensemble, using Verlet integration and a variable timestep (Marks and Robinson, 2015). However, annealing simulations are performed in an NVT ensemble using a velocity-rescaling thermostat. Periodic boundary conditions are not employed. All simulations use a 4999-atom ND with a diameter of 3.9 nm (see Figure 4.2); this size is similar to synthetic and meteoritic NDs (Huss and Lewis, 1994a,b;

Table 5.1: Parameters of the Lennard-Jones potential, the Fermi functions and the total interaction energy for both helium–carbon (He–C) and xenon–carbon (Xe–C) interactions. Xe–C parameters are the same as used in Chapter 4, while ε and σ for He–C are taken from Nguyen et al. (2008). As discussed in previous chapter, the other parameters (b_F , r_F and δ) are chosen manually to provide a smooth transition from the strong repulsive region of the ZBL potential to the weakly attractive region of the LJ potential.

	Lennard-Jones potential (Equation 4.1)		Fermi-type switching (Equation 4.3)		Total interaction energy (Equation 4.2)
	ε (eV)	σ (Å)	b_F (Å)	r_F (Å)	δ (Å)
He–C	0.0013	2.89	9.2	2.2	0.09
Xe–C	0.0114	3.332	8.0	2.7	0.07

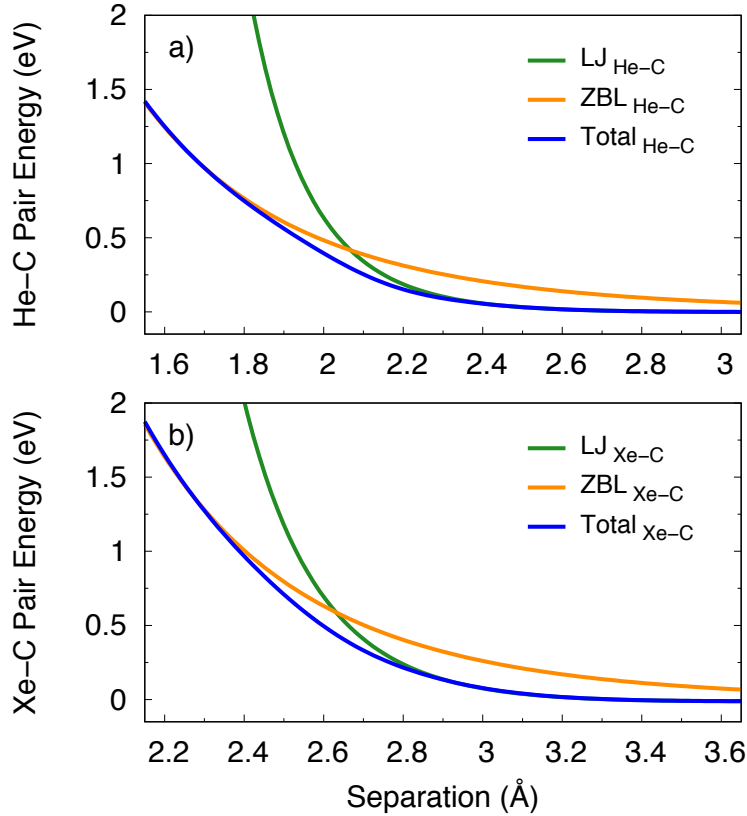


Figure 5.1: Pairwise interaction energies (blue line) for (a) helium–carbon, and (b) xenon–carbon. At close approach the interaction is pure ZBL (orange line), while at distances around equilibrium and greater, a Lennard-Jones expression is used (green line). Data in panel (b) is from Chapter 4 and replotted.

Koscheev et al., 2001). Similar to the previous chapter, the ND has a truncated octahedral form which is the stable geometry for dehydrogenated NDs (Barnard and Zapol, 2004). The $\{100\}$ faces of the ND are reconstructed in a 2×1 manner to eliminate dangling bonds. The coordinates of the ND are generated using the methodology described in Chapter 4. The key idea is to cut the ND out of an infinite crystal using clipping planes in the $\langle 100 \rangle$ and $\langle 111 \rangle$ directions. Using the notation of Chapter 4, the ND use here is generated with $d_{\{100\}} = 20 \text{ \AA}$ and $d_{\{111\}} = 17 \text{ \AA}$. Prior to implantation, the ND is equilibrated at 300 K.

All the simulations in this chapter have two steps; (i) noble gas atom (helium or xenon) is implanted into the ND and once the system has equilibrated, (ii) the entire cluster is heated to find the temperature at which the implanted noble gas

atom escapes. Implantation simulations are 1 ps in length, sufficient to model the ballistic phase of ion implantation into the ND. To generate a wide variety of implantation conditions, the initial position and direction of the implanted species (either helium or xenon) is systematically varied. Following Chapter 4 and previous studies (Buchan et al., 2015; Christie et al., 2015; Shiryayev et al., 2018; Fogg et al., 2019), the initial position is taken from a 25-point solution to the Thomson problem (Thomson, 1904) which distributes coordinates uniformly on a sphere (see Section 1.2.5 and Figure 4.3(b)). Some implantations are performed directly towards the centre of the ND, while others are directed slightly (up to 10 Å) away from the centre-of-mass (see Figure 4.3(a)). After the system equilibrates, the implantation depth is computed relative to the nearest crystallographic face, {100} or {111}. For the helium implantations the mass is 4 amu, while the xenon implantations use a mass of 133 amu, the same as in Chapter 4, and slightly higher than the average isotopic value of 131.3 amu. Additional xenon simulations use masses of 124 and 136 amu, corresponding to the lightest and heaviest stable isotopes. Finally, annealing simulations extending up to 1 ns are performed to study the thermal release process. We note that during the annealing simulations if release has occurred, the simulation is terminated. If thermal release does not occur, the simulation is rerun at a higher temperature.

5.2.2 Mapping to experimental temperatures

Generally speaking, the timescale of MD simulations is on the order of nanoseconds, around 13 orders of magnitude shorter than the experimental annealing time. This enormous difference complicates comparison between simulations and experiments, as thermally activated events will be suppressed in the simulations due to vastly shorter time. Many different solutions to the MD timescale problem have been proposed (Voter, 1997, 1998; Sørensen and Voter, 2000), but here we employ a simple temperature-acceleration approach that de Tomas et al. (2017) have used successfully on other carbon systems. The first step is to assume Ar-

Arrhenius behavior and a single activation energy, which corresponds to the relation

$$f = A \exp\left(-\frac{E_a}{k_B T}\right), \quad (5.1)$$

where f is the frequency of events, A is the attempt frequency, T is the temperature, k_B is Boltzmann's constant and E_a is the activation energy. The correspondence between the experimental and simulation temperature is determined by equating the time-frequency product (i.e., $f_{\text{expt}} \times t_{\text{expt}} = f_{\text{sim}} \times t_{\text{sim}}$) to ensure that for the same activation energy the same number of events occur in both simulation and experiment. This yields the following expressions

$$\frac{1}{t_{\text{sim}}} \exp\left(-\frac{E_a}{k_B T_{\text{expt}}}\right) = \frac{1}{t_{\text{expt}}} \exp\left(-\frac{E_a}{k_B T_{\text{sim}}}\right) \quad (5.2)$$

and

$$T_{\text{sim}} = -\frac{E_a}{k_B} \times \left[\log\left(\frac{t_{\text{expt}}}{t_{\text{sim}}}\right) - \frac{E_a}{k_B T_{\text{expt}}} \right]^{-1}. \quad (5.3)$$

This equation links the experimental temperature and time (T_{expt} and t_{expt}) with those of the simulation (T_{sim} and t_{sim}) with the only parameter being the activation energy. To determine E_a , we make use of experimental data on graphitization of NDs, where it is known that $\sim 1500^\circ\text{C}$ is required to convert NDs into a carbon onion (Kuznetsov et al., 1994; Tomita et al., 2002; Kuznetsov et al., 1994; Qiao et al., 2006; Xiao et al., 2014). To identify the corresponding temperature on the MD timescale we perform a set of 1 ns simulations at different annealing temperatures and found that spherical graphitization of the ND occurs at around 3500 K (see Figure 5.3). Further discussion of the spherical graphitization of pristine ND at various temperatures is provided later in this section. Using these two temperatures and suitable times ($t_{\text{sim}} = 10^{-9}$ s and $t_{\text{expt}} = 3600$ s (Kuznetsov et al., 1994; Tomita et al., 2002; Kuznetsov et al., 1994; Qiao et al., 2006; Xiao et al., 2014)), we obtain via Equation 5.3 a value of $E_a = 9$ eV. Having determined the activation energy, we can employ Equation 5.3 to map any simulation temperature to its experimental equivalent using the relation shown in Figure 5.2.

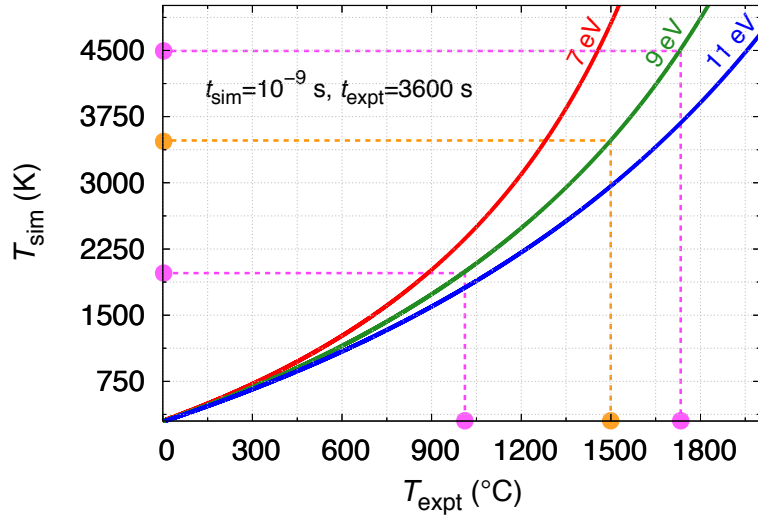


Figure 5.2: Calibration curve between simulation and experimental temperatures via the Arrhenius approach. The orange dashed line indicates data for the spherical graphitization of a ND used to determine the value of $E_a = 9$ eV. The pink lines indicate two examples of the mapping process as described in the text.

For example, the pink lines in the figure show that a simulation temperature of 4500 K is equivalent to an experimental temperature of $\sim 1730^\circ\text{C}$, and a simulation at 2000 K is equivalent to an experiment at $\sim 1000^\circ\text{C}$. The latter also serves as a convenient dividing line between the P3 and HL peaks for xenon (Huss and Lewis, 1994a,b). To provide a sense of scale, Figure 5.2 also shows calibration curves for two other activation energies. Note that due to the logarithm term in Equation 5.3 the value of E_a has minimal sensitivity to the choice of t_{expt} . For example, if t_{expt} were 30 minutes instead of 60 minutes, the changes in equivalent t_{sim} would be at most ~ 80 K. This point is discussed in detail in de Tomas et al. (2017).

As described earlier, calibration of the simulation temperatures with their experimental equivalent is performed using the graphitization of NDs into carbon onions as a reference point. Figure 5.3 illustrates cross-sectional snapshots of the annealed ND for nine different temperatures. Panel (a) shows that at 1000 K there is insufficient temperature to graphitize the ND on this timescale, while at 1500 and 2000 K (panels (b) and (c)) some of the bonds on the $\{111\}$ face are broken and graphitic shells form. The reason this occurs is that sp^3 hybridized

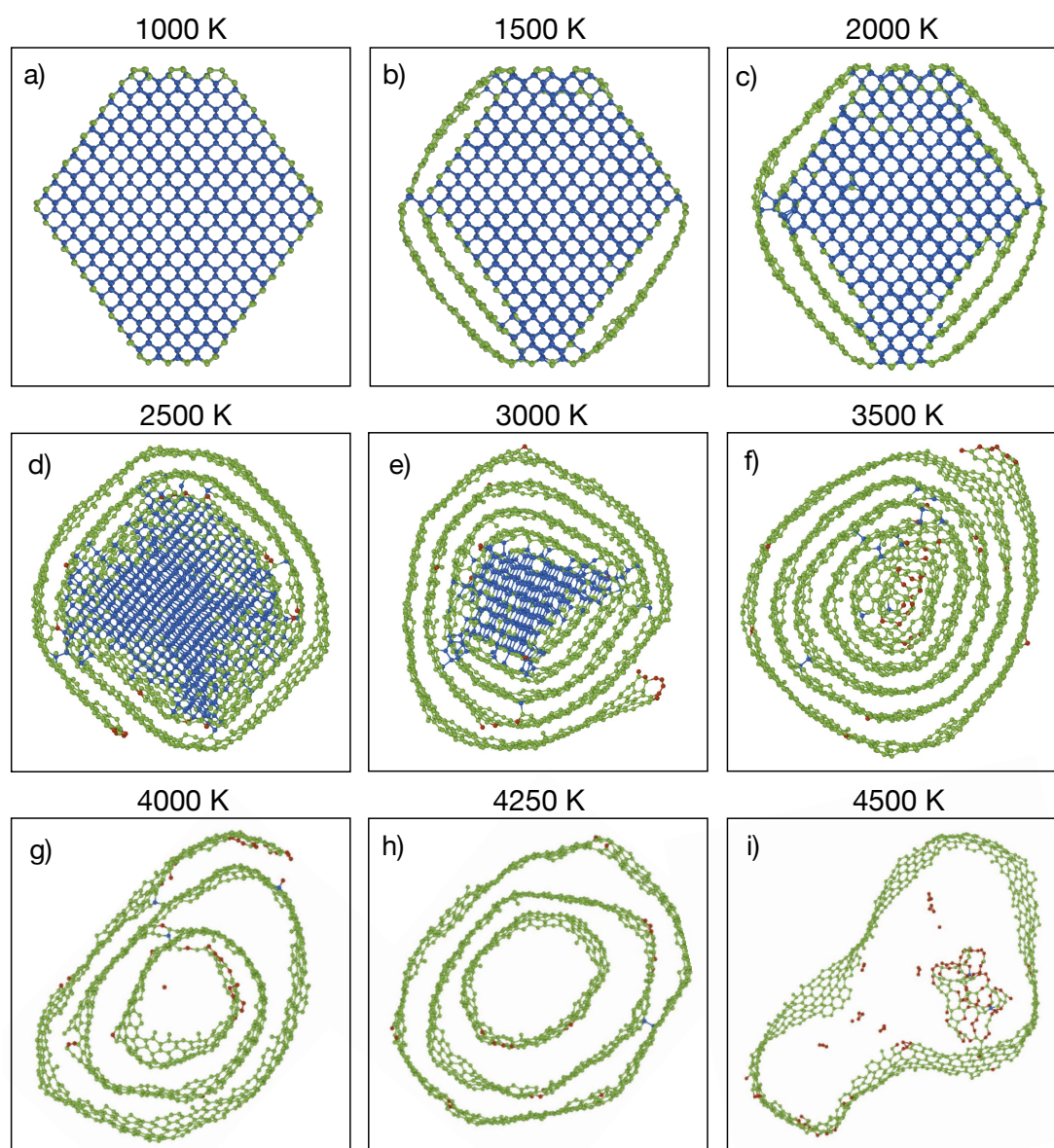


Figure 5.3: Cross-sectional snapshots (1 nm slices) of pristine ND after annealing for 1 ns at various temperatures. Panel (f) shows that at 3500 K the experimentally observed result, namely a carbon onion, is obtained. Red, green and blue circles denote sp , sp^2 and sp^3 hybridization, respectively.

atoms near the surface can easily rearrange into graphite with sp^2 hybridization (Kuznetsov et al., 1994; Wang et al., 2000; Pantea et al., 2002; Barnard et al., 2003b). At higher annealing temperatures of 2500 and 3000 K (panels (d) and (e)), graphitization proceeds further inwards, creating structures with a diamond core surrounded by a graphitic shell. This core-shell structure is in good agree-

ment with previous experimental and simulation studies (Kuznetsov et al., 1994; Tomita et al., 2002; Los et al., 2005a; Bródka et al., 2006; Qiao et al., 2006; Kuznetsov et al., 1994; Bródka et al., 2008; Ganesh et al., 2011). At 3500 K (panel (f)), a pure carbon onion (or concentric fullerene) is obtained and only a few small number of atoms ($\sim 1\%$) have been lost via evaporation. At this point we have identified the temperature at which the experimental result is reproduced on the timescale that is affordable in the simulation. At the slightly higher temperature of 4000 K (panel (g)), around 8% of the atoms evaporate and the carbon atom develops a hollow core. At the highest temperature of 4500 K (panel (i)), the ND is completely destroyed and more than 29% of atoms are evaporated, creating a large, disordered fullerene. Note that throughout this chapter we adopt the convention that experimental temperatures are given in Celsius and simulation temperatures are in Kelvin. This helps conceptually separate the two quantities which otherwise might be confused with one another.

5.3 Results and discussion

The results of the simulations are presented in four parts. Our first results are qualitative, using visualization and movies of the implantation and thermal-release processes to highlight the differences between helium and xenon. The second part of results involves robust statistical analysis of a large number of simulations spanning many implantation energies, implantation directions and annealing temperatures. After that, we use the Arrhenius approach to make direct comparison between meteoritic data and the simulations. In the final section we study the isotopic effects on the thermal release pattern of xenon.

5.3.1 Individual implantation and thermal release events

Representative examples of the implantation and thermal release processes for helium and xenon are shown in Figure 5.4. Panels (a) and (c) show that the

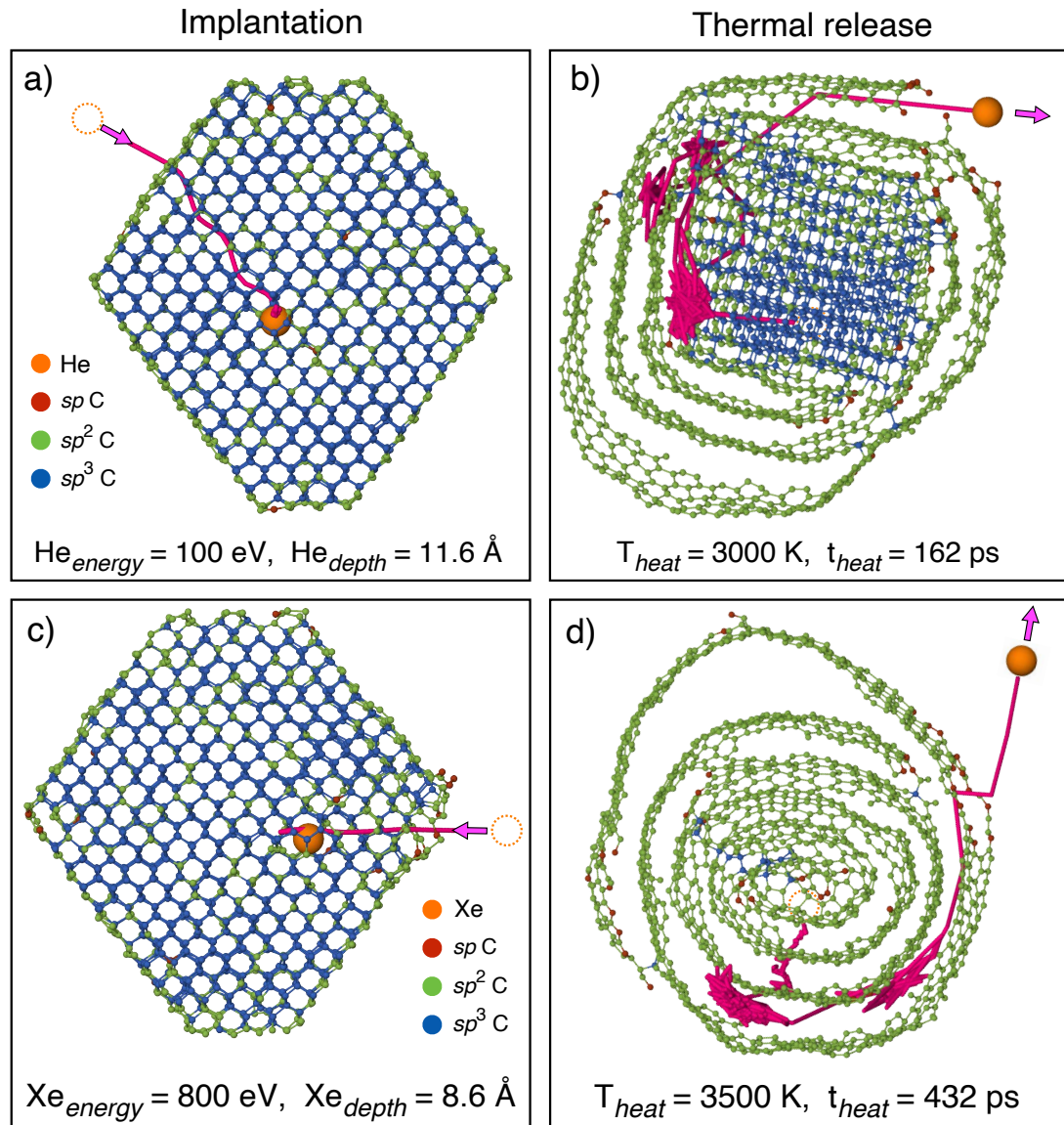


Figure 5.4: Typical implantation (left panels) and thermal release (right panels) processes involving helium (panels (a) and (b)) and xenon (panels (c) and (d)). The pink lines indicate the helium and xenon trajectories, and the helium and xenon are shown as an orange circles. The colour codings and cross-sectional slice details are the same as Figure 5.3.

implantation processes for helium and xenon differ substantially, with the higher mass and size of the xenon having a large effect. For helium, only a relatively modest of energy ($\sim 100 \text{ eV}$) is needed to implant the atom into the centre of the ND, and the helium undergoes multiple deviations along the implantation trajectory (pink line) since the carbon atoms are three times heavier. In contrast,

the implanting xenon simply slows down, and it is the carbon atoms which move. Around ~ 800 eV of kinetic energy is needed to implant into the central region, similar to the value of circa 700 eV used by [Koscheev et al. \(2001\)](#) in their experiments.

Once the implanted ND system has equilibrated, the entire cluster is heated to find the temperature at which the noble gas atom escapes. Examples of this process are shown in [Figure 5.4\(b\)](#) and (d). For both species, thermal release occurs at relatively high simulation temperatures; 3000 K for helium and 3500 K for xenon. As seen in [Figure 5.3](#), these temperatures are sufficient to transform portions of the ND into an onion-like structure. Due to its small size, the helium is able to escape before the ND has completely spherical graphitized. The complexity of the process can be appreciated in [Movie 5.1](#) which shows how the helium travels along multiple $\langle 110 \rangle$ channels, and traverses a substantial fraction of the ND before escaping. In the case of xenon, the ND is fully transformed into a carbon onion and the release process is more difficult as the xenon must pass through the graphitic shells. The pink trajectory in panel (d) shows that the release process involves two local minima in which the xenon moves back-and-forth many times before escaping. An animation sequence of this process is provided in [Movie 5.2](#).

To determine the temperature at which helium and xenon are released we perform 1 ns annealing simulations at many different temperatures and monitor the distance between the noble gas species and the center of the mass of the system. An example of our methodology is provided in [Figure 5.5](#) which shows this quantity ($r_{\text{c.m.}}$) for xenon as a function of time for three different annealing temperatures, using the implanted ND in [Figure 5.4\(c\)](#) as the starting structure. At 3000 K (blue line) the xenon remains the same distance from the center of mass. This occurs because the xenon becomes trapped at the interface between the ND core and graphitized outer layers (see [Figure 5.3\(e\)](#)). At 3250 K (violet line) the xenon moves towards the surface of the ND during the first ~ 170 ps of

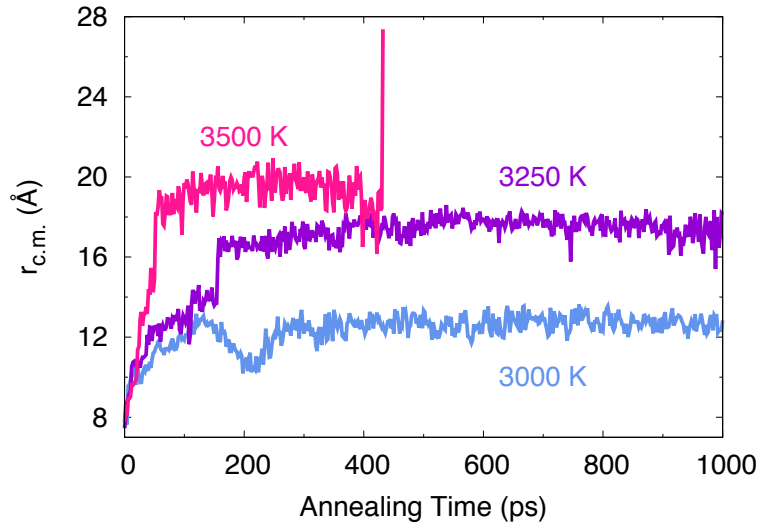


Figure 5.5: Distance between xenon and the center of mass of the ND as a function of annealing time for three different annealing temperatures. The structure in Figure 5.4(c) is the starting point for all three simulations.

annealing, but afterwards it is trapped between the graphitic shells. Note that at around 30 and 160 ps, there are two significant surges in $r_{c.m.}$ where the xenon atom passes through the graphitic shells. At 3500 K (pink line), the xenon is initially trapped between graphitic shells, but after moving between them, finally exits through a gap in the outer shell at 432 ps, producing a sharp jump in $r_{c.m.}$.

5.3.2 Statistical analysis

To collect a statistically significant data set a large number of implantation and thermal release simulations need to be performed. The first step is to perform simulations that implant helium and xenon into a wide variety of configurations within the ND. For each species a total of 1875 implantations were performed; 25 different energies, each with 75 different initial conditions (i.e., directions and/or impact parameters). A summary of the resultant implantation depth and incorporation probability is shown in Figure 5.6. Panels (a) and (b) show the implantation depth of helium and xenon as a function of implantation energy, where each dot indicates an implantation event whereby the noble gas species remains with the ND. Impacts where the helium or xenon leave the ND are not

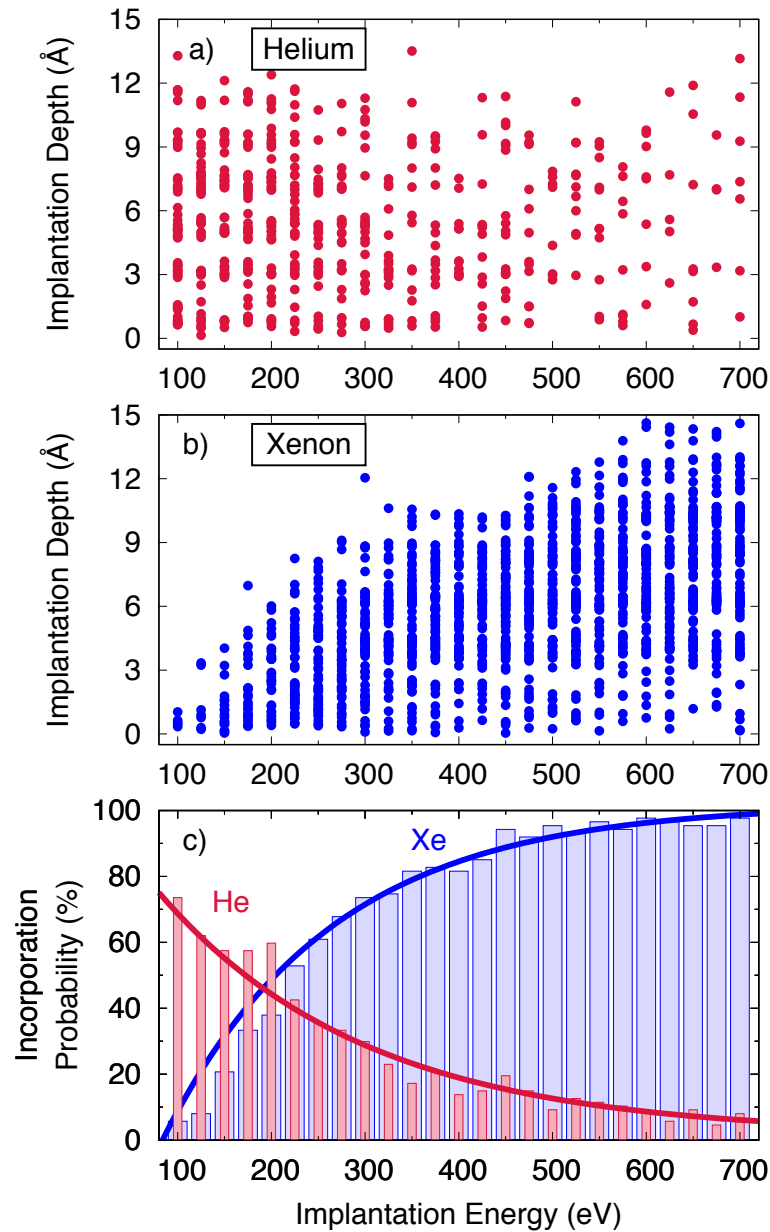


Figure 5.6: Implantation depth of (a) ^4He and (b) ^{133}Xe as a function of implantation energy. Panel (c) shows the incorporation probability of implanted helium (red) and xenon (blue) as a function of implantation energy. The solid lines in (c) are exponential fits to guide the eye, and have decay constants of 0.22 and 0.16 eV for helium and xenon, respectively.

shown. The fewest dots occur for high helium implantation energies (where helium passes through the ND) and low xenon implantation energies (where xenon is reflected). The distribution of depths differs considerably between the two

species. For helium, the implantation depth spans the maximum possible range, extending from the surface to the centre of the ND, and the implantation depth is uncorrelated with energy. In contrast, low energies result in only shallow implantation of xenon, while nearly 600 eV is required to span the full range of depths. High xenon implantation energies still produce a large number of shallow implantation depths, which is perhaps due to the small size of the ND.

Figure 5.6(c) quantifies the incorporation probability of helium and xenon as a function of implantation energy. The probabilities for the two species are strikingly different, and are driven by the mass difference relative to carbon. This data shows that low energies are optimal for helium implantation, while efficient xenon implantation requires many hundreds of eV. Noting that helium is the most abundant noble gas in meteoritic NDs (Huss, 2005), this data imposes constraints on the astrophysical conditions for helium incorporation via implantation. In the case of xenon, the simulation data confirms the experimental observations of Koscheev et al. (2001) that circa 700 eV is a suitable energy for implanting xenon into NDs.

The second step in performing the statistical analysis uses the coordinates associated with each dot in Figure 5.6 as the starting structure of thousands of thermal release simulations. As explained before, all simulations run for 1 ns, except for when $r_{c.m.}$ indicates that release has occurred; in such cases the simulation is terminated. If thermal release does not occur, the simulation is rerun at a higher temperature. Typically, the temperature increment between successive simulations is 100–250 K. The raw simulation data showing the relationship between the release temperature of the noble gas and the implantation depth is shown in Figure 5.7. The dots and error bars indicate the precision, meaning that if a noble gas atom releases at a temperature T_2 but not at a lower temperature T_1 , then the dot denotes $(T_1 + T_2)/2$ and the error bar indicates the range $[T_1 : T_2]$. Panel (b) shows that the xenon release temperatures cluster into two groups and correlate with the depth of the implanted atom. The average

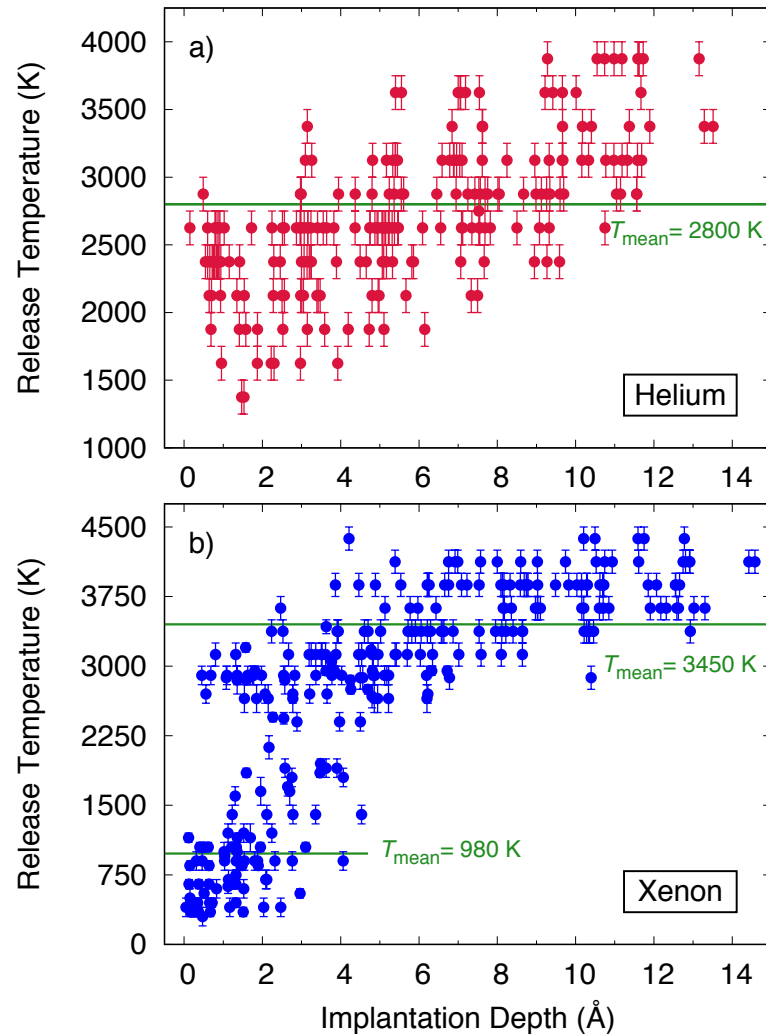


Figure 5.7: Thermal release data of (a) ^4He and (b) ^{133}Xe as a function of implantation depth. Mean release temperatures (T_{mean}) are shown by horizontal green lines and error bars indicate the degree of uncertainty; the precise meanings are explained in the text.

temperature for these two clusters are indicated by the green lines, with a dividing line of 2000 K used to separate the groups. Varying this number by several hundred Kelvin makes little difference to the averages. Note that as discussed before in Section 5.2.2, 2000 K is equivalent to an experimental temperature of $\sim 1000^\circ\text{C}$ and it serves as a convenient dividing line between the P3 and HL peaks for xenon (Huss and Lewis, 1994a,b). For helium, no clustering occurs, and the release temperature gradually increases with implantation depth. In this case the green line indicates the average temperature for the full data set.

5.3.3 Comparison with experiment

Figure 5.7(a) shows that a minimum of 1300 K is required to release helium and by 4000 K all helium is released. In contrast, the xenon data in panel (b) spans a broader range, with a minimum release temperature of only 400 K and a maximum of nearly 4500 K, at which point the ND is effectively destroyed (see Figure 5.3(i)). The observation of two temperature clusters for xenon and a single broad distribution for helium is in good qualitative agreement with the meteoritic ND observations. To map the simulation temperatures onto their experimental equivalents, we employ the Arrhenius approach explained before in Section 5.2.2, using an activation energy of $E_a = 9$ eV. By histogram binning the simulation data in Figure 5.7 and applying the transformation in Equation 5.3 we obtain a data set shown as thick blue lines in Figure 5.8. On the same scale we show experimental data for the Orgueil meteorite extracted from (Huss and Lewis, 1994a,b). The agreement is remarkable, with the simulations reproducing all of the main meteoritic ND characteristics, including (i) the unimodal vs bimodal character, (ii) the position of the peaks, (iii) the widths of the distributions, and (iv) the maximum and minimum release temperatures. This is the first time that MD simulation has predicted these important effects.

The high level of experimental detail reproduced by the simulations provides post-hoc justification for the Arrhenius approach, confirming that the presumption of a dominant activation energy is reasonable for this class of problem. All of the predicted temperatures are correctly positioned relative to their experimental equivalents; this includes the onset of helium and xenon release, the position of the release peaks, and even the upper limit at ~ 1800 °C, which corresponds to destruction of the ND and the release of any remaining gases. Regarding Figure 5.8(b), it is important to note that the simulations cannot predict the relative height of the peaks in the bimodal distribution, since this is function of the balance between shallow and deeply implanted xenon which is not known.

Having reproduced the essential characteristics of noble gas release, we can

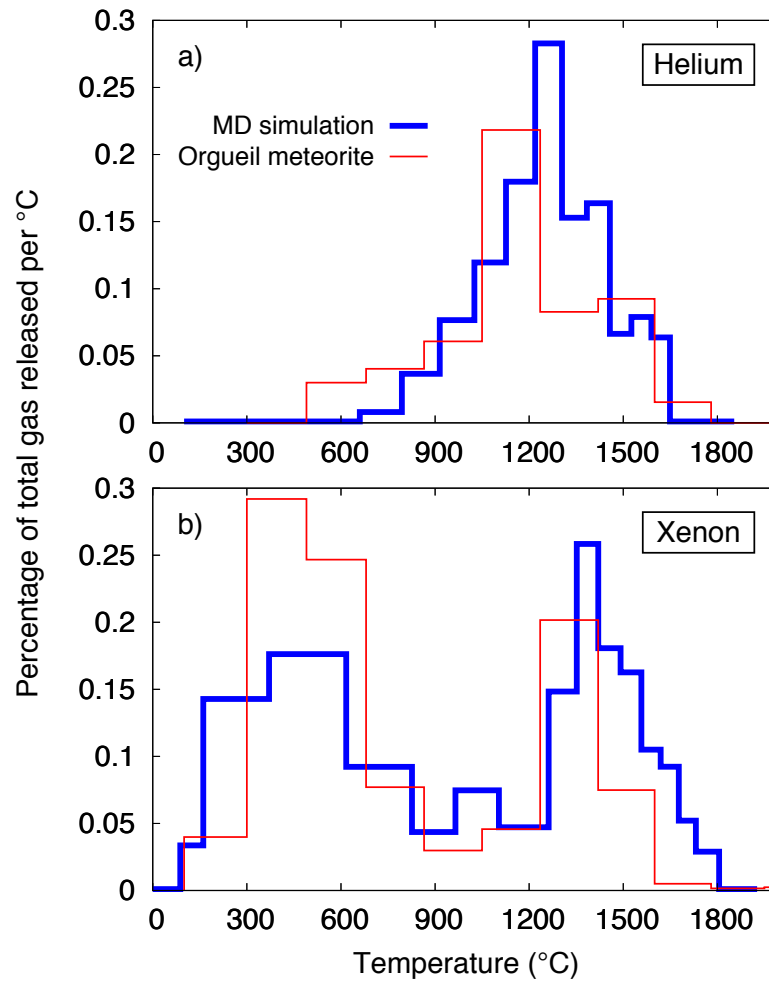


Figure 5.8: Measured and simulated ND thermal release patterns for (a) ^4He and (b) ^{133}Xe . Experimental values (red lines) are taken from data from the Orgueil meteorite (Huss and Lewis, 1994a,b), while the MD values (blue lines) are from this work.

address some of the most fundamental questions in the pre-solar meteoritic literature. Specifically, we can examine the atomistic origin of the Xe-P3 and Xe-HL peaks, and understand why helium exhibits unimodal behavior. Considering first the question of xenon, the raw simulation data in Figure 5.7(b) provides clues as to why release occurs at two distinct temperatures. The low-temperature peak is seen to be strongly correlated with proximity to the surface, with 4.5 \AA being the critical depth beyond which low-temperature release is impossible. In contrast, high-temperature release is possible for all implantation depths, and even for depths around 1 \AA there are two distinct temperature-release populations. The

origin of this behaviour is that the surface of the ND progressively graphitizes with temperature, with the $\{111\}$ face transforming prior to the $\{100\}$ face (see Figure 5.3). As a result, xenon located close to a $\{111\}$ face can become trapped by the developing graphitic layers, and once the layer has fully formed, the xenon is too large to easily diffuse through the hexagonal graphene-like network. This effect is quantified in Figure 5.9 which replots the xenon data in Figure 5.7(b) for shallow depths. Panel (a) colour codes each configuration according to the closest crystallographic face, while panel (b) shows a histogram of the thermal release temperatures. It is apparent that the low-temperature peak contains roughly equal contributions from xenon near the $\{100\}$ and $\{111\}$ faces, while the high-temperature component is dominated by xenon close to the $\{111\}$ face. Placing these observations in a meteoritic context, we can assert that Xe-HL is associated with either deeply buried xenon or shallow burial near a $\{111\}$ face, while Xe-P3 sits just a few ångströms from the surface, and has no crystallographic preference.

The other major result in Figure 5.7 is the prediction of the unimodal release distribution for helium. Inspection of animation sequences reveals that this

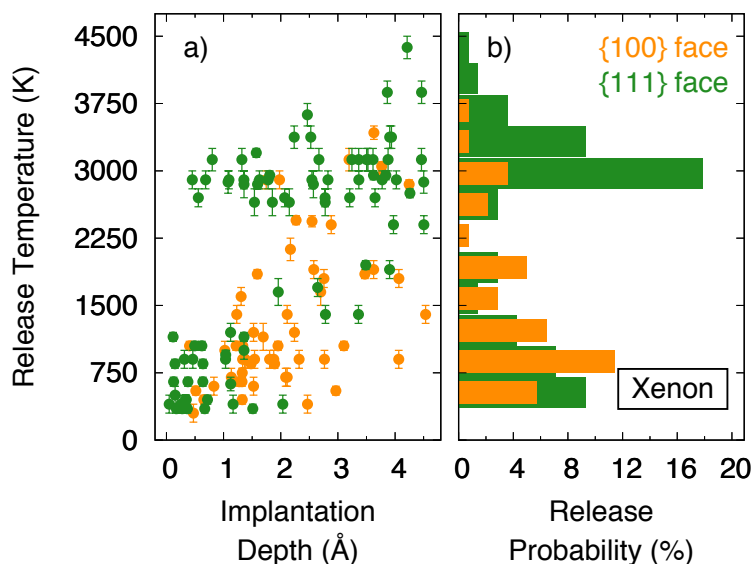


Figure 5.9: (a) Classification of shallow-implantation xenon data in Figure 5.7 according to proximity to a $\{100\}$ face (orange circles) or a $\{111\}$ face (green circles). (b) Histogram analysis of the data in (a).

behavior can be linked to the nature of the helium defect within the ND. The simulations show that helium prefers a tetrahedral interstitial (T-site) in the diamond lattice. The geometry of this defect is shown in Figure 5.10(a), with the four orange lines between helium and carbon highlighting the tetrahedral symmetry. The interstitial helium diffuses amongst the $\langle 110 \rangle$ channels in the lattice, passing through a hexagonal interstitial (H-site) transition state enroute to another T-site. This behavior means that in the low-temperature range, the helium effectively performs a random walk around the ND. Even if the $\{111\}$ face has graphitized, which typically occurs at around 1500 K in the simulations (see Figure 5.3(b)) which is equivalent to $\sim 800^\circ\text{C}$ in the experiments, the helium cannot escape through the graphitic layer. Only once the $\{100\}$ face begins to graphitize does the helium atom escape. These observations elegantly explain why the onset of helium release is so much higher than xenon. Additionally, the smaller size of helium means that it is more mobile than xenon, which in turn explains why the peak release temperature for helium is lower than that of the corresponding xenon high-temperature peak.

The analysis of helium migration in our MD simulations is supported by density-functional-theory (DFT) calculations of noble gas defects in bulk diamond (Goss et al., 2009) which similarly conclude that helium forms an interstitial defect on the T-site and diffuses via the H-site. For xenon they find that a

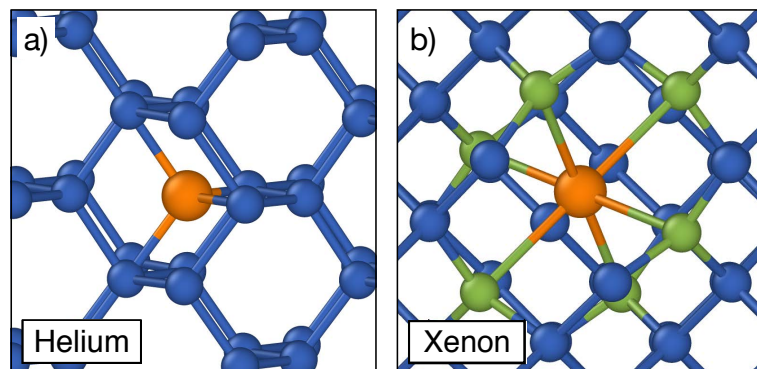


Figure 5.10: (a) tetrahedral interstitial (T-site) of helium and (b) $\text{Xe}_s\text{-V}$ defect of xenon in ND. The colour codings details are the same as Figure 5.3 and the helium and xenon are shown as an orange circles.

substitutional site is preferred and involves an adjacent vacancy, with the xenon placed at the midpoint (Figure 5.10(b)). Further DFT studies by Drumm et al. (2010) show this configuration ($\text{Xe}_s\text{-V}$) is substantially more stable than an alternative $\text{Xe}_s\text{-3V}$ defect involving three vacancies. Our MD approach reproduces the same behavior as the DFT studies, including the preference for $\text{Xe}_s\text{-V}$ over $\text{Xe}_s\text{-3V}$. Returning our attention to the simulation data in Figure 5.8(b), we can assign the low-temperature xenon release peak to an $\text{Xe}_s\text{-V}$ defect near the surface. Since this defect compromises the stability of the diamond surface, the xenon is able to escape at modest temperatures of a few hundred degrees Celsius, while the helium in the T-site is far more stable.

The DFT study by Goss et al. (2009) also studies other noble gases and divides them into two groups: (i) helium and neon which occupy the interstitial T-site and diffuse via the H-site, and (ii) argon, krypton and xenon which occupy substitutional sites with vacancies. This distinction between the interstitial T-site and the substitutional-vacancy provides a plausible explanation for the ND meteoritic data, where helium and neon have unimodal release peaks, while argon, krypton and xenon have bimodal distributions. To the best of our knowledge, this connection between defect type and temperature-release behavior has not previously been made.

5.3.4 Isotopic effects

One of the strengths of our MD approach is the simplicity of performing virtual experiments which are challenging or even impossible in a laboratory setting. For example, obtaining isotopically pure noble gases is an expensive proposition, while with MD one can study isotopic effects easily by simply changing the mass and rerunning the entire simulation set. To illustrate this capability, we repeated the entire implantation and thermal release protocols for ^{124}Xe and ^{136}Xe , both of which are naturally abundant. Thermal release data for these isotopes is shown in Figure 5.11, and as seen earlier, the release profile is again bimodal. For the

low-temperature peak, the release temperature is similar across all three isotopes, spanning a narrow range between 950 and 980 K, but for the high-temperature peak, there is a large isotopic effect with the simulation release temperature varying from 3180 K for ^{124}Xe to 3485 K for ^{136}Xe . Figure 5.12 plots the mean release temperature for the high-temperature peak for all three xenon isotopes, with the left-axis showing the simulation temperature and the right-axis the equivalent experimental value. With the error bars denoting the standard-error-in-the-mean, a

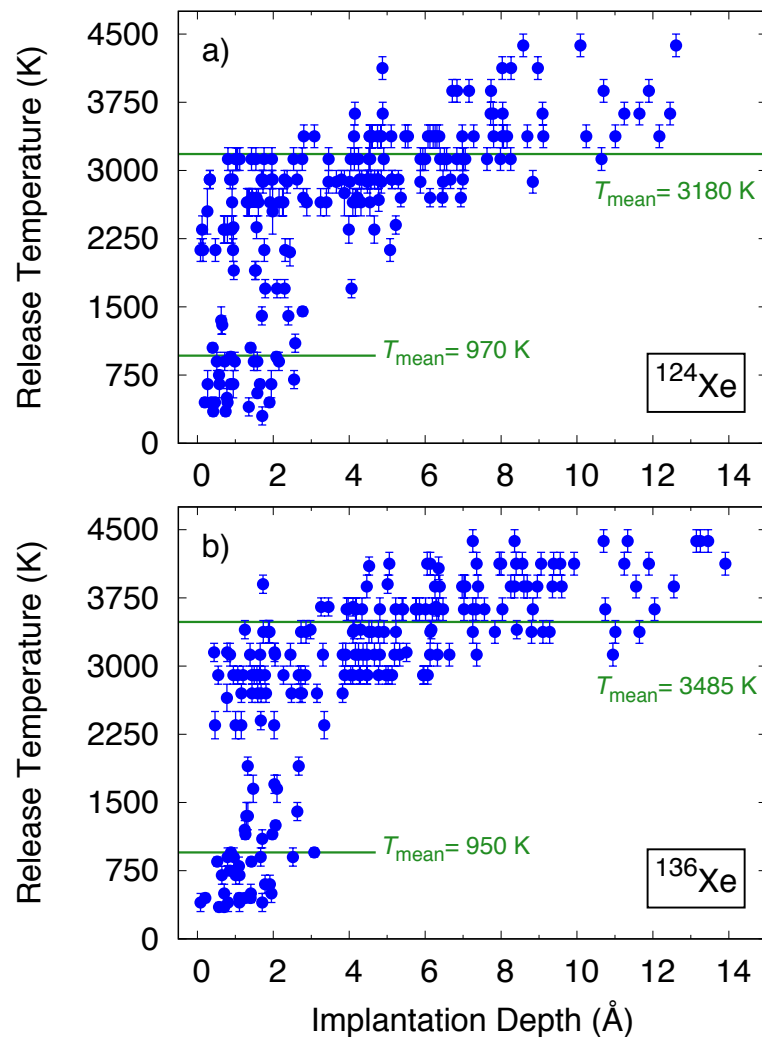


Figure 5.11: Thermal release data of (a) ^{124}Xe and (b) ^{136}Xe as a function of implantation depth. Mean release temperatures (T_{mean}) are shown by horizontal green lines and error bars indicate the degree of uncertainty. Due to the computational cost, the number of data points for the two isotopes is around two-thirds of that in Figure 5.7(b).

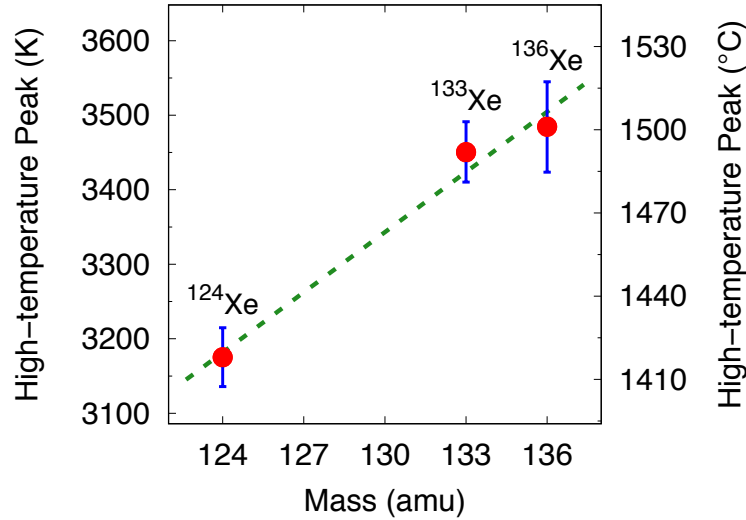


Figure 5.12: High-temperature release values for three different xenon isotopes as shown in Figures 5.7(b) and 5.11. Left-axis indicates raw simulation data in Kelvin while the right-axis indicates the equivalent experimental temperature in Celsius. Error bars show the standard error of the mean (SEM). The green dashed line is a linear fit to guide the eye.

substantial and statistically significant effect is evident. Between the lightest and heaviest isotopes, the predicted temperature difference is over 80°C , sufficient to be measurable in a well-designed experiment employing isotopically pure xenon.

The isotopic effect in Figure 5.12 can be plausibly attributed to the effect of mass on the vibrational frequency during thermal release. An alternative explanation focusing on implantation is less attractive, since a spectrum of implantation energies are employed and there is no obvious reason why a mass difference would generate different types of defects. Regarding the thermal release process, Figure 5.4(d) (and Movie 5.2) shows that the ^{133}Xe atom escapes after an extended period of constant “jiggling”. For about 350 ps (between $t = 50$ and $t = 400$ ps), the xenon is trapped between two graphitic shells and can be seen to move back-and-forth many times before eventually escaping. This observation helps explain why the lighter xenon isotopes release at the lower temperatures as the smaller mass implies a higher vibrational frequency and hence faster reaction rate.

5.4 Conclusion

In this chapter we developed a molecular dynamics approach to address the important unresolved question of the origin of the unimodal and bimodal thermal release patterns of noble gases from meteoritic NDs. Our technique employs a large number (circa 10^4) of small MD simulations to calculate the thermal release pattern of implanted noble gases in ND and provides detailed atomistic insight. We reproduce the known experimental profiles for helium and xenon, and propose that the nature of the noble-gas defect is the origin of the unimodal and bimodal patterns, respectively. In the case of xenon, we show that the Xe-P3 component is associated with shallow implantation on the (100) face, while the Xe-HL component is a mixture of deeply buried defects and shallow implantation on the (111) face.

The MD methodology is a natural fit for cloud-computing facilities and can be easily extended to other systems where noble gases are found in pre-solar grains. In NDs, obvious directions for future work include unimodal release in ^3He , ^{20}Ne , ^{21}Ne and ^{22}Ne and bimodal behaviour of ^{38}Ar , ^{36}Ar , ^{84}Kr and ^{86}Kr . As an additional investigation tool, it is also possible to exaggerate the effect of mass, and study isotopes that do not have a laboratory equivalent (e.g., ^{100}Xe). Aside from NDs, there are several other important pre-solar materials where our MD methodology can be applied. These include silicon carbide and graphite (Ott, 1993, 2007, 2014; Amari et al., 1990, 1993; Davis, 2011). All three of these pre-solar materials have high melting points and therefore are suitable for our Arrhenius-based approach. While we are unaware of any study of noble gas incorporation in these pre-solar materials, there are a number of successful atomistic simulation studies of high-temperature effects in silicon-carbide (Fujisawa et al., 2019), graphite and carbide-derived-carbons (de Tomas et al., 2017, 2018). These structures provide a natural starting point for further atomistic simulations to reveal the astrophysical secrets of noble gases in pre-solar grains.

Chapter 6

Plastic deformation of single crystal diamond nanopillars

The main text and most of the figures comprising this chapter have been published in *Advanced Materials*, (2020) 1906458. This chapter is motivated by an experimental study of bending diamond nanopillars in an electron microscope performed by colleagues at the University of Technology Sydney (see Section 1.1.2). Here, molecular dynamics simulations are performed to demonstrate that nanoscale diamond nanopillars can undergo a new form of plastic deformation that depends critically on the nanopillar dimensions and crystallographic orientation of the diamond. The plastic deformation is potentially explained by the emergence of an ordered allotrope of carbon that we name O8-carbon. The new phase is predicted by our atomistic simulations of the deformation dynamics, which show how the sp^3 bonds of (001)-oriented diamond restructure into O8-carbon in localized regions of deforming diamond nanopillars. Our results demonstrate novel mechanical behaviour of diamond and provide important understanding into the deformation dynamics of nanostructured materials.

6.1 Introduction

Understanding mechanical deformation and failure mechanisms of carbon-based materials is very important in technological applications. For example, one-dimensional carbon nanotubes possess high stiffness and tensile strengths of tens of gigapascals. Diamond possesses the highest known Young's modulus amongst bulk materials and is considered the hardest natural crystal with extreme stiffness and chemical stability (Klein and Cardinale, 1993; Wort and Balmer, 2008). Diamond is also a frontrunner for emerging applications in nanophotonics (Aharonovich et al., 2011; Burek et al., 2016), microelectromechanical systems (Wu et al., 2018) and radiation shielding (Gupta et al., 2004), which require a fundamental understanding of its mechanical deformation behaviour at the nanoscale. Previous reports suggested that improvements in nanodiamond strength can be achieved by a controlled introduction of nanotwinning (Huang et al., 2014; Li et al., 2016). On the other hand, localized plastic deformation can be induced by mechanical indentation at very high temperatures (Howell et al., 2012; Gasc et al., 2015). However, due to challenges in nanofabrication of diamond, all earlier studies were done on bulk or microstructured diamond, and our understanding of the mechanical properties of nanoscale single crystal diamond is poor.

Recently, elastic deformation of diamond nanopillars was investigated by *in-situ* nanoscale indentation that demonstrated reversible elastic deformation of diamond (Banerjee et al., 2018). As discussed earlier, our colleagues (Regan et al., 2020) at the University of Technology Sydney used advances in diamond nanofabrication and a contact-free electrostatic deformation technique (Martin et al., 2015; Rajput et al., 2018) to show unprecedented plastic deformation of diamond nanopillars. The plastic deformation occurs only in nanopillars with diameters smaller than ~ 40 nm, and is dependent on the crystallographic orientation of the diamond. Specifically, it occurs only in (001)-oriented crystals, while (111)-oriented crystals undergo conventional elastic deformation and brit-

tle fracture. Full details of their deformation experiment are discussed in Section 1.1.2 and full details of their fabrication methods have been provided in the supplementary information of [Regan et al. \(2020\)](#). In this chapter, we perform molecular dynamics simulations of diamond undergoing stretching and bending deformation. Our atomistic simulations reproduce the orientation-dependence, and reveal that the plastic deformation proceeds through the formation of a new phase of ordered carbon, namely O8-carbon that is localized to the deformed regions of the bent nanopillars.

6.2 Methodology

Molecular dynamics (MD) simulations are used to model the stretching and bending of the diamond nanopillars. Nanopillars are modelled for two different orientations: (001) and (111). In the experiments by our colleagues surface of the diamond nanopillars are hydrogenated (see the supplementary information of [Regan et al. \(2020\)](#)). In this regards, in our simulation the (100) surface of the nanopillar is reconstructed in a 2×1 manner, and therefore, no hydrogen is needed to saturate carbon dangling bonds. All MD simulations are performed using LAMMPS, and similar to the two previous chapters, the Environment-Dependent Interaction Potential (EDIP) is used for carbon-carbon interactions. As shown in Chapter 3, EDIP is a highly transferable carbon potential. Energy minimization using a conjugate gradient scheme is performed prior to all simulations.

The stretching simulations are performed for three systems: (1) a bulk diamond cell of 5832 atoms ($3.2 \times 3.2 \times 3.2$ nm), which is originally from an initial $32 \times 32 \times 32$ simple cubic lattice of carbon atoms, with periodic boundary conditions in all three directions; (2) a (001)-oriented nanopillar of octagonal cross-section containing 10760 atoms of ~ 3 nm in diameter (i.e., ~ 9 simple cubic lattice) and ~ 7 nm long (i.e, 20 simple cubic lattice) with periodic boundary conditions along the (001) direction; and (3) a (111)-oriented nanopillar of hexagonal cross-section containing 10080 atoms of approximately the same size ($\sim 15 \times 29$

orthorhombic unit cells) as the other nanopillar and periodic boundary conditions along the (111) direction. Every 0.1 ps the system (coordinates and box length) is stretched along the z axial direction at a rate of 0.001 ps^{-1} . Perspective views of the three systems are illustrated in Figure 6.1. Note that the nanopillars in our simulations contain sufficiently many unit cells that the central region is bulk-like. The temperature in the systems is fixed at 300 K using the Bussi thermostat (Bussi et al., 2007) and simulations are performed in an NVT ensemble (constant number of particles, volume and temperature) with a timestep of 0.2 fs.

For the bending simulations, we consider the same diameter (001) and (111)-oriented nanopillars as for the stretching simulations (i.e., $\sim 3 \text{ nm}$), but we elongate them to $\sim 30 \text{ nm}$ in length. The (001)-oriented nanopillar contains 44245 atoms (34 simple cubic lattice in length) and the (111)-oriented nanopillar has 40320 atoms (29 orthorhombic lattice in length). Periodicity along the nanopillar longitudinal axis is removed and instead two small regions (about 1 nm height)

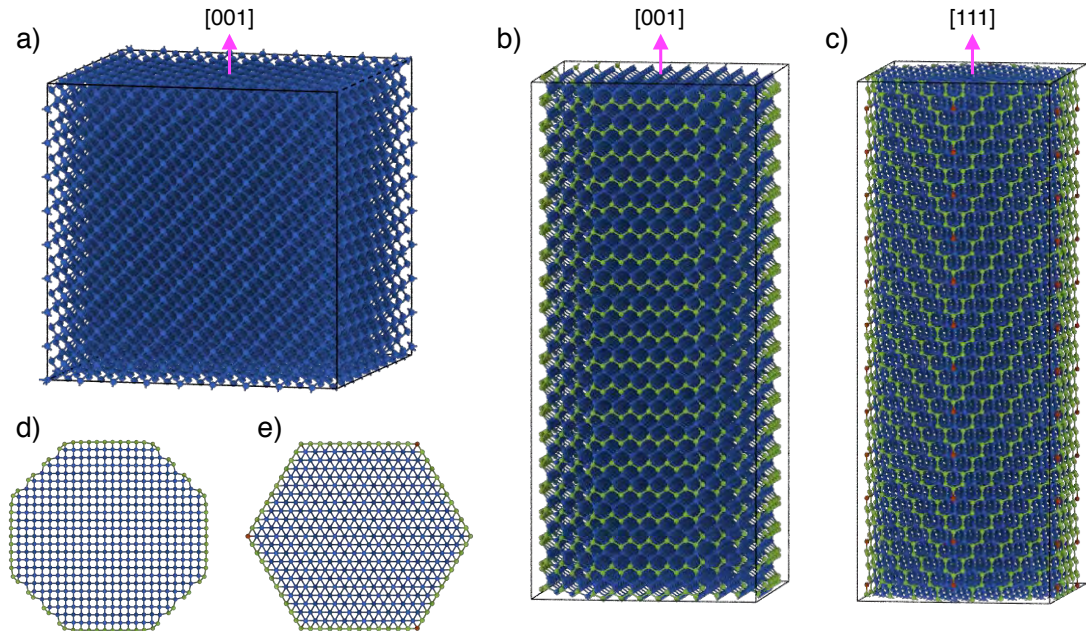


Figure 6.1: Perspective view of (a) bulk diamond, (b) (001)-oriented nanopillar and (c) (111)-oriented nanopillar. (d) Octagonal cross-section of (001)-oriented nanopillar. (e) Hexagonal cross-section of (111)-oriented nanopillar. Red, green and blue circles denote sp , sp^2 and sp^3 hybridization, respectively.

in the bottom and top of the nanopillars are fixed.* The thermostat is applied to all atoms outside those regions. In order to mimic the bending that occurs in the experiments by [Regan et al. \(2020\)](#) and was previously discussed in more details in Section 1.1.2, the upper fixed region is rotated around a $\langle\bar{1}00\rangle$ -axis for the (001)-oriented nanopillar and around $\langle\bar{2}11\rangle$ -axis for the (111)-oriented at a rate of 1.8 deg.ps^{-1} , while the position of the atoms which belong to the bottom region is fixed. Note that for both cases the origin point of axis of rotation is at $(x = 0, y = 0, z = 1 \text{ nm})$. Same as for the stretching simulations, the simulations are performed in an NVT ensemble with a timestep of 0.2 fs and by using the Bussi thermostat, the temperature in the systems is fixed at 300 K.

To study the crystal structure and energy stability of a new form of carbon, called O8-carbon, we perform density functional theory (DFT) as well as three common empirical potentials (EDIP, AIREBO ([Stuart et al., 2000](#)) and ReaxFF ([van Duin et al., 2001](#))) calculations of O8 structure. The DFT calculations which are performed by Irene Suarez-Martinez (my co-supervisor) implemented in the Vienna *ab initio* simulation package (VASP) ([Kresse and Hafner, 1993](#); [Kresse and Furthmüller, 1996](#)). The PAW pseudopotentials ([Blöchl, 1994](#); [Kresse and Joubert, 1999](#)) is used to treat outermost $2s^2 2p^2$ electrons as valence electrons of carbon atoms. The Perdew-Burke-Ernzerh of (PBE) parameterization ([Perdew et al., 1996](#)) within the generalized gradient approximation (GGA) is adopted to describe the exchange and correlation interactions. The interatomic potential calculations are performed in LAMMPS using the same approach as the EDIP calculations.

To compute the elastic constants for O8-carbon and investigate its mechanical stability, we follow a numerical approach by [de Tomas et al. \(2018\)](#). These calculations are performed using LAMMPS and the EDIP potential is used. First, we relax the simulation box (which is containing 3200 atoms, i.e., $10 \times 10 \times 4$ unit cell) and coordinates of atoms to zero pressure, followed by a small deformation

* These regions are shown in blue in Figure 6.8 and pink in [Movie 6.2](#) and [Movie 6.3](#).

(1 part in 10^3) in the three principal directions. The corresponding term of the elastic tensor C_{ij} is calculated as the ratio between the stress and the strain in the corresponding direction (Odegard et al., 2002; Caruta, 2006) via the stiffness tensor as given by

$$\begin{bmatrix} \sigma_{11} \\ \sigma_{22} \\ \sigma_{33} \\ \sigma_{23} \\ \sigma_{13} \\ \sigma_{12} \end{bmatrix} = \begin{bmatrix} C_{11} & C_{12} & C_{13} & 0 & 0 & 0 \\ & C_{22} & C_{23} & 0 & 0 & 0 \\ & & C_{33} & 0 & 0 & 0 \\ & & & C_{44} & 0 & 0 \\ & \text{Symmetric} & & & C_{55} & 0 \\ & & & & & C_{66} \end{bmatrix} \begin{bmatrix} \varepsilon_{11} \\ \varepsilon_{22} \\ \varepsilon_{33} \\ 2\varepsilon_{23} \\ 2\varepsilon_{13} \\ 2\varepsilon_{12} \end{bmatrix} \quad (6.1)$$

where σ_{ij} and ε_{ij} are components of the stress and strain tensors, respectively. To compute the elastic moduli, i.e., bulk modulus, shear modulus, Poisson's ratio and Young's moduli, we use the elastic constants C_{ij} , and by inverting the elastic constant tensor, the elastic compliance tensor S_{ij} is determined. The bulk modulus (B) and the shear modulus (G) are calculated using Hill averaging approach between the Voigt and the Reuss values (ed Levy et al., 2001a,b,c; Caruta, 2006) as follows,

$$B_{\text{Hill}} = \frac{1}{2} \left(B_{\text{Voigt}} + B_{\text{Reuss}} \right), \quad (6.2)$$

$$G_{\text{Hill}} = \frac{1}{2} \left(G_{\text{Voigt}} + G_{\text{Reuss}} \right), \quad (6.3)$$

where the B_{Voigt} and G_{Voigt} are calculated by the following equations:

$$B_{\text{Voigt}} = \frac{C_{11} + C_{22} + C_{33} + 2(C_{12} + C_{13} + C_{23})}{9}, \quad (6.4)$$

$$G_{\text{Voigt}} = \frac{C_{11} + C_{22} + C_{33} + 3(C_{44} + C_{55} + C_{66}) - (C_{12} + C_{13} + C_{23})}{15}. \quad (6.5)$$

Whereas, according to Reuss formula, B_{Reuss} and G_{Reuss} in the Equations 6.2 and 6.3 are calculated using the components of the compliance tensor S_{ij} as:

$$B_{\text{Reuss}} = \frac{1}{S_{11} + S_{22} + S_{33} + 2(S_{12} + S_{13} + S_{23})}, \quad (6.6)$$

$$G_{\text{Reuss}} = \frac{15}{4(S_{11} + S_{22} + S_{33} - S_{12} - S_{13} - S_{23}) + 3(S_{44} + S_{55} + S_{66})}. \quad (6.7)$$

Poisson' ratio ν is calculated by the elastic constants as

$$\nu = \left[1 + \frac{(C_{11} + C_{22} + C_{33})}{(C_{12} + C_{13} + C_{23})} \right]^{-1}. \quad (6.8)$$

The Young's modulus which is the average of Young's moduli in each direction is given by

$$Y = \frac{Y_x + Y_y + Y_z}{3}, \quad (6.9)$$

where the Young's moduli in each direction is calculated from the elastic compliance:

$$Y_x = \frac{1}{S_{11}}, \quad Y_y = \frac{1}{S_{22}}, \quad Y_z = \frac{1}{S_{33}}. \quad (6.10)$$

Finally, to test the thermal stability and study the strength of O8 phase, we are performed our simulations in LAMMPS using the EDIP potential. For the thermal simulations, we consider the same supercell as for computing the elastic constants, which contains 3200 carbon atoms ($10 \times 10 \times 4$ unit cell of O8-carbon), with periodic boundary conditions in all three directions. Here, after the energy minimization process to relax the simulation cell, we anneal the structure at a fixed temperature for 500 ps. The annealing simulations are performed in the NVT ensemble using the Bussi thermostat to control the temperature with a timestep of 0.1 fs. To study the strength of O8-carbon structure, we simulate the uniaxial tensile strain along with the three principal directions. A strain rate of 0.001 ps^{-1} is applied to the system every 0.1 ps. The simulations run for 400 ps in the NPT ensemble where a Nosé-Hoover thermostat is used to keep the temperature at 300 K and the pressure at zero in other directions; so the systems respond dynamically to the applied strain.

6.3 Results and discussion

The results of the simulations are presented in three parts. The first part involves the stretching of bulk diamond and two oriented nanopillars. In the second part, the crystal structure of a new form of carbon, called O8-carbon, is shown. Also, mechanical and elastic properties of O8-carbon are investigated. The final part of the results shows the simulation of bending the nanopillars.

6.3.1 Stretching simulations

The stretching simulations (Figure 6.2(a), (b) and (c)) are motivated by the tensile forces that develop on the outer surface of the diamond nanopillars during the bending experiments. For bulk diamond stretched in the (001) direction (Figure 6.2(a) and blue curve in Figure 6.2(d)), the behaviour is as expected, with the elastic region in the stress-strain curve reproducing the experimental Young's modulus in the elastic region, followed by brittle fracture along the (111) planes at a strain of $\sim 18\%$. We note that our calculations agree well with the experiments by Yu et al. (2012), where they reported that the deformation of the bulk diamond at room temperature is essentially brittle and mostly accommodated by fracturing on $\{111\}$ plane at uniaxial strains up to $\sim 15\%$. However, very different behaviour occurs when a diamond nanopillar with the same crystallographic orientation is stretched in the same manner. In this case (Figure 6.2(b) and violet curve in panel (d)) plastic deformation occurs, as seen by the terrace-like steps in the stress-strain curve that appear beyond a strain of 10.5% . The plastic deformation is associated with a phase transformation, denoted orange in Figure 6.2(b) and discussed in more detail below.

The third stretching simulation employs a nanopillar with (111) orientation, and in this case (Figure 6.2(c) and pink curve in panel (d)) brittle fracture occurs along a (111) plane. Our results are in agreement with previous theoretical and experimental results. Recently, Banerjee et al. (2018) showed experimental that single-crystal nanoneedles had a maximum tensile strain of $\sim 10\%$ in agreement

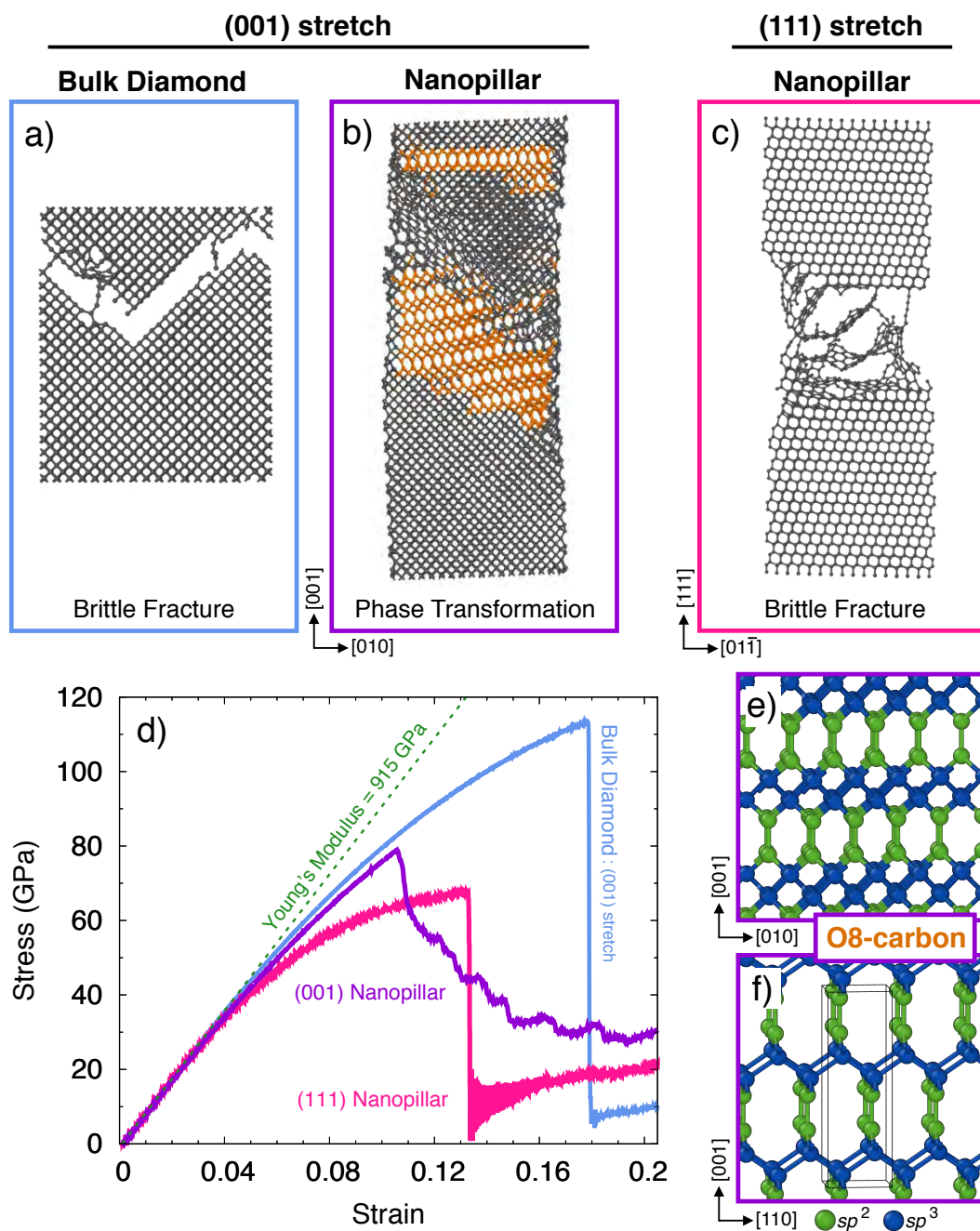


Figure 6.2: Molecular dynamics simulations of diamond under uniaxial tensile stretching. (a) Bulk diamond, exhibiting conventional brittle fracture. (b) Nanopillar with (001) orientation, exhibiting plastic deformation via a transformation to the new O8-carbon phase (orange). (c) Nanopillar with (111) orientation, exhibiting brittle fracture. (d) Stress-strain curves for the three cases, with the Young's modulus of diamond shown in green (e). (f) Two views of the new O8-carbon phase (8-atoms in an orthogonal unit cell, indicated by black lines) with sp^2 and sp^3 hybridization denoted by green and blue spheres, respectively. Snapshots in (a)–(c) are slabs of 1 nm thickness.

with their critical strain of 13% calculation through DFT modeling.

We thus see that the simulations reproduce two key experimental observations by Regan et al. (2020) (see Section 1.1.2). First, the simulations exhibit the same orientation effect seen in the experiments, with plastic deformation occurring for (001)-oriented nanopillars and brittle fracture for (111)-oriented nanopillars (see Figure 6.3 for an image sequence showing the differing behaviour as a function of strain). Second, the simulations exhibit the same nanoscale effect, with plastic deformation occurring for nanopillars, but not for bulk diamond.

Interestingly, our simulation finds a previously unknown phase of carbon that forms as a result of continuous mechanical deformation of (001)-oriented diamond nanopillars. The phase is a 50:50 mix of sp^2 (graphite-like) and sp^3 (diamond-like) hybridizations, in which the sp^2 -bonded atoms form an ethylene-like double bond unit, linked together by sp^3 -bonds. There are two types of σ -bond, one between an sp^2 and sp^3 atom and another between two sp^3 atoms. The former is slightly shorter than the bond length in diamond, while the latter is slightly larger. Due to π - π repulsion between ethylene units, symmetry is broken in the (001) plane, leading to an orthorhombic unit cell with 8 atoms. The unit cell and two different views (separated by a 45° rotation) of this structure are shown in Figure 6.2(e) and (f), with the colour coding showing the hybridization (blue = sp^3 and green = sp^2).

Further details on the crystal structure of this new form of carbon and its mechanical and elastic properties are provided in the next section. Following literature naming schemes for novel carbon phases, we assign the name O8-carbon to this structure. While a number of mixed-hybridization structures have been proposed for carbon (Hoffmann et al., 2016; Pang et al., 2016; Wu et al., 2017), none have the same unit cell and symmetry as O8-carbon. Unlike many other hypothetical phases of carbon (Zhang and Jiang, 2018) and discussed in more detail in Chapter 1, the O8 phase was not found by *ab initio* structure searches or chemical intuition whereby atoms are placed in a box. Instead, it appears

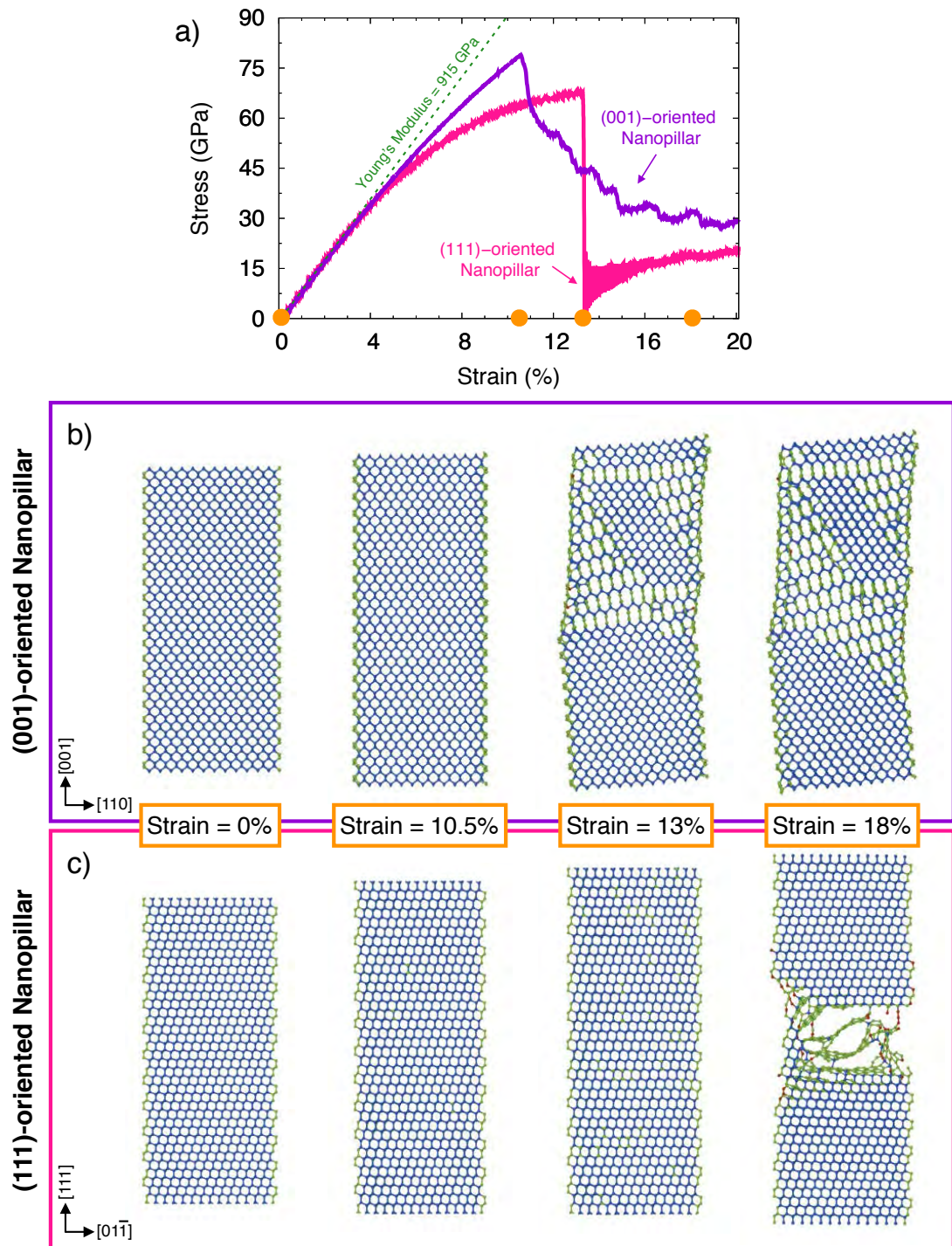


Figure 6.3: Molecular dynamics simulations of the stretching process. (a) Stress-Strain curve for (001)- and (111)-oriented nanopillars. (b) and (c) Snapshots of the stretched nanopillars along the z -direction for four different strain values (see orange circles in panel (a)). Second and third slices correspond to the maximum tensile strain for (001)- and (111)-oriented nanopillars, respectively. The largest strain corresponds to plastic behaviour at the (001)-oriented nanopillar and brittle fracture of the (111) case. The thickness of the slices is 1 nm, and the colour codings details are the same as Figure 6.1.

spontaneously under strain. This gives O8-carbon the distinguishing feature of being the result of an energetically plausible, continuous mechanical deformation from a known parent structure.

The appearance of O8-carbon during the (001) stretching simulations is shown in detail in Figure 6.4 and Movie 6.1. The sequence in Figure 6.4 shows the gradual development of the ethylene units, forming a characteristic stretched-hexagon shape as seen in Figure 6.2(f). With increasing strain, diamond bonds (shown in blue), progressively break in a zipper-like manner, transforming a large region from diamond into O8-carbon. The transformation process involves a small amount of lateral shearing, and can be clearly seen in Movie 6.1 which shows the cross-section of the nanopillar. This lateral shearing nucleates at the edge of the nanopillar and involves atomic displacements which can only occur in a nanoscale context. This explains why O8-carbon appears in the nanopillar (Figure 6.2(b)) but not in the bulk diamond simulation (Figure 6.2(a)).

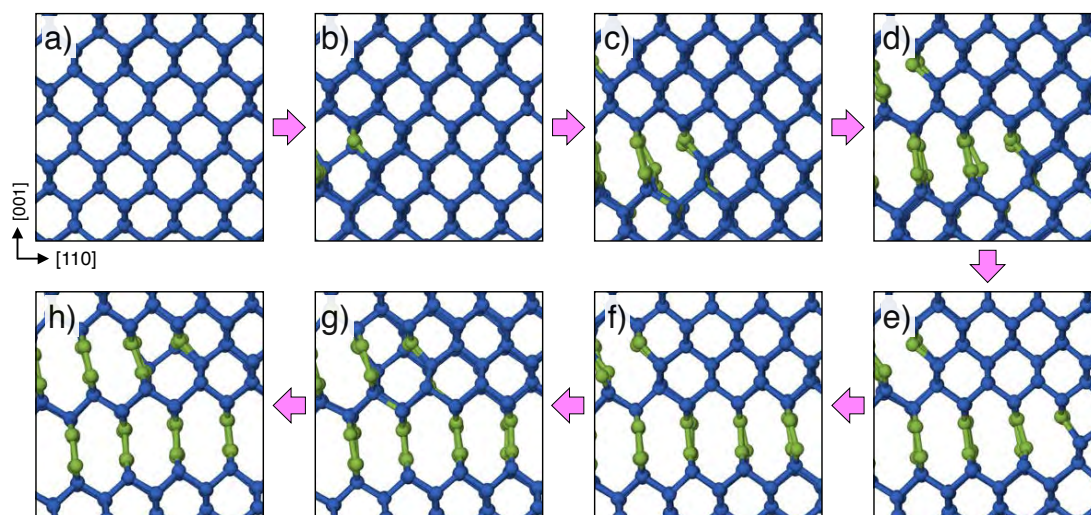


Figure 6.4: Close-up view showing the transformation of diamond into O8-carbon. The sequence shows the gradual development of the ethylene units, with increasing strain in the (001) direction. Diamond bonds (shown in blue), progressively break in a zipper-like manner, transforming a large region from diamond into O8-carbon. The thickness of the slices and the colour codings details are the same as Figure 6.3.

6.3.2 Crystal structure and properties of O8-carbon

In this Section, the crystal structure and some mechanical and elastic properties of O8-carbon are presented. In addition, the energetic, mechanical and thermal stability of O8-carbon is investigated. Figure 6.5 and Movie 6.2 show the optimized crystal structure of O8-carbon. As discussed earlier, this structure has an orthorhombic unit cell which contains 8 carbon atoms. Using the EDIP potential, lattice parameters of O8-carbon are $a = 2.487 \text{ \AA}$, $b = 2.669 \text{ \AA}$ and $c = 7.928 \text{ \AA}$, and cartesian coordinates and the hybridization type of each atom in the unit cell are provided in Table 6.1.

Energetic stability

To confirm the validity of the O8-carbon structure, in addition to the EDIP calculations, we also perform density functional theory (DFT) as well as AIREBO and ReaxFF calculations of O8 structure. As shown in Table 6.2, the lattice parameters of the EDIP simulations are all within 1.1% of those found from DFT

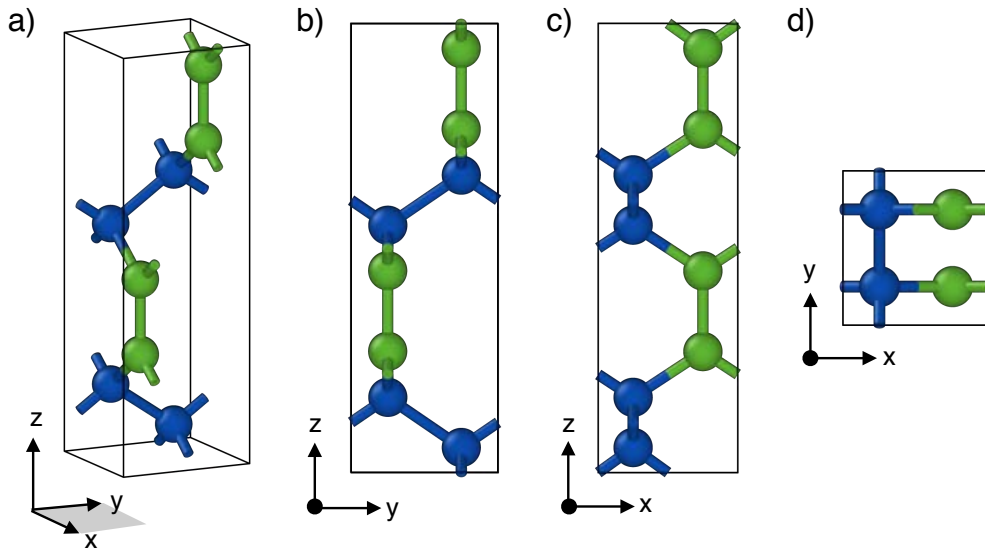


Figure 6.5: Schematic illustration of the unit cell structure of O8-carbon. (a) Perspective view of the orthorhombic crystalline structure (also see Movie 6.2). (b)–(d) Views along the x-, y- and z-directions of O8-carbon. Colour codings are the same as Figure 6.3.

Table 6.1: Cartesian coordinates and hybridization of the unit cell of O8-carbon from EDIP potential. Note that the lattice parameters are $a = 2.487 \text{ \AA}$, $b = 2.669 \text{ \AA}$ and $c = 7.928 \text{ \AA}$.

Atom ID	Cartesian coordinate (\AA)			Hybridization
	x	y	z	
1	1.865	0.657	2.159	sp^2
2	1.865	0.657	3.595	sp^2
3	1.865	1.970	6.123	sp^2
4	1.865	1.970	7.560	sp^2
5	0.627	0.657	1.343	sp^3
6	0.627	1.970	0.447	sp^3
7	0.627	0.657	4.411	sp^3
8	0.627	1.970	5.306	sp^3

calculations, confirming the general correctness and stability of the structure. In terms of density, EDIP potential predicts that O8-phase has a density of 3.08 g/cc, compared to 3.01 g/cc with DFT calculations. We also examine the energetic stability of O8-carbon with respect to diamond. All three potentials have almost exactly the same energy difference relative to diamond, being 0.2 eV/atom less stable. The DFT calculations found a similar value of 0.3 eV/atom. Given that

Table 6.2: Lattice parameter, density and energy difference (ΔE) between O8-carbon and diamond. Calculations performed using DFT and three interatomic potentials for carbon. The O8 phase is stable in all calculations, and differences in energetics and lattice parameters are minor.

Method	Lattice parameters (\AA)			Density (g/cm^3)	ΔE (eV/atom)
	a	b	c		
DFT	2.513	2.697	7.832	3.01	0.30
EDIP	2.487	2.669	7.928	3.08	0.19
AIREBO	2.524	2.691	7.988	3.06	0.21
ReaxFF	2.532	2.746	7.952	2.89	0.19

DFT calculations have inherent uncertainties arising from the choice of functional and pseudopotential, these cohesive energies are reasonable. Furthermore, recent experiments involving laser irradiation of nanowires (Zhang et al., 2017) found evidence for a novel carbon phase, known as T-carbon (see Figure 1.10(d)), which is a full 1 eV/atom less stable than diamond (Sheng et al., 2011), and hence the present calculations using EDIP are well within the realms of plausibility.

Mechanical stability

Next, we study the mechanical stability of O8-carbon by computing the elastic constants, following a numerical approach as discussed in the Methodology. O8-carbon has nine independent elastic constants C_{ij} , which are listed in Table 6.3, and for a mechanically stable orthorhombic structure its corresponding elastic constants C_{ij} should satisfy the following criteria (Wu et al., 2007):

$$\begin{aligned} C_{11} > 0, \quad C_{22} > 0, \quad C_{33} > 0 \\ C_{44} > 0, \quad C_{55} > 0, \quad C_{66} > 0 \end{aligned} \quad (6.11)$$

$$\left[C_{11} + C_{22} + C_{33} + 2(C_{12} + C_{13} + C_{23}) \right] > 0 \quad (6.12)$$

Table 6.3: Elastic constants and elastic moduli of O8-carbon. Calculated elastic constants, bulk modulus, shear modulus, Poisson’s ratio and Young’s moduli in each direction of O8-Carbon.

Elastic constants (GPa)								
C_{11}	C_{22}	C_{33}	C_{44}	C_{55}	C_{66}	C_{12}	C_{13}	C_{23}
1052	473	1083	57	391	221	107	221	98
Elastic moduli								
Bulk modulus (GPa)	Shear modulus (GPa)	Poisson’s ratio	Young’s moduli (GPa)					
			Y_x	Y_y	Y_z			
354	408	0.15	991	457	1025			

$$\begin{aligned}
(C_{11} + C_{22} - 2C_{12}) &> 0 \\
(C_{11} + C_{33} - 2C_{13}) &> 0 \\
(C_{22} + C_{33} - 2C_{23}) &> 0
\end{aligned}
\tag{6.13}$$

Note that all the calculated elastic constants obey all of the above-mentioned conditions, indicating that the O8-carbon structure is mechanically stable. Table 6.3 also provides the computed bulk modulus, shear modulus, Poisson's ratio and Young's moduli for O8-carbon.

Thermal stability

To check the thermal stability of O8-carbon at high temperature, we perform MD simulations at three different annealing temperatures, 500, 750 and 1000 K. Figure 6.6 shows the fluctuations of the potential energy as a function of simulation time at 1000 K. The structures around 1 ps and 500 ps are also given in Figure 6.6. We found that the geometry of O8-carbon remains intact after heating for more than 500 ps, and the potential energy remains almost invariant.

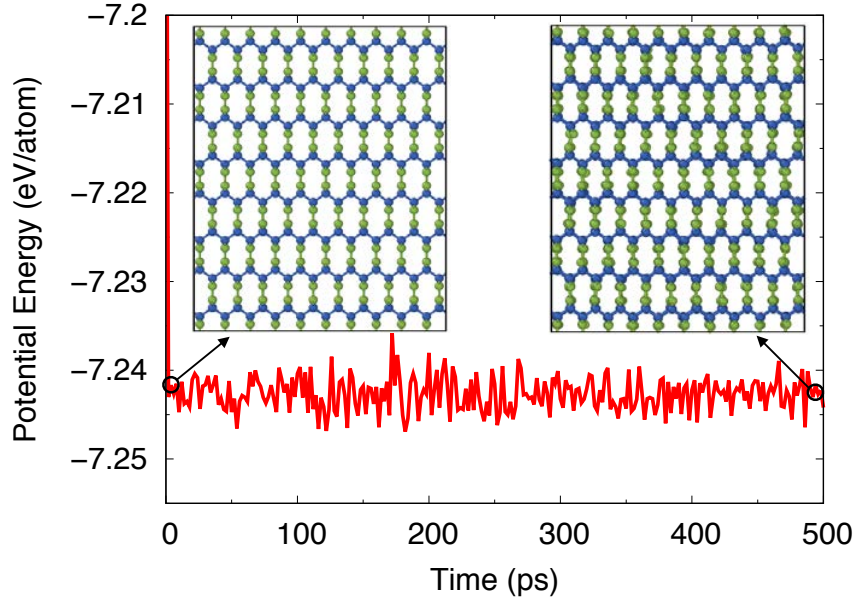


Figure 6.6: Molecular dynamics simulation of thermal stability of O8-carbon. Potential energy fluctuations as a function of the simulation time at 1000 K. Inset depicts the snapshots of the simulated system. The thickness of the slices are 1 nm and colour codings details are the same as Figure 6.5.

These results suggest that O8-carbon is stable at high temperatures.

Strength of O8-carbon

To examine the strength of O8-carbon, as discussed before in Section 6.2, we calculate tensile stress-strain curves along the x -, y - and z -directions. Figure 6.7 illustrates stress-strain curves for three directions of O8-carbon. The structure can resist considerable strain (~ 0.21 in x -direction and ~ 0.19 in y and z -directions) in the linear/elastic regime indicating that O8-carbon is quite ductile. Beyond the maximum tensile strength, the structure is fractured. Figure 6.7 also shows that the ultimate tensile strength, which is obtained from the point of maximum stress in the stress-strain curves, is dependent on the crystallographic orientation. The ultimate tensile strength in the y -direction is about 50 GPa, significantly lower than the ultimate tensile strength in the x and z -directions, of ~ 120 GPa and ~ 130 GPa, respectively. Another point to be considered is that we can calculate the Young's modulus from the slope of the stress-strain curves in the elastic

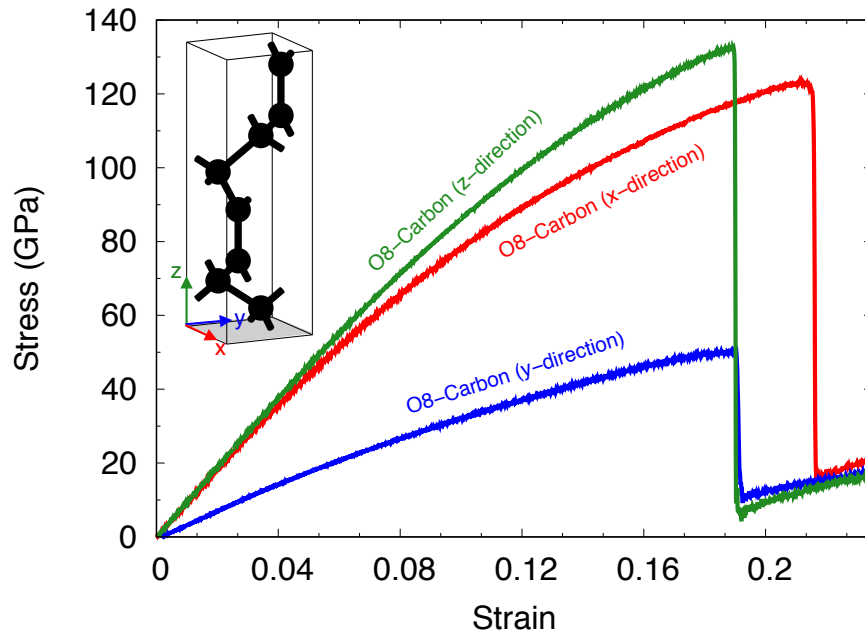


Figure 6.7: Stress-strain curve for tensile strain along the three principal axes of O8-carbon. Inset shows the perspective view of the unit cell of O8-carbon (similar to Figure 6.5(a)).

region. Young's moduli in x , y and z -directions are ~ 910 GPa, ~ 380 GPa and ~ 950 GPa, which have a good correlation with the values obtained from the elastic constant tensor (see Table 6.3), with differences of about 8% for Y_x and Y_z , and $\sim 20\%$ for Y_y . These difference could be arising from the choice of elastic region and calculation of the slope of the stress-strain curves.

6.3.3 Bending simulations

The second set of bending simulations assess how the stretching results translate into a curved geometry. Using diamond nanopillars with a 3 nm diameter, the same as the stretching simulations, nanopillars 30 nm long were bent to large angles. As discussed before in Section 6.2, all atoms are free to move, except for the atoms at the top and bottom regions of the pillar (denoted blue in Figure 6.8). Consistent with the stretching simulations, the (001) nanopillar develops a region of O8-carbon once the nanopillar is sufficiently bent (Figure 6.8(a)–(c) and Movie 6.3), while the (111) nanopillar undergoes brittle fracture (Figure 6.8(d)–(f) and Movie 6.4). Simulations of a 2 nm diameter (001) nanopillar show that the deflection angle needed to produce the O8 phase increases with decreasing pillar diameter. That is consistent with experiments in which the minimum diameter was 7 nm.

Finally, it should be noted that our experimental colleagues tried very hard to obtain transmission electron microscopy (TEM) image of the bent regions to identify the O8 phase, but it proved to be very difficult due to the small size of the pillars. Therefore, rigorous aberration-corrected TEM analysis will also be needed to identify O8-carbon experimentally. From simulation point of view, it is essential to calculate the phonon dispersion to examine the dynamical stability of O8-carbon. In addition, to investigate the electrical properties, the electronic band structures and the density of states should be calculated in future studies.

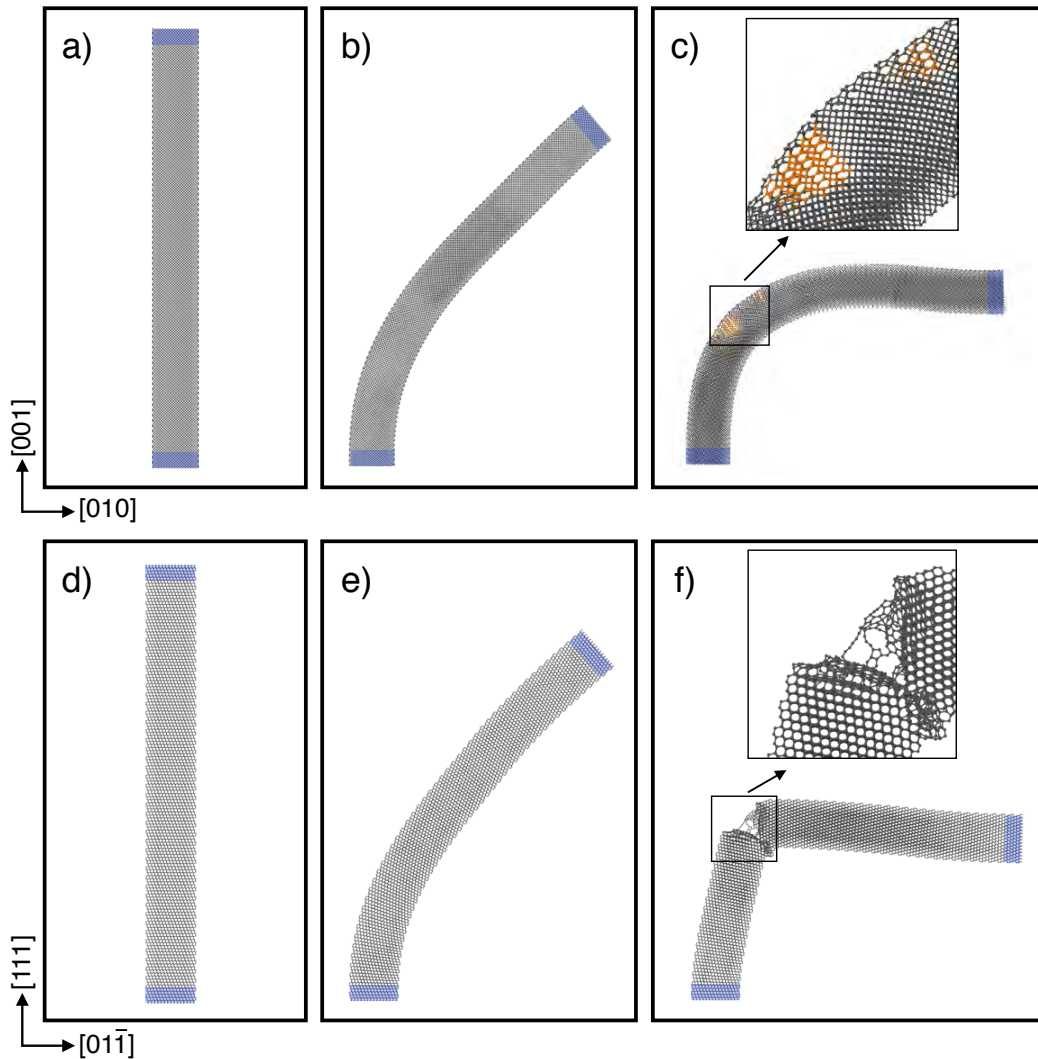


Figure 6.8: Molecular dynamics simulation of bending of 3 nm diameter nanopillars. The top row is a sequence for a (001)-oriented nanopillar while the bottom row is for a (111)-oriented nanopillar. Snapshots are slabs with a thickness of 1 nm. Blue atoms are constrained as described in the text. (a) and (d) Initial configuration, (b) and (e), pillars bent to 45 degrees, (e) (001)-oriented nanopillar, showing the appearance of O8-carbon indicated by orange atoms, and (f) (111)-oriented nanopillar, that has undergone brittle fracture along a (111) plane.

6.4 Conclusion

In this chapter, we used molecular dynamics simulations to study the mechanical deformation of diamond nanopillars. Following an experimental study of macroscopic plastic deformation of single-crystal diamond nanopillars by colleagues at

the University of Technology Sydney, we provided atomistic details of the plastic, elastic and brittle failure of diamond nanopillars. Atomistic simulations reproduced all experimental observations and indicated that the plastic deformation is strongly dependent on the size of the nanopillar and crystallographic orientation of the diamond. Simulations also suggested a phase transition from pure sp^3 carbon to an O8-carbon phase that forms spontaneously under strain and mediates the plastic deformation. The nanopillars used in the simulations have a finite size (diameter), and their length is smaller than the one in the experiment, but they contain sufficient number of unit cells so that the central region becomes bulk-like. Accordingly, the appearance of the O8-carbon and its propagation across the full width of the nanopillar in the stretching simulations represent the experimental length scale. Our results highlight the need to expand the present understanding of nanostructured materials' mechanical properties, particularly that of carbon-based materials. Our findings will inform the design and engineering of new devices based on nanostructured materials, with improved performance in a range of fields such as sensing, energy generation and optomechanics.

Chapter 7

Epitaxial formation of silicon carbide on (100) diamond

The main text and most of the figures comprising this chapter have been published in *ACS Applied Electronic Materials* 2, (2020) 2003–2009, and also have been highlighted on the front cover of the journal (see Appendix D). This chapter is motivated by an experimental study of heteroepitaxial growth of silicon carbide on diamond performed by colleagues at the University of Melbourne and discussed earlier in Section 1.1.3. Here, molecular dynamics simulations are performed to understand the nature of the interface between diamond and silicon carbide. The results indicate that there is an optimal bonding scheme with no dangling bonds that could cover the entire surface area in a regular pattern with 11×11 diamond to 9×9 silicon carbide supercell arrays. We also show that this lattice mismatch ($\sim 22\%$) requires defects in a two-dimensional plane without forming extended defects in three-dimensions. At a fundamental level, these results redefine our understanding of heterostructure formation with a large lattice mismatch.

7.1 Introduction

Diamond is a wide-bandgap semiconductor with an extreme thermal conductivity of 2400 W/m/K (Isberg et al., 2002) that is of acute interest for novel quantum and high power electronic devices (Trew et al., 1991; Okushi, 2001; Wort and Balmer, 2008; Willander et al., 2006). It would be highly desirable to incorporate diamond into electronic structures such as high power silicon carbide converters to improve device effectiveness through enhanced cooling; this is also true for nanoscale silicon device structures that are limited by high temperature (Weitzel et al., 1996; Meyer et al., 2003). The small lattice parameter of single crystal diamond, however, limits the choice of materials which can form heterostructures without significant interfacial strain relief by defects such as screw dislocations, threading faults, and twinned growth (Bean et al., 1984; People and Bean, 1985; Chen and Washburn, 1996; Freund and Suresh, 2004). Defects compromise the quality of the heteroepitaxial layer by extending through the grown material and are undesirable for high quality heterostructures as they degrade thermal transport and layer adhesion (Goyal et al., 2010; Imura et al., 2011; Cervenka et al., 2012). Furthermore, growth of single crystal diamond on different materials is prohibitively difficult and typically results in polycrystalline material (Jiang and Jia, 1995; Schreck et al., 2014; Khmelnitskiy, 2015).

Heteroepitaxy with single crystal diamond growth is difficult and subjects the substrate material to the harsh diamond growth environment (Schreck et al., 2001, 2014) and also typically results in polycrystallinity (Aleksov et al., 2003; Koizumi et al., 2018; Stoner and Glass, 1992). These considerations, together with the recent introduction of wafer-scale single crystal diamond (Yamada et al., 2013, 2014; Schreck et al., 2014), make it highly desirable to use diamond as the substrate upon which high-power electronic materials are then epitaxially grown and formed. To date, only aluminium nitride (AlN) and aluminium gallium nitride (AlGaN)/gallium nitride (GaN) heterostructures have successfully used diamond as a substrate for growth, with the diamond interface studied

in detail (Hirama et al., 2010, 2011; Alomari et al., 2010). Unfortunately, the mismatch-induced strain in the AlN and AlGaN/GaN structures is relieved by a high density of defects in the AlN lattice which also created a large amount of dangling bonds (Hirama et al., 2010). In addition, high electron mobility transistors made of AlGaN/GaN on diamond required thick buffer layers to construct operational devices (Alomari et al., 2010; Hirama et al., 2011, 2012). There is evidence that coherent interfaces are possible when diamond is grown onto silicon carbide (Koizumi et al., 2018), but they lie amongst typically unoriented polycrystalline diamond with poor interface characteristics. Growth of silicon carbide onto diamond produces similar results, although it has been shown that a silicon buffer layer prior to silicon carbide formation can enable growth of oriented silicon carbide by chemical vapor deposition (Soulière et al., 2014). Domain matching epitaxy is a technique used to minimize the interface mismatch in high lattice misfit materials (Narayan and Larson, 2003), but diamond's extremely high lattice density prohibits such matching in most cases.

Our colleagues (Tsai et al., 2020) at the University of Melbourne demonstrate experimentally that silicon carbide can be grown heteroepitaxially on single-crystal diamond (see Section 1.1.3 and Figure 7.1). They produced a coherent and seemingly strain-free interface in localized regions. This builds on a silicon surface termination procedure developed in earlier work (Schenk et al., 2015) and may explain the observed benefit of silicon-rich deposition prior to chemical vapor deposition growth of silicon carbide on diamond (Soulière et al., 2014). The absence of measured strain is remarkable given the large lattice mismatch (22%) of silicon carbide relative to diamond. Furthermore, the high degree of coherence between the lattices suggests that additional strain relief mechanisms are present, beyond standard domain matching epitaxy, such as that seen in titanium nitride/silicon (Narayan and Larson, 2003; Pizzagalli et al., 2003). In this chapter, atomistic simulations are performed to understand the nature of the interface and suggest that the lattice mismatch is resolved through bonding reconstructions that are

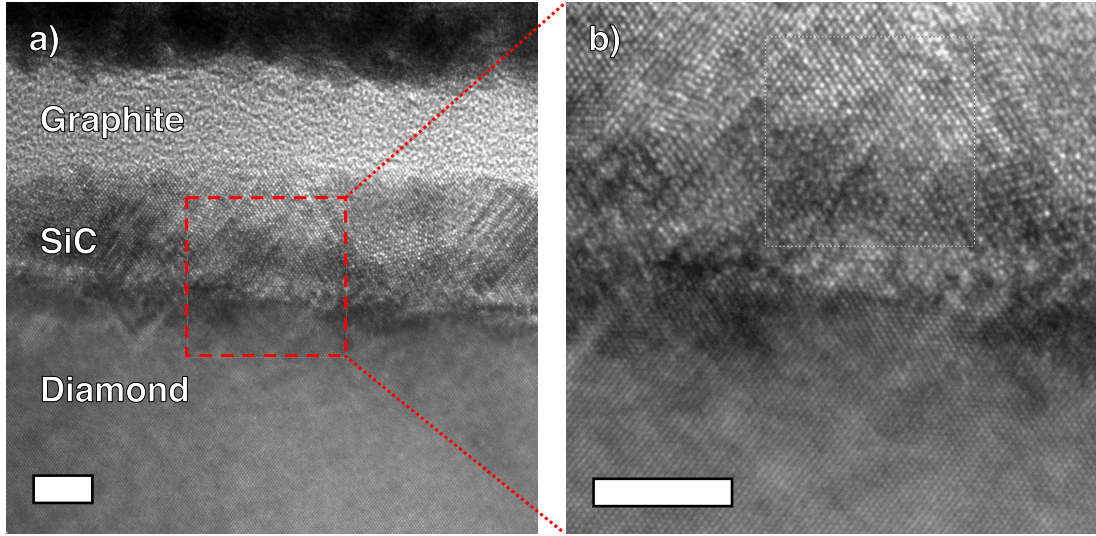


Figure 7.1: (a) Cross-sectional high-resolution TEM (5 nm scale bar) of the graphite, silicon carbide (SiC) and diamond layers structure. (b) Magnification of the selected area in (a) demonstrating a coherent interface between SiC and diamond. Both panels are taken from Figure 1.22.

restricted to the interfacial layers without extending into the grown film. These relaxed reconstructions, similar in form to those simulated at silicon and silicon carbide interfaces (Cicero et al., 2002b; Pizzagalli et al., 2003), effectively passivate the atomic coordination structures that give rise to the dangling bonds that are otherwise abundant in low-quality, highly mismatched interfaces.

7.2 Methodology

The molecular dynamics (MD) simulations are performed using the LAMMPS package (Plimpton, 1995). Interactions are described using the Tersoff potential for silicon carbide (Tersoff, 1989), which is based on earlier Tersoff potentials for silicon (Tersoff, 1986) and carbon (Tersoff, 1988). With this potential all interactions are captured in a single framework. The interface was rectangular in shape, with the silicon carbide side containing 18 silicon carbide unit-cells in the $[1\bar{1}0]$ direction, 9 silicon carbide unit cells in the $[110]$ direction and 9 silicon carbide unit-cells in the $[001]$ direction. On the other side of the interface,

the corresponding number of diamond unit cells is 22, 11 and 11, respectively. Note that a full discussion of the determination of the number of unit cells is provided later in Section 7.3.1. The atomistic model of the prepared silicon carbide/diamond interface is illustrated in Figure 7.2.

To reproduce the experimental conditions discussed in Section 1.1.3, periodic boundary conditions were employed in the $[110]$ and $[1\bar{1}0]$ directions but not in the transverse direction (see Figure 7.2). The system dimensions are approximately $54 \text{ \AA} \times 27 \text{ \AA} \times 40 \text{ \AA}$. No attempt is made to manually reconstruct the interface, and the initial coordinates simply consisted of a cleaved silicon carbide crystal adjacent to cleaved diamond crystal. Temperature control was achieved using the Bussi thermostat (Bussi et al., 2007) and simulations were performed in an NVT ensemble (constant number of particles, volume and temperature) with a timestep of 0.2 fs. Further details about the thermostat, NVT ensemble and periodic boundary conditions are provided in Section 1.2.1. Coordination analysis

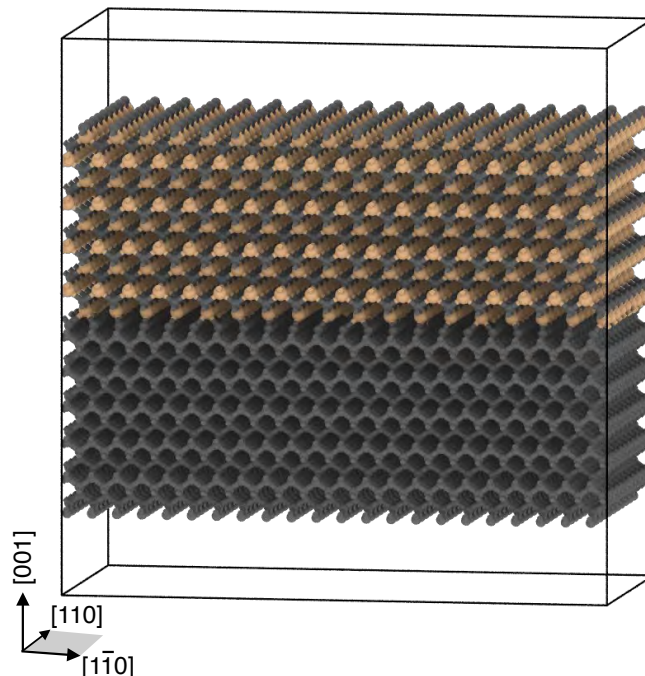


Figure 7.2: Perspective view of the structure of the silicon carbide/diamond interface. Black lines represent the simulation cell and periodic boundary conditions are applied only in the $[110]$ and $[1\bar{1}0]$ directions. Gray and light brown spheres represent carbon and silicon atoms, respectively.

involved counting the number of neighbors within cutoffs of 1.85, 2.35 and 2.8 Å for carbon–carbon, carbon–silicon and silicon–silicon distances, respectively. For the purposes of analysis and visualization, atoms are considered to be sp^2 and sp^3 hybridized if they had three and four neighbors, respectively.

7.3 Results and discussion

To understand the origin of the low-strain epitaxial growth of silicon carbide on diamond as shown in Figure 7.1 and discussed in more details in Section 1.1.3, MD simulations are performed to establish how strain could be resolved at the interface without propagation of dislocations in silicon carbide. The results are presented in three parts. Firstly, we investigated the number of the unit cells required to minimize the lattice mismatch. Secondly, we model the interface reconstruction of the silicon carbide/diamond structure. Lastly, in order to quantify the energetics of the reconstruction, the interfacial energy is computed.

7.3.1 Number of unit cells

The first step is the determination of the smallest commensurate matching lattice cells (Narayan and Larson, 2003), as summarized schematically in Figure 7.3. Panel (a) shows four layers at the interface where each sphere represents a 4-atom tetragonal unit cell with height a and in-plane width of $a/\sqrt{2}$. The blue and red shading highlights the large (22%) in-plane mismatch between 3×3 supercells of silicon carbide and diamond. Note that the lattice parameters for silicon carbide (SiC) and diamond, respectively, are $a_{\text{SiC}} = 4.360 \text{ \AA}$ (Taylor and Jones, 1960; Järrendahl and Davis, 1998) and $a_{\text{diamond}} = 3.567 \text{ \AA}$ (Krüger, 2010). It is visually apparent in Figure 7.3(a) that 4 unit cells of silicon carbide match reasonably closely to 5 unit cells of diamond, and here the supercell mismatch is just 2.3%. Aligning the two interfaces for this ratio of 4:5 unit cells results in the Moiré pattern shown in Figure 7.3(b). From an atomic perspective, the Moiré pattern

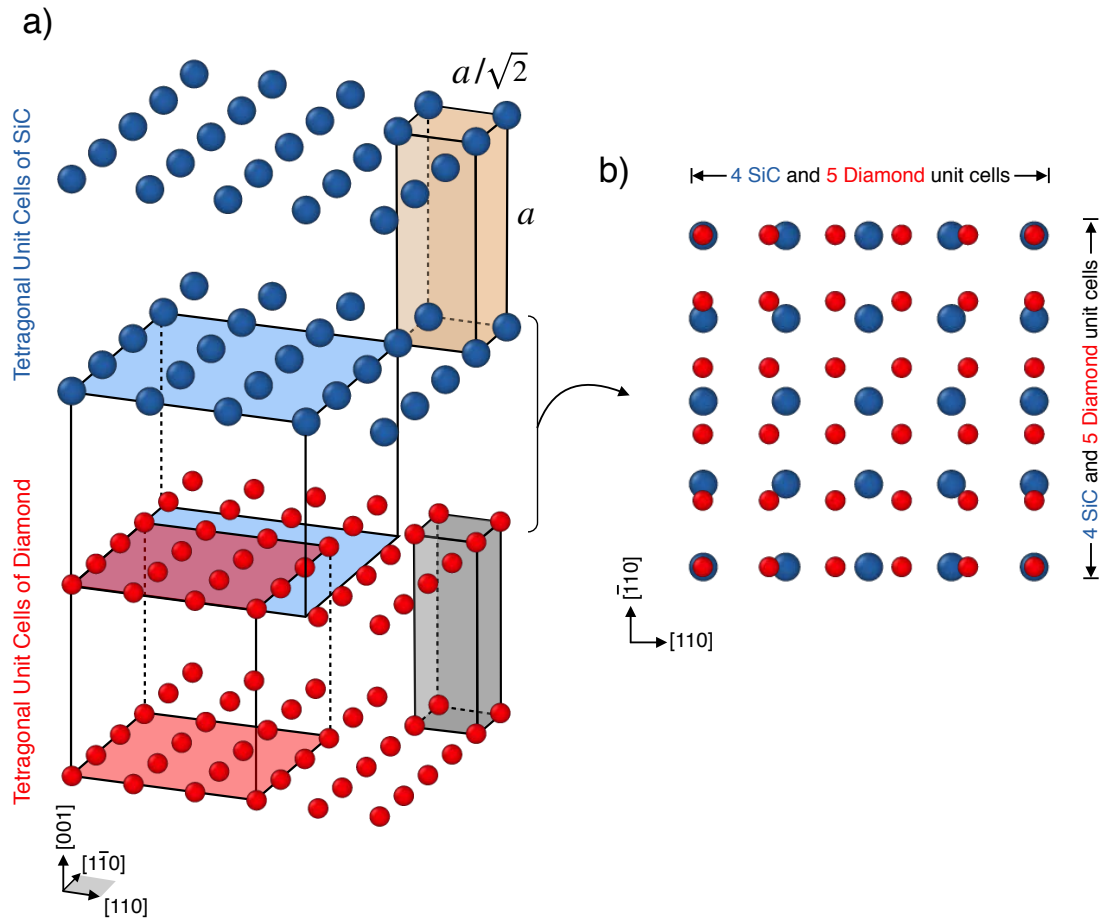


Figure 7.3: (a) Schematic of four interfacial layers, where each sphere represents a tetragonal unit cell with a 4-atom basis. Shaded areas compare 3×3 unit supercells, showing large deviations between cubic polytype silicon carbide (3C-SiC) and diamond. (b) Strained 4×4 silicon carbide supercell overlaid on a 5×5 diamond supercell resulting in a Moiré pattern.

raises a challenge as it is unclear how to reconstruct the interface without creating dangling bonds and other high energy configurations. Studies of lattice mismatch sometimes trivialize these interfaces with one-dimensional schematics that do not account for the more difficult two-dimensional problem. Figure 7.4 shows that the 4:5 combination is not the only possibility for the silicon carbide/diamond interface, since adding an extra unit cell to both sides of the interface yields a 5:6 ratio with a slightly lower supercell mismatch of 1.8%. More interesting is a 9:11 ratio for which the mismatch falls to an astonishingly low 0.008%. The 9:11 ratio has previously been noted when patches of coherent diamond grew on cubic poly-

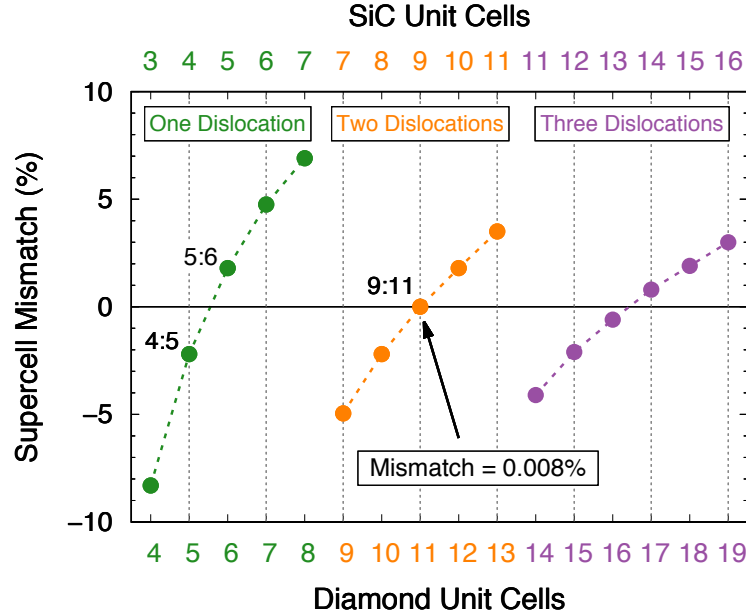


Figure 7.4: Plot of supercell mismatch percentage between various combinations of silicon carbide and diamond unit cells. Ratios denote the number of silicon carbide and diamond unit cells, respectively.

type silicon carbide (3C-SiC) (Koizumi et al., 2018), but no quantitative bonding arrangement was provided. This configuration, which involves two dislocations as indicated by the orange text in Figure 7.4, is the focus of our attention for the remainder of this chapter.

7.3.2 Interface reconstruction

We explore possible interface reconstructions for the 9:11 ratio using the Tersoff potential (Tersoff, 1989). This involves: (i) energy minimization to relax the initial structure, (ii) annealing at a fixed temperature, and (iii) minimization back to zero Kelvin. Four annealing temperatures are used (500, 1000, 1500 and 2000 K) and the annealing time is 20 ps. Note that as the goal of the annealing is to reconstruct the interface without melting the structure, these annealing temperatures are sufficiently high to have some atomic motion, but not high that it melts. Figure 7.5 shows the snapshots of four annealed silicon carbide/diamond structures. The best results are achieved at 1000 and 1500 K

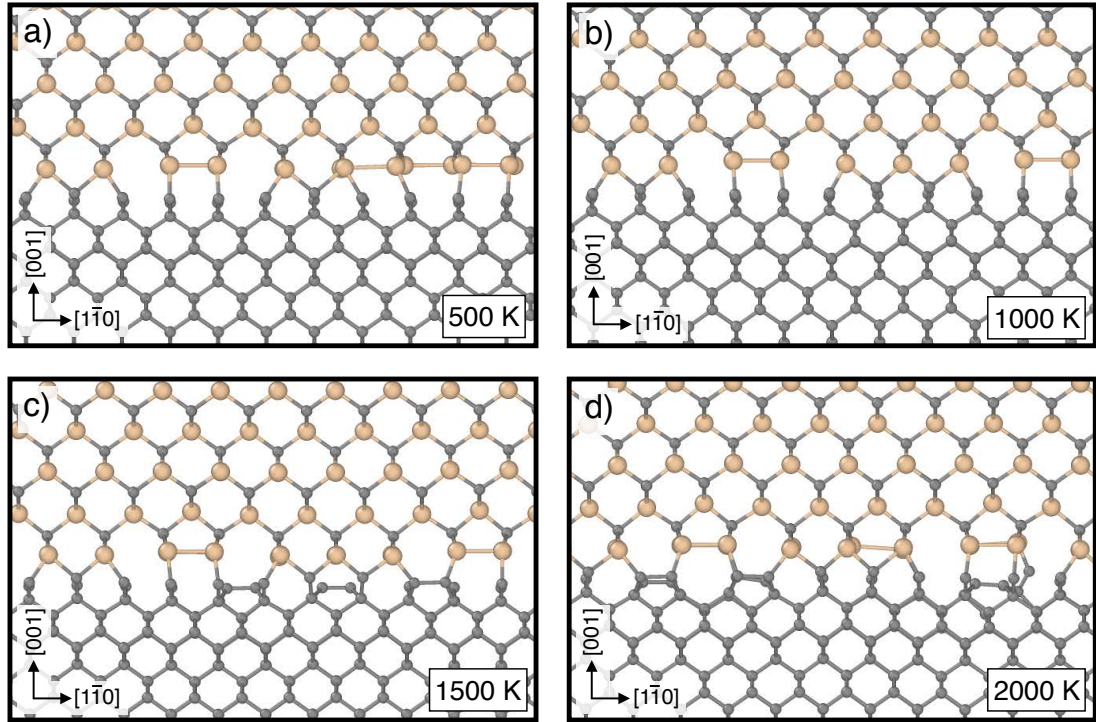


Figure 7.5: Structures of the four annealed silicon carbide/diamond interfaces. Views looking along the $[110]$ direction. Structures are annealed at (a) 500, (b) 1000, (c) 1500 and (d) 2000 K annealing temperatures for 20 ps. The carbon and silicon atoms are shown as gray and light brown spheres.

(see Figure 7.5(b) and (c)), where the interface spontaneously reconstructed to form silicon–silicon and carbon–carbon dimers in two characteristic motifs. One motif spanned 4 silicon carbide unit cells and 5 diamond unit cells, while the other motif spanned 5 silicon carbide unit cells and 6 diamond unit cells. Pleasingly, both of these ratios correspond to small supercell mismatches (2.2% and 1.8%) as seen in Figure 7.4.

We manually assemble the 4:5 motif adjacent to a 5:6 motif to create a 9:11 reconstruction. Most of the atoms have four neighbours and are sp^3 bonded, with the exception of two rows of sp -bonded atoms extending along the $[1\bar{1}0]$ direction. These atoms are manually converted to sp^2 by displacing the atoms to form pairs. Since a pairing arrangement requires an even number of diamond unit cells, we duplicate the system along one axis to achieve an 18:22 ratio. For clarity, the discussion and figures consider only a single 9:11 section.

Diagrams of the 9:11 interface are illustrated in Figure 7.6. Panel (a) shows that the sp^2 carbons are separated by either five or six diamond unit cells in the [110] direction and represent the termination of a dislocation, labelled in red. Rotation of the section indicated by the dashed boxes in panel (a) shows more repeating motifs, as seen in Figures 7.6(b) and (c). Panel (b) reveals a second pair of dislocations associated with dimers. silicon–silicon bonds form every 4 or 5 silicon carbide unit cells at the silicon carbide interface and carbon–carbon bonds form on either side in the diamond lattice. This combination of point defects in the [110] and $[\bar{1}\bar{1}0]$ directions allows the additional lattice units of diamond to terminate at the interface without creating extended defects in the grown film. Figures 7.6(f) and (g) are the same as panels (a) and (b) but with guidelines added to highlight how the additional diamond unit cells terminate at the dislocation core. As a result, defects in the heterostructure are restricted to the two-dimensional plane of the interface, as opposed to propagating through the third-dimension of the grown film.

The dislocation highlighted in Figure 7.6(b) is magnified in panel (d), demonstrating how the core of the dislocation involves heptagonal and pentagonal rings to accommodate the extra diamond unit cell. This creates a symmetry around the silicon–silicon bond which is present elsewhere in the interface, as seen in the other dislocation at the right of Figure 7.6(b). Similarly, Figure 7.6(e) expands the shaded area in panel (a) to highlight how the core of the dislocation involves sp^2 carbon atoms along the $[\bar{1}\bar{1}0]$ direction. Figure 7.7 shows full details of bond lengths of two types of point defect, as highlighted in Figure 7.6(d) and (e). In Figure 7.6(h), the carbon and silicon atoms at the interface are displayed in plan-view, showing the four dislocations. The peach lines indicates the dislocations associated with the dimers, while the sp^2 carbons in blue indicate the other pair of dislocations. It is worth noting that the sp^2 carbons do not affect the bonding scheme of the remaining interface and that the dislocation core is self-contained within its own row. We note that in our model, carbon–carbon and

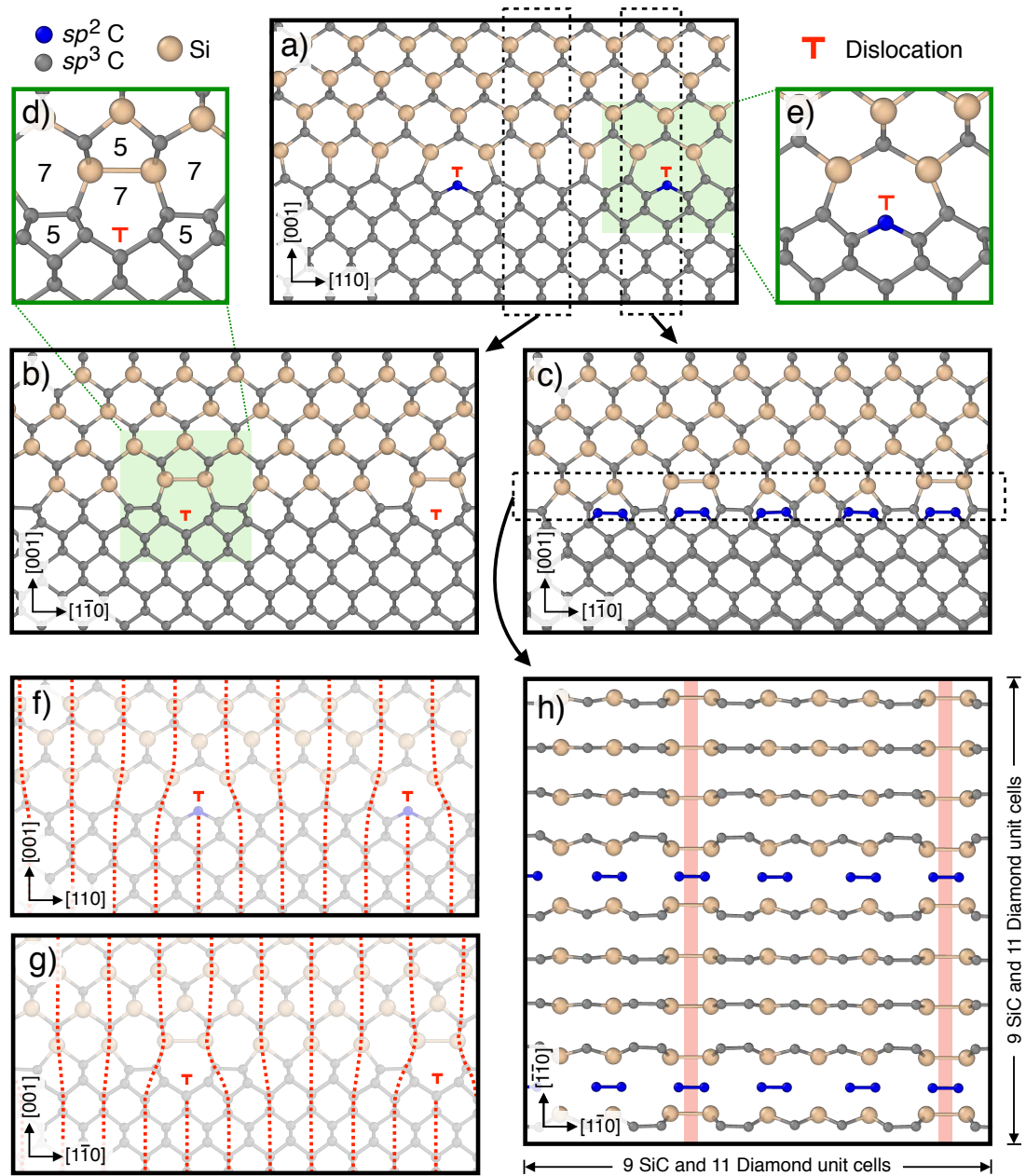


Figure 7.6: Simulated structure for a silicon carbide/diamond heterojunction with periodic carbon-carbon and silicon-silicon dimerizations, found to satisfy all bonding requirements and act as interface pinned dislocations. (a) View looking down the $[1\bar{1}0]$ direction. Carbon point dislocations (red) correspond with sp^2 bonded atoms (blue) every five or six diamond units. Dashed boxes are lattice slices that are viewed down the $[110]$ direction in (b) and (c). Magnified view of shaded green regions are shown in (d) and (e). Point dislocations in (a) and (b) are highlighted via dashed guidelines in (f) and (g). Dashed box in (c) is a lattice slice shown in plan view in (h). Peach lines indicate columns of silicon-silicon covalent bonds.

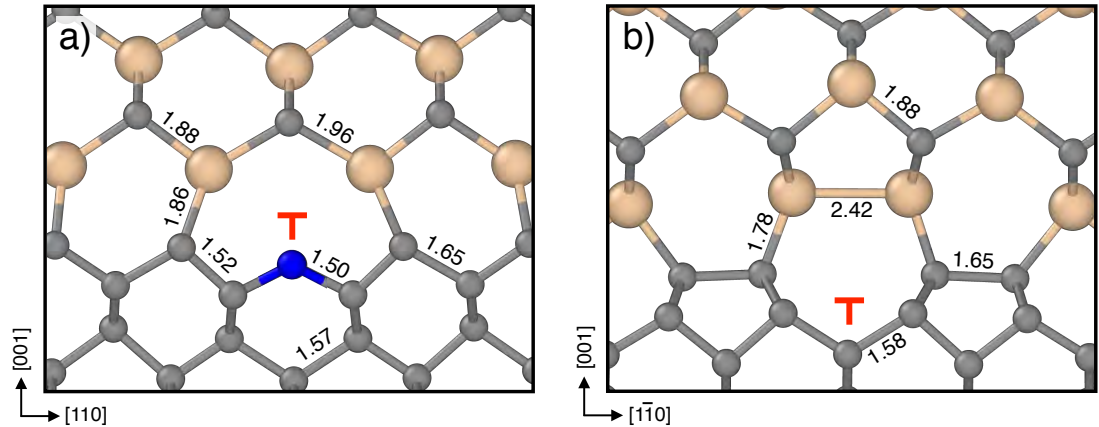


Figure 7.7: Local environment and bond lengths of atoms in the two types of point defect in the silicon carbide/diamond interface. Panels (a) and (b) are the same as Figure 7.6(e) and (d), respectively. All the bond lengths values are in Å and colour codings are the same as Figure 7.6.

silicon–silicon dimerization is sufficient to both relax the interface strain and fully satisfy all interface atomic bonds without the need to consider non-stoichiometric interfaces. This contrasts with the modelling done on silicon/silicon carbide interfaces by Pizzagalli et al. (2003) where carbon-poor stoichiometries needed to be considered.

7.3.3 Interfacial energy

To quantify the energetics of the reconstruction, the total potential energy was decomposed into atomic contributions and visualised (Figure 7.8(a) and (b)) where the atoms adopt the bulk values of diamond and silicon carbide away from the interface, as expected. The potential energy gradient seen in Figure 7.8(a) and (b) shows that strain is confined to the interfacial region. The atoms with the highest potential energy are the interfacial silicon atoms (-5.70 eV/atom) and the π -bonded carbon atoms (-6.28 eV/atom). However, within a few atomic layers of the interface the potential energy returns to the bulk values, indicative of zero strain. This effect is quantified in Figure 7.8(c) which plots the layer-averaged potential energy as a function of distance from the interface. Note that to simplify, the zero dividing line (green dashed vertical line in panel (c)) shows a

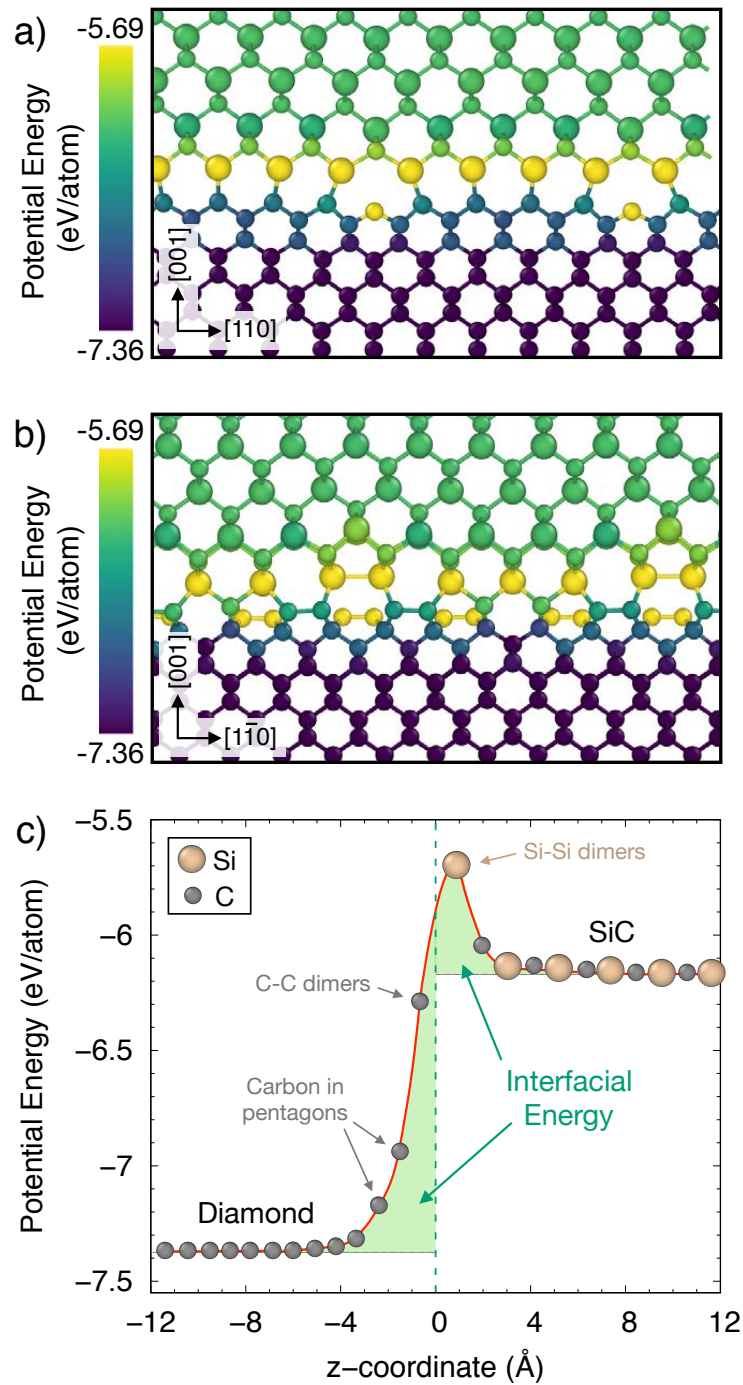


Figure 7.8: (a) and (b) silicon carbide/diamond interface with atoms coloured by their potential energy per atom. (c) Layer-averaged potential energy as a function of distance from the interface. Green shading indicates contributions to the interfacial energy and the green dashed line shows the reference dividing line.

distance reference point in the z-direction (i.e., [001] direction) from the middle of the interface. On the silicon carbide side only two layers deviate significantly from

the bulk, showing that strain is quickly removed as distance from the interface increases. On the diamond side the strain field penetrates slightly further, reflecting the high stiffness of diamond and non-ideal structures such as pentagonal and heptagonal rings (Figure 7.6(d)). Adding the energy cost over the entire supercell interface, represented by the green shading in Figure 7.8(c), yields a relatively modest interfacial energy of 2.87 J/m^2 , consistent with a low strain interface. For comparison, the surface energy for the a sub-stoichiometric optimized silicon/silicon carbide interface was calculated to be approximately 1.55 J/m^2 (Pizzagalli et al., 2003). The slightly higher value calculated for silicon carbide/diamond is expected, given the denser interface compared to the silicon carbide/silicon case. The calculated surface energy of the known reconstructed bare 2×1 diamond with the Tersoff potential is 6.20 J/m^2 , while the corresponding value for the silicon-rich surface of silicon carbide is 4.01 J/m^2 .

We note that the 9:11 surface reconstruction is the most likely interface for the region of high crystalline quality as it resolves the surprising coherence and strain observed experimentally (Figure 7.1). Due to the inhomogeneity at the interface with the fabrication procedure; however, it would be challenging for the uniform periodic structure to form across the entire interface. This is partially accommodated by the ability of carbon to form π and σ bonds which resolves instances of high strain but will result in extended defects in larger regions, as seen in Figure 7.1(a). If greater control over carbon bond manufacturing at the interface was available, not only 3C-SiC, but other materials with large lattice mismatches could form low strain and highly coherent heterostructures with diamond.

7.4 Conclusion

In this chapter, we showed that molecular dynamics simulation can provide atomistic details of the interface of silicon carbide/diamond heterostructure. Following on experimental studies of heteroepitaxial growth of silicon carbide on diamond by colleagues at the University of Melbourne, we have shown theoretically that

it is possible to form an atomically sharp and minimally strained cubic polytype silicon carbide (3C-SiC) film on a single crystal diamond substrate in localized regions. Simulations indicate that this is achieved with an optimal supercell ratio of 9:11 that removes dangling bonds and requires two rows of dislocations in the $[1\bar{1}0]$ and $[110]$ direction. Once these misfit dislocations are generated, supercell matching occurs between the nine silicon carbide lattice ($9 \times a_{\text{SiC}} = 39.240 \text{ \AA}$) and eleven diamond lattice ($11 \times a_{\text{diamond}} = 39.237 \text{ \AA}$). Atomistic simulations also showed that this lattice mismatch that exceeds 20% can be resolved through bonding reconstruction at the interface and requires defects in a two-dimensional plane without forming extended defect in three-dimensional. This is further emphasized through strain calculations that demonstrate that the misfit strain is relieved within five monolayers of the interface. Thus, the high quality interface observed in the experiment is a likely realization of this simulation in localized areas despite the auto-nucleation at the interface. Such a high crystalline quality interface is expected to allow for a minimal thermal barrier junction, enabling improved device performance for high temperature electronic applications. From the perspective of fundamental material design, the study redefines our understanding of silicon carbide and diamond possibilities and furthers our understanding of large lattice mismatched interfaces.

Chapter 8

Conclusion and future work

The molecular dynamics simulation studies in this thesis sought to provide atomistic details of the not-well-understood mechanism of the incorporation and thermal release patterns of noble gases in meteorite nanodiamonds (NDs). The thesis also aimed to investigate the plastic deformation of diamond and examined the interface of diamond-based heterojunctions. All these objectives have been achieved, and our simulated results have reproduced all experimental observations from our collaborators and the literature. In this final chapter, we summarize the main conclusions of the presented studies and outline some of the potential directions that the work presented within this thesis can take.

8.1 Conclusion

Firstly, we carried out a study that compare fourteen interatomic potential for carbon. To this end, in Chapter 2 we examined a modified widely-used Tersoff potential, and in Chapter 3 benchmarked some of the most commonly used interatomic potentials to test their transferability and evaluate their ability to describe disordered carbon structures. In Chapter 2, we examine the extended cutoff Tersoff potential when the upper cutoff parameter is increased to 2.45 Å. The results indicated that this modification led to the nucleation of diamond crys-

talline during the annealing process of amorphous carbon. Time evolution of the fraction of atoms in a nanocrystalline diamond environment for different densities showed that at 2.8 and 2.9 g/cc, ND grows up to the size of the simulation cell. However, at higher densities, i.e., 3.0, 3.1 and 3.2 g/cc, a quite small nanocrystal is observed. Due to the significant difference between the density range at which the diamond nucleated and the experimental diamond density of 3.52 g/cc, we concluded that this behavior is unphysical and does not represent a new pathway for synthesising diamond. In fact, this behaviour is artificial due to the interaction between the cutoff function and the 2^{nd} neighbour shell as demonstrated by radial distribution function analysis. Viewed from a broader perspective, this observation provides a cautionary tale against altering the parameters of empirical potentials without fully considering the wider implications.

In Chapter 3, we studied fourteen well-known and commonly used interatomic potentials for carbon (i.e., Tersoff, Extended-cutoff Tersoff, Tersoff/Nordlund, Tersoff-S, REBO-II, REBO2-S, EDIP, LCBOP-I, ReaxFF, COMB3, AIREBO, ABOP, Erhart/Albe and GAP) and compared their capability to model carbon nanostructures. Since the amorphous carbon system provides a critical test of the transferability of carbon potentials and the annealing simulations illustrate the graphitization process, we used the liquid quenching method to produce amorphous carbon at four different densities, which were subsequently annealed at a high temperature. Based on coordination analysis, ring statistics, radial distribution functions and diffraction intensity, we found that no two potentials give the same result. GAP, ReaxFF and EDIP potentials presented the best transferable capabilities. We showed that although GAP potential offers a promising way forward as a machine learning framework, it is extremely computationally costly. Also, for long simulation times and large systems, EDIP potential was found to be the most reliable and computationally efficient interatomic potential. In addition, to facilitate interactive analysis of data from our findings, we developed a web application tool at www.carbonpotentials.org.

Using EDIP potential, we investigated ion-implantation and thermal annealing process to enhance understanding of how noble gases become incorporated into meteorite NDs and how the noble gases are released upon thermal annealing. In Chapter 4, we introduced a model to reproduce the ion-implantation experiments conducted at the University of Huddersfield, UK. We modeled the implantation of xenon into NDs of different sizes (from 2 to 10 nm) and with different implantation energies (50 eV up to 40 keV). The results were in excellent agreement with all experimental observations. For example, we found that the implantation energy of around 6 keV destroys small-sized NDs. In addition, these results provided strong evidence that low energy implantation of noble gases (about 700 eV) into an ND with a diameter of ~ 4 nm (this size is similar to meteoritic NDs) is a suitable mechanism for entrapment of noble gases by meteoritic diamond grains.

In Chapter 5, we employed molecular dynamics approach to calculate the thermal release distribution of implanted noble gases in NDs. The results reproduced the meteoritic and laboratory experimental observations. We showed that helium the lightest noble gas, has a unimodal temperature release pattern, while bimodal behavior was observed for xenon a much heavier noble gas. The thermal release process is strongly sensitive to impact and annealing parameters, as well as to crystallographic orientation and type of defect. From an astrophysical point of view, our model provided a clear explanation of bimodal release distribution of heavy noble gases during the pyrolysis process of the meteoritic nanodiamonds. Also, we explained that P3 component in meteoritic literature, which is located near the surface of ND grains, releases not only at the low-temperature but also at the high-temperature along with HL component.

In Chapter 6, we successfully provided an atomistic observation of the mechanical deformation as well as the brittle failure of diamond nanopillars. Our simulations reproduced and explained the experimental results from our colleagues from University of Technology Sydney, where the nanopillar had been found to

bend in an electron microscope. We found that the plastic deformation is strongly dependent on the nanopillar dimensions and crystallographic orientation of the diamond. This mechanical deformation of (001)-oriented nanopillar is associated with a formation of a new phase of carbon called O8-carbon, which is localized to the deformed regions of the bent diamond nanopillars. Furthermore, we found that the plastic deformation occurs only in (001)-oriented nanopillars, while in the (111)-oriented nanopillars, conventional elastic deformation and brittle fracture behavior is observed.

Finally, in Chapter 7, we created a model to reproduce an experiment on epitaxial growth of silicon carbide on diamond conducted at the University of Melbourne and provided atomistic details of the interface between the bulk diamond and silicon carbide heterojunctions. We showed that the lattice mismatch of 22% can be resolved through bonding reconstructions at the interface. We found that forming an atomically sharp and minimally strained silicon carbide film on a diamond substrate is achieved with an optimal supercell matching between the 9 silicon carbide unit cells and 11 diamond unit cells that removes dangling bonds and requires two rows of point dislocations. Our findings in this chapter can also be applied to the study of the heterostructure formation of different types of materials with large lattice mismatch.

To summarise, in this thesis, molecular dynamics simulations were performed to: (i) benchmark fourteen well-known and commonly used interatomic potentials for carbon, (ii) provide atomic-level details on the mechanism of the incorporation of noble gases in meteorite-sized NDs and thermal release mechanism, (iii) explain the deformation of diamond nanopillars, and (iv) provide atomistic details of the epitaxial diamond interface in semiconductor heterostructures. Overall, in this thesis, we have shown that computational modeling is a useful tool for studying the nature of atomic-level effects in diamond-based materials and provides insight into experimental studies.

8.2 Future work

Based on the results presented and methodologies developed in this thesis, several directions can be considered for future work. One logical step would be to extend the comparative study of interatomic potentials for carbon in Chapters 2 and 3 and benchmark the performance of other potentials. Also, researchers can modify the functional form of potentials to improve their transferability properties. In addition, we can extend our work by performing a comparative study of mechanical and elastic properties of different carbon-based materials such as diamond, graphite, glassy carbon, and carbon nanotubes, and benchmarking well-known interatomic potentials performance.

The methodologies developed in Chapters 4 and 5 can be easily extended to other noble gases. In order to do so, we need to take Lennard-Jones parameters for noble gas interactions with carbon and bridge to the short-range ZBL expression. These parameters are easily obtainable from previous reports of gas-absorption into carbon networks and are conceptually straightforward due to the weak interactions between carbon and noble gas atoms. Implantation involving other chemical species is also possible, but the interactions are less trivial due to the formation of formal chemical bonds. Beyond NDs, the noble gas implantation methodology can also be usefully applied to the study of ion-irradiation effects in a wide variety of different carbon nanoforms, such as graphene, graphene bilayers, fullerenes and nanotubes, as well as bulk materials such as glassy carbon, silicon carbide, graphite and diamond.

As discussed in Chapter 1, from an astrophysical point of view, another hypothesis for the incorporation of noble gases into the NDs, in addition to implantation, is entrapment of noble gases by diamond grains as they grow. Although the origin of meteoritic NDs is still very much an open issue, [Marks et al. \(2012\)](#) reported a novel mechanism by which, based on atomistic simulation evidence and under the right condition, carbon onion can convert to ND

in a rapid non-equilibrium process. Figure 8.1 illustrates the cross-sectional view of their molecular dynamics simulation of high energy carbon onion colliding with a diamond substrate, generating conical ND, which is shown by the orange line. One potentially avenue of future research would be to extend our methodologies in Chapters 4 and 5 and perform simulations to implant noble gases into individual onions before they get deposited onto diamond substrate. Similar to Chapter 5, we can investigate the thermal release pattern of implanted noble gases as well. Note that the above-mentioned non-equilibrium mechanism can also potentially be used as a new source of ND thin-films, which can offer new possibilities in advancing carbon-based technology.

Another area for future studies would be to study the mechanical, thermodynamical, optical and electronic properties of O8-carbon. Moreover, we can extend the methodology in Chapter 6 to study the mechanical deformation of different nanostructured materials such as silicon carbide and boron nitride. The method developed in Chapter 7 can potentially be applied to a study of the heterostructure formation of different types of materials with large lattice mismatch, such as silicon on silicon carbide, silicon on diamond, boron nitride on diamond and boron nitride on silicon carbide. Similarly, we can employ this methodology to design and study the properties of a single layer diamond called diamane, which has a 2D form of diamond with a bilayer sp^3 carbon nanostructure. As a final point, similar to recent work done by Fujisawa et al. (2019), this methodology can be easily modified to study the transformation mechanism of silicon carbide into graphene upon thermal annealing.

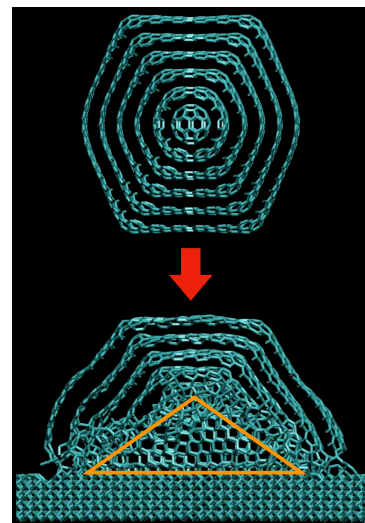


Figure 8.1: Cross-sectional view of simulation of carbon onion impacting onto diamond substrate. Figure adapted from Marks et al. (2012).

Appendices

Appendix A

Co-author contribution on statements

In this appendix, co-author contribution on the papers are provided, five of which have already been published and one will be submitted for publication in peer-reviewed journal.

- Chapter 2: *Molecular Simulation* 44, (2018) 164–171.
(doi: [10.1080/08927022.2017.1355555](https://doi.org/10.1080/08927022.2017.1355555))
- Chapter 3: *Carbon* 155, (2019) 624–634.
(doi: [10.1016/j.carbon.2019.07.074](https://doi.org/10.1016/j.carbon.2019.07.074))
- Chapter 4: *Nuclear Instruments and Methods in Physics Research Section B* 453, (2019) 32–40.
(doi: [10.1016/j.nimb.2019.05.062](https://doi.org/10.1016/j.nimb.2019.05.062))
- Chapter 5: (to be submitted)
- Chapter 6: *Advanced Materials* 32, (2020) 1906458.
(doi: [10.1002/adma.201906458](https://doi.org/10.1002/adma.201906458))
- Chapter 7: *ACS Applied Electronic Materials* 2, (2020) 2003–2009.
(doi: [10.1021/acsaelm.0c00289](https://doi.org/10.1021/acsaelm.0c00289))



Department of Physics and Astronomy

Curtin University

Perth, Western Australia, Australia

Telephone: +61 (0) 8 9266 3919

Email: alireza.aghajamali@postgrad.curtin.edu.au

Sunday, 2 February 2020

To whom it may concern,

I, Alireza Aghajamali, was the major contributor to the conceptualisation and coordination of the research resulting in the following publication entitled:

Aghajamali, A., C. de Tomas, I. Suarez-Martinez and N. A. Marks (2018). Unphysical nucleation of diamond in the extended cutoff Tersoff potential. *Molecular Simulation* 44, 164–171.

It was primarily my responsibility to conceptualise, collect and analyse data, write and edit the paper above, which is included in my PhD thesis. Commensurate with the extent of my contribution, I am the first author on this paper.

Alireza Aghajamali

We, as a Co-Authors, endorse that the level of contribution specified by the candidate above is appropriate.

- Dr. Carla de Tomas
- Dr. Irene Suarez-Martinez
- A/Prof. Nigel Marks



Department of Physics and Astronomy

Curtin University

Perth, Western Australia, Australia

Telephone: +61 (0) 8 9266 3919

Email: alireza.aghajamali@postgrad.curtin.edu.au

Sunday, 2 February 2020

To whom it may concern,

I, Alireza Aghajamali, was the major contributor to the conceptualisation and coordination of the research resulting in the following publication entitled:

de Tomas, C., **A. Aghajamali**, J. L. Jones, D. L. Lim, M. L. Lopez, I. Suarez-Martinez and N. A. Marks (2019). Transferability of interatomic potentials for carbon. *Carbon* 155, 624–634.

It was primarily my responsibility to conceptualise, collect and analyse data, write and edit the paper above, which is included in my PhD thesis. Commensurate with the extent of my contribution, Carla and I contributed equally to this work, and both of us are the first author on this paper.

Alireza Aghajamali

We, as a Co-Authors, endorse that the level of contribution specified by the candidate above is appropriate.

- Dr. Carla de Tomas

- Dr. Irene Suarez-Martinez

- A/Prof. Nigel Marks
(on behalf of the other co-authors)



Department of Physics and Astronomy

Curtin University

Perth, Western Australia, Australia

Telephone: +61 (0) 8 9266 3919

Email: alireza.aghajamali@postgrad.curtin.edu.au

Sunday, 2 February 2020

To whom it may concern,

I, Alireza Aghajamali, was the major contributor to the conceptualisation and coordination of the research resulting in the following publication entitled:

Fogg, J. L., **A. Aghajamali**, J. A. Hinks, S. E., Donnelly, A. A. Shiryayev and N. A. Marks (2019). Modification of nanodiamonds by xenon implantation: A molecular dynamics study. *Nuclear Instruments and Methods in Physics Research Section B* 453, 32–40.

It was primarily my responsibility to analyse data, write and edit the paper above, which is included in my PhD thesis. Commensurate with the extent of my contribution, I am the second author on this paper.

Alireza Aghajamali

We, as a Co-Authors, endorse that the level of contribution specified by the candidate above is appropriate.

- Jason Fogg
- Prof. Andrey A. Shiryayev
- Dr. Jonathan Hinks
- A/Prof. Nigel Marks
- Prof. Steve Donnelly



Department of Physics and Astronomy

Curtin University

Perth, Western Australia, Australia

Telephone: +61 (0) 8 9266 3919

Email: alireza.aghajamali@postgrad.curtin.edu.au

Sunday, 2 February 2020

To whom it may concern,

I, Alireza Aghajamali, was the major contributor to the conceptualisation and coordination of the research resulting in the following prepared manuscript entitled:

Aghajamali, A. and N. A. Marks (2020). Molecular dynamics approach for predicting release temperatures of noble gases in pre-solar nanodiamonds. (to be submitted)

It was primarily my responsibility to conceptualise, collect and analyse data, write and edit the paper above, which is included in my PhD thesis. Commensurate with the extent of my contribution, I am the first author on this paper.

Alireza Aghajamali

I, Nigel Marks, as a Co-Author, endorse that the level of contribution specified by the candidate above is appropriate.

A/Prof. Nigel Marks



Department of Physics and Astronomy

Curtin University

Perth, Western Australia, Australia

Telephone: +61 (0) 8 9266 3919

Email: alireza.aghajamali@postgrad.curtin.edu.au

To whom it may concern,

I, Alireza Aghajamali, was the major contributor to the conceptualisation and coordination of the research resulting in the following publication entitled:

Regan. B., **A. Aghajamali**, J. Froech, T. T. Tran, J. Scott, J. Bishop, I. Suarez-Martinez, Y. Liu, J. M. Cairney, N. A. Marks, M. Toth and I. Aharonovich (2020). Plastic deformation of single crystal diamond nanopillars. *Advanced Materials* 32, 1906458.

In the simulation study of the paper, it was primarily my responsibility to conceptualise, collect and analyse data, write and edit the paper above, which is included in my PhD thesis. Commensurate with the extent of my contribution, I am the second author (and the first author in the simulation study) on this paper.

Alireza Aghajamali

We, as a Co-Authors, endorse that the level of contribution specified by the candidate above is appropriate.

- Blake Regan
- Dr. Irene Suarez-Martinez
- Prof. Igor Aharonovich
- Johannes Froech
- Prof. Julie Cairney
- Dr. Toan Trang Tran
- A/Prof. Nigel Marks
- Dr. John Scott
- Prof. Milos Toth



Department of Physics and Astronomy

Curtin University

Perth, Western Australia, Australia

Telephone: +61 (0) 8 9266 3919

Email: alireza.aghajamali@postgrad.curtin.edu.au

To whom it may concern,

I, Alireza Aghajamali, was the major contributor to the conceptualisation and coordination of the research resulting in the following publication entitled:

A. Tsai, **A. Aghajamali**, N. Dontschuk, B. C. Johnson, M. Usman, A. K. Schenk, M. Sear, C. I. Pakes, L. C. L. Hollenberg, J. C. McCallum, S. Rubanov, A. Tadich, N. A. Marks, and A. Stacey. (2020). Epitaxial formation of SiC on (100) diamond. *ACS Applied Electronic Materials* 2, 2003-2009.

In the simulation study of the paper, it was primarily my responsibility to conceptualise, collect and analyse data, write and edit the paper above, which is included in my PhD thesis. Commensurate with the extent of my contribution, I am the second author (and the first author in the simulation study) on this paper.

Alireza Aghajamali

We, as a Co-Authors, endorse that the level of contribution specified by the candidate above is appropriate.

- Alexander Tsai
- Dr. Muhammad Usman
- A/Prof. Nigel Marks
- Dr. Alastair Stacey
(on behalf of the other co-authors)

Appendix B

Copyright information

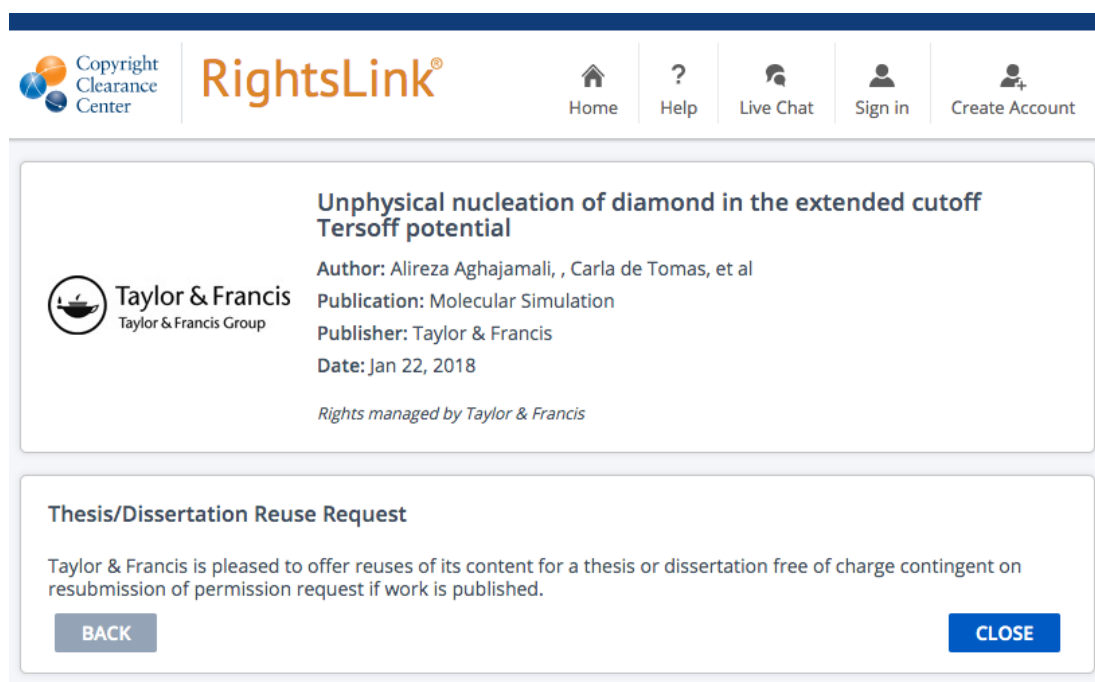
In this appendix, copyright information of the following published papers are provided:

- Chapter 2: *Molecular Simulation 44*, (2018) 164–171.
(doi: [10.1080/08927022.2017.1355555](https://doi.org/10.1080/08927022.2017.1355555))
- Chapter 3: *Carbon 155*, (2019) 624–634.
(doi: [10.1016/j.carbon.2019.07.074](https://doi.org/10.1016/j.carbon.2019.07.074))
- Chapter 4: *Nuclear Instruments and Methods in Physics Research Section B 453*, (2019) 32–40.
(doi: [10.1016/j.nimb.2019.05.062](https://doi.org/10.1016/j.nimb.2019.05.062))
- Chapter 6: *Advanced Materials 32*, (2020) 1906458.
(doi: [10.1002/adma.201906458](https://doi.org/10.1002/adma.201906458))
- Chapter 7: *ACS Applied Electronic Materials 2*, (2020) 2003–2009.
(doi: [10.1021/acsaelm.0c00289](https://doi.org/10.1021/acsaelm.0c00289))

Copyright information for the following published paper:

Aghajamali, A., C. de Tomas, I. Suarez-Martinez and N. A. Marks (2018). Unphysical nucleation of diamond in the extended cutoff Tersoff potential. *Molecular Simulation* 44, 164–171.

doi: [10.1080/08927022.2017.1355555](https://doi.org/10.1080/08927022.2017.1355555)

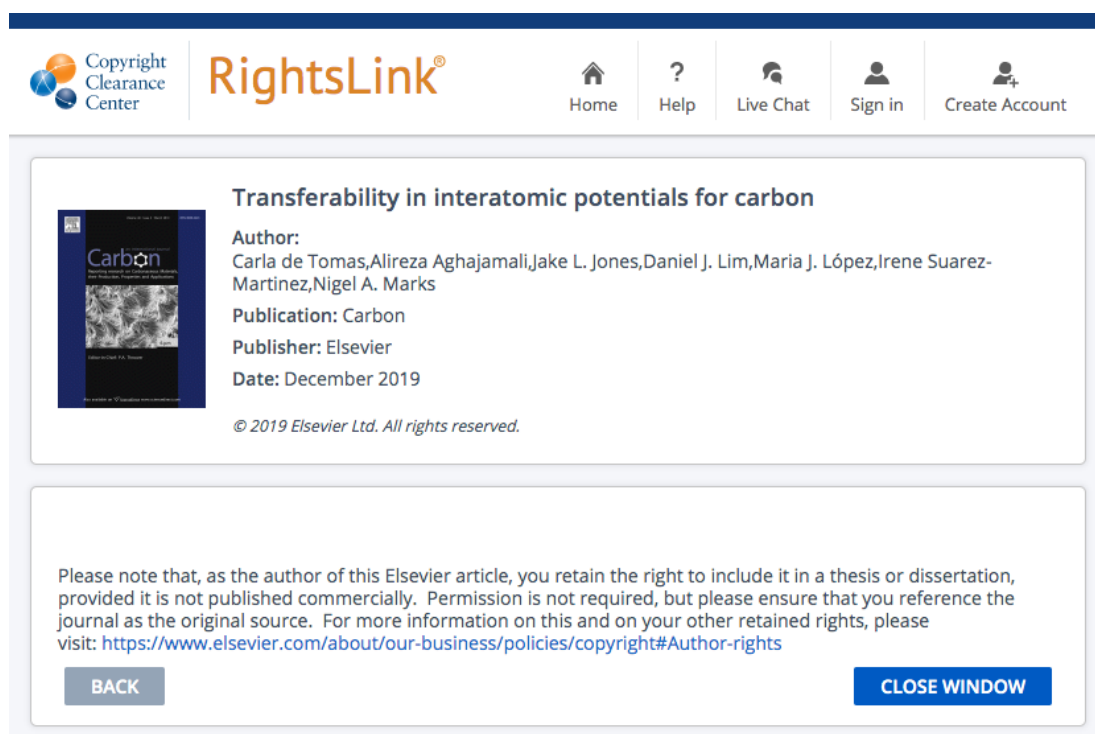


The screenshot shows a web interface for Taylor & Francis RightsLink. At the top, there is a navigation bar with the Copyright Clearance Center logo, the RightsLink logo, and icons for Home, Help, Live Chat, Sign in, and Create Account. Below this is a main content area with a white background and a light blue border. On the left side of this area is the Taylor & Francis logo. To the right of the logo, the title of the paper is displayed: "Unphysical nucleation of diamond in the extended cutoff Tersoff potential". Below the title, the author information is listed: "Author: Alireza Aghajamali, , Carla de Tomas, et al". Further down, the publication details are provided: "Publication: Molecular Simulation", "Publisher: Taylor & Francis", and "Date: Jan 22, 2018". At the bottom of this section, it states "Rights managed by Taylor & Francis". Below the main content area, there is a section titled "Thesis/Dissertation Reuse Request". This section contains the text: "Taylor & Francis is pleased to offer reuses of its content for a thesis or dissertation free of charge contingent on resubmission of permission request if work is published." At the bottom of this section, there are two buttons: a grey "BACK" button on the left and a blue "CLOSE" button on the right.

Copyright information for the following published paper:

de Tomas, C. [†], A. Aghajamali [†], J. L. Jones, D. L. Lim, M. L. Lopez, I. Suarez-Martinez and N. A. Marks (2019). Transferability of interatomic potentials for carbon. *Carbon* 155, 624–634.

doi: [10.1016/j.carbon.2019.07.074](https://doi.org/10.1016/j.carbon.2019.07.074)



The screenshot shows the RightsLink interface. At the top, there is a navigation bar with the Copyright Clearance Center logo, the RightsLink logo, and navigation links for Home, Help, Live Chat, Sign in, and Create Account. Below the navigation bar, the main content area displays the title "Transferability in interatomic potentials for carbon" and a thumbnail of the journal cover. The author information is listed as "Author: Carla de Tomas, Alireza Aghajamali, Jake L. Jones, Daniel J. Lim, Maria J. López, Irene Suarez-Martinez, Nigel A. Marks". The publication details are "Publication: Carbon", "Publisher: Elsevier", and "Date: December 2019". A copyright notice states "© 2019 Elsevier Ltd. All rights reserved." Below this, a disclaimer reads: "Please note that, as the author of this Elsevier article, you retain the right to include it in a thesis or dissertation, provided it is not published commercially. Permission is not required, but please ensure that you reference the journal as the original source. For more information on this and on your other retained rights, please visit: <https://www.elsevier.com/about/our-business/policies/copyright#Author-rights>". At the bottom of the content area, there are two buttons: "BACK" and "CLOSE WINDOW".

[†] These authors contributed equally to this work.

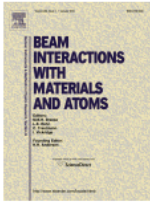
Copyright information for the following published paper:

Fogg, J. L., **A. Aghajamali**, J. A. Hinks, S. E., Donnelly, A. A. Shiryayev and N. A. Marks (2019). Modification of nanodiamonds by xenon implantation: A molecular dynamics study. *Nuclear Instruments and Methods in Physics Research Section B* 453, 32–40.

doi: [10.1016/j.nimb.2019.05.062](https://doi.org/10.1016/j.nimb.2019.05.062)



Home Help Live Chat Sign in Create Account



Modification of nanodiamonds by xenon implantation: A molecular dynamics study

Author:
Jason L. Fogg, Alireza Aghajamali, Jonathan A. Hinks, Stephen E. Donnelly, Andrey A. Shiryayev, Nigel A. Marks

Publication:
Nuclear Instruments and Methods in Physics Research Section B: Beam Interactions with Materials and Atoms

Publisher: Elsevier

Date: 15 August 2019

© 2019 Elsevier B.V. All rights reserved.

Please note that, as the author of this Elsevier article, you retain the right to include it in a thesis or dissertation, provided it is not published commercially. Permission is not required, but please ensure that you reference the journal as the original source. For more information on this and on your other retained rights, please visit: <https://www.elsevier.com/about/our-business/policies/copyright#Author-rights>

[BACK](#) [CLOSE WINDOW](#)

Copyright information for the following published paper:

Regan. B., **A. Aghajamali**, J. Froech, T. Trong Tran, J. Scott, J. Bishop, I. Suarez-Martinez, Y. Liu, J. M. Cairney, N. A. Marks, M. Toth and I. Aharonovtch (2020). Plastic deformation of single crystal diamond nanopillars. *Advanced Materials* 32, 1906458.

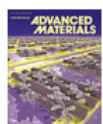
doi: [10.1002/adma.201906458](https://doi.org/10.1002/adma.201906458)



RightsLink[®]

[Home](#)
[?](#)
[Help](#)
[Email Support](#)


Alireza Aghajamali ▾



Plastic Deformation of Single-Crystal Diamond Nanopillars

Author: Blake Regan, Alireza Aghajamali, Johannes Froech, et al

Publication: Advanced Materials

Publisher: John Wiley and Sons

Date: Jan 28, 2020

© 2020 WILEY-VCH Verlag GmbH & Co. KGaA, Weinheim

Order Completed

Thank you for your order.

This Agreement between 2/623 Hay Street, JOLIMONT ("You") and John Wiley and Sons ("John Wiley and Sons") consists of your license details and the terms and conditions provided by John Wiley and Sons and Copyright Clearance Center.

Your confirmation email will contain your order number for future reference.

License Number	4760031419654	Printable Details
License date	Feb 01, 2020	

Licensed Content	Order Details
Licensed Content Publisher	Type of use
Licensed Content Publication	Requestor type
Licensed Content Title	Format
Licensed Content Author	Portion
Licensed Content Date	Will you be translating?
Licensed Content Volume	
Licensed Content Issue	
Licensed Content Pages	

About Your Work	Additional Data
Title of your thesis / dissertation	
Expected completion date	
Expected size (number of pages)	

Requestor Location	Tax Details
Requestor Location	Publisher Tax ID

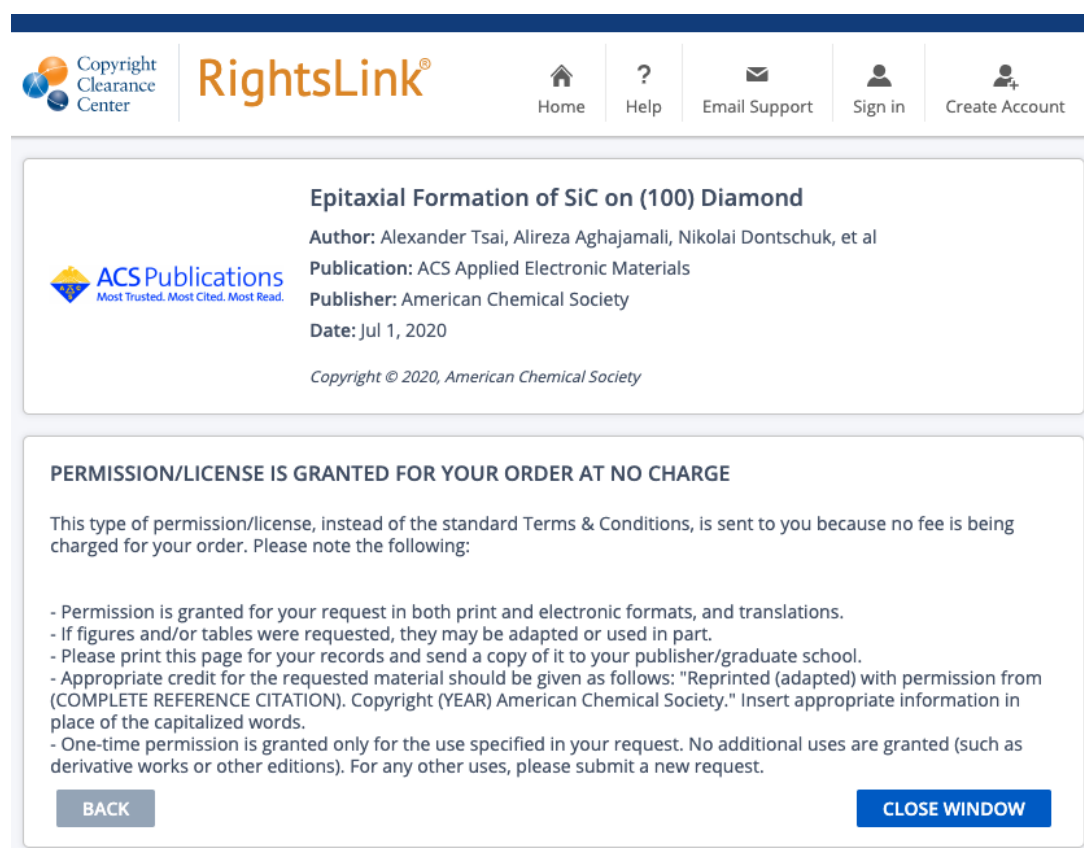
\$ Price	
Total	0.00 AUD

216

Copyright information for the following published paper:

A. Tsai, **A. Aghajamali**, N. Dontschuk, B. C. Johnson, M. Usman, A. K. Schenk, M. Sear, C. I. Pakes, L. C. L. Hollenberg, J. C. McCallum, S. Rubanov, A. Tadich, N. A. Marks, and A. Stacey. (2020). Epitaxial formation of SiC on (100) diamond. *ACS Applied Electronic Materials* 2, 2003–2009.

doi: [10.1021/acsaelm.0c00289](https://doi.org/10.1021/acsaelm.0c00289)



The screenshot shows the RightsLink interface. At the top, there is a navigation bar with the Copyright Clearance Center logo, the RightsLink logo, and icons for Home, Help, Email Support, Sign in, and Create Account. Below this, a white box contains the following information:

Epitaxial Formation of SiC on (100) Diamond
Author: Alexander Tsai, Alireza Aghajamali, Nikolai Dontschuk, et al
Publication: ACS Applied Electronic Materials
Publisher: American Chemical Society
Date: Jul 1, 2020
Copyright © 2020, American Chemical Society

Below this box, another white box contains the following text:

PERMISSION/LICENSE IS GRANTED FOR YOUR ORDER AT NO CHARGE

This type of permission/license, instead of the standard Terms & Conditions, is sent to you because no fee is being charged for your order. Please note the following:

- Permission is granted for your request in both print and electronic formats, and translations.
- If figures and/or tables were requested, they may be adapted or used in part.
- Please print this page for your records and send a copy of it to your publisher/graduate school.
- Appropriate credit for the requested material should be given as follows: "Reprinted (adapted) with permission from (COMPLETE REFERENCE CITATION). Copyright (YEAR) American Chemical Society." Insert appropriate information in place of the capitalized words.
- One-time permission is granted only for the use specified in your request. No additional uses are granted (such as derivative works or other editions). For any other uses, please submit a new request.

At the bottom of this box, there are two buttons: "BACK" and "CLOSE WINDOW".

Appendix C

www.carbonpotentials.org

As discussed in Chapter 3, we have developed an online application tool which collates all of the data from our study. In this appendix, screenshots of the *Home* page, the *Compare* page and the *Potentials* page of www.carbonpotentials.org are provided.

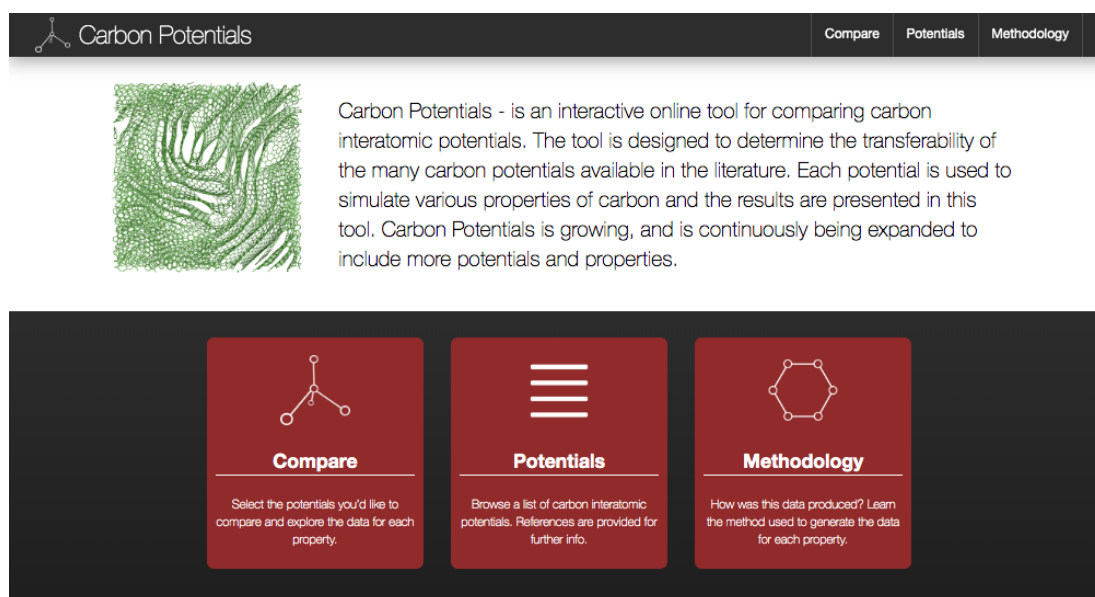


Figure C.1: Screenshot of the *Home* page of our interactive online tool for comparing carbon interatomic potentials (www.carbonpotentials.org).

Figure C.2: Screenshot of the *Compare* page. Sidebar shows the list of potentials with data. Sections and subsections are used to organize properties and their data.

Carbon Potentials							
Compare Potentials Methodology							
Tersoff							
Name of potential	Year	Main characteristic	Builds on	Other Species	LAMMPS	Data	Ref.
Tersoff	1988	Reparametrization for carbon	Si Tersoff		yes	●	📄
Tersoff	1989	Generalization to multicomponent systems	Si Tersoff	Si	yes		📄
Tersoff	1990	Reparametrization to treat C defects in Si	Tersoff 1989	Si	yes		📄
Tersoff	1994	Minor change in parameters	Tersoff 1990	Si	yes		📄
Tersoff	1995	Variable cutoff rescaled with system volume	Tersoff 1989	Si	no		📄
Nordlund	1996	Adds van der Waals and uses larger cutoff	Tersoff 1988		no		📄
Tersoff	1998	Adds nitrogen and boron.	Tersoff 1989	Si/B/N	no		📄
Extended Tersoff	2005	Extended cutoff	Tersoff 1988		no	●	📄
mTersoff/Nordlund	2011	Fermi-type cutoff. Adds van der Waals	Tersoff/Nordlund		no	●	📄
Tersoff-S	2013	Environment-dependent screening function	Tersoff 1988		yes	●	📄
REBO - (Reactive Empirical Bond Order)							
Name of potential	Year	Main characteristic	Builds on	Other Species	LAMMPS	Data	Ref.
REBO	1990	Adds hydrogen. Treats carbon radicals.	Tersoff	H	no		📄
AIREBO	2000	Adds van der Waals (Lennard-Jones)	REBO-II	H	yes	●	📄
REBO-II	2002	Adds dihedral. New short-range treatment.	REBO	H	yes	●	📄
AIREBO-II	2002	Minor change in two parameters	AIREBO	H	no		📄
REBO-CHO	2004	Adds oxygen	REBO-II	H/O	no		📄
AIREBO	2006	Environment-dependent van der Waals	AIREBO	H	no		📄

Figure C.3: Snapshot of the *Potentials* page, which contains essential information for each carbon potential. Full list of potentials are provided before in Tables 1.1, 1.2 and 1.3.

Appendix D

Front cover image of journal

In this Appendix, the front cover image of the *ACS Applied Electronic Materials* journal which published on July 2020, Volume 2, and Number 7 ([link](#)) is provided, where it highlighted our results that presented in Chapter 7:

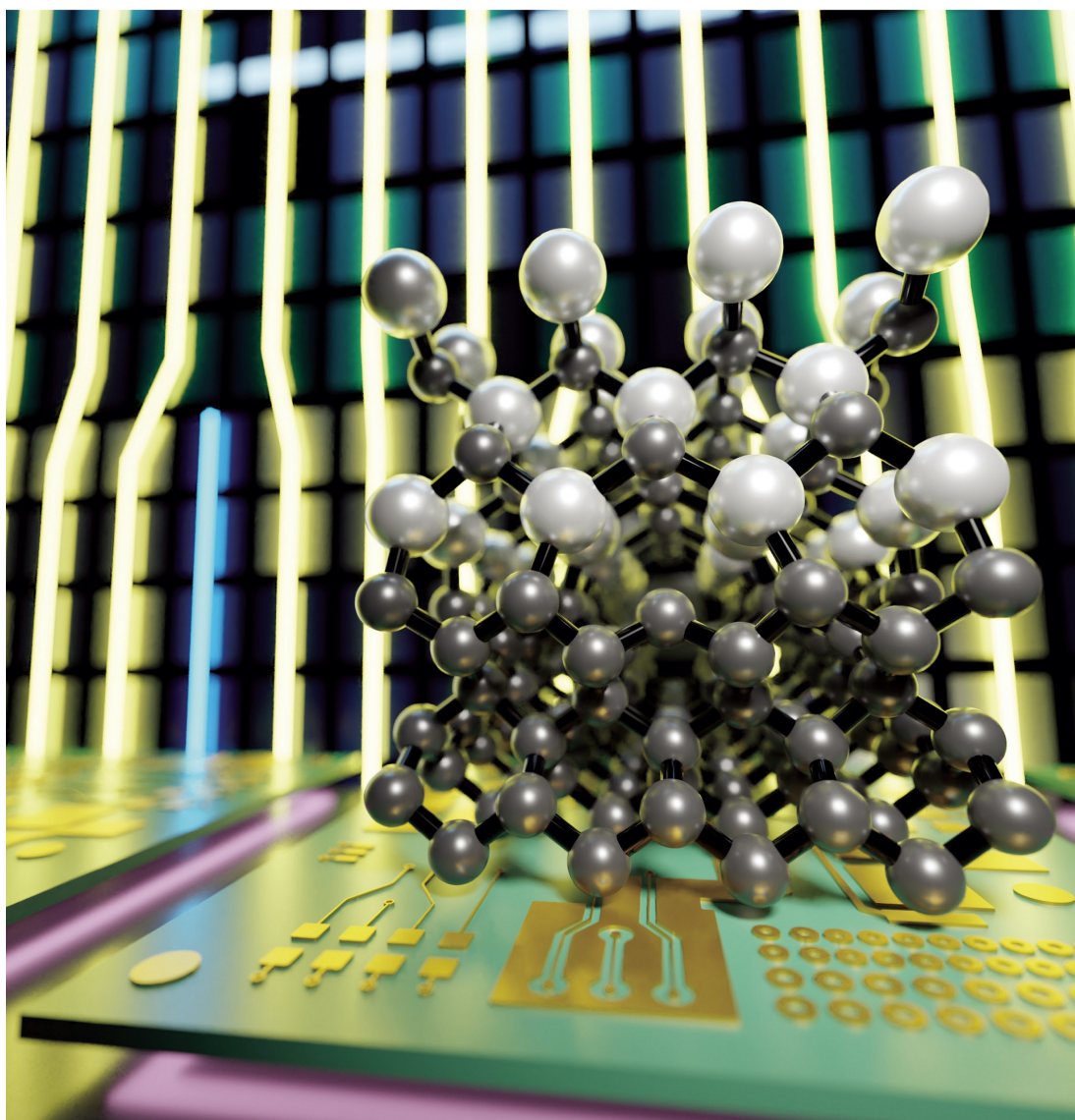
The details of the paper:

A. Tsai, **A. Aghajamali**, N. Dontschuk, B. C. Johnson, M. Usman, A. K. Schenk, M. Sear, C. I. Pakes, L. C. L. Hollenberg, J. C. McCallum, S. Rubanov, A. Tadich, N. A. Marks, and A. Stacey. (2020). “Epitaxial formation of SiC on (100) diamond,” *ACS Applied Electronic Materials* 2, 2003–2009.

doi: [10.1021/acsaelm.0c00289](https://doi.org/10.1021/acsaelm.0c00289)

ACS **APPLIED**
ELECTRONIC MATERIALS

July 2020
Volume 2
Number 7
pubs.acs.org/acsaem



Appendix E

List of additional publications during the Ph.D. program

A list of additional publications are included below which are not included as part of this thesis.

1. S. Best, J. B. Wasley, C. de Tomas, **A. Aghajamali**, I. Suarez-Martinez and N. A. Marks (2020). Evidence for glass behaviour in amorphous carbon. *C – Journal of Carbon Research* 6, 50.
[doi: 10.3390/c6030050](https://doi.org/10.3390/c6030050)

In addition to the MD simulation of nanostructures, during my Ph.D. I have been working on optical properties of one-dimensional photonic crystal as a side project. In which, I study theoretically the light waves propagation in periodic/quasi-periodic/random multilayer structures which are composed of different materials such as double- and single-negative metamaterials, magnetized cold plasma, high- and low-temperature superconductors, semiconductor metamaterials, semiconductors and dielectrics. The results of these studies have been published in 18 peer-reviewed papers. They are listed below in chronological order:

2. Srivastava, S. K. and **A. Aghajamali** (2016). Study of optical reflectance

properties in 1D annular photonic crystal containing double negative (DNG) metamaterials. *Physica B: Condensed Matter* 489, 67–72.

doi: [10.1016/j.physb.2016.01.036](https://doi.org/10.1016/j.physb.2016.01.036)

3. **Aghajamali, A.** and C.-J. Wu (2016). Single-negative metamaterial periodic multilayer doped by magnetized cold plasma.” *Applied Optics* 55, 2086–2090.

doi: [10.1364/AO.55.002086](https://doi.org/10.1364/AO.55.002086)

4. Srivastava, S. K. and **A. Aghajamali** (2016). Investigation of reflectance properties in one-dimensional ternary annular photonic crystal containing semiconductor and high- T_c superconductor. *Journal of Superconductivity and Novel Magnetism* 29, 1423–1431.

doi: [10.1007/s10948-016-3413-6](https://doi.org/10.1007/s10948-016-3413-6)

5. **Aghajamali, A** (2016). Transmittance properties in a magnetized cold plasma-superconductor periodic multilayer. *Applied Optics* 55, 6336–6340.

doi: [10.1364/AO.55.006336](https://doi.org/10.1364/AO.55.006336)

6. Aly, A. H., **A. Aghajamali**, H. A. Elsayed and M. Mobarak (2016). Analysis of cutoff frequency in a one-dimensional superconductor-metamaterial photonic crystal. *Physica C: Superconductivity and its applications* 526, 5–8.

doi: [10.1016/j.physc.2016.05.025](https://doi.org/10.1016/j.physc.2016.05.025)

7. **Aghajamali, A** (2016). Near-infrared tunable narrow filter in a periodic multi-nanolayer doped by superconductor photonic quantum-well. *Applied Optics* 55, 9797–9802.

doi: [10.1364/AO.55.009797](https://doi.org/10.1364/AO.55.009797)

8. **Aghajamali, A.**, T. Alamfard and A. H. Aly (2016). Periodic structure containing lossy metamaterial and defect mode. *International Journal of*

Advanced Applied Physics Research 3, 26–33.

doi: [10.15379/2408-977X.2016.03.02.01](https://doi.org/10.15379/2408-977X.2016.03.02.01)

9. Srivastava, S. K. and **A. Aghajamali** (2017). Analysis of reflectance properties in 1D photonic crystal containing metamaterial and high temperature superconductor. *Journal of Superconductivity and Novel Magnetism* 30, 343–351.

doi: [10.1007/s10948-016-3788-4](https://doi.org/10.1007/s10948-016-3788-4)

10. Alamfard, T. **A. Aghajamali** and A. H. Aly (2017). Absorption in one-dimensional lossy photonic crystal. *International Journal of Advanced Applied Physics Research* 4, 14–21.

doi: [10.15379/2408-977X.2017.04.01.03](https://doi.org/10.15379/2408-977X.2017.04.01.03)

11. Nayak, C., **A. Aghajamali**, F. Scotognella and A. Saha (2017). Effect of standard deviation, strength of magnetic field and electron density on the photonic band gap of an extrinsic disorder plasma photonic structure. *Optical Materials* 72, 25–30.

doi: [10.1016/j.optmat.2017.05.021](https://doi.org/10.1016/j.optmat.2017.05.021)

12. Nayak, C., **A. Aghajamali** and A. Saha (2017). Double-negative multilayer containing an extrinsic random layer thickness magnetized cold plasma photonic quantum-well defect. *Superlattices and Microstructures* 111, 248–254.

doi: [10.1016/j.spmi.2017.06.041](https://doi.org/10.1016/j.spmi.2017.06.041)

13. Nayak, C., **A. Aghajamali**, T. Alamfard and A. Saha (2017). Tunable photonic band gaps in an extrinsic Octonacci magnetized cold plasma quasicrystal. *Physica B: Condensed Matter* 525, 41–45.

doi: [10.1016/j.physb.2017.08.075](https://doi.org/10.1016/j.physb.2017.08.075)

14. Nayak, C., A. Saha and **A. Aghajamali** (2018). Periodic multilayer magnetized cold plasma containing a doped semiconductor. *Indian Journal of*

Physics 92, 911–917.

doi: [10.1007/s12648-018-1176-6](https://doi.org/10.1007/s12648-018-1176-6)

15. Srivastava, S. K. and **A. Aghajamali** (2019). Narrow transmission mode in 1D symmetric defective photonic crystal containing metamaterial and high- T_c superconductor. *Optica Applicata* 49, 37–50.

doi: [10.5277/oa190104](https://doi.org/10.5277/oa190104)

16. Nayak, C., **A. Aghajamali** and D. P. Patil (2019). Extrinsic magnetized plasma multilayer Fabry-Perot resonator. *Indian Journal of Physics* 93, 401–406.

doi: [10.1007/s12648-018-1282-5](https://doi.org/10.1007/s12648-018-1282-5)

17. Nayak, C., **A. Aghajamali**, A. Saha and N. Das (2019). Near- and Mid-infrared band gaps in a 1D photonic crystal containing superconductor and semiconductor-metamaterial. *International Journal of Modern Physics B* 33, 1950219–13.

doi: [10.1142/S0217979219502199](https://doi.org/10.1142/S0217979219502199)

18. Nayak, C., C. H. Costa and **A. Aghajamali** (2019). Robust photonic bandgaps in quasiperiodic and random extrinsic magnetized plasma. *IEEE Transactions on Plasma Science* 47, 1726–1733.

doi: [10.1109/TPS.2019.2899140](https://doi.org/10.1109/TPS.2019.2899140)

19. Solaimani, M., M. Ghalandari and **A. Aghajamali** (2020). Band gap engineering in constant total length nonmagnetized plasma-dielectric multilayers. *Optik-International Journal for Light and Electron Optics* 207, 164476.

doi: [10.1016/j.ijleo.2020.164476](https://doi.org/10.1016/j.ijleo.2020.164476)

Bibliography

- Abell, G. C. (1985). Empirical chemical pseudopotential theory of molecular and metallic bonding. *Physical Review B* 31, 6184–6196.
- Adler, J., Y. Gershon, T. Mutat, A. Sorokin, E. Warszawski, R. Kalish, and Y. Yaish (2009). Visualizing nanodiamond and nanotubes with AViz. In D. P. Landau, S. P. Lewis, and H. B. Schöttler (Eds.), *Computer Simulation Studies in Condensed-Matter Physics XIX*, Berlin, Heidelberg, pp. 56–60. Springer Berlin Heidelberg.
- Adler, J. and P. Pine (2009). Visualization techniques for modelling carbon allotropes. *Computer Physics Communications* 180, 580–582.
- Aghajamali, A., C. de Tomas, I. Suarez-Martinez, and N. A. Marks (2018). Unphysical nucleation of diamond in the extended cutoff Tersoff potential. *Molecular Simulation* 44, 164–171.
- Aghajamali, A. and N. A. Marks (2018). Noble gases release upon thermal annealing of nanodiamonds: A molecular dynamics study. In *Australian Institute of Physics Western Australian Postgraduate*, pp. 16.
- Aharonovich, I., A. D. Greentree, and S. Prawer (2011). Diamond photonics. *Nature Photonics* 5, 397.
- Akimov, A. V. and O. V. Prezhdo (2015). Large-scale computations in chemistry: A bird’s eye view of a vibrant field. *Chemical Reviews* 115, 5797–5890.

- Aleksov, A., M. Kubovic, N. Kaeb, U. Spitzberg, A. Bergmaier, G. Dollinger, T. Bauer, M. Schreck, B. Stritzker, and E. Kohn (2003). Diamond field effect transistors—concepts and challenges. *Diamond and Related Materials* 12, 391–398.
- Allen, M. P. and D. J. Tildesley (1989). *Computer Simulation of Liquids*. Oxford Science Publ. Clarendon Press.
- Alomari, M., A. Dussaigne, D. Martin, N. Grandjean, C. Gaquière, and E. Kohn (2010). AlGa_N/Ga_N HEMT on (111) single crystalline diamond. *Electronics Letters* 46, 299–301.
- Amari, S. (2009). Presolar diamond in meteorites. *Publications of the Astronomical Society of Australia* 26, 266—270.
- Amari, S., E. Anders, A. Virag, and E. Zinner (1990). Interstellar graphite in meteorites. *Nature* 345, 238–240.
- Amari, S., P. Hoppe, E. Zinner, and R. S. Lewis (1993). The isotopic compositions and stellar sources of meteoritic graphite grains. *Nature* 365, 806–809.
- Anders, E. and E. Zinner (1993). Interstellar grains in primitive meteorites: Diamond, silicon carbide, and graphite. *Meteoritics* 28, 490–514.
- Andersen, H. C. (1980). Molecular dynamics simulations at constant pressure and/or temperature. *The Journal of Chemical Physics* 72, 2384–2393.
- Ando, Y., Y. Nishibayashi, and A. Sawabe (2004). “nano-rods” of single crystalline diamond. *Diamond and Related Materials* 13, 633–637.
- Andribet, E. P., J. Domínguez-Vázquez, A. M. C. Pérez-Martín, E. V. Alonso, and J. J. Jiménez-Rodríguez (1996). Empirical approach for the interatomic potential of carbon. *Nuclear Instruments and Methods in Physics Research B* 115, 501–504.

- Angus, J. C. and C. C. Hayman (1988). Low-pressure, metastable growth of diamond and "diamondlike" phases. *Science* *241*, 913–921.
- Appell, D. (2002). Wired for success. *Nature* *419*, 553–555.
- Ashraf, C. and A. C. van Duin (2017). Extension of the ReaxFF combustion force field toward syngas combustion and initial oxidation kinetics. *The Journal of Physical Chemistry A* *121*, 1051–1068.
- Bachmann, P. K., D. Leers, and H. Lydtin (1991). Towards a general concept of diamond chemical vapour deposition. *Diamond and Related Materials* *1*, 1–12.
- Badziag, P., W. S. Verwoerd, W. P. Ellis, N. G. Nature, and 1990 (1990). Nanometre-sized diamonds are more stable than graphite. *Nature* *343*, 244.
- Baik, E.-S., Y.-J. Baik, S. Lee, and D. Jeon (2000). Fabrication of diamond nano-whiskers. *Thin Solid Films* *377–378*, 295–298.
- Balaban, A., C. C. Rentia, and E. Ciupitu (1968). Chemical graphs. 6. estimation of relative stability of several planar and tridimensional lattices for elementary carbon. *Revue Roumaine de Chimie* *13*, 231.
- Balandin, A. A., S. Ghosh, W. Bao, I. Calizo, D. Teweldebrhan, F. Miao, and C. N. Lau (2008). Superior thermal conductivity of single-layer graphene. *Nano Letters* *8*, 902–907.
- Banerjee, A., D. Bernoulli, H. Zhang, M.-F. Yuen, J. Liu, J. Dong, F. Ding, J. Lu, M. Dao, W. Zhang, Y. Lu, and S. Suresh (2018). Ultralarge elastic deformation of nanoscale diamond. *Science* *360*, 300–302.
- Barnard, A. S. (2004). Structural properties of diamond nanowires: theoretical predictions and experimental progress. *Reviews on Advanced Materials Science* *6*, 94–119.

- Barnard, A. S. (2005). From nanodiamond to nanowires. In D. M. Gruen, O. A. Shenderova, and A. Y. Vul' (Eds.), *Synthesis, Properties and Applications of Ultrananocrystalline Diamond*, pp. 25–38. Springer Netherlands.
- Barnard, A. S. (2011). Useful equations for modeling the relative stability of common nanoparticle morphologies. *Computer Physics Communications* 182, 11–13.
- Barnard, A. S. (2014a). Clarifying stability, probability and population in nanoparticle ensembles. *Nanoscale* 6, 9983–9990.
- Barnard, A. S. (2014b). *Diamond Nanoparticle Structure Set. v1. CSIRO. Data Collection.*
- Barnard, A. S., S. P. Russo, and I. K. Snook (2003a). Ab Initio Modeling of Diamond Nanowire Structures. *Nano Letters* 3, 1323–1328.
- Barnard, A. S., S. P. Russo, and I. K. Snook (2003b). Structural relaxation and relative stability of nanodiamond morphologies. *Diamond and Related Materials* 12, 1867–1872.
- Barnard, A. S., S. P. Russo, and I. K. Snook (2005). Modeling of stability and phase transformations in quasi-zero dimensional nanocarbon systems. *Journal of Computational and Theoretical Nanoscience* 2, 180–201.
- Barnard, A. S. and P. Zapol (2004). A model for the phase stability of arbitrary nanoparticles as a function of size and shape. *The Journal of Chemical Physics* 121, 4276–4283.
- Bartók, A. P., R. Kondor, and G. Csányi (2013). On representing chemical environments. *Physical Review B* 87, 184115.
- Bartók, A. P., M. C. Payne, R. Kondor, and G. Csányi (2010). Gaussian approximation potentials: The accuracy of quantum mechanics, without the electrons. *Physical Review Letters* 104, 136403.

- Bauer, J., A. Schroer, R. Schwaiger, and O. Kraft (2016). Approaching theoretical strength in glassy carbon nanolattices. *Nature Materials* 15, 438.
- Bean, J., L. C. Feldman, A. Fiory, S. t. Nakahara, and I. Robinson (1984). Ge x Si_{1-x}/Si strained-layer superlattice grown by molecular beam epitaxy. *Journal of Vacuum Science & Technology A: Vacuum, Surfaces, and Films* 2, 436–440.
- Becker, C. A., F. Tavazza, Z. T. Trautt, and R. A. B. de Macedo (2013). Considerations for choosing and using force fields and interatomic potentials in materials science and engineering. *Current Opinion in Solid State and Materials Science* 17, 277–283.
- Belytschko, T., S. P. Xiao, G. C. Schatz, and R. S. Ruoff (2002). Atomistic simulations of nanotube fracture. *Physical Review B* 65, 235430.
- Bernstein, N., M. J. Aziz, and E. Kaxiras (2000). Atomistic simulations of solid-phase epitaxial growth in silicon. *Physical Review B* 61, 6696–6700.
- Best, S., J. B. Wasley, C. d. Tomas, A. Aghajamali, I. Suarez-Martinez, and N. A. Marks (2020). Evidence for glass behavior in amorphous carbon. *C — Journal of Carbon Research* 6, 50.
- Biersack, J. P. and L. Haggmark (1980). A monte carlo computer program for the transport of energetic ions in amorphous targets. *Nuclear instruments and methods* 174, 257–269.
- Blöchl, P. E. (1994). Projector augmented-wave method. *Physical Review B* 50, 17953.
- Brenner, D. W. (1990). Empirical potential for hydrocarbons for use in simulating the chemical vapor deposition of diamond films. *Physical Review B* 42, 9458–9471.
- Brenner, D. W., O. A. Shenderova, J. A. Harrison, S. J. Stuart, B. Ni, and S. B. Sinnott (2002). A second-generation reactive empirical bond order (REBO)

- potential energy expression for hydrocarbons. *Journal of Physics: Condensed Matter* 14, 783–802.
- Brinckmann, S., J.-Y. Kim, and J. R. Greer (2008). Fundamental differences in mechanical behavior between two types of crystals at the nanoscale. *Physical Review Letters* 100, 155502.
- Bródka, A., L. Hawełek, A. Burian, S. Tomita, and V. Honkimäki (2008). Molecular dynamics study of structure and graphitization process of nanodiamonds. *Journal of Molecular Structure* 887, 34–40.
- Bródka, A., T. W. Zerda, and A. Burian (2006). Graphitization of small diamond cluster — Molecular dynamics simulation. *Diamond and Related Materials* 15, 1818–1821.
- Broughton, J. Q. and M. J. Mehl (1999). Transferable potential for carbon without angular terms. *Physical Review B* 59, 9259–9270.
- Buchan, J. T., M. Robinson, H. J. Christie, D. L. Roach, D. K. Ross, and N. A. Marks (2015). Molecular dynamics simulation of radiation damage cascades in diamond. *Journal of Applied Physics* 117, 245901–9.
- Bundy, F. P., W. A. Bassett, M. S. Weathers, R. J. Hemley, H. K. Mao, and A. F. Goncharov (1996). The Pressure-Temperature Phase and Transformation Diagram for Carbon; Updated Through 1994. *Carbon* 34, 141–153.
- Burchfield, L. A., M. Al Fahim, R. S. Wittman, F. Delodovici, and N. Manini (2017). Novamene: A new class of carbon allotropes. *Heliyon* 3, e00242.
- Burek, M. J., J. D. Cohen, S. M. Meenehan, N. El-Sawah, C. Chia, T. Ruelle, S. Meesala, J. Rochman, H. A. Atikian, M. Markham, et al. (2016). Diamond optomechanical crystals. *Optica* 3, 1404–1411.
- Buseck, P. R., S. J. Tsipursky, and R. Hettich (1992). Fullerenes from the geological environment. *Science* 257, 215–217.

- Bussi, G., D. Donadio, and M. Parrinello (2007). Canonical sampling through velocity rescaling. *The Journal of Chemical Physics* 126, 014101.
- Butenko, Y. V., L. Siller, and M. R. C. Hunt (2010). Carbon onions. In K. D. Sattler (Ed.), *Handbook of Nanophysics: Clusters and Fullerenes*, pp. 10–15. CRC Press.
- Cabioch, T., J. C. Girard, M. Jaouen, M. F. Denanot, and G. Hug (1997). Carbon onions thin film formation and characterization. *Europhysics Letters (EPL)* 38, 471–476.
- Cami, J., J. Bernard-Salas, E. Peeters, and S. E. Malek (2010). Detection of c60 and c70 in a young planetary nebula. *Science* 329, 1180–1182.
- Cao, A. and J. Qu (2013). Atomistic simulation study of brittle fracture in nanocrystalline graphene under uniaxial tension. *Applied Physics Letters* 102, 071902.
- Cao, L., C. Gao, H. Sun, G. Zou, Z. Zhang, X. Zhang, M. He, M. Zhang, Y. Li, J. Zhang, D. Dai, L. Sun, and W. Wang (2001). Synthesis of diamond from carbon nanotubes under high pressure and high temperature. *Carbon* 39, 311–314.
- Caro, M. A., V. L. Deringer, J. Koskinen, T. Laurila, and G. Csányi (2018). Growth mechanism and origin of high sp^3 content in tetrahedral amorphous carbon. *Physical Review Letters* 120, 166101.
- Caruta, B. (2006). *Ceramics and composite materials: new research*. Nova Publishers.
- Cazaux, J. and P. Lehuede (1992). Some physical descriptions of the charging effects of insulators under incident particle bombardment. *Journal of Electron Spectroscopy and Related Phenomena* 59, 49–71.

- Cervenka, J., N. Dontschuk, F. Ladouceur, S. Duvall, and S. Prawer (2012). Diamond/aluminium nitride composites for efficient thermal management applications. *Applied Physics Letters* 101, 051902.
- Chang, L., J. Yan, F. Chen, and J. Kai (2000). Deposition of heteroepitaxial diamond on 6h-sic single crystal by bias-enhanced microwave plasma chemical vapor deposition. *Diamond and Related Materials* 9, 283–289.
- Chang, Y., H. Hsieh, W. Pong, M.-H. Tsai, T. Dann, F. Chien, P. Tseng, L. Chen, S. Wei, K. Chen, et al. (1999). X-ray absorption of Si–C–N thin films: A comparison between crystalline and amorphous phases. *Journal of Applied Physics* 86, 5609–5613.
- Chen, J.-H., M. Ishigami, C. Jang, D. Hines, M. Fuhrer, and E. Williams (2007). Printed graphene circuits. *Advanced Materials* 19, 3623–3627.
- Chen, P., F. Huang, and S. Yun (2003). Characterization of the condensed carbon in detonation soot. *Carbon* 41, 2093–2099.
- Chen, X. and W. Zhang (2017). Diamond nanostructures for drug delivery, bioimaging, and biosensing. *Chemical Society Reviews* 46, 734–760.
- Chen, Y. and J. Washburn (1996). Structural transition in large-lattice-mismatch heteroepitaxy. *Physical Review Letters* 77, 4046.
- Cheng, Y., R. Melnik, Y. Kawazoe, and B. Wen (2016). Three dimensional metallic carbon from distorting sp³-bond. *Crystal Growth & Design* 16, 1360–1365.
- Chenoweth, K., A. C. T. van Duin, and W. A. Goddard III (2008). ReaxFF reactive force field for molecular dynamics simulations of hydrocarbon oxidation. *The Journal of Physical Chemistry A* 112, 1040–1053.

- Christie, H. J., M. Robinson, D. L. Roach, D. K. Ross, I. Suarez-Martinez, and N. A. Marks (2015). Simulating radiation damage cascades in graphite. *Carbon* 81, 105–114.
- Cicero, G., L. Pizzagalli, and A. Catellani (2002a). A molecular dynamics study of the β -SiC/Si(001) interface. *Journal of Physics: Condensed Matter* 14, 13031–13036.
- Cicero, G., L. Pizzagalli, and A. Catellani (2002b). Ab initio Study of Misfit Dislocations at the SiC/Si(001) Interface. *Physical Review Letters* 89, 19–4.
- Clayton, D. D. (1989). Origin of heavy xenon in meteoritic diamonds. *The Astrophysical Journal* 540, 613–619.
- Cordiner, M. A., H. Linnartz, N. L. J. Cox, J. Cami, F. Najarro, C. R. Proffitt, R. Lallement, P. Ehrenfreund, B. H. Foing, T. R. Gull, P. J. Sarre, and S. B. Charnley (2019). Confirming interstellar c60 + using the hubble space telescope. *The Astrophysical Journal* 875, L28.
- Dai, Z. R., J. P. Bradley, D. J. Joswiak, D. E. Brownlee, H. G. M. Hill, and M. J. Genge (2002). Possible in situ formation of meteoritic nanodiamonds in the early Solar System. *Nature* 418, 157–159.
- Daulton, T. L. (2006). 2 - extraterrestrial nanodiamonds in the cosmos. In O. A. Shenderova and D. M. Gruen (Eds.), *Ultrananocrystalline Diamond*, pp. 23–78. Norwich, NY: William Andrew Publishing.
- Daulton, T. L., D. D. Eisenhour, T. J. Bernatowicz, R. S. Lewis, and P. R. Buseck (1996). Genesis of presolar diamonds: Comparative high-resolution transmission electron microscopy study of meteoritic and terrestrial nano-diamonds. *Geochimica et Cosmochimica Acta* 60, 4853–4872.
- Davis, A. M. (2011). Stardust in meteorites. *Proceedings of the National Academy of Sciences of the United States of America* 108, 19142–19146.

- de Brito Mota, F., J. F. Justo, and A. Fazzio (1998). Structural properties of amorphous silicon nitride. *Physical Review B* 58, 8323–8328.
- de Tomas, C., A. Aghajamali, J. L. Jones, D. J. Lim, M. J. López, I. Suarez-Martinez, and N. A. Marks (2019). Transferability in interatomic potentials for carbon. *Carbon* 155, 624–634.
- de Tomas, C., I. Suarez-Martinez, and N. A. Marks (2016). Graphitization of amorphous carbons: A comparative study of interatomic potentials. *Carbon* 109, 681–693.
- de Tomas, C., I. Suarez-Martinez, and N. A. Marks (2018). Carbide-derived carbons for dense and tunable 3D graphene networks. *Applied Physics Letters* 112, 251907–6.
- de Tomas, C., I. Suarez Martinez, F. Vallejos-Burgos, M. J. López, K. Kaneko, and N. A. Marks (2017). Structural prediction of graphitization and porosity in carbide-derived carbons. *Carbon* 119, 1–9.
- Delodovici, F., D. S. Choi, M. Al Fahim, L. A. Burchfield, and N. Manini (2019). Carbon *sp* chains in diamond nanocavities. *Physical Chemistry Chemical Physics* 21, 21814–21823.
- Delodovici, F., N. Manini, R. S. Wittman, D. S. Choi, M. A. Fahim, and L. A. Burchfield (2018). Protomene: A new carbon allotrope. *Carbon* 126, 574–579.
- Deringer, V. L. and G. Csányi (2017). Machine learning based interatomic potential for amorphous carbon. *Physical Review B* 95, 094203–15.
- Dewapriya, M. A. N., R. K. N. D. Rajapakse, and A. S. Phani (2004). Atomistic and continuum modelling of temperature-dependent fracture of graphene. *International Journal of Fracture* 187, 199–212.

- Ding, M. (2014). *Molecular Simulations of Reverse Osmosis Membranes*. Ph. D. thesis, Institut des Sciences Chimiques de Rennes, Composante universitaire SPM, Paris, France.
- Dozhdikov, V. S., A. Y. Basharin, P. R. Levashov, and D. V. Minakov (2017). Atomistic simulations of the equation of state and hybridization of liquid carbon at a temperature of 6000 K in the pressure range of 1–25 GPa. *The Journal of Chemical Physics* *147*, 214302–10.
- Dresselhaus, M. S. and G. Dresslhaus (1995). Fullerenes and fullerene derived solids as electronic materials. *Annual Review of Materials Science* *25*, 487–523.
- Drumm, D. W., M. C. Per, S. P. Russo, and L. C. L. Hollenberg (2010). Thermodynamic stability of neutral xe defects in diamond. *Physical Review B* *82*, 054102.
- Du, Q.-S., P.-D. Tang, H.-L. Huang, F.-L. Du, K. Huang, N.-Z. Xie, S.-Y. Long, Y.-M. Li, J.-S. Qiu, and R.-B. Huang (2017). A new type of two-dimensional carbon crystal prepared from 1,3,5-trihydroxybenzene. *Scientific Reports* *7*, 40796.
- Eaton-Magana, S. and J. E. Shigley (2016). Observations on CVD-Grown synthetic diamonds: A review. *Gems & Gemology* *52*.
- ed Levy, M., E. Henry, R. Richard, and V. Keppens (2001a). *Handbook of Elastic Properties of Solids, liquids, and Gasses Vol. 1: dynamic Methods for Measuring the Elastic Properties of Solids*, Volume 1. Academic Press.
- ed Levy, M., E. Henry, R. Richard, and V. Keppens (2001b). *Handbook of Elastic Properties of Solids, liquids, and Gasses Vol. 2: elastic Properties of Solids: theory, elements and Compounds, novel Materials, technological Materials, alloys, and Building Materials*, Volume 2. Academic Press.

- ed Levy, M., E. Henry, R. Richard, and V. Keppens (2001c). *Handbook of Elastic Properties of Solids, liquids, and Gasses Vol. 3: elastic Properties of Solids: biological and Organic Materials, earth and Marine Sciences*, Volume 3. Academic Press.
- Erhart, P. and K. Albe (2005). Analytical potential for atomistic simulations of silicon, carbon, and silicon carbide. *Physical Review B* 71(3), 35211.
- Evans, T. and C. Phaal (1962). Imperfections in type i and type ii diamonds. *Proceedings of the Royal Society of London. Series A, Mathematical and Physical Sciences* 270(1343), 538–552.
- Fairchild, B. A., S. Rubanov, D. W. M. Lau, M. Robinson, I. Suarez Martinez, N. A. Marks, A. D. Greentree, D. McCulloch, and S. Praver (2012). Mechanism for the Amorphisation of Diamond. *Advanced Materials* 24, 2024–2029.
- Fan, D., S. Lu, A. A. Golov, A. A. Kabanov, and X. Hu (2018). D-carbon: Ab initio study of a novel carbon allotrope. *The Journal of Chemical Physics* 149, 114702.
- Fedorov, I. I., A. A. Chepurov, and J. M. Dereppe (2002). Redox conditions of metal-carbon melts and natural diamond genesis. *Geochemical Journal* 36(3), 247–253.
- Fisenko, A., L. Semenova, A. Verchovsky, and K. Pillinger (2004). Noble gases in the grain-size fractions of presolar diamond from the Boriskino CM2 meteorite. *Geochemistry International* 42, 708–719.
- Fisenko, A. V. and L. F. Semjonova (2010). On nature of bimodal release of noble gases during pyrolysis of the meteoritic nanodiamonds. *Geochemistry International* 48, 1177–1184.
- Fisenko, A. V., A. B. Verchovsky, and L. F. Semjonova (2014). Kinetics of Xe-P3

- release during pyrolysis of the coarse-grained fractions of Orgueil (CI) meteorite nanodiamonds. *Meteoritics & Planetary Science* 49, 611–620.
- Fitzer, E., K.-H. Kochling, B. H. P., and H. Marsh (1995). Recommended terminology for the description of carbon as a solid. *Pure and Applied Chemistry* 67, 473–506.
- Fogg, J. L., A. Aghajamali, J. A. Hinks, S. E. Donnelly, A. A. Shiryaev, and N. A. Marks (2019). Modification of nanodiamonds by xenon implantation: A molecular dynamics study. *Nuclear Instruments and Methods in Physics Research Section B* 453, 32–40.
- Fowler, J. D., M. J. Allen, V. C. Tung, Y. Yang, R. B. Kaner, and B. H. Weiller (2009). Practical chemical sensors from chemically derived graphene. *ACS Nano* 3, 301–306.
- Franzblau, D. S. (1991). Computation of ring statistics for network models of solids. *Physical Review B* 44, 4925–4930.
- Frenkel, D. and B. Smit (2001). *Understanding Molecular Simulation: From Algorithms to Applications*. Computational science. Elsevier Science.
- Frenklach, M., W. Howard, D. Huang, J. Yuan, K. E. Spear, and R. Koba (1991). Induced nucleation of diamond powder. *Applied Physics Letters* 59, 546–548.
- Freund, L. B. and S. Suresh (2004). *Thin film materials: stress, defect formation and surface evolution*. Cambridge University Press.
- Fujii, Y., M. Maruyama, N. T. Cuong, and S. Okada (2020). Pentadiamond: A Hard Carbon Allotrope of a Pentagonal Network of sp² and sp³ C Atoms. *Physical Review Letters* 125, 016001.
- Fujisawa, K., Y. Lei, C. de Tomas, I. Suarez Martinez, C. Zhou, Y.-C. Lin, S. Subramanian, A. L. Elías, M. Fujishige, K. Takeuchi, J. A. Robinson, N. A. Marks, M. Endo, and M. Terrones (2019). Facile 1D graphene fiber synthesis from an

- agricultural by-product: A silicon-mediated graphenization route. *Carbon* *142*, 78–88.
- Gale, J. D. (1997). GULP: A computer program for the symmetry-adapted simulation of solids. *Journal of the Chemical Society, Faraday Transactions* *93*, 629–637.
- Gamboa, A., B. Farbos, P. Aurel, G. L. Vignoles, and J. M. Leyssale (2015). Mechanism of strength reduction along the graphenization pathway. *Science Advances* *1*, e1501009.
- Ganesh, P., P. R. C. Kent, and V. N. Mochalin (2011). Formation, characterization, and dynamics of onion-like carbon structures for electrical energy storage from nanodiamonds using reactive force fields. *Journal of Applied Physics* *110*, 073506–9.
- Gasc, J., Y. Wang, T. Yu, I. C. Benea, B. R. Rosczyk, T. Shinmei, and T. Irifune (2015). High-pressure, high-temperature plastic deformation of sintered diamonds. *Diamond and Related Materials* *59*, 95–103.
- Gayk, F., J. Ehrens, T. Heitmann, P. Vorndamme, A. Mrugalla, and J. Schnack (2018). Young’s moduli of carbon materials investigated by various classical molecular dynamics schemes. *Physica E: Low-dimensional Systems and Nanostructures* *99*, 215–219.
- Ghiringhelli, L. M., J. H. Los, A. Fasolino, and E. J. Meijer (2005). Improved long-range reactive bond-order potential for carbon. II. Molecular simulation of liquid carbon. *Physical Review B* *72*, 214103.
- Ghiringhelli, L. M., J. H. Los, E. J. Meijer, A. Fasolino, and D. Frenkel (2004). High-pressure diamondlike liquid carbon. *Physical Review B* *69*, 100101(R).
- Gilmour, J. D., A. B. Verchovsky, A. V. Fisenko, G. Holland, and G. Turner

- (2005). Xenon isotopes in size separated nanodiamonds from Efremovka: $^{129}\text{Xe}^*$, Xe-P3, and Xe-P6. *Geochimica et Cosmochimica Acta* 69, 4133–4148.
- Gogotsi, Y., S. Welz, D. A. Ersoy, and M. J. McNallan (2001). Conversion of silicon carbide to crystalline diamond-structured carbon at ambient pressure. *Nature* 411, 283–287.
- Gorelik, T., S. Urban, F. Falk, U. Kaiser, and U. Glatzel (2003). Carbon onions produced by laser irradiation of amorphous silicon carbide. *Chemical Physics Letters* 373, 642–645.
- Goss, J. P., R. J. Eyre, P. R. Briddon, and A. Mainwood (2009). Density functional simulations of noble-gas impurities in diamond. *Physical Review B* 80, 085204.
- Goyal, V., S. Subrina, D. Nika, and A. Balandin (2010). Reduced thermal resistance of the silicon-synthetic diamond composite substrates at elevated temperatures. *Applied Physics Letters* 97, 031904.
- Grantab, R., V. B. Shenoy, and R. S. Ruoff (2010). Anomalous Strength Characteristics of Tilt Grain Boundaries in Graphene. *Science* 330, 946–948.
- Gu, X. W., C. N. Loynachan, Z. Wu, Y.-W. Zhang, D. J. Srolovitz, and J. R. Greer (2012). Size-dependent deformation of nanocrystalline pt nanopillars. *Nano Letters* 12, 6385–6392.
- Guo, C., H. Yang, Z. Sheng, Z. Lu, Q. Song, and C. Li (2010). Layered graphene/quantum dots for photovoltaic devices. *Angewandte Chemie International Edition* 49, 3014–3017.
- Guo, J., B. Wen, R. Melnik, S. Yao, and T. Li (2011). Molecular dynamics study on diamond nanowires mechanical properties: Strain rate, temperature and size dependent effects. *Diamond and Related Materials* 20, 551–555.

- Gupta, S., R. J. Patel, and N. D. Smith (2004). Advanced carbon-based material as space radiation shields. *MRS Online Proceedings Library Archive 851*, NN6.3.
- Haggerty, S. E. (1986). Diamond genesis in a multiply-constrained model. *Nature 320*, 34–38.
- Haggerty, S. E. (1999). A Diamond Trilogy: Superplumes, supercontinents, and supernovae. *Science 285*, 851–860.
- Haley, M. M., S. C. Brand, and J. J. Pak (1997). Carbon networks based on dehydrobenzoannulenes: Synthesis of graphdiyne substructures. *Angewandte Chemie International Edition in English 36*, 836–838.
- Hanneman, R. E., H. M. Strong, and F. P. Bundy (1967). Hexagonal diamonds in meteorites: Implications. *Science 155*, 995–997.
- Harris, P. J. F. (2004). Fullerene-related structure of commercial glassy carbons. *Philosophical Magazine 84*, 3159–3167.
- Harrison, J. A., J. D. Schall, S. Maskey, P. T. Mikulski, M. T. Knippenberg, and B. H. Morrow (2018). Review of force fields and intermolecular potentials used in atomistic computational materials research. *Applied Physics Reviews 5*, 031104–25.
- He, C. and N. Zhao (2010). Production of carbon onions. In K. D. Sattler (Ed.), *Handbook of Nanophysics: Clusters and Fullerenes*, pp. 1–22. CRC Press.
- He, L., G. Siusiu, J. Lei, and Z. Liu (2014). The effect of Stone-Thrower-Wales defects on mechanical properties of graphene sheets - A molecular dynamics study. *Carbon 75*, 124–132.
- Heggie, M. I. (1991). Semiclassical interatomic potential for carbon and its application to the self-interstitial in graphite. *Journal of Physics: Condensed Matter 3*, 3065–3079.

- Hirama, K., M. Kasu, and Y. Taniyasu (2012). Growth and device properties of algan/gan high-electron mobility transistors on a diamond substrate. *Japanese Journal of Applied Physics* 51, 01AG09.
- Hirama, K., Y. Taniyasu, and M. Kasu (2010). Heterostructure growth of a single-crystal hexagonal AlN (0001) layer on cubic diamond (111) surface. *Journal of Applied Physics* 108, 013528.
- Hirama, K., Y. Taniyasu, and M. Kasu (2011). AlGaN/GaN high-electron mobility transistors with low thermal resistance grown on single-crystal diamond (111) substrates by metalorganic vapor-phase epitaxy. *Applied Physics Letters* 98, 162112.
- Hoffmann, R., A. A. Kabanov, A. A. Golov, and D. M. Proserpio (2016). Homo citans und kohlenstoffallotrope: Für eine ethik des zitierens. *Angewandte Chemie* 128, 11122–11139.
- Hong, S. and M. Chou (1998). Effect of hydrogen on the surface-energy anisotropy of diamond and silicon. *Physical Review B* 57, 6262.
- Hoover, W. G. (1985). Canonical dynamics: Equilibrium phase-space distributions. *Physical Review A* 31, 1695–1697.
- Howard, W. M., B. S. Meyer, and D. D. Clayton (1992). Heavy-element abundances from a neutron burst that produces Xe-H. *Meteoritics* 27, 404–412.
- Howell, D., S. Piazzolo, D. Dobson, I. Wood, A. Jones, N. Walte, D. Frost, D. Fisher, and W. Griffin (2012). Quantitative characterization of plastic deformation of single diamond crystals: A high pressure high temperature (hpht) experimental deformation study combined with electron backscatter diffraction (ebstd). *Diamond and Related Materials* 30, 20–30.
- Huang, Q., D. Yu, B. Xu, W. Hu, Y. Ma, Y. Wang, Z. Zhao, B. Wen, J. He,

- Z. Liu, et al. (2014). Nanotwinned diamond with unprecedented hardness and stability. *Nature* 510, 250.
- Huang, X., T. B. Shiell, C. d. Tomas, I. Suarez-Martinez, S. Wong, S. Mann, D. R. McKenzie, N. A. Marks, D. G. McCulloch, and J. E. Bradby (2020). The mechanical response of glassy carbon recovered from high pressure. *Journal of Applied Physics* 127, 145105.
- Humble, P. and R. Hannink (1978). Plastic deformation of diamond at room temperature. *Nature* 273, 37.
- Huss, G. R. (2005). Meteoritic Nanodiamonds: Messengers from the Stars. *Elements* 1, 97–100.
- Huss, G. R. and R. S. Lewis (1994a). Noble gases in presolar diamonds I: Three distinct components and their implications for diamond origins. *Meteoritics* 29, 791–810.
- Huss, G. R. and R. S. Lewis (1994b). Noble gases in presolar diamonds II: Component abundances reflect thermal processing. *Meteoritics* 29, 811–829.
- Iijima, S. (1980). Direct observation of the tetrahedral bonding in graphitized carbon black by high resolution electron microscopy. *Journal of Crystal Growth* 50, 675–683.
- Imura, M., R. Hayakawa, E. Watanabe, M. Liao, Y. Koide, and H. Amano (2011). Demonstration of diamond field effect transistors by AlN/diamond heterostructure. *physica status solidi (RRL)–Rapid Research Letters* 5, 125–127.
- Isberg, J., J. Hammersberg, E. Johansson, T. Wikström, D. J. Twitchen, A. J. Whitehead, S. E. Coe, and G. A. Scarsbrook (2002). High carrier mobility in single-crystal plasma-deposited diamond. *Science* 297, 1670–1672.
- Itoh, M., M. Kotani, H. Naito, T. Sunada, Y. Kawazoe, and T. Adschiri (2009). New metallic carbon crystal. *Physical Review Letters* 102, 055703.

- Jäger, H. U. and K. Albe (2000). Molecular-dynamics simulations of steady-state growth of ion-deposited tetrahedral amorphous carbon films. *Journal of Applied Physics* 88, 1129–1135.
- Jang, D. and J. R. Greer (2010). Transition from a strong-yet-brittle to a stronger-and-ductile state by size reduction of metallic glasses. *Nature Materials* 9, 215.
- Jeng, D. G., H. Tuan, R. F. Salat, and G. J. Fricano (1990). Oriented cubic nucleations and local epitaxy during diamond growth on silicon {100} substrates. *Applied Physics Letters* 56, 1968–1970.
- Jensen, B. D., K. E. Wise, and G. M. Odegard (2015). Simulation of the Elastic and Ultimate Tensile Properties of Diamond, Graphene, Carbon Nanotubes, and Amorphous Carbon Using a Revised ReaxFF Parametrization. *The Journal of Physical Chemistry A* 119, 9710–9721.
- Jhon, Y. I., Y. M. Jhon, G. Y. Yeom, and M. S. Jhon (2014). Orientation dependence of the fracture behavior of graphene. *Carbon* 66, 619–628.
- Jiang, J.-W., J. Leng, J. Li, Z. Guo, T. Chang, X. Guo, and T. Zhang (2017). Twin graphene: A novel two-dimensional semiconducting carbon allotrope. *Carbon* 118, 370–375.
- Jiang, X. and C. Jia (1995). Diamond epitaxy on (001) silicon: An interface investigation. *Applied Physics Letters* 67, 1197–1199.
- Jiang, X., C.-P. Klages, M. Rösler, R. Zachai, M. Hartweg, and H.-J. Füsser (1993). Deposition and characterization of diamond epitaxial thin films on silicon substrates. *Applied Physics A* 57, 483–489.
- Jiang, X., J. Zhao, and X. Jiang (2011). Mechanical and electronic properties of diamond nanowires under tensile strain from first principles. *Nanotechnology* 22, 405705–11.

- Justo, J. a. F., M. de Koning, W. Cai, and V. V. Bulatov (2000). Vacancy interaction with dislocations in silicon: The Shuffle-Glide competition. *Physical Review Letters* 84, 2172–2175.
- Järrendahl, K. and R. F. Davis (1998). Chapter 1 materials properties and characterization of SiC. In Y. S. Park (Ed.), *SiC Materials and Devices*, Volume 52 of *Semiconductors and Semimetals*, pp. 1–20. Elsevier.
- Kaiser, K., L. M. Scriven, F. Schulz, P. Gawel, L. Gross, and H. L. Anderson (2019). An *sp*-hybridized molecular carbon allotrope, cyclo[18]carbon. *Science* 365, 1299–1301.
- Khaliullin, R. Z., H. Eshet, T. D. Kühne, J. Behler, and M. Parrinello (2010). Graphite-diamond phase coexistence study employing a neural-network mapping of the ab initio potential energy surface. *Physical Review B* 81, 100103.
- Kharisov, B. I., O. V. Kharissova, and L. Chávez-Guerrero (2010). Synthesis techniques, properties, and applications of nanodiamonds. *Synthesis and Reactivity in Inorganic, Metal-Organic, and Nano-Metal Chemistry* 40, 84–101.
- Kharisov, B. I., O. V. Kharissova, and U. Ortiz-Mendez (2012). Nanodiamond. In *Handbook of Less-Common Nanostructures*, pp. 598–601. CRC Press.
- Khmelnitskiy, R. (2015). Prospects for the synthesis of large single-crystal diamonds. *Physics-Uspokhi* 58, 134.
- Kiyohara, K., K. Asaka, H. Monobe, N. Terasawa, and Y. Shimizu (2006). Surface anchoring of rodlike molecules on corrugated substrates. *The Journal of Chemical Physics* 124, 034704.
- Klein, C. A. and G. F. Cardinale (1993). Young’s modulus and Poisson’s ratio of CVD diamond. *Diamond and Related Materials* 2, 918–923.
- Knippenberg, M. T., P. T. Mikulski, K. E. Ryan, S. J. Stuart, G. Gao, and J. A. Harrison (2012). Bond-order potentials with split-charge equilibration:

- Application to C-, H-, and O-containing systems. *The Journal of Chemical Physics* *136*, 164701.
- Koeberl, C., V. L. Masaitis, G. I. Shafranovsky, I. Gilmour, F. Langenhorst, and M. Schrauder (1997). Diamonds from the Popigai impact structure, Russia. *Geology* *25*, 967–970.
- Koizumi, S., H. Umezawa, J. Pernot, and M. Suzuki (2018). *Power Electronics Device Applications of Diamond Semiconductors*. Woodhead Publishing.
- Kolmogorov, A. N. and V. H. Crespi (2005). Registry-dependent interlayer potential for graphitic systems. *Physical Review B* *71*, 759–6.
- Koscheev, A., M. Gromov, P. Gorokhov, U. Ott, G. Huss, and T. Daulton (2005). Ion implantation into nanodiamonds and the mechanism of high temperature release of noble gases from meteoritic diamonds. *Meteoritics and Planetary Science Supplement* *40*, 5337.
- Koscheev, A., M. Gromov, S. Herrmann, and U. Ott (1998). Mass fractionation and thermal release from nanodiamonds of low-energy implanted xenon. *Meteoritics and Planetary Science Supplement* *33*, A87.
- Koscheev, A., M. Gromov, N. Zaripov, and U. Ott (2004). Release of noble gases during pyrolysis of meteoritic and synthetic diamonds: A new approach. *Meteoritics and Planetary Science Supplement* *39*, A55.
- Koscheev, A. P., M. D. Gromov, R. K. Mohapatra, and U. Ott (2001). History of trace gases in presolar diamonds inferred from ion-implantation experiments. *Nature* *412*, 615–617.
- Kresse, G. and J. Furthmüller (1996). Efficiency of ab-initio total energy calculations for metals and semiconductors using a plane-wave basis set. *Computational Materials Science* *6*, 15–50.

- Kresse, G. and J. Hafner (1993). Ab initio molecular dynamics for liquid metals. *Physical Review B* 47, 558.
- Kresse, G. and D. Joubert (1999). From ultrasoft pseudopotentials to the projector augmented-wave method. *Physical Review b* 59, 1758.
- Kroto, H. W., J. R. Heath, S. C. O'Brien, R. F. Curl, and R. E. Smalley (1985). C₆₀: Buckminsterfullerene. *Nature* 318, 162–163.
- Krüger, A. (2010). *Carbon Materials and Nanotechnology*. Wiley.
- Kum, O., F. H. Ree, S. J. Stuart, and C. J. Wu (2003). Molecular dynamics investigation on liquid-liquid phase change in carbon with empirical bond-order potentials. *The Journal of Chemical Physics* 119, 6053–6056.
- Kumagai, T., S. Hara, J. Choi, S. Izumi, and T. Kato (2009). Development of empirical bond-order-type interatomic potential for amorphous carbon structures. *Journal of Applied Physics* 105, 064310.
- Kumar, A., P. Ann Lin, A. Xue, B. Hao, Y. Khin Yap, and R. M. Sankaran (2013). Formation of nanodiamonds at near-ambient conditions via microplasma dissociation of ethanol vapour. *Nature Communications* 4, 2618.
- Kuznetsov, V. L., A. Chuvilin, E. Moroz, V. Kolomiichuk, S. Shaikhutdinov, Y. Butenko, and I. Mal'kov (1994). Effect of explosion conditions on the structure of detonation soots: Ultradisperse diamond and onion carbon. *Carbon* 32, 873–882.
- Kuznetsov, V. L., A. L. Chuvilin, Y. V. Butenko, I. Y. Mal'kov, and V. M. Titov (1994). Onion-like carbon from ultra-disperse diamond. *Chemical Physics Letters* 222, 343–348.
- Lau, D. W. M., D. McCulloch, N. A. Marks, N. R. Madsen, and A. V. Rode (2007). High-temperature formation of concentric fullerene-like structures

- within foam-like carbon: Experiment and molecular dynamics simulation. *Physical Review B* 75, 035401–4.
- Lebedeva, I. V., A. S. Minkin, A. M. Popov, and A. A. Knizhnik (2019). Elastic constants of graphene: Comparison of empirical potentials and dft calculations. *Physica E: Low-dimensional Systems and Nanostructures* 108, 326–338.
- Lee, B.-J. and J. W. Lee (2005). A modified embedded atom method interatomic potential for carbon. *Calphad* 29, 7–16.
- Lee, C., X. Wei, J. W. Kysar, and J. Hone (2008). Measurement of the elastic properties and intrinsic strength of monolayer graphene. *Science* 321, 385–388.
- Lee, S. T., H. Y. Peng, X. T. Zhou, N. Wang, C. S. Lee, I. Bello, and Y. Lifshitz (2000). A nucleation site and mechanism leading to epitaxial growth of diamond films. *Science* 287, 104–106.
- Lewis, R. S. and E. Anders (1981). Isotopically anomalous xenon in meteorites - A new clue to its origin. *The Astrophysical Journal* 247, 1122–1124.
- Lewis, R. S., T. Ming, J. F. Wacker, E. Anders, and E. Steel (1987). Interstellar diamonds in meteorites. *Nature* 326(6109), 160–162.
- Lewis III, D., M. A. Imam, A. W. Fliflet, R. W. Bruce, L. Kurihara, A. Kinkead, M. Lombardi, and S. H. Gold (2007). Recent advances in microwave and millimeter-wave processing of materials. In *THERMEC 2006*, Volume 539 of *Materials Science Forum*, pp. 3249–3254. Trans Tech Publications Ltd.
- Li, B., H. Sun, and C. Chen (2016). Extreme mechanics of probing the ultimate strength of nanotwinned diamond. *Physical Review Letters* 117, 116103.
- Li, K., H. Zhang, G. Li, J. Zhang, M. Bouhadja, Z. Liu, A. A. Skelton, and M. Barati (2018). Reaxff molecular dynamics simulation for the graphitization of amorphous carbon: A parametric study. *Journal of Chemical Theory and Computation* 14, 2322–2331.

- Li, Q., Y. Ma, A. R. Oganov, H. Wang, H. Wang, Y. Xu, T. Cui, H.-K. Mao, and G. Zou (2009). Superhard monoclinic polymorph of carbon. *Physical Review Letters* *102*, 175506.
- Li, X., A. Wang, and K.-R. Lee (2018). Comparison of empirical potentials for calculating structural properties of amorphous carbon films by molecular dynamics simulation. *Computational Materials Science* *151*, 246–254.
- Liang, T., T.-R. Shan, Y.-T. Cheng, B. D. Devine, M. Noordhoek, Y. Li, Z. Lu, S. R. Phillpot, and S. B. Sinnott (2013). Classical atomistic simulations of surfaces and heterogeneous interfaces with the charge-optimized many body (COMB) potentials. *Materials Science and Engineering R: Reports* *74*, 255–279.
- Lindsey, R. K., L. E. Fried, and N. Goldman (2017). ChIMES: A force matched potential with explicit three-body interactions for molten carbon. *Journal of Chemical Theory and Computation* *13*, 6222–6229.
- Liu, A. and S. J. Stuart (2008). Empirical bond-order potential for hydrocarbons: Adaptive treatment of van der Waals interactions. *Journal of Computational Chemistry* *29*, 601–611.
- Liu, J., T. Zhao, S. Zhang, and Q. Wang (2017). A new metallic carbon allotrope with high stability and potential for lithium ion battery anode material. *Nano Energy* *38*, 263–270.
- Liu, L., Y. Liu, S. V. Zybin, H. Sun, and W. A. Goddard III (2011). ReaxFF-lg: Correction of the ReaxFF reactive force field for London dispersion, with applications to the equations of state for energetic materials. *The Journal of Physical Chemistry A* *115*, 11016–11022.
- Liu, M., X. Yang, Y. Gao, R. Liu, H. Huang, X. Zhou, and T. Sham (2017). Investigation of the damage behavior in CVD SiC irradiated with 70 keV He ions

- by NEXAFS, Raman and TEM. *Journal of the European Ceramic Society* 37, 1253–1259.
- Liu, P., H. Cui, and G. W. Yang (2008). Synthesis of body-centered cubic carbon nanocrystals. *Crystal Growth & Design* 8, 581–586.
- Liu, Y., X. Jiang, J. Fu, and J. Zhao (2018). New metallic carbon: Three dimensionally carbon allotropes comprising ultrathin diamond nanostripes. *Carbon* 126, 601–610.
- Long, C., S. A. Ustin, and W. Ho (1999). Structural defects in 3c-sic grown on si by supersonic jet epitaxy. *Journal of Applied Physics* 86, 2509–2515.
- López, M. J., I. Cabria, and J. A. Alonso (2011). Simulated porosity and electronic structure of nanoporous carbons. *The Journal of Chemical Physics* 135, 104706.
- Los, J. H. and A. Fasolino (2003). Intrinsic long-range bond-order potential for carbon: Performance in Monte Carlo simulations of graphitization. *Physical Review B* 68, 24107.
- Los, J. H., L. M. Ghiringhelli, E. J. Meijer, and A. Fasolino (2005a). Improved long-range reactive bond-order potential for carbon. I. Construction. *Physical Review B* 72, 214102–14.
- Los, J. H., L. M. Ghiringhelli, E. J. Meijer, and A. Fasolino (2005b). Improved long-range reactive bond-order potential for carbon. I. Construction. *Physical Review B* 72, 214102–14.
- Lothrop, W. C. (1994). Biphenylene. *Journal of the American Chemical Society* 63, 1187–1191.
- Luo, J., J. Wang, E. Bitzek, J. Y. Huang, H. Zheng, L. Tong, Q. Yang, J. Li, and S. X. Mao (2015). Size-dependent brittle-to-ductile transition in silica glass nanofibers. *Nano Letters* 16, 105–113.

- Ma, Y., G. Zou, H. Yang, and J. Meng (1994). Conversion of fullerenes to diamond under high pressure and high temperature. *Applied Physics Letters* 65, 822–823.
- Maras, E., O. Trushin, A. Stukowski, T. Ala-Nissila, and H. Jónsson (2016). Global transition path search for dislocation formation in ge on si(001). *Computer Physics Communications* 205, 13–21.
- Marks, N. (2002a). Modelling diamond-like carbon with the environment-dependent interaction potential. *Journal of Physics: Condensed Matter* 14, 2901–2927.
- Marks, N., J. Bell, G. Pearce, D. McKenzie, and M. Bilek (2003). Atomistic simulation of energy and temperature effects in the deposition and implantation of amorphous carbon thin films. *Diamond and Related Materials* 12, 2003–2010.
- Marks, N. A. (1997). Evidence for subpicosecond thermal spikes in the formation of tetrahedral amorphous carbon. *Physical Review B* 56, 2441–2446.
- Marks, N. A. (2000). Generalizing the environment-dependent interaction potential for carbon. *Physical Review B* 63, 2879–7.
- Marks, N. A. (2001). Generalizing the environment-dependent interaction potential for carbon. *Physical Review B* 63(3), 035401.
- Marks, N. A. (2002b). Modelling diamond-like carbon with the environment-dependent interaction potential. *Journal of Physics: Condensed Matter* 14, 2901–2927.
- Marks, N. A. (2010). *Amorphous Carbon and Related Materials*, pp. 129–169. Dordrecht: Springer Netherlands.
- Marks, N. A., N. C. Cooper, D. R. McKenzie, D. G. McCulloch, P. Bath, and S. P. Russo (2002). Comparison of density-functional, tight-binding, and em-

- pirical methods for the simulation of amorphous carbon. *Physical Review B* 65, 075411.
- Marks, N. A., M. Lattemann, and D. R. McKenzie (2012). Nonequilibrium Route to Nanodiamond with Astrophysical Implications. *Physical Review Letters* 108, 343–5.
- Marks, N. A. and M. Robinson (2015). Variable timestep algorithm for molecular dynamics simulation of non-equilibrium processes. *Nuclear Instruments and Methods in Physics Research, B* 352, 3–8.
- Martin, A. A., A. Bahm, J. Bishop, I. Aharonovich, and M. Toth (2015). Dynamic pattern formation in electron-beam-induced etching. *Physical Review Letters* 115, 255501.
- Masuda, H., H. Asoh, M. Watanabe, K. Nishio, M. Nakao, and T. Tamamura (2001). Square and triangular nanohole array architectures in anodic alumina. *Advanced Materials* 13, 189–192.
- Matsuda, J.-i., K. Fukunaga, and K. Ito (1991). Noble gas studies in vapor-growth diamonds: Comparison with shock-produced diamonds and the origin of diamonds in ureilites. *Geochimica et Cosmochimica Acta* 55, 2011–2023.
- Matsuda, J.-I., A. Kusumi, H. Yajima, and Y. Syono (1995). Noble gas studies in diamonds synthesized by shock loading in the laboratory and their implications on the origin of diamonds in ureilites. *Geochimica et Cosmochimica Acta* 59, 4939–4949.
- Matsunaga, K., C. Fisher, and H. Matsubara (2000). Tersoff potential parameters for simulating cubic boron carbonitrides. *Jpn. Journal of Applied Physics Pt. 2, Letters* 39, L48–L51.
- Matthey, B., S. Höhn, A.-K. Wolfrum, U. Mühle, M. Motylenko, D. Rafaja, A. Michaelis, and M. Herrmann (2017). Microstructural investigation of

- diamond-SiC composites produced by pressureless silicon infiltration. *Journal of the European Ceramic Society* 37, 1917–1928.
- Meyer, L., S. Dasgupta, D. Shaddock, J. Tucker, R. Fillion, P. Bronecke, L. Yorinks, and P. Kraft (2003). A silicon-carbide micro-capillary pumped loop for cooling high power devices. In *Nineteenth Annual IEEE Semiconductor Thermal Measurement and Management Symposium, 2003.*, pp. 364–368.
- Mochalin, V. N., O. Shenderova, D. Ho, and Y. Gogotsi (2012). The properties and applications of nanodiamonds. *Nature Nanotechnology* 7, 11.
- Mrovec, M., M. Moseler, C. Elsässer, and P. Gumbsch (2007). Atomistic modeling of hydrocarbon systems using analytic bond-order potentials. *Progress in Materials Science* 52, 230–254.
- Mun, S., A. L. Bowman, S. Nouranian, S. R. Gwaltney, M. I. Baskes, and M. F. Horstemeyer (2017). Interatomic potential for hydrocarbons on the basis of the modified embedded-atom method with bond order (meam-bo). *The Journal of Physical Chemistry A* 121, 1502–1524.
- Nair, R. R., P. Blake, A. N. Grigorenko, K. S. Novoselov, T. J. Booth, T. Stauber, N. M. R. Peres, and A. K. Geim (2008). Fine structure constant defines visual transparency of graphene. *Science* 320, 1308–1308.
- Narayan, J. and B. Larson (2003). Domain epitaxy: A unified paradigm for thin film growth. *Journal of Applied Physics* 93, 278–285.
- Narayan, J., A. Srivatsa, M. Peters, S. Yokota, and K. Ravi (1988). On epitaxial growth of diamond films on (100) silicon substrates. *Applied Physics Letters* 53, 1823–1825.
- Nguyen, T. X., N. Cohaut, J.-S. Bae, and S. K. Bhatia (2008). New Method for Atomistic Modeling of the Microstructure of Activated Carbons Using Hybrid Reverse Monte Carlo Simulation. *Langmuir* 24, 7912–7922.

- Ni, B., K.-H. Lee, and S. B. Sinnott (2004). A reactive empirical bond order (REBO) potential for hydrocarbon-oxygen interactions. *Journal of Physics: Condensed Matter* 16, 7261–7275.
- Nickel, K. G., T. Kraft, and Y. G. Gogotsi (2008). *Hydrothermal Synthesis of Diamond*, Chapter 3, pp. 374–389. John Wiley & Sons, Ltd.
- Nittler, L. R. (2003). Presolar stardust in meteorites: recent advances and scientific frontiers. *Earth and Planetary Science Letters* 209, 259–273.
- Niu, C.-Y., X.-Q. Wang, and J.-T. Wang (2014). K6carbon: A metallic carbon allotrope in sp³ bonding networks. *The Journal of Chemical Physics* 140, 054514–4.
- Nord, J., K. Nordlund, and J. Keinonen (2002). Amorphization mechanism and defect structures in ion-beam-amorphized Si, Ge, and GaAs. *Physical Review B* 65, 165329.
- Nordlund, K., J. Keinonen, and T. Mattila (1996). Formation of ion irradiation induced small-scale defects on graphite surfaces. *Physical Review Letters* 77, 699–702.
- Nouranian, S., M. A. Tschopp, S. R. Gwaltney, M. I. Baskes, and M. F. Horstemeyer (2014). An interatomic potential for saturated hydrocarbons based on the modified embedded-atom method. *Physical Chemistry Chemical Physics* 16, 6233–6249.
- Novoselov, K. S., A. K. Geim, S. V. Morozov, D. Jiang, Y. Zhang, S. V. Dubonos, I. V. Grigorieva, and A. A. Firsov (2004). Electric field effect in atomically thin carbon films. *Science* 306, 666–669.
- Nowicki, T., B. Crawford, D. Dyck, J. Carlson, R. McElroy, P. Oshust, and H. Helmstaedt (2004). The geology of kimberlite pipes of the ekati property, northwest territories, canada. *Lithos* 76, 1–27.

- Nuth, J. A. and J. E. Allen (1992). Supernovae as sources of interstellar diamonds. *Astrophysics and Space Science* 196, 117–123.
- O’Connor, T. C., J. Andzelm, and M. O. Robbins (2015). AIREBO-M: A reactive model for hydrocarbons at extreme pressures. *The Journal of Chemical Physics* 142, 024903.
- Odegard, G. M., T. S. Gates, L. M. Nicholson, and K. E. Wise (2002). Equivalent-continuum modeling of nano-structured materials. *Composites Science and Technology* 62, 1869–1880.
- Okada, S. (2009). Formation of graphene nanostructures on diamond nanowire surfaces. *Chemical Physics Letters* 483, 128–132.
- Okushi, H. (2001). High quality homoepitaxial cvd diamond for electronic devices. *Diamond and Related Materials* 10, 281–288.
- Oleinik, I. I. and D. G. Pettifor (1999). Analytic bond-order potentials beyond Tersoff-Brenner. II. Application to the hydrocarbons. *Physical Review B* 59, 8500–8507.
- Ott, U. (1993). Interstellar grains in meteorites. *Nature* 364, 25–33.
- Ott, U. (1996). Interstellar diamond xenon and timescales of supernova eject. *The Astrophysical Journal* 463, 344–348.
- Ott, U. (2007). Presolar grains in meteorites and their compositions. *Space Science Reviews* 130, 87–95.
- Ott, U. (2014). Planetary and pre-solar noble gases in meteorites. *Chem Erde-Geochemistry* 74, 519–544.
- Pan, Y., C. Xie, M. Xiong, M. Ma, L. Liu, Z. Li, S. Zhang, G. Gao, Z. Zhao, Y. Tian, B. Xu, and J. He (2017). A superhard sp³ microporous carbon with direct bandgap. *Chemical Physics Letters* 689, 68–73.

- Pang, Z., X. Gu, Y. Wei, R. Yang, and M. S. Dresselhaus (2016). Bottom-up design of three-dimensional carbon-honeycomb with superb specific strength and high thermal conductivity. *Nano Letters* *17*, 179–185.
- Pantea, C., J. Qian, G. A. Voronin, and T. W. Zerda (2002). High pressure study of graphitization of diamond crystals. *Journal of Applied Physics* *91*, 1957–1962.
- Pantea, D., S. Brochu, S. Thiboutot, G. Ampleman, and G. Scholz (2006). A morphological investigation of soot produced by the detonation of munitions. *Chemosphere* *65*, 821–831.
- Park, J. S., R. Sinclair, D. Rowcliffe, M. Stern, and H. Davidson (2006). FIB and TEM studies of interface structure in diamond–SiC composites. *Journal of Materials Science* *41*, 4611–4616.
- Park, J. S., R. Sinclair, D. Rowcliffe, M. Stern, and H. Davidson (2007). Orientation relationship in diamond and silicon carbide composites. *Diamond and Related Materials* *16*, 562–565.
- Parrinello, M. and A. Rahman (1981). Polymorphic transitions in single crystals: A new molecular dynamics method. *Journal of Applied Physics* *52*, 7182–7190.
- Pastewka, L., A. Klemenz, P. Gumbsch, and M. Moseler (2013). Screened empirical bond-order potentials for Si-C. *Physical Review B* *87*, 205410.
- Pastewka, L., P. Pou, R. Pérez, P. Gumbsch, and M. Moseler (2008). Describing bond-breaking processes by reactive potentials: Importance of an environment-dependent interaction range. *Physical Review B* *78*, 161402 (R).
- Pearce, G., N. Marks, D. McKenzie, and M. Bilek (2005). Molecular dynamics simulation of the thermal spike in amorphous carbon thin films. *Diamond and Related Materials* *14*, 921–927.

- People, R. and J. Bean (1985). Calculation of critical layer thickness versus lattice mismatch for $\text{Ge}_x\text{Si}_{1-x}/\text{Si}$ strained-layer heterostructures. *Applied Physics Letters* 47, 322–324.
- Perdew, J. P., K. Burke, and M. Ernzerhof (1996). Generalized gradient approximation made simple. *Physical Review Letters* 77, 3865.
- Perriot, R., X. Gu, Y. Lin, V. V. Zhakhovsky, and I. I. Oleynik (2013). Screened environment-dependent reactive empirical bond-order potential for atomistic simulations of carbon materials. *Physical Review B* 88, 064101.
- Pettifor, D. G. and I. I. Oleinik (1999). Analytic bond-order potentials beyond Tersoff-Brenner. I. Theory. *Physical Review B* 59, 8487–8499.
- Pierson, H. O. (1993a). 2 - the element carbon. In H. O. Pierson (Ed.), *Handbook of Carbon, Graphite, Diamonds and Fullerenes*, pp. 11–42. Oxford: William Andrew Publishing.
- Pierson, H. O. (1993b). 3 - graphite structure and properties. In H. O. Pierson (Ed.), *Handbook of Carbon, Graphite, Diamonds and Fullerenes*, pp. 43–69. William Andrew Publishing.
- Pizzagalli, L., G. Cicero, and A. Catellani (2003). Theoretical investigations of a highly mismatched interface: $\text{SiC}/\text{Si}(001)$. *Physical Review B* 68, 337–10.
- Plimpton, S. (1995). Fast parallel algorithms for short-range molecular dynamics. *The Journal of Chemical Physics* 117, 1–19.
- Powles, R. C., N. A. Marks, and D. W. M. Lau (2009). Self-assembly of sp^2 -bonded carbon nanostructures from amorphous precursors. *Physical Review B* 79, 075430.
- Prado, R., T. D’addio, M. C. d. A. Fantini, I. Pereyra, and A. Flank (2003). Annealing effects of highly homogeneous a-Si_{1-x}C_x: H. *Journal of Non-Crystalline Solids* 330, 196–215.

- Qiao, Z., J. Li, N. Zhao, C. Shi, and P. Nash (2006). Graphitization and microstructure transformation of nanodiamond to onion-like carbon. *Scripta Materialia* 54, 225–229.
- Rajasekaran, G., R. Kumar, and A. Parashar (2016). Tersoff potential with improved accuracy for simulating graphene in molecular dynamics environment. *Materials Research Express* 3, 035011.
- Rajput, N. S., F. Le Marrec, M. El Marssi, and M. Jouiad (2018). Fabrication and manipulation of nanopillars using electron induced excitation. *Journal of Applied Physics* 124, 074301.
- Regan, B., A. Aghajamali, J. Froech, T. T. Tran, J. Scott, J. Bishop, I. Suarez-Martinez, Y. Liu, J. M. Cairney, N. A. Marks, M. Toth, and I. Aharonovich (2020). Plastic deformation of single crystal diamond nanopillars. *Advanced Materials* 32, 1906458.
- Regueiro, M. D. N., P. Monceau, and J.-L. Hodeau (1992). Crushing C60 to diamond at room temperature. *Nature* 355, 237–239.
- Richardson, S. H., J. J. Gurney, A. J. Erlank, and J. W. Harris (1984). Origin of diamonds in old enriched mantle. *Nature* 310, 198–202.
- Robertson, J. (1995). Mechanism of bias-enhanced nucleation and heteroepitaxy of diamond on Si. *Diamond and Related Materials* 4, 549–552.
- Robinson, A. L. (1986). Is diamond the new wonder material? *Science* 234, 1074–1077.
- Robinson, M. and N. Marks (2014). NanoCap: A framework for generating capped carbon nanotubes and fullerenes. *Computer Physics Communications* 185, 2519–2526.

- Robinson, M., N. A. Marks, and G. R. Lumpkin (2012). Sensitivity of the threshold displacement energy to temperature and time. *Physical Review B* *86*, 134105–8.
- Robinson, M., N. A. Marks, and G. R. Lumpkin (2014). Structural dependence of threshold displacement energies in rutile, anatase and brookite TiO₂. *Materials Chemistry and Physics* *147*, 311–318.
- Robinson, M., N. A. Marks, K. R. Whittle, and G. R. Lumpkin (2012). Systematic calculation of threshold displacement energies: Case study in rutile. *Physical Review B* *85*, 104105–11.
- Robinson, M., I. Suarez-Martinez, and N. A. Marks (2013). Generalized method for constructing the atomic coordinates of nanotube caps. *Physical Review B* *87*, 155430–8.
- Roundy, D. and M. L. Cohen (2001). Ideal strength of diamond, Si, and Ge. *Physical Review B* *64*, 212103.
- Rowe, P., G. Csányi, D. Alfè, and A. Michaelides (2018). Development of a machine learning potential for graphene. *Physical Review B* *97*, 054303.
- Salzmann, C. G., B. J. Murray, and J. J. Shephard (2015). Extent of stacking disorder in diamond. *Diamond and Related Materials* *59*, 69–72.
- Sand, A. E. (2015). *Molecular Dynamics Simulations of Primary Radiation Damage from Collision Cascades*. Ph. D. thesis, Division of Materials, Physics Department of Physics, Faculty of Science, University of Helsinki Helsinki, Finland.
- Savvatimskiy, A. (2015). *Carbon at High Temperatures*, Volume 134. Switzerland: Springer Series in Materials Science.

- Schedin, F., A. K. Geim, S. V. Morozov, E. W. Hill, P. Blake, M. I. Katsnelson, and K. S. Novoselov (2007). Detection of individual gas molecules adsorbed on graphene. *Nature Materials* 6, 625–655.
- Schenk, A., A. Tadich, M. Sear, K. M. O’Donnell, L. Ley, A. Stacey, and C. Pakes (2015). Formation of a silicon terminated (100) diamond surface. *Applied Physics Letters* 106, 191603.
- Schreck, M., J. Asmussen, S. Shikata, J.-C. Arnault, and N. Fujimori (2014). Large-area high-quality single crystal diamond. *Mrs Bulletin* 39, 504–510.
- Schreck, M., F. Hörmann, H. Roll, J. Lindner, and B. Stritzker (2001). Diamond nucleation on iridium buffer layers and subsequent textured growth: A route for the realization of single-crystal diamond films. *Applied Physics Letters* 78, 192–194.
- Schreck, M. and B. Stritzker (1996). Nucleation and growth of heteroepitaxial diamond films on silicon. *physica status solidi (a)* 154, 197–217.
- Schwan, J., S. Ulrich, H. Roth, H. Ehrhardt, S. R. P. Silva, R. J., and *et al.* (1996). Tetrahedral amorphous carbon films prepared by magnetron sputtering and dc ion plating. *Journal of Applied Physics* 79, 1416–1422.
- Schwan, J., S. Ulrich, H. Roth, H. Ehrhardt, S. R. P. Silva, J. Robertson, R. Samlenski, and R. Brenn (1996). Tetrahedral amorphous carbon films prepared by magnetron sputtering and dc ion plating. *Journal of Applied Physics* 79, 1416–1422.
- Schwander, M. and K. Partes (2011). A review of diamond synthesis by CVD processes. *Diamond and Related Materials* 20, 1287–1301.
- Sha, Z. D., P. S. Branicio, Q. X. Pei, V. Sorkin, and Y. W. Zhang (2013). A modified Tersoff potential for pure and hydrogenated diamond-like carbon. *Chem. Materials Science* 67, 146–150.

- Shenderova, O., D. Brenner, and R. S. Ruoff (2003). Would Diamond Nanorods Be Stronger than Fullerene Nanotubes? *Nano Letters* 3, 805–809.
- Shenderova, O. and G. McGuire (2006). *Nanocrystalline Diamond*, pp. 175–209. CRC Press.
- Shenderova, O. A., D. W. Brenner, A. Omeltchenko, X. Su, and L. H. Yang (2000). Atomistic modeling of the fracture of polycrystalline diamond. *Physical Review B* 61, 3877–3888.
- Shenderova, O. A., I. I. Vlasov, S. Turner, G. Van Tendeloo, S. B. Orlinskii, A. A. Shiryaev, A. A. Khomich, S. N. Sulyanov, F. Jelezko, and J. Wrachtrup (2011). Nitrogen control in nanodiamond produced by detonation shock-wave-assisted synthesis. *The Journal of Physical Chemistry C* 115, 14014–14024.
- Sheng, X.-L., Q.-B. Yan, F. Ye, Q.-R. Zheng, and G. Su (2011). T-carbon: A novel carbon allotrope. *Physical Review Letters* 106, 155703.
- Shi, Y. (2008). A mimetic porous carbon model by quench molecular dynamics simulation. *The Journal of Chemical Physics* 128, 234707.
- Shiell, T. B., C. de Tomas, D. McCulloch, D. R. McKenzie, A. Basu, I. Suarez Martinez, N. A. Marks, R. Boehler, B. Haberl, and J. E. Bradby (2019). In situ analysis of the structural transformation of glassy carbon under compression at room temperature. *Physical Review B* 99, 024114.
- Shiell, T. B., D. McCulloch, D. R. McKenzie, M. R. Field, B. Haberl, R. Boehler, B. A. Cook, C. de Tomas, I. Suarez Martinez, N. A. Marks, and J. E. Bradby (2018). Graphitization of Glassy Carbon after Compression at Room Temperature. *Physical Review Letters* 120, 215701.
- Shiomi, H. (1997). Reactive ion etching of diamond in O_2 and CF_4 plasma, and fabrication of porous diamond for field emitter cathodes. *Japanese Journal of Applied Physics* 36, 7745–7748.

- Shiryaev, A. A., J. A. Hinks, N. A. Marks, G. Greaves, F. J. Valencia, S. E. Donnelly, R. I. González, M. Kiwi, A. L. Trigub, E. M. Bringa, J. L. Fogg, and I. I. Vlasov (2018). Ion implantation in nanodiamonds: size effect and energy dependence. *Scientific Reports* 8, 992.
- Si, C., Z. Sun, and F. Liu (2016). Strain engineering of graphene: A review. *Nanoscale* 8, 3207–3217.
- Simonyan, V. V., J. K. Johnson, A. Kuznetsova, and J. T. Yates Jr. (2001). Molecular simulation of xenon adsorption on single-walled carbon nanotubes. *The Journal of Chemical Physics* 114, 4180–4185.
- Smith, R., K. Jolley, C. Latham, M. Heggie, A. van Duin, D. van Duin, and H. Wu (2017). A ReaxFF carbon potential for radiation damage studies. *Nuclear Instruments and Methods in Physics Research B* 393, 49–53.
- Sobolev, N., A. Logvinova, D. Zedgenizov, Y. Seryotkin, E. Yefimova, C. Floss, and L. Taylor (2004). Mineral inclusions in microdiamonds and macrodiamonds from kimberlites of yakutia: a comparative study. *Lithos* 77, 225–242.
- Sørensen, M. R. and A. F. Voter (2000). Temperature-accelerated dynamics for simulation of infrequent events. *The Journal of Chemical Physics* 112, 9599–9606.
- Soulière, V., A. Vo-Ha, D. Carole, A. Tallaire, O. Brinza, J. C. Pinero, D. Araújo, and G. Ferro (2014). Heteroepitaxial CVD Growth of 3C-SiC on Diamond Substrate. In *Materials Science Forum*, Volume 778, pp. 226–229.
- Srinivasan, S. G., A. C. T. van Duin, and P. Ganesh (2015). Development of a ReaxFF potential for carbon condensed phases and its application to the thermal fragmentation of a large fullerene. *The Journal of Physical Chemistry A* 119, 571–580.

- Stoner, B. and J. Glass (1992). Textured diamond growth on (100) β -SiC via microwave plasma chemical vapor deposition. *Applied Physics Letters* 60, 698–700.
- Stuart, S. J., M. T. Knippenberg, O. Kum, and P. S. Krstic (2006). Simulation of amorphous carbon with a bond-order potential. *Physica Scripta* 2006, 58.
- Stuart, S. J., A. B. Tutein, and J. A. Harrison (2000). A reactive potential for hydrocarbons with intermolecular interactions. *The Journal of Chemical Physics* 112, 6472–6486.
- Stukowski, A. (2010). Visualization and analysis of atomistic simulation data with OVITO: the Open Visualization Tool. *Modelling and Simulation in Materials Science and Engineering* 18, 015012.
- Suarez-Martinez, I., P. J. Higginbottom, and N. A. Marks (2010). Molecular dynamics simulations of the transformation of carbon peapods into double-walled carbon nanotubes. *Carbon* 48, 3592–3598.
- Suarez-Martinez, I. and N. A. Marks (2012). Amorphous carbon nanorods as a precursor for carbon nanotubes. *Carbon* 50, 5441–5449.
- Sung, H.-J., S. Kim, I.-H. Lee, and K. J. Chang (2017). Semimetallic carbon allotrope with a topological nodal line in mixed sp²-sp³ bonding networks. *Nature Publishing Group Asia Materials* 9, e361–6.
- Suto, T., J. Yaita, T. Iwasaki, and M. Hatano (2017). Highly oriented diamond (111) films synthesized by pulse bias-enhanced nucleation and epitaxial grain selection on a 3c-sic/si (111) substrate. *Applied Physics Letters* 110, 062102.
- Tadmor, E. B., R. S. Elliott, S. R. Phillpot, and S. B. Sinnott (2013). Nsf cyber-infrastructure: A new paradigm for advancing materials simulation. *Current Opinion in Solid State and Materials Science* 17, 298–304.

- Tadmor, E. B., R. S. Elliott, J. P. Sethna, R. E. Miller, and C. A. Becker (2011). The potential of atomistic simulations and the knowledgebase of interatomic models. *JOM* 63, 17.
- Taloni, A., M. Vodret, G. Costantini, and S. Zapperi (2018). Size effects on the fracture of microscale and nanoscale materials. *Nature Reviews Materials* 3, 211–224.
- Tang, M. and S. Yip (1995). Atomistic simulation of thermomechanical properties of β -SiC. *Physical Review B* 52, 15150–15159.
- Tangarife, E., R. I. Gonzalez, C. Cardenas, E. M. Bringa, and F. Munoz (2019). Molecular simulations of carbon allotropes in processes with creation and destruction of chemical bonds. *Carbon* 144, 177–184.
- Taylor, A. and R. M. Jones (1960). *Silicon Carbide – A High Temperature Semiconductor*. Pergamon Press.
- Telling, R., C. Pickard, M. Payne, and J. Field (2000). Theoretical strength and cleavage of diamond. *Physical Review Letters* 84, 5160.
- Tersoff, J. (1986). New empirical model for the structural properties of silicon. *Physical Review Letters* 56, 632–635.
- Tersoff, J. (1988). Empirical interatomic potential for carbon, with applications to amorphous carbon. *Physical Review Letters* 61, 2879–2882.
- Tersoff, J. (1989). Modeling solid-state chemistry: Interatomic potentials for multicomponent systems. *Physical Review B* 39, 5566–5568.
- Tersoff, J. (1990). Carbon defects and defect reactions in silicon. *Physical Review Letters* 64, 1757–1760.
- Tersoff, J. (1994). Chemical order in amorphous silicon carbide. *Physical Review B* 49, 16349–16352.

- Tewary, V. K. and B. Yang (2009). Parametric interatomic potential for graphene. *Physical Review B* 79, 075442–9.
- Thomson, J. (1904). Xxiv. on the structure of the atom: an investigation of the stability and periods of oscillation of a number of corpuscles arranged at equal intervals around the circumference of a circle; with application of the results to the theory of atomic structure. *The London, Edinburgh, and Dublin Philosophical Magazine and Journal of Science* 7, 237–265.
- Thune, E., T. Cabioch, M. Jaouen, and F. Bodart (2003). Nucleation and growth of carbon onions synthesized by ion implantation at high temperatures. *Physical Review B* 68, 115434.
- Titantah, J. T. and D. Lamoen (2005). sp^3/sp^2 characterization of carbon materials from first-principles calculations: X-ray photoelectron versus high energy electron energy-loss spectroscopy techniques. *Carbon* 43, 1311–1316.
- Tomita, S., A. Burian, J. C. Dore, D. LeBolloch, M. Fujii, and S. Hayashi (2002). Diamond nanoparticles to carbon onions transformation: X-ray diffraction studies. *Carbon* 40, 1469–1474.
- Totani, R., C. Grazioli, T. Zhang, I. Bidermane, J. Lüder, M. de Simone, M. Coreno, B. Brena, L. Lozzi, and C. Puglia (2017). Electronic structure investigation of biphenylene films. *The Journal of Chemical Physics* 146, 054705.
- Trew, R. J., J.-B. Yan, and P. M. Mock (1991). The potential of diamond and silicon electronic devices for microwave and millimeter-wave power applications. *Proceedings of the IEEE* 79, 598–620.
- Troiani, H. E., A. Camacho-Bragado, V. Armendariz, J. L. Gardea Torresday, and M. Jose Yacaman (2003). Synthesis of carbon onions by gold nanoparticles and electron irradiation. *Chemistry of Materials* 15, 1029–1031.

- Tsai, A., A. Aghajamali, N. Dontschuk, B. C. Johnson, M. Usman, A. K. Schenk, M. Sear, C. I. Pakes, L. C. L. Hollenberg, J. C. McCallum, S. Rubanov, A. Tadich, N. A. Marks, and A. Stacey (2020). Epitaxial formation of SiC on (100) diamond. *ACS Applied Electronic Materials* 2, 2003–2009.
- Uddin, J., M. I. Baskes, S. G. Srinivasan, T. R. Cundari, and A. K. Wilson (2010). Modified embedded atom method study of the mechanical properties of carbon nanotube reinforced nickel composites. *Physical Review B* 81, 104103.
- Uemura, Y. (1994). Atomistic model for the evaluation of the stability of diamond under uniaxial tensile force. *Physical Review B* 49, 6528.
- Uemura, Y. (1995). Atomistic simulation of the behavior of diamond under compressive stress. *Physical Review B* 51, 6704.
- Ugarte, D. (1992). Curling and closure of graphitic networks under electron-beam irradiation. *Nature* 359, 707–709.
- Vahvaselka, K. S. and J. M. Mangs (1988). X-ray diffraction study of liquid sulfur. *Physica Scripta* 38, 737–741.
- van Duin, A. C. T., S. Dasgupta, F. Lorant, and W. A. Goddard III (2001). ReaxFF: A reactive force field for hydrocarbons. *The Journal of Physical Chemistry A* 105, 9396–9409.
- Verchovsky, A., I. Wright, A. Fisenko, and C. Pillinger (2001). A numerical model of ion implantation into presolar grains. *Nuclear Physics A* 688, 106–109.
- Verchovsky, A., I. Wright, and C. Pillinger (2003). Ion implantation into presolar grains: a theoretical model. *Publications of the Astronomical Society of Australia* 20, 329–336.
- Verchovsky, A. B., A. V. Fisenko, L. F. Semjonova, I. P. Wright, M. R. Lee, and C. T. Pillinger (1998). C, N, and Noble Gas Isotopes in Grain Size Separates of Presolar Diamonds from Efremovka. *Science* 281, 1165–1168.

- Verchovsky, A. B., I. P. Wright, A. V. Fisenko, L. F. Semjonova, and C. T. Pillinger (2000). Ion Implantation into Presolar Diamonds: Experimental Simulation. *Journal of Conference Abstracts* 5, 1050.
- Verchovsky, A. B., I. P. Wright, and C. T. Pillinger (2004). Astrophysical significance of asymptotic giant branch stellar wind energies recorded in meteoritic SiC grains. *The Astrophysical Journal* 607, 611–619.
- Verlet, L. (1967). Computer "experiments" on classical fluids. i. thermodynamical properties of lennard-jones molecules. *Physical Review* 159, 98–103.
- Vlasov, I. I., O. Shenderova, S. Turner, O. I. Lebedev, A. A. Basov, I. Sildos, M. Rähn, A. A. Shiryaev, and G. Van Tendeloo (2010). Nitrogen and luminescent nitrogen-vacancy defects in detonation nanodiamond. *Small* 6, 687–694.
- Voronin, G., C. Pantea, T. Zerda, and K. Ejsmont (2001). Oriented growth of β -SiC on diamond crystals at high pressure. *Journal of Applied Physics* 90, 5933–5935.
- Voter, A. F. (1997). Hyperdynamics: Accelerated molecular dynamics of infrequent events. *Physical Review Letters* 78, 3908–3911.
- Voter, A. F. (1998). Parallel replica method for dynamics of infrequent events. *Physical Review B* 57, R13985–R13988.
- Voyles, P. M., N. Zotov, S. M. Nakhmanson, D. A. Drabold, J. M. Gibson, M. M. J. Treacy, and P. Keblinski (2001). Structure and physical properties of paracrystalline atomistic models of amorphous silicon. *Journal of Applied Physics* 90, 4437–4451.
- Vuković, F., J.-M. Leyssale, P. Aurel, and N. A. Marks (2018). Evolution of Threshold Displacement Energy in Irradiated Graphite. *Physical Review Applied* 10, 176.

- Wales, D. J., J. P. K. Doye, A. Dullweber, M. P. Hodges, F. Y. Naumkin, F. Calvo, J. Hernández-Rojas, and T. F. Middleton (2006). *The Cambridge Cluster Database*.
- Wales, D. J. and S. Ulker (2006). Structure and dynamics of spherical crystals characterized for the thomson problem. *Physical Review B* *74*, 212101.
- Wallace, P. R. (1947). The band theory of graphite. *Physical Review* *71*, 622–634.
- Walmsley, J. and A. Lang (1983). Transmission electron microscopic observations of deformation and microtwinning in a synthetic diamond compact. *Journal of Materials Science Letters* *2*, 785–788.
- Wang, C. Z., K. M. Ho, M. D. Shirk, and P. A. Molian (2000). Laser-Induced Graphitization on a Diamond (111) Surface. *Physical Review Letters* *85*, 4092–4095.
- Wang, J.-Q., C.-X. Zhao, C.-Y. Niu, Q. Sun, and Y. Jia (2016). C₂₀-Tcarbon: a novel superhard sp³ carbon allotrope with large cavities. *Journal of Physics: Condensed Matter* *28*, 475402.
- Wang, J.-T., C. Chen, and Y. Kawazoe (2011). Low-temperature phase transformation from graphite to sp³ orthorhombic carbon. *Physical Review Letters* *106*, 075501.
- Wang, J.-T., C. Chen, and Y. Kawazoe (2012). Orthorhombic carbon allotrope of compressed graphite: Ab initio calculations. *Physical Review B* *85*, 033410.
- Wang, Y., Y. Yang, L. Yan, S. Y. Kwok, W. Li, Z. Wang, X. Zhu, G. Zhu, W. Zhang, X. Chen, et al. (2014). Poking cells for efficient vector-free intracellular delivery. *Nature Communications* *5*, 4466.
- Wang, Z., X.-F. Zhou, X. Zhang, Q. Zhu, H. Dong, M. Zhao, and A. R. Oganov (2015). Phagraphene: A low-energy graphene allotrope composed of 5–6–7 carbon rings with distorted dirac cones. *Nano Letters* *15*, 6182–6186.

- Warren, B. E. (1990). *X-ray Diffraction*. Courier Corporation.
- Waseda, Y. (1980). *The structure of non-crystalline materials: liquids and amorphous solids*. Advanced Book Program. McGraw-Hill International Book Co.
- Wei, Q., Q. Zhang, H. Yan, and M. Zhang (2017). A new superhard carbon allotrope: tetragonal C64. *Journal of Materials Science* 52, 2385–2391.
- Wei, Y., J. Wu, H. Yin, X. Shi, R. Yang, and M. Dresselhaus (2012). The nature of strength enhancement and weakening by pentagon–heptagon defects in graphene. *Nature Materials* 11, 759–763.
- Weitzel, C. E., J. W. Palmour, C. H. Carter, K. Moore, K. Nordquist, S. Allen, C. Thero, and M. Bhatnagar (1996). Silicon carbide high-power devices. *IEEE transactions on Electron Devices* 43, 1732–1741.
- Wen, C., Y. M. Wang, W. Wan, F. H. Li, J. W. Liang, and J. Zou (2009). Nature of interfacial defects and their roles in strain relaxation at highly lattice mismatched 3C-SiC/Si (001) interface. *Journal of Applied Physics* 106, 073522–8.
- Wen, M., S. Carr, S. Fang, E. Kaxiras, and E. B. Tadmor (2018). Dihedral-angle-corrected registry-dependent interlayer potential for multilayer graphene structures. *Physical Review B* 98, 235404.
- Willander, M., M. Friesel, Q.-u. Wahab, and B. Straumal (2006). Silicon carbide and diamond for high temperature device applications. *Journal of Materials Science: Materials in Electronics* 17, 1.
- Williams, B. and J. Glass (1989). Characterization of diamond thin films: Diamond phase identification, surface morphology, and defect structures. *Journal of Materials Research* 4, 373–384.
- Wort, C. J. and R. S. Balmer (2008). Diamond as an electronic material. *Materials Today* 11, 22–28.

- Wu, H., L. Sang, Y. Li, T. Teraji, T. Li, M. Imura, J. You, Y. Koide, M. Toda, and M. Liao (2018). Reducing intrinsic energy dissipation in diamond-on-diamond mechanical resonators toward one million quality factor. *Physical Review Materials* 2, 090601.
- Wu, J. and Y. Wei (2013). Grain misorientation and grain-boundary rotation dependent mechanical properties in polycrystalline graphene. *Journal of the Mechanics and Physics of Solids* 61, 1421–1432.
- Wu, X., X. Shi, M. Yao, S. Liu, X. Yang, L. Zhu, T. Cui, and B. Liu (2017). Superhard three-dimensional carbon with metallic conductivity. *Carbon* 123, 311–317.
- Wu, Z.-j., E.-j. Zhao, H.-p. Xiang, X.-f. Hao, X.-j. Liu, and J. Meng (2007). Crystal structures and elastic properties of superhard IrN₂ and IrN₃ from first principles. *Physical Review B* 76, 054115.
- Wyckoff, R. (1963). *Crystal Structures*. Number v. 1 in Crystal Structures. Wiley.
- Xiao, J., G. Ouyang, P. Liu, C. X. Wang, and G. W. Yang (2014). Reversible Nanodiamond-Carbon Onion Phase Transformations. *Nano Letters* 14, 3645–3652.
- Xiong, L. (2011). *A concurrent atomistic-continuum methodology and its applications*. Ph. D. thesis, University of Florida, USA.
- Xiong, L., Y. Chen, and J. D. Lee (2007). Atomistic simulation of mechanical properties of diamond and silicon carbide by a field theory. *Modelling and Simulation in Materials Science and Engineering* 15, 535–551.
- Xu, B. and S.-i. Tanaka (1995). Phase transformation and bonding of ceramic nanoparticles in a TEM. *Nanostructured Materials* 6, 727–730.

- Xu, K., H. Liu, Y.-C. Shi, J.-Y. You, X.-Y. Ma, H.-J. Cui, Q.-B. Yan, G.-C. Chen, and G. Su (2019). Preparation of T-carbon by plasma enhanced chemical vapor deposition. *Carbon* 157, 270–276.
- Xu, L.-C., X.-J. Song, R.-Z. Wang, Z. Yang, X.-Y. Li, and H. Yan (2015). Designing electronic anisotropy of three-dimensional carbon allotropes for the all-carbon device. *Applied Physics Letters* 107, 021905.
- Yacoby, A. (2011). Tri and tri again. *Nature Physics* 7, 925–926.
- Yaita, J., T. Iwasaki, and M. Hatano (2018). Heteroepitaxy of diamond on sic. In S. Koizumi, H. Umezawa, J. Pernot, and M. Suzuki (Eds.), *Power Electronics Device Applications of Diamond Semiconductors*, Woodhead Publishing Series in Electronic and Optical Materials, pp. 81–97. Woodhead Publishing.
- Yaita, J., M. Natal, S. E. Saddow, M. Hatano, and T. Iwasaki (2017). Influence of high-power density plasma on heteroepitaxial diamond nucleation on 3C-SiC surface. *Applied Physics Express* 10, 045502.
- Yamada, H., A. Chayahara, Y. Mokuno, Y. Kato, and S. Shikata (2014). A 2-in. mosaic wafer made of a single-crystal diamond. *Applied Physics Letters* 104, 102110.
- Yamada, H., A. Chayahara, Y. Mokuno, N. Tsubouchi, and S.-i. Shikata (2013). Uniform growth and repeatable fabrication of inch-sized wafers of a single-crystal diamond. *Diamond and Related Materials* 33, 27–31.
- Yin, Z., Q. He, X. Huang, J. Zhang, S. Wu, P. Chen, G. Lu, P. Chen, Q. Zhang, Q. Yan, and H. Zhang (2012). Real-time DNA detection using pt nanoparticle-decorated reduced graphene oxide field-effect transistors. *Nanoscale* 4, 293–297.
- Yu, X., P. Rateron, J. Zhang, Z. Lin, L. Wang, and Y. Zhao (2012). Constitutive law and flow mechanism in diamond deformation. *Scientific Reports* 2, 1–7.

- Yu, Y., L. Wu, and J. Zhi (2014). Diamond nanowires: Fabrication, structure, properties, and applications. *Angewandte Chemie International Edition* 53, 14326–14351.
- Zalizniak, V. E. and O. A. Zolotov (2017). Efficient embedded atom method interatomic potential for graphite and carbon nanostructures. *Molecular Simulation* 43, 1480–1485.
- Zeiger, M., N. Jäckel, V. N. Mochalin, and V. Presser (2016). Review: carbon onions for electrochemical energy storage. *Journal of Materials Chemistry A* 4, 3172–3196.
- Zepeda-Ruiz, L. A., B. Sadigh, J. Biener, A. M. Hodge, and A. V. Hamza (2007). Mechanical response of freestanding Au nanopillars under compression. *Applied Physics Letters* 91, 101907.
- Zhang, B., L. Mei, and H. Xiao (2012). Nanofracture in graphene under complex mechanical stresses. *Applied Physics Letters* 101, 121915.
- Zhang, J., R. Wang, X. Zhu, A. Pan, C. Han, X. Li, D. Zhao, C. Ma, W. Wang, H. Su, and C. Niu (2017). Pseudo-topotactic conversion of carbon nanotubes to T-carbon nanowires under picosecond laser irradiation in methanol. *Nature Communications* 8(683), 1–7.
- Zhang, R.-S. and J.-W. Jiang (2018). The art of designing carbon allotropes. *Frontiers of Physics* 14, 10962–17.
- Zhang, S., J. Zhou, Q. Wang, X. Chen, Y. Kawazoe, and P. Jena (2015). Pentagraphene: A new carbon allotrope. *Proceedings of the National Academy of Sciences* 112, 2372–2377.
- Zhang, Y., J. Shang, W. Fu, L. Zeng, T. Tang, and Y. Cai (2018). A sp^2+sp^3 hybridized carbon allotrope transformed from AB stacking graphyne and THD-graphene. *AIP Advances* 8, 015028–8.

- Zhao, C.-X., C.-Y. Niu, Z.-J. Qin, X. Y. Ren, J.-T. Wang, J.-H. Cho, and Y. Jia (2016). H18 Carbon: A New Metallic Phase with sp^2 - sp^3 Hybridized Bonding Network. *Scientific Reports* 6(21879), 1–9.
- Zhao, H. and N. R. Aluru (2010). Temperature and strain-rate dependent fracture strength of graphene. *Journal of Applied Physics* 108, 064321.
- Zhong, C., Z.-M. Yu, Y. Xie, H. Wang, S. Zhang, Y. Chen, and S. A. Yang (2017). Three-dimensional Pentagon Carbon with a genesis of emergent fermions. *Nature Communications* 8, 1–7.
- Zhou, X. W., D. K. Ward, and M. E. Foster (2015). An analytical bond-order potential for carbon. *Journal of Computational Chemistry* 36, 1719–1735.
- Zhu, W., G. Kochanski, and S. Jin (1998). Low-field electron emission from undoped nanostructured diamond. *Science* 282, 1471–1473.
- Zhu, X. and M. Wang (2016). Porous CY carbon: a new semiconducting phase with an sp^1 - sp^2 - sp^3 bonding network. *RSC Advances* 6, 112035–112039.
- Zhu, X., M. F. Yuen, L. Yan, Z. Zhang, F. Ai, Y. Yang, P. K. Yu, G. Zhu, W. Zhang, and X. Chen (2016). Diamond-nanoneedle-array-facilitated intracellular delivery and the potential influence on cell physiology. *Advanced Healthcare Materials* 5, 1157–1168.
- Ziegler, J., J. Biersack, and U. Littmark (1985). *The Stopping and Range of Ions in Solids*, Volume 1. New York: Pergamon.
- Ziegler, J. F. (2004). SRIM-2003. *Nuclear Instruments and Methods in Physics Research Section B: Beam Interactions with Materials and Atoms* 219-220, 1027–1036.

Every reasonable effort has been made to acknowledge the owners of copyright material. I would be pleased to hear from any copyright owner who has been omitted or incorrectly acknowledged.